



University
of Glasgow

Ireland, Murray L. (2014) Investigations in multi-resolution modelling of the quadrotor micro air vehicle. PhD thesis.

<http://theses.gla.ac.uk/5719/>

Copyright and moral rights for this thesis are retained by the author

A copy can be downloaded for personal non-commercial research or study, without prior permission or charge

This thesis cannot be reproduced or quoted extensively from without first obtaining permission in writing from the Author

The content must not be changed in any way or sold commercially in any format or medium without the formal permission of the Author

When referring to this work, full bibliographic details including the author, title, awarding institution and date of the thesis must be given.



University
of Glasgow

INVESTIGATIONS IN MULTI-RESOLUTION
MODELLING OF THE QUADROTOR MICRO
AIR VEHICLE

MURRAY L IRELAND

Submitted in fulfilment of the requirements for the
Degree of Doctor of Philosophy

Aerospace Sciences Research Division
School of Engineering
College of Science and Engineering
University of Glasgow

May 2014

© 2014 Murray L Ireland

“One should never regret one’s excesses, only one’s failures of nerve.”

– Iain M. Banks (1954 – 2013)

PREFACE

This thesis presents work carried out by the author in the Aerospace Sciences Research Division at the University of Glasgow in the period from November 2010 to May 2014. The content is original except where otherwise stated.

ACKNOWLEDGEMENTS

This thesis describes a rather large portion of my adventure in academia over the last three and a half years, an experience which would have been far less enjoyable without the presence of some individuals, and near-impossible with some others.

First mention must go to Dave Anderson, who set me on this path with the phone call that brought me back to Glasgow. Without his expertise, enthusiasm and pragmatism, this thesis would not exist. I must also thank Selex ES for partially funding my research and providing valuable experience with the industrial side of engineering.

I'd like to thank my examiners, Euan McGookin and James Biggs, for making my viva actually quite enjoyable and for their constructive feedback which has only added to the value of this thesis. I must also thank Eric Gillies and Dougie Thomson for their advice on writing this thesis and surviving my viva, respectively. Thanks must also be extended to the rest of the academic staff in the Aerospace Sciences Research Division, whose collective knowledge has proven invaluable in reaching this stage. The support staff in the School of Engineering have also been a tremendous help with both practical and administrative tasks.

My colleagues in the postgraduate office must be thanked profusely for their part in making my postgraduate studies an enjoyable experience. Thank you for the extended tea breaks, lunches in the park, heated office discussions and adventures in the lab. In particular, I'd like to thank John, Aldo, Kevin, Ed and Nuno for their roles in helping me survive my PhD.

Likewise, my friends outside of the university have made my life in Glasgow over the last few years immeasurably rewarding and have been instrumental in keeping me out of the office when I needed it. To both old friends and newer ones, you have all helped to alleviate the seemingly-constant pressure of postgraduate research. Having taken up climbing during my PhD and finding it to be a great stress-reliever, I must thank those who encouraged me to start climbing and the others I met in making it a regular activity.

As with the decade or two before my PhD, the support from my family has been unconditional and taken for granted at times. Without them, I would never have made it this far. For the opportunities afforded to me, both now and

throughout my life, I am eternally thankful to my parents. And to my brothers, thank you for your friendship and your constant reminders to keep my ego in check, whether warranted or not.

Finally, to Karen. Thank you for making the last few months infinitely more enjoyable than they might have been.

ABSTRACT

Multi-resolution modelling differs from standard modelling in that it employs multiple abstractions of a system rather than just one. In describing the system at several degrees of resolution, it is possible to cover a broad range of system behaviours with variable precision. Typically, model resolution is chosen by the modeller, however the choice of resolution for a given objective is not always intuitive. A multi-resolution model provides the ability to select optimal resolution for a given objective. This has benefits in a number of engineering disciplines, particularly in autonomous systems engineering, where the behaviours and interactions of autonomous agents are of interest.

To investigate both the potential benefits of multi-resolution modelling in an autonomous systems context and the effect of resolution on systems engineering objectives, a multi-resolution model family of the quadrotor micro air vehicle is developed. The model family is then employed in two case studies. First, non-linear dynamic inversion controllers are derived from a selection of the models in the model family, allowing the impact of resolution on a model-centric control strategy to be investigated. The second case study employs the model family in the optimisation of trajectories in a wireless power transmission. This allows both study of resolution impact in a multi-agent scenario and provides insight into the concept of laser-based wireless power transmission.

In addition to the two primary case studies, models of the quadrotor are provided through derivation from first principles, system identification experiments and the results of a literature survey. A separate model of the quadrotor is employed in a state estimation experiment with low-fidelity sensors, permitting further discussion of both resolution impact and the benefits of multi-resolution modelling.

The results of both the case studies and the remainder of the investigations highlight the primary benefit of multi-resolution modelling: striking the optimal balance between validity and efficiency in simulation. Resolution is demonstrated to have a non-negligible impact on the outcomes of both case studies. Finally, some insights in the design of a wireless power transmission are provided from the results of the second case study.

CONTENTS

PREFACE	ii
ACKNOWLEDGEMENTS	iii
ABSTRACT	v
LIST OF FIGURES	xii
LIST OF TABLES	xix
NOMENCLATURE	xxi
1 INTRODUCTION	1
1.1 BACKGROUND	3
1.1.1 MATHEMATICAL MODELLING	3
1.1.2 THE QUADROTOR	3
1.1.3 WIRELESS POWER TRANSMISSION	4
1.2 MULTI-RESOLUTION MODELLING	5
1.3 OBJECTIVES AND METHODOLOGY	6
1.4 OUTLINE OF THESIS	7
1.5 PUBLICATIONS BY THE AUTHOR	8
2 REVIEW OF LITERATURE	10
2.1 MODEL COMPLEXITY AND META-MODELS	10
2.1.1 COMPLEXITY	11
2.1.2 META-MODELS	12
2.1.3 MULTI-RESOLUTION MODELLING	13
2.1.4 TYPES OF MATHEMATICAL MODEL	14
2.1.5 DISCUSSION OF REVIEW FINDINGS	15
2.2 THE QUADROTOR MICRO AIR VEHICLE	15
2.2.1 QUADROTOR MODELS IN LITERATURE	16
2.2.2 DISCUSSION OF MODEL RESOLUTION AND TYPE IN QUADRO- TOR LITERATURE	19

2.3	WIRELESS POWER TRANSMISSION	21
2.3.1	A BRIEF HISTORY OF WIRELESS POWER TRANSMISSION	22
2.3.2	LASERS VS MICROWAVES	23
2.3.3	STATE-OF-THE-ART	25
2.3.4	FUTURE DIRECTION	26
3	MODELLING THE QUADROTOR SYSTEM	27
3.1	VEHICLE DESCRIPTION	27
3.2	FRAMES OF REFERENCE AND KINEMATICS	28
3.2.1	CHOOSING AN APPROPRIATE KINEMATIC REPRESENTATION	30
3.2.2	FRAMES OF REFERENCE	31
3.2.3	KINEMATIC RELATIONSHIPS	32
3.3	RIGID BODY DYNAMICS	33
3.3.1	DERIVATION FROM NEWTON-EULER FORMALISM	33
3.3.2	DERIVATION FROM EULER-LAGRANGE FORMALISM	34
3.3.3	LINEARISED MODEL	36
3.4	QUADROTOR FORCES AND MOMENTS	36
3.4.1	GRAVITATIONAL FORCE	36
3.4.2	PROPULSIVE FORCE AND MOMENT	36
3.4.3	GYROSCOPIC TORQUE	37
3.4.4	AERODYNAMIC DRAG	37
3.5	ROTOR MODEL	37
3.5.1	PROPELLER MODEL	38
3.5.2	MOTOR MODEL	39
3.6	INPUTS AND PSEUDO-INPUTS	40
3.7	ADDITIONAL PHENOMENA	41
3.7.1	GROUND EFFECT	41
3.7.2	AIRFRAME BLOCKAGE AND DRAG	42
3.7.3	ATMOSPHERIC TURBULENCE	42
3.7.4	PROCESS NOISE	42
4	SYSTEM IDENTIFICATION OF THE QBALL-X4 QUADROTOR	44
4.1	THE MAST LABORATORY	45
4.2	BASIC PROPERTIES	45
4.3	CENTRE OF MASS	47
4.3.1	METHODOLOGY	47
4.3.2	EXPERIMENTAL RESULTS	49
4.4	MOMENTS OF INERTIA	50
4.4.1	THE BIFILAR TORSIONAL PENDULUM	51
4.4.2	EXPERIMENTAL RESULTS	53
4.5	ROTOR PROPERTIES AND DYNAMICS	53
4.5.1	METHODOLOGY	53
4.5.2	IDENTIFYING PROPERTIES OF A MECHANISTIC ROTOR MODEL	54

4.5.3	AN EMPIRICAL MODEL OF ROTOR BEHAVIOUR	56
4.6	VALIDATION OF QUADROTOR MODELS	60
4.6.1	METHODOLOGY	60
4.6.2	RESULTS	62
4.6.3	DISCUSSION OF VALIDATION RESULTS	63
5	A MULTI-RESOLUTION FAMILY OF QUADROTOR MODELS	66
5.1	PROPERTIES OF THE IDENTIFIED QUADROTOR MODELS	67
5.1.1	LINEARITY OF MODELS	67
5.1.2	MECHANISTIC AND EMPIRICAL MODELS	68
5.1.3	DIFFERING FORMALISMS	69
5.1.4	RESOLUTION	69
5.2	DEFINING THE MODEL FAMILY	71
5.3	A CANDIDATE MULTI-RESOLUTION MODEL FAMILY	72
5.3.1	LEVEL 1	72
5.3.2	LEVEL 2	74
5.3.3	LEVEL 3	75
5.3.4	LEVEL 4	76
5.3.5	LEVEL 5	77
5.4	BEYOND THE DESCRIBED MODEL FAMILY	78
5.4.1	ALTERNATIVES TO THE PRESENTED MODELS	78
5.4.2	EXTENDING THE MODEL FAMILY	79
6	AN INVESTIGATION OF THE EFFECTS OF MODEL RESOLUTION ON NON-LINEAR DYNAMIC INVERSION CONTROLLER DESIGN AND TESTING	81
6.1	THEORY OF DYNAMIC INVERSION	82
6.2	QUADROTOR CONTROLLER DESIGN AND STRUCTURE	84
6.3	DYNAMIC INVERSION OF QUADROTOR MODELS	85
6.3.1	LEVEL 1	86
6.3.2	LEVEL 2	88
6.3.3	LEVEL 3	89
6.4	STATE FEEDBACK CONTROL FOR MULTIPLE RESOLUTIONS	92
6.4.1	HEIGHT CONTROL	93
6.4.2	YAW CONTROL	95
6.4.3	HORIZONTAL POSITION CONTROL	97
6.4.4	STABILITY OF CLOSED-LOOP FLAT OUTPUT DYNAMICS	100
6.5	CONTROLLER TESTING ON MODEL FAMILY	101
6.5.1	STEP CHANGE IN HEIGHT RESPONSE	102
6.5.2	STEP INPUT IN YAW DIRECTION	108
6.5.3	STEP INPUT IN HORIZONTAL POSITION	110
6.5.4	FOLLOWING A TRAJECTORY	115

6.6	A COMPARISON OF NON-LINEAR DYNAMIC INVERSION CONTROL AND CONVENTIONAL PID	119
6.6.1	STRUCTURE OF THE PID CONTROLLER	119
6.6.2	TUNING OF PID GAINS	120
6.6.3	COMPARISON OF HEIGHT RESPONSE	120
6.6.4	COMPARISON OF YAW RESPONSE	121
6.6.5	COMPARISON OF HORIZONTAL POSITION RESPONSE	122
6.6.6	COMPARISON OF TRAJECTORY FOLLOWING	122
6.6.7	DISCUSSION OF RESULTS	124
6.7	DISCUSSION AND CONCLUSIONS	124
6.7.1	DISCUSSION OF CONTROLLER DESIGN AND RESULTS	124
6.7.2	CONCLUSIONS	126
7	INVESTIGATING THE EFFECTS OF MODEL RESOLUTION ON OPTIMISATION OF TRAJECTORIES FOR WIRELESS POWER TRANSMISSION	127
7.1	DESCRIPTION OF WIRELESS POWER TRANSMISSION SCENARIO AND THE ENERGY TRANSMISSION SYSTEM	128
7.2	ADDITIONAL GEOMETRY AND FRAME OF REFERENCE	130
7.3	MODELLING AND CONTROL OF AN ENERGY TRANSMISSION SYSTEM	132
7.3.1	ENERGY TRANSMISSION SYSTEM DESCRIPTION	132
7.3.2	SYSTEM MODEL	133
7.3.3	TRACKING CONTROLLER	135
7.4	TRAJECTORY DEFINITION AND QUADROTOR CONTROLLER REVISION	137
7.4.1	SMOOTH TRAJECTORY DEFINITION WITH POLYNOMIALS	138
7.4.2	CONTROLLER REVISION	139
7.4.3	CONTROLLER PAIRING	139
7.5	PROBLEM DESCRIPTION AND OPTIMISATION SETTINGS	140
7.5.1	OPTIMISATION PROBLEM	140
7.5.2	ERRORS	140
7.5.3	OPTIMISATION ALGORITHMS	142
7.6	RESULTS	146
7.6.1	SIMULATION SETUP	146
7.6.2	OPTIMISATION WITH TWO VARIABLES	147
7.6.3	OPTIMISATION WITH FOUR VARIABLES	154
7.6.4	OPTIMISATION WITH SIX VARIABLES	158
7.7	DISCUSSION OF RESULTS AND CONCLUSIONS	164
7.7.1	OPTIMISING TRAJECTORIES FOR WIRELESS POWER TRANSMISSION	164
7.7.2	EFFECTS OF MODEL RESOLUTION ON OPTIMISATION SOLUTIONS	164

8	CONCLUSIONS AND FURTHER WORK	167
8.1	DEVELOPMENT OF A MULTI-RESOLUTION MODEL	167
8.2	THE IMPACT OF MODEL RESOLUTION ON SYSTEMS ENGINEERING OBJECTIVES	168
8.3	BENEFITS OF A MULTI-RESOLUTION MODEL	170
8.4	TOWARDS SAFE AND EFFICIENT WIRELESS POWER TRANSMISSION	171
8.5	FUTURE WORK	171
8.5.1	MULTI-RESOLUTION MODELLING	171
8.5.2	WIRELESS POWER TRANSMISSION	172
A	THE SiFRE SIMULATION ENGINE	175
A.1	CLASSES	175
A.1.1	SIMULATION CLASS	175
A.1.2	BLACK BOX CLASS	176
A.1.3	AGENT CLASS	176
A.1.4	QUADROTOR CLASS	176
A.1.5	ETS CLASS	176
A.1.6	OPTIMISER CLASS	176
A.2	OUTPUT VISUALS	177
B	HARDWARE SPECIFICATIONS	179
B.1	QBALL-X ₄	179
B.2	OPTITRACK MOTION CAPTURE SYSTEM	179
C	MAST LABORATORY SETUP	181
C.1	CAMERA OPTIMISATION	181
C.2	EXPERIMENTAL FLIGHTS	182
D	DERIVATION OF RIGID BODY DYNAMICS	184
D.1	USING NEWTON-EULER FORMALISM	184
D.1.1	TRANSLATIONAL MOTION	184
D.1.2	ROTATIONAL MOTION	185
D.2	USING EULER-LAGRANGE FORMALISM	186
D.2.1	TRANSLATIONAL MOTION WITH VELOCITIES IN THE INERTIAL FRAME	186
D.2.2	TRANSLATIONAL MOTION WITH VELOCITIES IN THE BODY-FIXED FRAME	186
D.2.3	ROTATIONAL MOTION	187
D.3	PROOF FOR DERIVATIVE OF ROTATION MATRIX	188
E	ROTOR CHARACTERISATION DATA	189
E.1	LOADCELL CALIBRATION	189
E.1.1	THRUST TRANSDUCER	189
E.1.2	TORQUE TRANSDUCER	189

E.2	STEADY-STATE RELATIONSHIPS	191
F	CONTROLLER DESIGN DETAILS	198
F.1	TUNING THE ATTITUDE CONTROLLER	198
F.2	STABILITY ANALYSES OF LATERAL AND LONGITUDINAL RESPONSE	198
F.2.1	WITH SECOND-ORDER ATTITUDE RESPONSE	198
F.2.2	WITH THIRD-ORDER ATTITUDE RESPONSE	199
G	DATA TABLES	204
G.1	QBALL- X_4 QUADROTOR PROPERTIES	204
G.2	ENERGY TRANSMISSION SYSTEM AND PHOTSENSITIVE SENSOR PROPERTIES	205
G.3	QUADROTOR CONTROLLER PROPERTIES FOR WPT SIMULATION	206
G.4	AGENT STEP-SIZE FOR WPT SIMULATION	206
	BIBLIOGRAPHY	207

LIST OF FIGURES

1.1	A QUADROTOR MICRO AIR VEHICLE.	2
1.2	QBALL-X ₄ QUADROTOR MICRO AIR VEHICLE.	4
1.3	EXAMPLE SCENARIO OF WIRELESS POWER TRANSMISSION. THE AIRBORNE SYSTEM IS CHARGED BY A LASER EMITTER WHICH IS POWERED BY A MAINS SUPPLY OR GENERATOR. THE AIRCRAFT MAY EITHER BE CHARGED WHILE ON-MISSION, OR DEVIATE FROM THE MISSION TO ENTER A CHARGING MODE, WHILE OTHER AIRCRAFT CONTINUE THE MISSION.	5
2.1	RELATIONSHIP BETWEEN MODEL CONFIDENCE AND RESOLUTION, FROM LOBÃO AND PORTO (1997).	12
2.2	NIKOLA TESLA'S APPARATUS FOR TRANSMITTING ELECTRICAL ENERGY (TESLA, 1914).	23
2.3	NASA'S LASER-POWERED AIRCRAFT (NASA, 2010)	24
2.4	EFFECTS OF ATMOSPHERIC ATTENUATION ON TRANSMITTANCE OF WAVE WITH WAVELENGTH $\lambda = 532$ nm	25
3.1	QUADROTOR BODY FRAME OF REFERENCE WITH RESPECT TO WORLD FRAME AND VEHICLE FORCES AND MOMENTS. THE THRUST OF EACH ROTOR ACTS ALONG THE AXIS OF ROTATION, WHILE THE TORQUE OPPOSES THE DIRECTION OF ROTATION.	29
3.2	DEMONSTRATION OF ROTOR OUTPUTS ON RIGID-BODY FORCES.	29
4.1	THE UNIVERSITY OF GLASGOW'S MAST LABORATORY, SHOWING THE OPTITRACK MOTION CAPTURE SYSTEM AND ONE OF SEVERAL QUADROTOR MAVs.	46
4.2	LOCATION OF AND FORCES AT THE CENTRE OF MASS OF THE QUADROTOR AND THE THREE SUPPORT POINTS AT THE VERTICES OF THE PROTECTIVE CAGE.	47
4.3	THE CENTRE OF MASS EXISTS AT THE INTERSECTION OF THE TWO LINES I_1 AND I_2 . THE LINES ARE NORMAL TO THE PLANES DEFINED BY THE SUPPORT POINTS OF EACH ORIENTATION.	48

4.4	EXPERIMENTAL DATA PROVIDES THE RESULTANT FORCES AND POSITIONS OF EACH POINT, ALLOWING TWO PLANES TO BE DEFINED. THE POSITION OF THE CENTRE OF MASS IN EACH PLANE THEN PROVIDES THE THREE-DIMENSIONAL POSITION AT THE INTERSECTION OF EACH LINE.	49
4.5	THE BIFILAR TORSIONAL PENDULUM. THE BODY IS SUSPENDED AT TWO POINTS ON EITHER SIDE OF THE CENTRE OF MASS. BY ROTATING THROUGH ANGLE θ , THE BODY GAINS HEIGHT z . THE MOMENT WHICH DRIVES THE ROTATIONAL RESPONSE OF THE SYSTEM IS THEN PROVIDED BY THE WEIGHT OF THE BODY.	51
4.6	EXPERIMENTAL RIG FOR ROTOR CHARACTERISATION.	54
4.7	MEASURED THRUST AND TORQUE RELATIONSHIPS WITH ROTORSPEED AT STEADY-STATE.	55
4.8	THRUST CHARACTERISATION RESULTS.	56
4.9	TORQUE CHARACTERISATION RESULTS.	57
4.10	IDENTIFIED STEADY-STATE THRUST AND TORQUE MODELS OF QBALL-X4 QUADROTOR.	59
4.11	DATA SAMPLE FROM ROTOR DYNAMICS IDENTIFICATION. EXPERIMENTAL DATA IS COMPARED TO THE RESULTS OF APPLYING A STEP INPUT TO THE DESCRIBED THRUST AND TORQUE TRANSFER FUNCTIONS.	61
4.12	TRANSLATIONAL AND ROTATIONAL ACCELERATIONS FROM AN EMPIRICAL TEST ARE COMPARED WITH EXPECTED RESULTS FROM SIMULATION. THE SIMULATION MODEL IS DRIVEN BY THE INPUT SIGNALS RECORDING DURING EMPIRICAL TESTING.	64
4.13	TRANSLATIONAL AND ROTATIONAL ACCELERATIONS FROM AN ADDITIONAL EMPIRICAL TEST ARE COMPARED WITH EXPECTED RESULTS FROM SIMULATION.	65
5.1	BLOCK DIAGRAM OF MINIMUM INFORMATION REQUIRED FOR INPUT-OUTPUT MAPPING.	71
5.2	EXAMPLE OF MODELS AVAILABLE TO DESCRIBE THE QUADROTOR SYSTEM.	73
6.1	NESTED LOOP STRUCTURE OF QUADROTOR CONTROLLER WITH LINEARISING FEEDBACK BLOCKS.	85
6.2	COMPARISON OF THE CLOSED-LOOP RESPONSES IN HEIGHT FOR LEVELS 1 TO 3, WHERE THE ADDITIONAL POLE IN THE LEVEL 3 RESPONSE IS SPECIFIED TO BE $p_z = 20\omega_{n,z}$. THE ERROR e_z IS DEFINED BY $e_z = z_{1/2} - z_3$, WHERE z_i DENOTES THE RESPONSE AT LEVEL i .	96
6.3	COMPARISON OF THE CLOSED-LOOP RESPONSES IN HORIZONTAL POSITION FOR LEVELS 1 TO 3, WITH ATTITUDE RESPONSE NATURAL FREQUENCY $\omega_{n,a} = 10\omega_{n,p}$. THE ERROR e_x IS DEFINED BY $e_x = x_{DES} - x_i$, WHERE x_{DES} IS THE DESIRED RESPONSE AND x_i DENOTES THE RESPONSE AT LEVEL i .	99

6.4	UNIT STEP RESPONSE IN HEIGHT FOR LEVEL 1 CONTROLLER APPLIED TO MODEL FAMILY.	103
6.5	UNIT STEP RESPONSE IN HEIGHT FOR LEVEL 1 CONTROLLER APPLIED TO MODEL FAMILY, WITH LIMITS ON MAGNITUDE OF CONTROL INPUTS.	104
6.6	PHASE PLANE PLOT OF z AND \dot{z} FOR LEVEL 1 CONTROLLER APPLIED TO MODEL FAMILY, WITH LIMITED INPUT RANGE AND DESIRED SETTLING TIME $\tau_{s,z} = 0.2$ s.	105
6.7	UNIT STEP RESPONSE IN HEIGHT FOR LEVEL 2 CONTROLLER APPLIED TO LEVELS 2 TO 5 OF THE MODEL FAMILY.	106
6.8	UNIT STEP RESPONSE IN HEIGHT FOR LEVEL 3 CONTROLLER APPLIED TO LEVELS 3 TO 5 OF THE MODEL FAMILY.	107
6.9	UNIT STEP RESPONSE IN HEIGHT FOR LEVEL 3 CONTROLLER APPLIED TO LEVELS 3 TO 5 OF THE MODEL FAMILY, WITH LIMITS ON MAGNITUDE OF CONTROL INPUTS.	107
6.10	UNIT STEP RESPONSE IN YAW DISPLACEMENT FOR LEVEL 1 CONTROLLER APPLIED TO MODEL FAMILY.	108
6.11	UNIT STEP RESPONSE IN YAW DISPLACEMENT FOR LEVEL 2 CONTROLLER APPLIED TO LEVELS 2 TO 5 OF THE MODEL FAMILY.	109
6.12	UNIT STEP RESPONSE IN YAW DISPLACEMENT FOR LEVEL 3 CONTROLLER APPLIED TO LEVELS 3 TO 5 OF THE MODEL FAMILY.	110
6.13	UNIT STEP RESPONSE IN HORIZONTAL POSITION FOR LEVEL 1 CONTROLLER APPLIED TO MODEL FAMILY.	111
6.14	HEIGHT RESPONSE TO UNIT STEP INPUT IN x_d . THE DIFFERENCE IN BEHAVIOUR BETWEEN THE LEVEL 1 MODEL AND HIGHER-RESOLUTION LEVELS BECOMES APPARENT WHEN ROLLING OR PITCHING THE QUADROTOR. THE LEVEL 5 MODEL IS SHOWN TO HAVE A STEADY-STATE ERROR DUE TO THE NON-LINEAR ROTOR MODEL.	112
6.15	UNIT STEP RESPONSE IN HORIZONTAL POSITION FOR LEVEL 2 CONTROLLER APPLIED TO LEVELS 2 TO 5 OF THE MODEL FAMILY.	113
6.16	UNIT STEP RESPONSE IN HORIZONTAL POSITION FOR LEVEL 2 CONTROLLER APPLIED TO LEVELS 2 TO 5 OF THE MODEL FAMILY.	114
6.17	REFERENCE TRAJECTORY FOR MODEL COMPARISON.	115
6.18	RESPONSE OF EACH MODEL f_i , WHERE $i = \{1, 2, 3, 4, 5\}$, TO A SMOOTH TRAJECTORY COMMAND $\mathbf{y}_{t,d}(t)$ SUPPLIED TO CONTROLLER c_1 .	116
6.19	RESPONSE OF EACH MODEL f_i , WHERE $i = \{2, 3, 4, 5\}$, TO A SMOOTH TRAJECTORY COMMAND $\mathbf{y}_{t,d}(t)$ SUPPLIED TO CONTROLLER c_2 .	117
6.20	RESPONSE OF EACH MODEL f_i , WHERE $i = \{3, 4, 5\}$, TO A SMOOTH TRAJECTORY COMMAND $\mathbf{y}_{t,d}(t)$ SUPPLIED TO CONTROLLER c_3 .	118
6.21	COMPARISON OF NDI AND PID CONTROLLERS IN HEIGHT RESPONSE AND CORRESPONDING PSEUDO-INPUT.	121
6.22	COMPARISON OF NDI AND PID CONTROLLERS IN YAW RESPONSE AND CORRESPONDING PSEUDO-INPUT.	122

6.23	COMPARISON OF NDI AND PID CONTROLLERS IN HORIZONTAL POSITION RESPONSE AND CORRESPONDING PSEUDO-INPUT.	123
6.24	COMPARISON OF TRAJECTORIES FOLLOWED BY QUADROTORS UNDER NDI AND PID CONTROL.	124
6.25	COMPARISON OF NDI AND PID CONTROLLERS IN FOLLOWING A TRAJECTORY, DEMONSTRATING THE DIFFERENCES IN INPUT AND OUTPUT RESPONSES.	125
7.1	POOR BEAM STEERING OR INSUFFICIENT PROJECTED SENSOR AREA CAN RESULT IN OVERFILL OF THE SENSOR AND POSE A SAFETY HAZARD.	129
7.2	GEOMETRY OF QUADROTOR AND ETS AGENTS WITH RESPECT TO INERTIAL FRAME \mathcal{W} .	131
7.3	AXES DEFINITION OF REFERENCE FRAME \mathcal{E} , FIXED ON THE ENERGY TRANSMISSION SYSTEM'S ACTUATED PLATFORM.	132
7.4	PARTIALLY-CONSTRUCTED ENERGY TRANSFER SYSTEM, LACKING ONLY CAMERA AND LASER EMITTER.	133
7.5	GEOMETRY OF THE PINHOLE CAMERA MODEL. THE CAMERA CENTRE \mathbf{r}_C IS AT THE CENTRE OF THE COORDINATE SYSTEM. THE COORDINATES OF A POINT WITH POSITION \mathbf{r} IN EUCLIDEAN 3-SPACE ARE MAPPED TO 2-SPACE BY CONSIDERING THE INTERSECTION OF THE POINT WITH THE IMAGE PLANE, FIXED AT THE PRINCIPLE POINT \mathbf{p} ALONG THE PRINCIPLE AXIS x (HARTLEY AND ZISSERMAN, 2003).	134
7.6	ETS ROTATIONAL RESPONSE WITH VISUAL FEEDBACK FOR TARGET INITIALLY AT $\mathbf{r}^c = [200, 100]^T$.	137
7.7	EXAMPLE OF NELDER-MEAD SIMPLEX OF THREE VERTICES ON THE TWO-DIMENSIONAL HIMMELBLAU FUNCTION (HIMMELBLAU, 1972).	142
7.8	ERROR AND COST FUNCTION HISTORIES FOR EACH LEVEL DURING FLIGHTS WITH TRAJECTORY PROPERTIES DETERMINED BY TWO-PARAMETER OPTIMISATION OF 10 SECOND FLIGHT.	148
7.9	NEAR-OPTIMAL TRAJECTORIES FOR A 10 SECOND FLIGHT OF THE QUADROTOR AT EACH LEVEL, DETERMINED BY A TWO-PARAMETER OPTIMISATION.	149
7.10	COMPARISON OF COST FUNCTION MINIMA AND AVERAGE RUN-TIME PER FUNCTION CALL FOR EACH LEVEL, FOR TWO-PARAMETER OPTIMISATION OF 10 SECOND FLIGHT.	149
7.11	ERROR AND COST FUNCTION HISTORIES FOR EACH LEVEL DURING FLIGHTS WITH TRAJECTORY PROPERTIES DETERMINED BY TWO-PARAMETER OPTIMISATION OF 20 SECOND FLIGHT.	151
7.12	NEAR-OPTIMAL TRAJECTORIES FOR A 20 SECOND FLIGHT OF THE QUADROTOR AT EACH LEVEL, DETERMINED BY A TWO-PARAMETER OPTIMISATION.	151

7.13	COMPARISON OF COST FUNCTION MINIMA AND AVERAGE RUN-TIME PER FUNCTION CALL FOR EACH LEVEL, FOR TWO-PARAMETER OPTIMISATION OF 20 SECOND FLIGHT.	152
7.14	COMPARISON OF COST FUNCTION SURFACE CONTOURS FOR EACH LEVEL IN TWO-VARIABLE OPTIMISATION OF A 20 SECOND FLIGHT.	152
7.15	COST FUNCTIONS MANIFOLDS IN TWO-VARIABLE OPTIMISATION OF 20 SECOND FLIGHT, DEMONSTRATING HOW THE DIFFERENCE IN THE MANIFOLD GRADIENT BETWEEN LEVELS CAN PRODUCE DIFFERENT SOLUTIONS FOR IDENTICAL INITIAL CONDITIONS.	153
7.16	ERROR AND COST FUNCTION HISTORIES FOR EACH LEVEL DURING FLIGHTS WITH TRAJECTORY PROPERTIES DETERMINED BY FOUR-PARAMETER OPTIMISATION WITH INITIAL PARAMETER SET $\mathbf{X}_0 = [5, 0, -5, 0]^T$.	155
7.17	NEAR-OPTIMAL TRAJECTORIES OF QUADROTOR FLIGHT AT EACH LEVEL, DETERMINED BY A FOUR-PARAMETER OPTIMISATION WITH INITIAL PARAMETER SET $\mathbf{X}_0 = [5, 0, -5, 0]^T$.	155
7.18	ERROR AND COST FUNCTION HISTORIES FOR EACH LEVEL DURING FLIGHTS WITH TRAJECTORY PROPERTIES DETERMINED BY FOUR-PARAMETER OPTIMISATION WITH INITIAL PARAMETER SET $\mathbf{X}_0 = [5, -1.5, -8, 1.5]^T$.	157
7.19	NEAR-OPTIMAL TRAJECTORIES OF QUADROTOR FLIGHT AT EACH LEVEL, DETERMINED BY A FOUR-PARAMETER OPTIMISATION WITH INITIAL PARAMETER SET $\mathbf{X}_0 = [5, -1.5, -8, 1.5]^T$.	157
7.20	COMPARISON OF COST FUNCTION MINIMA AND AVERAGE RUN-TIME PER FUNCTION CALL FOR EACH LEVEL, FOR FOUR-PARAMETER OPTIMISATION.	158
7.21	ERROR AND COST FUNCTION HISTORIES FOR EACH LEVEL DURING FLIGHTS WITH TRAJECTORY PROPERTIES DETERMINED BY SIX-PARAMETER LINE-SEARCH OPTIMISATION WITH ARBITRARY INITIAL SEARCH SPACE.	160
7.22	NEAR-OPTIMAL TRAJECTORIES FOR A FLIGHT OF THE QUADROTOR AT EACH LEVEL, DETERMINED BY A SIX-PARAMETER LINE-SEARCH OPTIMISATION WITH ARBITRARY INITIAL SEARCH SPACE.	160
7.23	ERROR AND COST FUNCTION HISTORIES FOR EACH LEVEL DURING FLIGHTS WITH TRAJECTORY PROPERTIES DETERMINED BY SIX-PARAMETER LINE-SEARCH OPTIMISATION WITH NARROWED INITIAL SEARCH SPACE.	162
7.24	NEAR-OPTIMAL TRAJECTORIES FOR A FLIGHT OF THE QUADROTOR AT EACH LEVEL, DETERMINED BY A SIX-PARAMETER LINE-SEARCH OPTIMISATION WITH NARROWED INITIAL SEARCH SPACE.	162
7.25	COMPARISON OF COST FUNCTION MINIMA AND AVERAGE RUN-TIME PER FUNCTION CALL FOR EACH LEVEL, FOR SIX-PARAMETER OPTIMISATION.	163
7.26	COMPARISON OF APPLYING THE COST FUNCTION SOLUTIONS RESULTING FROM APPLYING THE OPTIMISED TRAJECTORY PROPERTIES OBTAINED FROM ONE LEVEL TO THE OTHERS.	163

7.27	COST FUNCTION HISTORY AND TRAJECTORIES OF FLIGHT AT EACH LEVEL WHEN FOLLOWING A TRAJECTORY DETERMINED BY OPTIMISATION OF THE LEVEL 1 MULTI-AGENT MODEL.	166
A.1	STILL CAPTURE OF ANIMATION SHOWING AGENT MOVEMENTS, WITH A SINGLE QUADROTOR AND ETS. THE ETS TRACKS THE QUADROTOR, WHILE THE QUADROTOR'S YAW DISPLACEMENT IS DEPENDENT ON THE ETS POSITION.	177
A.2	STILL CAPTURE OF ANIMATION SHOWING AGENT MOVEMENTS, TWO QUADROTORS AND TWO ETSs. <i>Quad1</i> IS A QUADROTOR DESCRIBED BY A LEVEL 1 MODEL WHILE <i>Quad5</i> IS A QUADROTOR DESCRIBED BY A LEVEL 5 MODEL. EACH QUADROTOR IS PAIRED WITH AN ETS.	178
A.3	STILL CAPTURE OF ANIMATION FROM THE VIEWPOINT OF THE CAMERA ON THE ETS. THE COMPASS IS USED TO SHOW THE DIRECTION AND INCLINATION OF THE CAMERA.	178
C.1	SIMULATED CAMERA COVERAGE OF FLIGHT VOLUME.	182
C.2	RECORDED FLIGHT TRAJECTORY COMPARED AGAINST COMMANDED TRAJECTORY, DURING AN AUTONOMOUS FLIGHT OF A MAST LABORATORY QUADROTOR.	183
C.3	CAPTURES OF QUADROTOR AUTONOMOUS FLIGHTS IN THE MAST LABORATORY.	183
E.1	DATA SAMPLES FOR THRUST LOADCELL CALIBRATION, DEMONSTRATING LINEAR RELATIONSHIP.	190
E.2	DATA SAMPLES FOR TORQUE LOADCELL CALIBRATION IN THE CLOCKWISE DIRECTION, WITH LINEAR LINE OF BEST FIT.	192
E.3	DATA SAMPLES FOR TORQUE LOADCELL CALIBRATION IN THE COUNTER-CLOCKWISE DIRECTION, WITH LINEAR LINE OF BEST FIT.	192
E.4	ROTOR 1 (REAR) CHARACTERISATION DATA.	193
E.5	ROTOR 2 (FRONT) CHARACTERISATION DATA.	194
E.6	ROTOR 3 (LEFT) CHARACTERISATION DATA.	195
E.7	ROTOR 4 (RIGHT) CHARACTERISATION DATA.	196
E.8	ROTOR CHARACTERISATION DATA WITH CONSTANT-VOLTAGE POWER SOURCE.	197
F.1	RESPONSE OF LEVEL 1 MODEL FOR STEP INPUT IN x_d TO LEVEL 1 CONTROLLER, WITH SETTINGS $\zeta_p = 1$, $\zeta_a = 1$, $\tau_{s,p} = 2$ s. VARYING THE NATURAL FREQUENCY OF THE CLOSED-LOOP ATTITUDE RESPONSE RELATIVE TO THE NATURAL FREQUENCY OF THE POSITION RESPONSE IS SHOWN TO IMPACT THE POSITION RESPONSE.	200

-
- F.2 INPUTS TO LEVEL 1 MODEL FOR STEP INPUT IN x_d TO LEVEL 1 CONTROLLER, WITH SETTINGS $\zeta_p = 1$, $\zeta_a = 1$, $\tau_{s,p} = 2$ s. VARYING THE NATURAL FREQUENCY OF THE CLOSED-LOOP ATTITUDE RESPONSE RELATIVE TO THE NATURAL FREQUENCY OF THE POSITION RESPONSE IS SHOWN TO IMPACT THE MAGNITUDE OF THE CONTROL INPUTS TO THE SYSTEM. 201
- F.3 RESPONSE OF LEVEL 1 MODEL FOR STEP INPUT IN x_d TO LEVEL 1 CONTROLLER, WITH SETTINGS $\zeta_p = 1$, $\omega_{n,a} = 10\omega_{n,p}$, $\tau_{s,p} = 2$ s. VARYING THE DAMPING RATIO ζ_a OF THE CLOSED-LOOP ATTITUDE RESPONSE IS SHOWN TO IMPACT THE POSITION RESPONSE. 202
- F.4 INPUTS TO LEVEL 1 MODEL FOR STEP INPUT IN x_d TO LEVEL 1 CONTROLLER, WITH SETTINGS $\zeta_p = 1$, $\zeta_a = 1$, $\tau_{s,p} = 2$ s. VARYING THE DAMPING RATIO ζ_a OF THE CLOSED-LOOP ATTITUDE RESPONSE IS SHOWN TO IMPACT THE MAGNITUDE OF THE CONTROL INPUTS TO THE SYSTEM. 203

LIST OF TABLES

4.1	BASIC QBALL- X_4 PROPERTIES.	46
4.2	MEASURED MOMENTS OF INERTIA, COMPARED WITH VALUES SUPPLIED BY THE VENDOR OF THE QBALL.	53
4.3	IDENTIFIED THRUST AND TORQUE COEFFICIENTS, COMPARED TO VALUES PROVIDED BY BRANDT AND SELIG (2011) FOR IDENTICAL PROPELLER AT COMPARABLE ROTORSPEED.	55
4.4	COEFFICIENTS OF POLYNOMIALS RELATING THRUST AND TORQUE TO PWM AND VOLTAGE.	57
4.5	GAINS OF LINEAR MODELS RELATING THRUST AND TORQUE TO ZEROED PWM COMMAND.	58
4.6	COEFFICIENTS OF THE TRANSFER FUNCTIONS DESCRIBING THRUST AND TORQUE RESPONSE.	59
5.1	CONTRIBUTIONS OF ADDITIONAL PHENOMENA TO THE RESOLUTION OF THE MODEL FAMILY, AND ANY PREREQUISITES WHICH ARE REQUIRED BY A MODEL OF THE PHENOMENON.	80
7.1	TRAJECTORY PROPERTIES OBTAINED FROM TWO-PARAMETER OPTIMISATION OF 10 SECOND FLIGHT.	148
7.2	TRAJECTORY PROPERTIES OBTAINED FROM TWO-PARAMETER OPTIMISATION OF 20 SECOND FLIGHT.	150
7.3	TRAJECTORY PROPERTIES OBTAINED FROM EXAMPLE FOUR-PARAMETER OPTIMISATION, WITH INITIAL PARAMETER SET $\mathbf{X}_0 = [5, 0, -5, 0]^T$.	154
7.4	TRAJECTORY PROPERTIES OBTAINED FROM EXAMPLE FOUR-PARAMETER OPTIMISATION, WITH INITIAL PARAMETER SET $\mathbf{X}_0 = [5, -1.5, -8, 1.5]^T$.	156
7.5	TRAJECTORY PROPERTIES OBTAINED FROM OPTIMISATION USING SIX-PARAMETER LINE-SEARCH ALGORITHM WITH ARBITRARY INITIAL SEARCH SPACE.	159
7.6	BOUNDARY CONDITIONS AND NEAR-OPTIMAL SOLUTIONS FOR GLOBAL MINIMISATION OF LEVEL 1 MODEL USING SIMULATED ANNEALING.	159

7.7	TRAJECTORY PROPERTIES OBTAINED FROM OPTIMISATION USING SIX-PARAMETER LINE-SEARCH ALGORITHM WITH NARROWED INITIAL SEARCH SPACE.	161
B.1	OPTITRACK MOTION CAPTURE SYSTEM SPECIFICATION.	180
E.1	DATA SAMPLES FOR THRUST LOADCELL CALIBRATION.	190
E.2	DATA SAMPLES FOR CLOCKWISE TORQUE LOADCELL CALIBRATION.	191
E.3	DATA SAMPLES FOR COUNTER-CLOCKWISE TORQUE LOADCELL CALIBRATION.	191
F.1	ROUTH-HURWITZ MATRIX FOR CLOSED-LOOP LONGITUDINAL/LATERAL STABILITY AS DESCRIBED BY LEVEL 1/2 MODEL.	199

NOMENCLATURE

UNITS

All units of measurement throughout this thesis conform to the *Système Internationale*, with deviations from this rule noted where appropriate.

NOTATION

This section describes the general form of notation for properties such as scalars, vectors and matrices and their derivatives.

TIME DERIVATIVES

\dot{x}	first derivative of x with respect to time
\ddot{x}	second derivative of x with respect to time
$x^{(n)}$	n th derivative of x with respect to time

SCALARS, VECTORS AND MATRICES

x	scalar
\mathbf{x}	vector or matrix
\mathbf{x}^T	transpose of vector or matrix
x_i	i th element of vector \mathbf{x}
$f(x)$	function of scalar x
$f(\mathbf{x})$	function of vector or matrix \mathbf{x}
$f_{\mathbf{x}}$	Jacobian of $f(\mathbf{x})$ with respect to \mathbf{x}
L_f	Lie derivative in the direction of $f(\mathbf{x})$

SYMBOLS

The following symbols are used throughout this thesis. Where a symbol is used only briefly, it is defined at the appropriate point in the text.

LATIN

C_Q	non-dimensional torque coefficient
C_T	non-dimensional thrust coefficient
\mathbf{C}	control matrix for mapping pseudo-inputs
$c_{Q1}, c_{Q2}, c_{Q3}, c_{Q4}$	coefficients of torque response transfer function
c_{T1}, c_{T2}	coefficients of thrust response transfer function
\mathbf{F}	force vector
g	acceleration due to gravity
I	moment of inertia
\mathbf{I}	inertia matrix
\mathbb{I}	identity matrix
\mathbf{J}_η	Jacobian matrix in angular rate transformation
K_Q	quadrotor torque coefficient
K_T	quadrotor thrust coefficient
k_{Q1}, k_{Q2}, k_{Q3}	coefficients of torque polynomial
k_{T1}, k_{T2}, k_{T3}	coefficients of thrust polynomial
L	rotor hub distance from centre of mass
\mathbf{M}	moment vector
m	mass
\hat{n}	unit surface normal or unit direction vector
p	pole of system
p, q, r	angular velocities about quadrotor body axes
Q	torque
\mathbf{q}	generalised co-ordinate vector
$\mathbf{R}_{\mathcal{A}}^{\mathcal{B}}$	transformation matrix from frame \mathcal{A} to frame \mathcal{B}

\mathbf{r}	position vector
T	thrust
t	time
u, v, w	components of inertial velocity in body-fixed frame
u_i	zeroed PWM input to rotor i
$u_{\text{col}}, u_{\text{lat}},$ $u_{\text{long}}, u_{\text{yaw}}$	pseudo-inputs
\bar{u}_0	zero-thrust PWM value
\bar{u}_i	raw PWM input to rotor i
\mathbf{u}	input vector
\mathbf{u}^*	pseudo-input vector
\mathbf{v}	linear velocity vector
\mathbf{X}	parameter set
x, y, z	components of position
\mathbf{x}	state vector
\mathbf{y}	output vector

GREEK

ζ	damping ratio of system
$\boldsymbol{\eta}$	attitude vector of Euler angles
ν	relative degree of system
ρ	atmospheric density
τ	time constant of ETS actuator open-loop response
Φ	cost function
ϕ, θ, ψ	roll, pitch and yaw displacements
Ω	rotorspeed
ω_R	bandwidth of simplified rotor response
ω_n	natural frequency of system
$\boldsymbol{\omega}$	angular velocity vector

SUBSCRIPTS

C	property of optical camera
E	property of energy transmission system
L	property of laser emitter
LS	property of laser spot
Q	property of quadrotor

SUPERSCRIPTS

\mathcal{C}	energy transmission system camera space
\mathcal{E}	energy transmission system platform-fixed frame
\mathcal{B}	quadrotor body-fixed frame
\mathcal{S}	photodiode sensor frame
\mathcal{W}	world frame

ABBREVIATIONS

DCM	direction cosine matrix
DES	discrete event system
DEVS	Discrete Event System Specification
EKF	extended Kalman filter
ESC	electronic speed controller
ETS	energy transmission system
FOV	field of view
GCS	ground control station
IMU	inertial measurement unit
LED	light-emitting diode
MAST	Micro Air Systems Technologies
MAV	micro air vehicle
MAVERIC	Modelling of Autonomous Vehicle Environments using Robust, Intelligent Computing
MRM	multi-resolution modelling

NASA	National Aeronautics and Space Administration
NDI	non-linear dynamic inversion
OOP	object-oriented programming
PID	proportional integral derivative
PWM	pulse-width modulation
SBSP	space-based solar power
SiFRe	Simulation Framework for investigations in Resolution
SISO	single-input, single-output
SLAM	simultaneous localisation and mapping
SPS	solar power satellite
SysML	Systems Modeling Language
UAV	unmanned aerial vehicle
UKF	unscented Kalman filter
UML	Unified Modeling Language
WPT	wireless power transmission

CHAPTER 1

INTRODUCTION

“Frustra fit per plura quod potest fieri per pauciora”

- William of Ockham (1323)

“It is futile to do with more things that which can be done with fewer.” Ockham’s (or Occam) razor is a useful principle to adhere to in problem solving. It states that, for a problem with more than one solution, the solution with the fewest elements or parts is preferable. In the context of mathematical modelling, the principle may be formulated slightly differently. If two models, describing the same system, provide the same prediction, the model with the fewest elements and simplest relationships is preferable. Justification for this choice is intuitive. A simpler model is faster to develop, faster to solve and has fewer elements to be subject to errors. In tribute to the principle, consider a simple example. A non-linear system is linearised about some trim state. Around this operating point, both the linear and non-linear models provide the same predictions. The linear model is therefore “better”, being inherently simpler. Deviating from this trim state, the predictions of each model begin to diverge. The linear model is no longer valid and the non-linear model is now better. However, what if the system spends significant time in the vicinity of this trim state? What if the non-linear model is *only* required when deviations from trim are significant enough that the linear model provides inaccurate predictions. If the linear model is better around trim on account of its simplicity, while the non-linear model is better at other times on account of its validity, is it possible to identify exactly when to use which model?

One solution to this problem is found in the concept of *Multi-Resolution Modelling* (MRM). A multi-resolution model describes the same system or phenomena with varying degrees of detail or resolution. This allows the optimal resolution to be used when predicting system behaviours in a given scenario.



FIGURE 1.1: A QUADROTOR MICRO AIR VEHICLE.

While popularised by Paul Davis in simulation of military engagements, applications in other areas such as model-based systems engineering are virtually non-existent. Recent efforts, such as the MAVERIC (Modelling of Autonomous Vehicle Environments using Robust, Intelligent Computing) simulation engine in ongoing development at the University of Glasgow (Anderson and Carson, 2009; Anderson and Thomson, 2014), represent an initial foray into this area. MAVERIC allows the speed and accuracy of predictions of autonomous system behaviours in single- and multi-agent scenarios to be balanced by automatically selecting agent model resolutions based on user input and incidental events. The question then becomes one of what resolution to employ in describing the autonomous system at any given time. How does one identify the “best” resolution for a model with a given objective? Or, recalling Ockham’s razor, how simple can a model be in providing an accurate solution to a problem?

The wealth of both autonomous systems and potential problems provides an indication of the difficulty in obtaining a general answer to this question. Instead, a specific case is studied, and some example problems are investigated, with the hope that some general conclusions relating to model complexity, fidelity and suitability against specific measures of effectiveness may be drawn. The quadrotor Micro Air Vehicle (MAV) is a small-scale Unmanned Aerial Vehicle (UAV) (Gremillion and Humbert, 2010) which has found popular use in the fields of aerial robotics (Michael, Mellinger, Lindsey, and Kumar, 2010), autonomous systems design (Cowling, 2008), advanced control theory (Das, Subbarao, and Lewis, 2009) and trajectory optimisation (Cowling, Yakimenko, Whidborne, and Cooke, 2007). As a result of its popularity and mechanical simplicity, models of the quadrotor are prolific in literature and are often tailored to a given objective.

Therefore, in an effort to determine whether model resolution impacts the outcome of such objectives, a multi-resolution model of the quadrotor is developed and employed to investigate two objectives. The first is control system design, using an approach which is highly dependent on a model of the system to be controlled. The second is trajectory optimisation, investigating which trajectories the quadrotor must follow to minimise risk in a wireless power transmission scenario. This latter objective represents a use of the quadrotor platform with contemporary relevance and is indicative of the applications MAVERIC is intended for.

1.1 BACKGROUND

1.1.1 MATHEMATICAL MODELLING

The aircraft design process has changed dramatically since the maiden flight of the Wright Flyer in 1903. The development of early aircraft was characterised by a trial-and-error approach which was costly and time-consuming. The invention and continued advancement of computers has provided the alternative design approach of simulation, where a model of a system may be used to predict its behaviour. A system may be modelled mathematically and tested in simulation before any empirical testing, reducing much of the uncertainty associated with initial practical experiments (NASA, 2007).

Such an approach is, however, dependent on the accuracy or validity of the model. A model is simply an abstraction of reality (Davis and Bigelow, 1998), describing behaviours in much simpler terms than the vastly complex processes of the real system. The level of abstraction from reality in a model can be inversely related to its resolution, or the level of detail with which the model describes the system behaviour. The resolution of a given model is typically at the discretion of the modeller, who draws upon experience to tailor the model to the requirements of an objective.

1.1.2 THE QUADROTOR

The quadrotor is a small-scale unmanned rotorcraft which has found popular use in both practical and research applications. Its hover and low-speed flight capabilities and comparative simplicity next to the traditional helicopter (Carrillo, López, Lozano, and Pégard, 2012) have found it roles primarily in surveillance, reconnaissance and aerial photography (Gupte, Mohandes, and Conrad, 2012). Suggested future applications include agricultural and environmental monitoring and construction, the latter accomplished through multi-vehicle co-ordination. Research applications of the quadrotor have seen its use as a platform for testing concepts in control theory (Voos, 2009), trajectory generation (Cowling et al., 2007), visual navigation (Blösch, Weiss, Scaramuzza, and Siegwart, 2010), robotics and multi-vehicle control and co-ordination (Mellinger,



FIGURE 1.2: QBALL-X4 QUADROTOR MICRO AIR VEHICLE.

Shomin, Michael, and Kumar, 2010b). Research applications typically employ a model of the quadrotor in the first stages of the investigation.

The quadrotor models described in this thesis are developed using a combination of approaches. First, the literature highlights a multitude of models describing various aspects of the quadrotor system. Second, relationships may be derived mechanistically using an appropriate formalism, as in Bouabdallah (2007). Thirdly, statistical models are developed using system identification of an actual quadrotor vehicle, as in Chamberlain (2011). Regardless of their source, the models are populated with empirical data obtained from the Qball-X4 (Figure 1.2).

1.1.3 WIRELESS POWER TRANSMISSION

Wireless Power Transmission (WPT) involves the transfer of power through the use of wireless media such as lasers or microwaves. Removed of the need for a human pilot, UAVs are limited in their endurance only by the capacity of their power source. Large aircraft such as the MQ-1 Predator (General Atomics, 2013) are typically very efficient in their power consumption due to their fixed-wing configuration. Qinetiq's Zephyr combined with a large wing surface area with solar panels and a rechargeable battery to provide record-breaking endurance (Putrich, 2010). Aircraft such as the quadrotor are far less efficient and have small payload capability, resulting in short endurance and a lack of capacity for significant onboard power reserves.

Combined with its short-range, low-altitude applications, the poor endurance of the quadrotor make it an ideal platform for narrow-beam wireless power, particularly laser-based transmission. While not a novel concept, the technology has recently reached a state of maturity where it has practical application to the unmanned systems industry and specifically the quadrotor

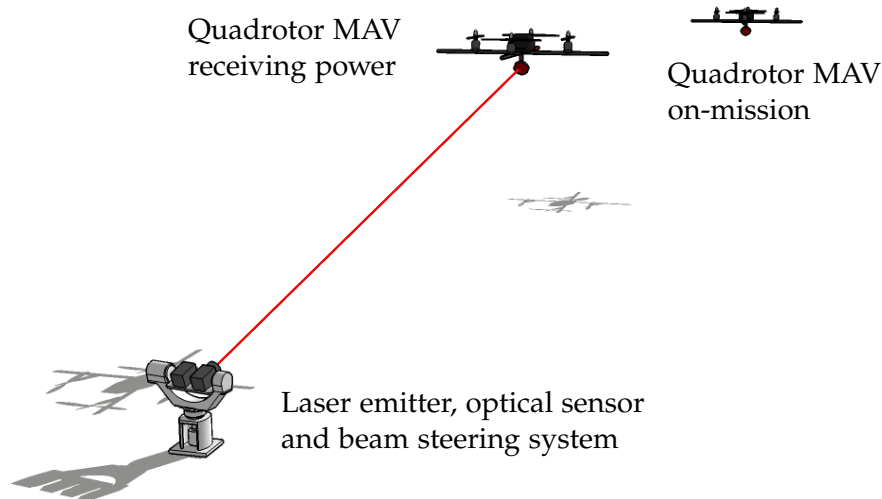


FIGURE 1.3: EXAMPLE SCENARIO OF WIRELESS POWER TRANSMISSION. THE AIRBORNE SYSTEM IS CHARGED BY A LASER EMITTER WHICH IS POWERED BY A MAINS SUPPLY OR GENERATOR. THE AIRCRAFT MAY EITHER BE CHARGED WHILE ON-MISSION, OR DEVIATE FROM THE MISSION TO ENTER A CHARGING MODE, WHILE OTHER AIRCRAFT CONTINUE THE MISSION.

(Achtelik, Stumpf, Gurdan, and Doth, 2011).

Figure 1.3 highlights the participant systems and interactions of a wireless power transmission. An airborne system such as the quadrotor is charged by a laser emitter which is powered by a mains supply or generator. The aircraft may either be charged while on-mission, or deviate from the mission to enter a charging mode. Regardless of the approach taken, laser-based WPT is a technology faced with numerous safety concerns. Both the safety and efficiency of the transmission are critically dependent on the precision of the target tracking and beam steering system. While a responsive PI controller contributes to this precision, it may be further augmented through robust co-operation of the Energy Transmission System (ETS) and the receiving aircraft. Reduction of tracking errors and improvement of power transfer efficiency are goals which can be accomplished through optimisation of the quadrotor's trajectory while receiving power. This represents an ideal case study for a multi-resolution model of the quadrotor.

1.2 MULTI-RESOLUTION MODELLING

Multi-resolution modelling involves the modelling of a system or phenomenon at multiple levels of *resolution*. This approach has most popularly been applied to military engagement simulation by Paul K. Davis , but the following definitions, provided in Davis and Bigelow (1998), hold true for mathematical modelling in general.

Detail in a model is primarily dependent on two properties: scope and resolution. Scope concerns the extent of the modelled system, its inputs and its outputs. A model with narrow scope might describe the inflow through a

single rotor, while a model with wide scope could describe the interactions and behaviour of several aircraft.

Resolution describes the level of detail with which components in the system are described. In the context of a dynamic system such as the quadrotor, this could be related to the size of the system state, the degree of non-linear coupling in the states or the number of phenomena described.

A multi-resolution model therefore describes the same system or phenomenon with multiple levels of resolution. According to Davis and Bigelow (1998), multi-resolution modelling is:

1. Building a single model with alternate user modes involving different levels of resolution for the same phenomena
2. Building an integrated family of two or more mutually consistent models of the same phenomena at different levels of resolution.
3. Both of the above.

The literature review highlights the lack of a single definition for resolution, or indeed multi-resolution modelling. This is likely due to the variance in both types of models and their applications. Definitions of both with reference to modelling of dynamic systems are therefore of great interest.

1.3 OBJECTIVES AND METHODOLOGY

The research objectives may be explicitly stated as follows:

1. Investigate how model resolution affects the outcomes of typical objectives in the design process, such as control system design and trajectory optimisation.
2. Determine the benefits, if any, that multi-resolution modelling brings to quadrotor design and autonomous system design in general.
3. Identify the principle parameters in the design of a wireless power transmission control system.

The first and second objectives require development of a multi-resolution model family and application of it to two case studies. First, a literature review is undertaken to identify existing efforts in multi-resolution modelling and any descriptions of meta-models and model complexity. Next, the use of quadrotor models in literature is examined, with reference to the resolution of the described models and their applications. A multi-resolution model family is then developed using the approaches of: deriving relationships from first principles; incorporating phenomena described in the literature; and identification of empirical models through testing of the Qball-X4 quadrotor. The multi-resolution model is then constructed as a family of models with successive increases in

resolution between each *level* and is employed in two case studies. The first case study is an investigation of the effects of resolution on model-centric controller design, using a heuristic approach. This involves the development of a control law which is strongly dependent on the model of the system: in this case, non-linear dynamic inversion. A heuristic approach is employed as the derived closed-loop systems are highly complex, making analytical stability analysis non-trivial. The second is the optimisation of vehicle trajectories in a wireless power transmission and investigation of the effects of model resolution on the optimisation solutions. The results of these case studies and the literature review then allow discussion of the effects of resolution on such systems engineering objectives and identification of the benefits of multi-resolution modelling to autonomous systems engineering of MAVs.

The third objective is accomplished through the case study on trajectory optimisation, by analysing the results of the wireless power transmission in a more general sense.

Each of the three objectives utilises the bespoke SiFRe (Simulation Engine for investigations in Resolution) simulation engine, which was developed in MATLAB[®] (The MathWorks, Inc, 2014b) during the course of this project. SiFRe is a multi-agent engine designed to permit simultaneous simulation of agents of same or different type, including similar agents of different resolution. Its primary benefits are: the ability to solve several quadrotor models of varying resolution simultaneously and compare the solutions; the ability to model the behaviours and interaction of two agents of different type, as required by the wireless power transmission model.

1.4 OUTLINE OF THESIS

Chapter 2 describes the results of a literature review in the areas of: multi-resolution modelling and model complexity; investigations which employ models of the quadrotor system and subsystems; and the history and state-of-the-art of wireless power transmission.

Chapter 3 presents mechanistic models of the quadrotor system. Rigid-body dynamics are derived from both Newton-Euler and Euler-Lagrange formalisms and compared. Force and moment contributions to the system are detailed. Some mechanistic rotor models are introduced.

Chapter 4 provides the results of performing system identification on the Qball-X4 quadrotor. A variety of system identification techniques are employed to populate the quadrotor rigid-body model with empirical data. Black-box system identification is used to determine a statistical rotor model, which is demonstrated to be both non-linear and dynamic. This model is abstracted to provide rotor models of lower resolution. Finally, empirical acceleration data from a flight of the Qball-X4 is contrasted with predictions from a candidate model of the quadrotor system, highlighting the presence of unmodelled dy-

namics.

Chapter 5 discusses the identified properties of the mechanistic and empirical quadrotor models described in Chapters 3 and 4 respectively. Reference is made to the results of the literature review. This discussion leads to the description of a candidate multi-resolution model family, describing the quadrotor system at several *levels* of resolution. Each level is discussed with reference to applications typical of its resolution and the source models highlighted. Some alternate models and additional phenomena for hypothetical higher levels of resolution are discussed.

Chapter 6 employs the multi-resolution model family in an investigation of controller design and stability. Dynamic inversion is applied to Levels 1 to 3 of the model family to derive three non-linear controllers of increasing resolution. The stability of each controller in loop with its source model is verified by a candidate Lyapunov function. Each controller is then tested in simulation on each level of the model family for several cases.

Chapter 7 employs the multi-resolution model family in investigating optimal trajectories for wireless power transmission. The quadrotor model family is employed in a multi-agent simulation which describes the interaction of the quadrotor with an energy transmission system. Operational safety is a primary concern when employing high-power laser beams. The trajectories of the quadrotor when receiving power via laser beam are optimised to maximise the safety of the operation. The differences in optimisation solutions between models of different resolution are investigated and the impact of these differences discussed. The multi-agent simulations are executed by the SiFRe simulation engine, inspired by MAVERIC.

Chapter 8 presents conclusions on the work described in this thesis and introduces some suggestions for future work in the areas of multi-resolution modelling, autonomous systems and wireless power transmission.

The appendices describe some additional information which is not crucial to the narrative of the main body of the thesis. This includes information on the Qball-X4 quadrotor, the SiFRe simulation engine, the MAST Laboratory used in empirical testing, greater detail on some model derivations, system identification data and a list of properties and their values.

1.5 PUBLICATIONS BY THE AUTHOR

The work described in this thesis has directly contributed to the following publications.

- Ireland, M and Anderson, D. Development of Navigation Algorithms for Nap-of-the-Earth UAV Flight in a Constrained Urban Environment. In *Proceedings of the 28th International Congress of the Aeronautical Sciences*, Brisbane, 2012.

-
- Murray, CWA, Ireland, ML and Anderson, D. On the Response of an Autonomous Quadrotor Operating in a Turbulent Environment. In *Proceedings of the 2014 AUVSI Unmanned Systems Conference*, Orlando, FL, 2014.
 - Ireland, ML and Anderson, D. An Investigation of the Effects of Model Resolution on Control of a Quadrotor Micro Air Vehicle. In *Proceedings of the 2014 World Congress on Unmanned Systems Engineering*. Oxford, 2014.
 - Vargas, A, Ireland, M and Anderson, D. Swing-Free Maneuver Controller for a RUAS Slung-Load System Using ESN. In *Proceedings of the 2014 World Congress on Unmanned Systems Engineering*. Oxford, 2014.

CHAPTER 2

REVIEW OF LITERATURE

The literature on multi-resolution modelling is broad and typically focussed on applications outside of systems engineering, but the general principles behind the idea, and the concept of *meta-models* (Simpson, Peplinski, Koch, and Allen, 2001) may be investigated and used to aid development of a multi-resolution quadrotor model. The quadrotor itself is a prominent fixture in literature relating to autonomous systems and robotics. A variety of topics involving the platform have been covered, including controller design, trajectory generation, development of high-resolution models and practical experiments which take advantage of the quadrotor's manoeuvrability and hover capabilities. Finally, the multi-resolution quadrotor model is used in a case study – wireless power transmission – to investigate its effectiveness. The history and state-of-the-art of this technology is briefly discussed.

2.1 MODEL COMPLEXITY AND META-MODELS

Models are used extensively in a variety of areas, including psychology, meteorology, military operations and, of course, engineering. As models are abstract descriptions of reality, development of a model requires consideration of the degree of abstraction used in describing that reality. This introduces the concepts of model complexity and meta-models. Resolution is considered one aspect of model complexity, thus some investigation of complexity and its effects on the system design process are of interest. A meta-model is a description of a model or models; essentially a model of models (Simpson et al., 2001). A multi-resolution model, typified by its very nature as a collection of several models, might therefore benefit from some ontology to describe its general structure and processes. Existing meta-models which might permit such a description are therefore investigated. Finally, the term *model* can be used to describe a variety of abstractions, including physical models, logical models and a variety of mathematical models. The latter is of specific interest in this

case and may be further categorised by a number of properties. Description of these properties is made in order to aid later discussion of the quadrotor models described in this thesis.

2.1.1 COMPLEXITY

As highlighted by Chwif, Barretto, and Paul (2000), complexity in modelling has no universal definition but can be interpreted in one of two ways. The first is related to one's understanding of the system being modelled, while the second is more concerned with the number of elements that comprise the model. These concepts are characterised by Ward (1989) as *transparency* and *constructive simplicity*, respectively. In the context of dynamic systems modelling, one would understand the behaviour of a model of high transparency fairly intuitively. The behaviours described by a model of low transparency would be less simple to comprehend. A model of high constructive simplicity would consist of fewer states and non-linear behaviours, while low constructive simplicity denotes the opposite. Detail in the model, as described by Davis and Bigelow (1998), is then analogous to constructive simplicity, or constructive complexity. Constructive complexity may then be further split into two properties: scope, concerning the extents of the simulation; and level of detail, which is analogous to resolution.

Chwif et al. (2000) describe the impact of scope and resolution on *model confidence* – effectively the validity of the model. A simpler model – one of narrower scope and lower resolution – is desired primarily because it is easier to implement, validate and analyse. A simple model is also easier to adjust if the system properties change or it can be discarded entirely, if necessary, at little cost. Low complexity models represent an ideal tool for performing a quick and rudimentary analysis of a system. These benefits contrast with the disadvantages of a simple model. If one interprets Ockham's razor as the rule, "a model must be as simple as possible, but not simpler," the issue of oversimplification is highlighted. A model which is too simple suffers from a loss of validity, having neglected or overly-abstracted certain behaviours in the system. However, Chwif et al. (2000) states that, at the time of publication, there is no method for determining the appropriate level of complexity of a model while maintaining validity. Narrowing the scope could provide a simpler model, described by Zeigler, Praehofer, and Kim (2000) as reducing the *experimental frame*. This can, however, come at a cost to the flexibility of the model.

Complex models are similarly analysed. Obvious disadvantages of a complex model are high computational requirements and a significant investment of time in its design and implementation. Additionally, while Zeigler et al. (2000) states that a more complex model more closely describes the reality, Chwif et al. (2000) and Salt (1993) introduce the concept of a complex and comprehensive model which is completely inaccurate. The greater number of

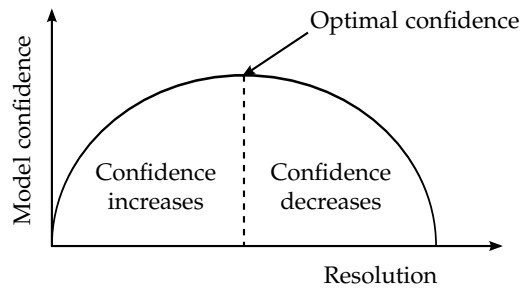


FIGURE 2.1: RELATIONSHIP BETWEEN MODEL CONFIDENCE AND RESOLUTION, FROM LOBÃO AND PORTO (1997).

elements of a complex model increase the number of variables which could be incorrect or inaccurate, resulting in behaviour which does not represent that of the true system. Lobão and Porto (1997) highlight the decrease in model confidence with continued increase in resolution, as shown in Figure 2.1. This is similarly described by Schoups, van de Giesen, and Savenije (2008) in the context of hydrological modelling, where the predictive validity of the model first increases and then decreases with complexity, while the fit of the model with calibration data decreases as complexity increases.

2.1.2 META-MODELS

As stated previously, a meta-model is a description or ontology of a model. The broad nature of models in the general sense precludes the development of a meta-model encompassing phenomena as diverse as physical, social and biological systems. Early discussions such as that by Simon (1962) attempt to present some abstract properties of models which are applicable to the mathematical model in general. The goal of this work was not to describe the specific nature of the complexities, but to simply highlight the general complexity of the system under investigation. More technical measures of complexity have been described by McCabe (1976), Wallace (1987) and Schruben and Yücesan (1993). Each of these requires the model to be described in a specific format to be able to measure its complexity.

Standard modelling languages such as UML (Unified Modeling Language) (Object Management Group, 2011) or SysML (Systems Modeling Language) (Object Management Group, 2012) demonstrate the capability to describe models using a standard format. UML is primarily focussed on software engineering applications, while SysML is employed in systems engineering. Of note is that SysML is an extension of UML, highlighting the limited capabilities of each language beyond the disciplines described.

The Discrete Event System Specification (DEVS) formalism developed by Zeigler (1984) is another example of meta-model, with application to both discrete event systems and continuous state systems. According to Ramadge and Wonham (1989), a Discrete Event System (DES) is a dynamic system in which

the state evolves as a series of physical events. Between consecutive events it is assumed that there is no change in the system. Conversely, a continuous state system continuously describes the state with time. This latter system is representative of the models used in the design of autonomous systems.

2.1.3 MULTI-RESOLUTION MODELLING

The concept of resolution, or level of detail, as described by Chwif et al. (2000) is extended to a model or family of models describing a system at multiple resolutions. A multi-resolution model has consistent scope across its submodels, each of which describe a system with different degrees of abstraction. MRM is primarily used in quantitative simulations for its predictive capabilities. Davis and Bigelow (1998) describe the use of a multi-resolution model for battlefield simulation, an example of a dynamic and strongly stochastic system with models typically derived from observations on the behaviour of agents, making it a predominantly empirical simulation.

Baohong (2007) presents a candidate ontology for multi-resolution modelling, using the DEVS formalism developed by Zeigler (1984). It is noted that existing formal specifications of MRM are few and those that do exist are too simple to be employed in practical problems involving multi-resolution models. Lee and Fishwick (1999) discuss the development of OOPM/RT (Object-Oriented Physical Modeler for Real-Time Simulation) methodology, which proposes methods for identifying the optimal model for an objective, in the sense that it balances validity with computational requirements and runtime. The benefits of employing a higher-resolution (or lower-abstraction) model are stated to be its greater validity. Sacrifices in validity are made to decrease the lead-time on simulation results. The benefit of a multi-resolution model is then in the ability to select the optimal resolution for producing results in a given time frame.

Singla and Junkins (2009) present some methods for identification, modelling and control of dynamic systems, using a multi-resolution approach. Their focus is specifically on empirical modelling of systems using dark grey box system identification and a variety of methods to fit abstract relationships to empirical data. Further investigations are presented in Singla (2006) with reference to aerospace engineering applications.

Some modern software packages facilitate multi-resolution modelling in the form of *multiphysics*, which employs multiple modelling tools including computational fluid dynamics, finite element methods and electrical models in what is effectively an expansion of multi-resolution modelling. Recent examples of this type of tool include COMSOL (2014) Multiphysics and several components of ANSYS (2014).

2.1.4 TYPES OF MATHEMATICAL MODEL

The difficulty in developing meta-models is highlighted by the myriad types of mathematical model. However, identification of these types permits later discussion on the quadrotor models described in this thesis. A mathematical model may be categorised by properties which described its composition and the type of system which it emulates. These categories are described by Bokil (2009) as follows.

A given system may be described by either a *deterministic* or *stochastic* model. A deterministic model ignores random variation in the system and so consistently produces the same result for a given input. This is in contrast to a stochastic model, which include random properties drawn from probability distributions and so can produce a range of results. An example of use for a deterministic model is controller design, while a stochastic model might be used to test the robustness of the controller to random disturbances. Stochastic modelling is also popularly applied in Monte Carlo simulations.

The system may be described by a *mechanistic* or *empirical* model. These are described by Isermann (2006) as theoretical or experimental models, respectively. A mechanistic or theoretical model considers the mechanisms involved in the behaviour of the system. These are typically the mathematical laws which represent the laws of physics. An empirical or experimental model provides a quantitative account of the changes in the system without regard to the mechanism. Each form of model may be considered on a spectrum of possible models, from white box to black box (Sjöberg, Zhang, Ljung, Benveniste, Delyon, Glorennec, Hjalmarsson, and Juditsky, 1995). In a white box model, the desired properties and behaviours are perfectly replicated by the model. A typical mechanistic model therefore is more representative of light grey box modelling. Conversely, a black box model involves no physical insight in its development. In systems engineering, empirical models are usually obtained by employing system identification to map the system output to its input through an arbitrary state. As this approach somewhat considers the mechanism of the system, it is considered dark grey box system identification. Examples of black box modelling include neural networks and fuzzy logic models (Sjöberg et al., 1995).

A system is either *static* or *dynamic*. A model of the system therefore has one of these properties. The state of a dynamic model changes with respect to time, while the state of a static model does not. A dynamic system may be approximated by a static model in a form of abstraction, but a static system cannot be described a dynamic model due to it lacking information in the required dimension, time. Additionally, a dynamic system may be described as an instantaneous response.

A dynamic system can be either *continuous* or *discrete*. All real-life systems are continuous, while all computer simulations and digital systems are discrete.

A continuous system may be represented by a continuous model, described using differential equations, or a discrete model, described using difference equations (Isermann, 2006).

Finally, a model may either be *quantitative*, where a numerical prediction of the system behaviour is provided; or *qualitative*, which provides a more general description of behaviours.

2.1.5 DISCUSSION OF REVIEW FINDINGS

The findings of the literature review which are presented here serve to highlight the significant variation with which a model may be characterised. Investigations into model complexity and meta-modelling encompass a variety of fields, including engineering, biology, psychology and philosophy. Even with relating it to a specific model, complexity is in itself a complex concept to investigate. While resolution is but one part of complexity, it is arguably a more opaque property than scope. The goal of the investigations presented in this thesis is then not to derive a meta-model or description of a multi-resolution quadrotor model. Rather, the goal is to investigate the differences in any results produced by simulation experiments with models of different resolution.

The concepts described by Davis and Bigelow (1998) are easily applied to deterministic systems such as aircraft, which are typically described mechanistically rather than empirically. Autonomous systems in particular are ideal for use in multi-resolution modelling, allowing agent behaviours and interactions to be described with varying complexity. This is the focus of ongoing work at the University of Glasgow and the impetus behind the MAVERIC simulation engine, the inspiration for the SiFRe simulation engine described in this thesis.

2.2 THE QUADROTOR MICRO AIR VEHICLE

Compared to the helicopter and other rotorcraft, the mechanics of the quadrotor are relatively simple. This, combined with the agility of the vehicle, have led to its prolific use in the field of robotics, acting as a testbed for investigations in areas such as non-linear control (Voos, 2009); trajectory generation and station-keeping (Cowling et al., 2007); co-ordinated lifting of loads (Mellinger et al., 2010b); visual navigation (Kemp, 2006); and Simultaneous Localisation And Mapping (SLAM) (Gupte et al., 2012). As a result of the popularity of the platform, models of the quadrotor system are in abundance and vary significantly in resolution. The complexity of these models is highly dependent on their applications. While investigations in control favour low-resolution models which describe the input-output relationship in as simple terms as possible, the literature demonstrates use of more complex models for investigations in areas such as aerodynamics (Fay, 2001) and aeroelastics (Pounds, Mahony, and Joel, 2004). Even within the bracket of simple or complex models, variation

in the approach taken to model the quadrotor can be seen. This section describes a broad cross-section of the literature relating to the quadrotor micro air vehicle. The models employed in the literature are related to their applications, which include control system design, optimisations and predictions of system behaviour. These models and their sources are discussed in this section of the literature review.

2.2.1 QUADROTOR MODELS IN LITERATURE

The quadrotor is employed in a variety of simulation experiments, many of which detail the model employed. While each of these models describes the quadrotor system with some level of abstraction, they are often designed such that they best fit the chosen investigation.

CONTROLLER DESIGN

The manoeuvrability of the quadrotor lends the platform to a wealth of investigations in controller designs. Linear or near-linear methods include PID (Proportional Integral Derivative) and state feedback algorithms, while non-linear approaches described in the literature include dynamic inversion and backstepping techniques.

The translational and rotational dynamics of the quadrotor are often represented as a series of integrator chains, blurring the distinction between PD and state feedback control. Mellinger, Michael, and Kumar (2010a) describes a linear PID controller for tracking of trajectories. A quadrotor model with non-linear rigid body dynamics and a first-order rotor response is described. This model is linearised and the rotor dynamics neglected in deriving the control law. Bouabdallah, Noth, and Siegwart (2004) derives the quadrotor model using Euler-Lagrange formalism and then employs the model in a comparison of PID and LQ control methods. The model describes the rigid body dynamics of the quadrotor with a non-linear model. The rotors are described by a linear, first-order model, abstracted from a non-linear model of the propeller and DC motor. Erginer and Altuğ (2007) describes a PD controller using a similar approach, also including gyroscopic torques in the model used for simulation testing. Balas (2007) also employs PID in an interesting approach to quadrotor control. The roll and pitch dynamics of the aircraft are neglected and the horizontal position is related directly to the system input by a fourth-order system. PID control on the horizontal position error then completes the closed-loop system. Balas tests this controller on both linear and non-linear quadrotor models and concludes that it is unsuitable. A nested-loop structure, typical of a quadrotor control system, is then employed to control the system. Hoffmann, Huang, Waslander, and Tomlin (2011) extends the concept of PID control by including a second-derivative term in the feedback law. The higher-bandwidth controller is then tested in simulation with a high-resolution model, using blade

element and momentum theories to describe flapping and other phenomena in the rotor blades.

A popular non-linear control technique is backstepping. Bouabdallah and Siegwart (2007) describes the control of a quadrotor vehicle using an integral backstepping approach. The controllers are tested in simulation on a high-resolution model which includes: gyroscopic torques arising from rotor rotation; ground effect; rotor hub forces; and a complex rotor model derived from blade element and momentum theories. Bouabdallah and Siegwart (2005) again consider backstepping control in addition to sliding mode techniques in control of the quadrotor. The model employed for simulation testing also describes a first-order linear rotor model. Hamel, Mahony, Lozano, and Ostrowski (2002) and Fang, Wang, and Sun (2010) both employ non-linear models in testing of backstepping control techniques. While Hamel et al. (2002) considers the effect of rotor dynamics, Fang et al. (2010) does not.

Another non-linear control approach is feedback linearisation, or input-output linearisation. This techniques uses dynamic inversion to derive a feedback which cancels the non-linearities in the model and results in a linear closed-loop system. A state feedback law is then typically employed to control the linearised system. This approach is demonstrated by Voos (2009), who describes a basic non-linear model which includes gyroscopic torques, and Mistler, Benallegue, and M'Sirdi (2001), who consider the robustness of the controller in the presence of external disturbances and parametric uncertainties. Das et al. (2009) also describes a feedback linearisation controller, first deriving the quadrotor model from Euler-Lagrange formalism and then controlling the linearised system using a backstepping approach.

SYSTEM PARAMETER ESTIMATION

Models are essential for parameter estimation, where measured data is used to predict and estimate unknown quantities. The Kalman filter, originally described by Kalman (1960), requires a linear model of a system in order to calculate an optimal observer for the system state. Application of the Kalman filter in quadrotor state estimation is described by Domingues (2009) and Chamberlain (2011), each of whom describe a linear model of the quadrotor dynamics. Alternatively, the quadrotor model can be used without linearisation in an algorithm such as the Extended Kalman Filter (EKF), described by Ireland and Anderson (2012), and the Unscented Kalman Filter (UKF), as described by Abas, Legowo, and Akmeliawati (2011). Awan, Park, and Kim (2011) use an adaptive observer in conjunction with a linearised model to estimate the thrust of the quadrotor during flight, a useful property to know with regards to control.

TRAJECTORY GENERATION

Trajectory generation and tracking is a popular topic of investigation in the field of robotics. Applications to the quadrotor typically describe the system dynamics in a form which is noted to be *differentially flat*, where all system inputs and states may be described in terms of a flat output and its derivatives. This approach then enables design of smooth trajectories, as evidenced by work described by Chamseddine, Li, Zhang, Rabbath, and Theilliol (2012), Cowling (2008) and Mellinger (2012). The models employed in these investigations are invariably described in a specific format which considers only the dynamics of the rigid body, facilitating the flatness of the system.

The concept of trajectory generation and differential flatness is extended to quadrotors bearing suspended loads, as described by Palunko, Fierro, and Cruz (2012) and Sreenath, Lee, and Kumar (2013).

VISION-BASED NAVIGATION

The hover-capability and manoeuvrability of the quadrotor make it ideal for vision-based guidance navigation. Altuğ, Ostrowski, and Mahony (2002) describe the control of a quadrotor using visual feedback, employing for testing a standard model with only the dynamics of the rigid-body considered. A more advanced form of vision-based navigation is simultaneous localisation and mapping. Blösch et al. (2010) describe application of the quadrotor to a SLAM problem, describing the non-linear translational dynamics of the system but simplifying the closed-loop attitude dynamics to a linear near-instantaneous system.

REDUCED-SCOPE MODELS

Investigations involving phenomena such as rotor dynamics and ground effect are not exclusive to the quadrotor, but rather are applicable to a variety of aircraft. Models which describe the quadrotor are therefore usually of consistent scope. Some investigations into complex phenomena involve an increase in resolution in a specific aspect of the quadrotor system. The remainder of the model is then of a standard or lower resolution, sufficient to facilitate simulation investigation of the phenomenon of interest. This is evident in the investigation by Bristeau, Martin, Salaün, and Petit (2009), where a high-resolution rotor model is described using blade element theory. The effects of rotor blade flexing on the control of the quadrotor is then investigated using a rigid-body model which is linearised about the hover state. Latorre (2011) also focusses primarily on the rotor behaviour of the quadrotor in an effort to optimise the aircraft's propulsion system. A rotor model described by blade element and momentum theories is corrected by empirical observations, combining both deterministic and statistical modelling approaches. Similar investigations in rotor behaviour

are described by Pounds et al. (2004) and Pounds, Mahony, and Corke (2010).

GENERAL SYSTEM MODELS

Several publications present a more complex model of the quadrotor, primarily as a platform for performing a variety of analyses. The most prominent of these is Bouabdallah (2007), who describes comprehensive quadrotor simulation, incorporating the rotor models and additional phenomena described in his other works. A similar approach is demonstrated by de Oliveira (2011). Beard (2008) describes a standard quadrotor model which is then simplified to provide models for controller design and state estimation, highlighting the fit-for-purpose nature of modelling.

Bresciani (2008) derives the rigid-body dynamics of the quadrotor from Newton-Euler formalism and describes a non-linear rotor model. These models are then simplified and partially linearised to allow design of a linear PID controller. Bresciani describes the structure of the quadrotor simulation and the capability for visual output in the form of a 3D animation.

Literature on the quadrotor primarily take the form of conference or journal publications which are focussed on a specific investigation. However, several theses such as those of Bouabdallah (2007), Chamberlain (2011) and Wierema (2008) present a broader model of the aircraft as a platform for multiple investigations. Some books have also been published which describe the derivation of models and control strategies with greater depth, such as that by Carrillo et al. (2012).

2.2.2 DISCUSSION OF MODEL RESOLUTION AND TYPE IN QUADROTOR LITERATURE

Some commonalities in the aforementioned models may be identified, highlighting the modular nature of modelling and the tendency of the modeller to tailor the model for purpose.

LINEARITY

The quadrotor is a non-linear system and is typically modelled as such to accurately represent the system behaviours. A useful property of the quadrotor is its ability to remain level at hover, presenting an excellent trim state around which to linearise the system. This is typically used in development of linear controllers, as in de Oliveira (2011) and state estimation. A linear rigid-body model may also be used so that the effects of more complex phenomena are more evident in the response, as in Bristeau et al. (2009).

Often, the non-linear quadrotor model is partially linearised such that only the translational dynamics retain a non-linear relationship. This is valid for relatively slow flight, where the cross-coupling in angular velocities is negligible.

This is evident in Altuğ et al. (2002).

Further non-linearities beyond the usual rigid body models are introduced by incorporating additional phenomena into the system description. An example of this is the rotor model employed by Sudiyanto, Muljowidodo, and Budiyo (2009), which employs blade element and momentum theories and is highly non-linear.

ROTOR MODELS

The propulsion system employed by the quadrotor typically consists of four small two-bladed rotors, each with an electric motor and an Electronic Speed Controller (ESC). This subsystem has its own dynamics, which may be neglected if they are sufficiently fast with respect to the rigid-body response of the aircraft. The resolution of the rotor models in the literature vary from describing the thrust and torque as instantaneous linear responses to the rotor input to describing the electro- and aerodynamics using non-linear models of multiple order.

Some trends in the rotor models found in the literature may be identified. Investigations which regard the quadrotor more as an aerial robot rather than an aircraft, such as those in trajectory generation, typically use simple rotor models which are sufficient to relate net forces and moments to the system inputs. This is evidenced by Voos (2009), Erginer and Altuğ (2007) and Cowling et al. (2007). On occasion, where the rotor dynamics are non-negligible, a first-order dynamic relationship is introduced, as in Michael et al. (2010) and Mellinger (2012). Both of these types of model use an empirical approach to describing the system relationships, where the mechanics of the rotors are not considered with any great detail.

Conversely, some publications treat the quadrotor as more of an aircraft, describing rotor behaviours from a deterministic approach. Sudiyanto et al. (2009) describe the rotor system using blade element and momentum theories. The result expresses the force and torque produced by each rotor as a non-linear function of its rotational speed. Pounds et al. (2010) describe the rotor behaviour using an actuator disk model which incorporates aeroelastic effects on the blades. The quadrotor vehicle employed by Pounds et al. is designed such that the rotor blades flex to an optimal operating angle under load. A model which describes this phenomenon is thus key in investigating its impact on the system. A similar investigation by Pounds et al. (2004) describes a quadrotor with actuated rotors.

SYSTEM INPUTS

While the quadrotor models described in the literature consistently describe four system inputs, the exact nature of these inputs varies. Several publications describe the thrust and torque produced by a rotor as varying linearly with the

square of its rotorspeed. This approach is best suited to simulation experiments, where the true rotor inputs are not required, only some property to which both the thrust and torque can be related. A similar approach to this is to employ the thrust of each rotor as its input. The rotor torque is then related to the thrust by some constant scale factor. This is evidenced by Altuğ et al. (2002). Again, this is only suitable for simulation experiments, as the thrust is not directly controllable in practice. Both of these approaches are interesting in that they neglect rotor effects which may impact the system. This is an example of the abstractions employed in some investigations.

The true motor input is typically employed when describing a comprehensive model of the quadrotor system (Bouabdallah and Siegwart, 2007); when applying controllers in practical experiments, where the relationship between state and actuator input must be known (Wierema, 2008); or when applying observers to experimental data; which require both empirical input and output measurements. Depending on the motors used to drive the rotors, this input may either be a direct voltage (Bouabdallah and Siegwart, 2007) or Pulse-Width Modulation (PWM) signal (Chamseddine et al., 2012).

The majority of quadrotor models briefly describe the individual inputs to each rotor and then introduce four pseudo-inputs which are related to the true inputs by a simple invertible matrix relationship. The pseudo-inputs are related to the net thrust and moments acting on the aircraft by constant gains, allowing the system to be decoupled into four Single-Input Single-Output (SISO) models in the majority of cases. This simplifies investigations such as controller design and trajectory generation significantly. Some publications neglect the individual rotor inputs entirely and employ the pseudo-inputs exclusively, as evidenced by Achtelik et al. (2011).

VISUALISATIONS

Animations such as those employed by Bresciani (2008) require a minimum amount of information in order to display system behaviours, thus potentially increasing the resolution of the model. A 3D visualisation of the quadrotor requires at least the position and attitude of the quadrotor to be modelled.

2.3 WIRELESS POWER TRANSMISSION

Wireless power transmission, or *power beaming*, is the transmission of electrical energy without the use of tangible conductors (Brown, 1996). The origins of the technology and its evolution throughout history are closely tied to efforts in wireless communication. In recent history, usage of the concept has focussed on supplying power to long-endurance mobile systems such as spacecraft and UAVs.

This section describes the origins of wireless power transmission, its development throughout history and the current state of the art, with specific

reference to its use in powering autonomous systems such as the quadrotor.

2.3.1 A BRIEF HISTORY OF WIRELESS POWER TRANSMISSION

The concept of wireless power transmission was introduced as early as the 1870s, when James Clerk Maxwell predicted that power could be transmitted through free space through the use of electromagnetic waves. Maxwell's equations were validated with a series of experiments conducted by Heinrich Rudolf Hertz in the 1880s (Brown, 1984).

Later experiments were performed by Nikola Tesla, an inventor famous for his work in the development of alternating current. Tesla's experiments with wired transmission of energy found that electricity would "leak" into the atmosphere, given sufficient power. A patent filed in 1902 describes the use of a "magnifying transmitter" (Figure 2.2), designed to use the Earth itself as a conductor (Tesla, 1914). These discoveries culminated in the construction of Wardenclyffe Tower, a large transmitter ostensibly designed to facilitate trans-Atlantic radio communication (Garnica, Chinga, and Lin, 2013). This venture ultimately failed due to the successes of Guglielmo Marconi in achieving trans-Atlantic transmissions using significantly less expensive equipment, resulting in funding being withdrawn from Tesla's efforts. In an attempt to secure additional funding, Tesla revealed an additional feature of the tower: the ability to transmit electricity wirelessly. Tesla's efforts were unsuccessful – Wardenclyffe Tower was dismantled during World War I and investigations into wireless power transmission effectively stopped until after World War II.

The invention of high-power microwave emitters during the Second World War reignited interest in wireless power, now with a focus on transmission through narrow microwave beams (Brown, 1996). Experimentation with high power microwave tubes eventually resulted in a survey paper by Brown (1961), describing the elements of a microwave-based power transmission system and highlighting its weaknesses. Brown's work led to a pivotal moment in the history of wireless power transmission: the 1964 flight of an unmanned helicopter powered by microwaves transmitted from the ground (Brown, 1965). The microwave-powered helicopter was limited in that it was required to be tethered, but achieved a continuous flight time of ten hours. Subsequent experiments employed the microwave beam to aid in controlling the helicopter while power was supplied via a wired connection Brown (1969), however a combined microwave-based stabilisation and power system was never implemented.

Brown's work in wireless power transmission allowed Glaser (1968) to publish a pioneering report on Solar Power Satellites (SPS). This concept involved collecting solar energy above the attenuating effects of the atmosphere and transmitting it to the Earth's surface in a focussed microwave beam. Prohibitive cost prevented large-scale implementation at the time, but the potential for exploitation of such a clean and abundant energy source ensured that Space-

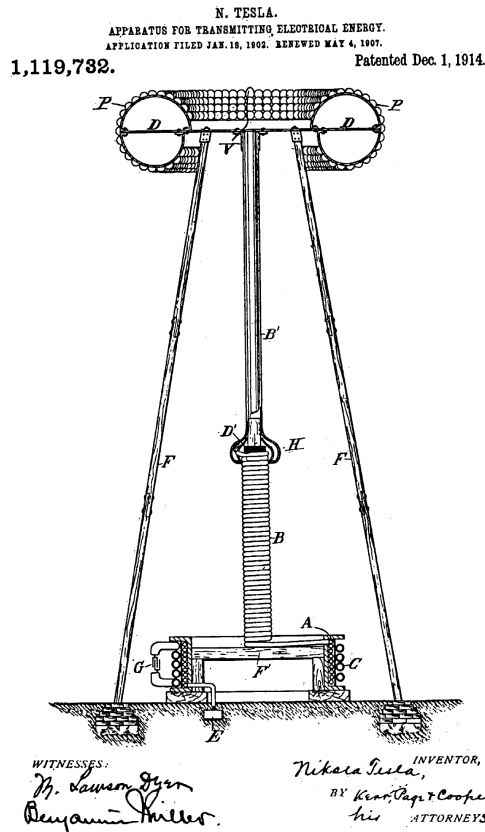


FIGURE 2.2: NIKOLA TESLA'S APPARATUS FOR TRANSMITTING ELECTRICAL ENERGY (TESLA, 1914).

Based Solar Power (SBSP) would remain a topic of great interest. With the introduction of a functioning laser emitter in 1960, laser-based power transmission from satellites began to be explored (Summerer and Purcell, 2008).

Recent advances in the efficiency of laser emitters and a reduction in cost have allowed the expansion of power beaming into other areas. A demonstration of laser power transmission to a UAV was performed by NASA in 2003, allowing a small radio-controlled fixed-wing aircraft to conduct several short flights, powered solely by energy received by a photovoltaic array mounted under the airframe (Mason, 2011). This was ultimately followed by application of the technology to the endurance-challenged quadrotor, resulting in a continuous 12-hour flight and a demonstration of the feasibility of the concept with the available technology of the current day (Nugent, Kare, Bashford, Erickson, and Alexander, 2011).

2.3.2 LASERS VS MICROWAVES

Dickinson and Grey (1999) compares the use of laser beams and microwaves with application to SBPS systems. Some of the considerations are, however, of consequence to shorter-range uses such as UAV power supply.

The most significant is the required size of the transmitting and receiving antennas. The wavelength of the electromagnetic radiation used in a focused

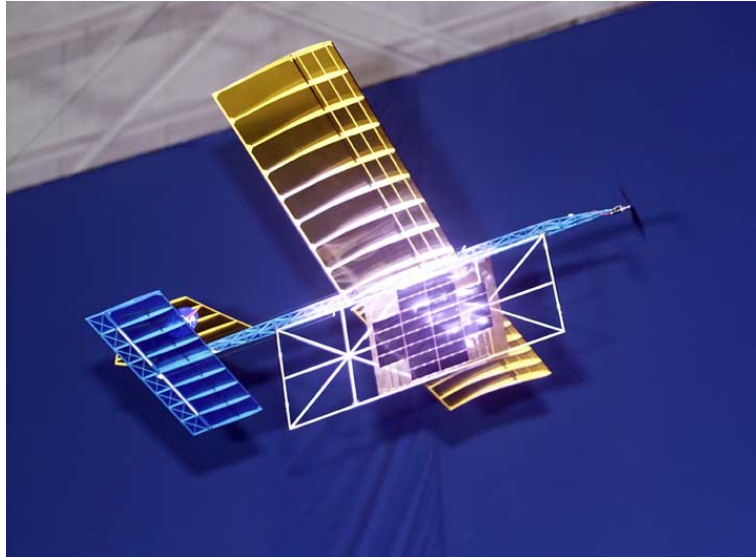


FIGURE 2.3: NASA'S LASER-POWERED AIRCRAFT (NASA, 2010)

beam directly affects the flux density of the transmission (Jacobs, 2006). Microwaves have a significantly longer wavelength than infrared light and therefore require a beam of greater diameter to transmit the same amount of power. A larger transmitter and receiver is therefore required for transmission of microwaves. Additionally, diffraction of the beam decreases with wavelength. A laser beam will therefore typically experience less divergence than a microwave beam, again reducing the required size of the receiving antenna. Since application of WPT technology to unmanned vehicles necessitates minimal size of the receiving antenna at the very least, these considerations alone make laser-based power transfer far more feasible.

The longer wavelength of microwaves does, however, yield some advantages. Low-frequency microwaves suffer far less attenuation in the Earth's atmosphere than waves of shorter length. Degenford, Sirkis, and Steier (1964) demonstrated a transmission efficiency of more than 99%, using microwaves of 4 m wavelength. Conversely, infrared waves are greatly affected by atmospheric attenuation over large distances and are particularly affected by adverse visibility. Al Naboulsi, Sizun, and de Fornel (2005) describes the approximate relationship between range, visibility and *transmittance*, the ratio of power at a given to range to the initial power output. An example of the relationship is shown in Figure 2.4, demonstrating the loss of power with range and visibility for a typical monochromatic laser beam.

Ultimately, the antennas required to generate sufficient power for microwave-based power transfer are prohibitively large for use with unmanned aircraft. Investigations of wireless power transmission for UAVs have therefore almost exclusively employed infrared lasers, despite the reduced long-range efficiency. Due to the highly mobile nature of aircraft, power transmission would likely be restricted to relatively short ranges so as to reduce beam pointing errors and

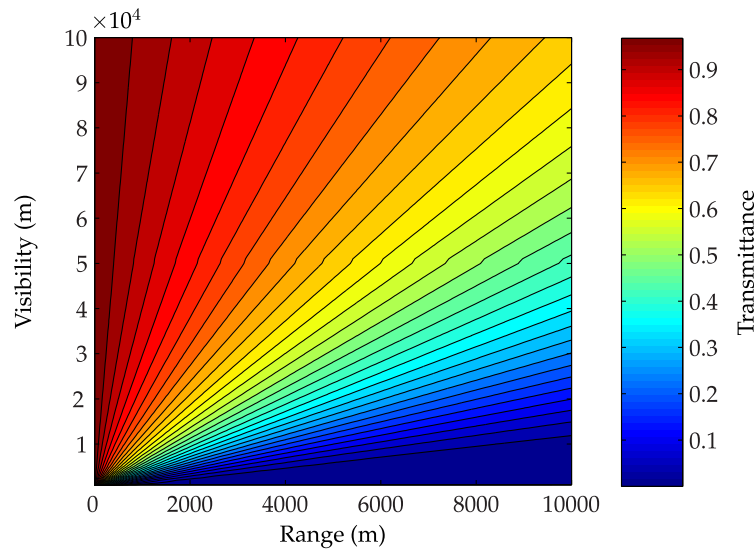


FIGURE 2.4: EFFECTS OF ATMOSPHERIC ATTENUATION ON TRANSMITTANCE OF WAVE WITH WAVELENGTH $\lambda = 532 \text{ nm}$

resultant damage from the high-powered laser.

2.3.3 STATE-OF-THE-ART

Laser-based wireless power transmission has only reached practical application in the last few years. A frontrunner of laser beaming technology is LaserMotive, who contributed to the endurance record set by the “Pelican” quadrotor and described by Achtelik et al. (2011) and Nugent et al. (2011).

The system developed by LaserMotive involves a focussed laser beam which is directed by a gimbaled mirror onto a photovoltaic sensor array mounted on the bottom of the receiving aircraft. The beam pointing and stabilisation system used in the experiment tracks a Light-Emitting Diode (LED) on the sensor array using an optical camera. The system has a rotational range of $\pm 15^\circ$ and a maximum beaming range of 1 km. At maximum range, the system has a pointing error of a few centimetres. At ranges of 15 to 20 m, the errors were of order 1 mm.

Two approaches to utilisation of the laser power are then available. The first is continuous powering of the aircraft, similar to Brown’s experiment with the microwave-powered helicopter. This would allow the aircraft to carry only a small energy storage device for regulating the power to the onboard systems. The second is intermittent recharging of the aircraft when it is in range of the power transmission system. This would require a standard onboard power source, which would be recharged by the laser energy.

Both scenarios are applicable to a micro air vehicle such as the quadrotor. The first favours operations such as aerial reconnaissance or surveillance, where the aircraft can remain in sight of the laser source at all times. The second is better suited to short-range missions where the aircraft can perform some task

such as exploring a building or transporting materials and then return to the ground station to be recharged.

2.3.4 FUTURE DIRECTION

The 12 hour flight of the Pelican suffered a notable limitation in that it was restricted to a 5 metre square flight space. This was primarily due to the restriction of flying indoors but is responsible for the small pointing error of the laser. In a less restricted environment, LaserMotive's energy transmission system is capable of powering a variety of unmanned aircraft, as described by Nugent and Kare (2011).

With the feasibility of laser-based wireless power transmission having been demonstrated, the goal becomes the refinement and improvement of the technology. Advances in laser emitter and receiver technologies can improve the efficiency of the power transfer, but the receiving and transmitting systems are still required to co-operate to ensure accurate vehicle tracking and improve the safety of the operation. From a flight dynamics perspective, this requires optimisation of aircraft trajectories with respect to the energy transmission system and accurate tracking of these trajectories. Optimisation of quadrotor trajectories in a wireless power transmission operation is described in Chapter 7, while controller design is covered in Chapter 6.

CHAPTER 3

MODELLING THE QUADROTOR SYSTEM

To investigate the effects of model resolution and determine the benefits of multi-resolution modelling, it is first necessary to develop a multi-resolution model of the quadrotor. To obtain a sufficient number of models to both populate the model family and satisfy the required scope of the models, two approaches to modelling are taken. The first approach identifies behaviours of the quadrotor which may be described mechanistically, wherein the system is described by models either derived from first principles or by relationships identified in the literature. The second approach employs system identification to obtain empirical models of quadrotor behaviours, based on data taken from the Qball-X4 quadrotor. This latter approach is described in Chapter 4, while the former is detailed in this chapter.

The literature review described in Chapter 2 highlights the range of models which can be used to describe the behaviour of the quadrotor system. In addition to detailing relationships described in the literature, this chapter presents the rigid-body model which is key to simulation of the quadrotor behaviour. This is derived twice, from the opposing formalisms of Newton-Euler and Euler-Lagrange, and the differences in the results of each approach discussed. Additional phenomena, highlighted by the literature, are introduced and their models described. Modelling of the rotor behaviour is of particular interest, as the range of resolution in the rotor models expressed by the literature is broad. Some observations are made on the described models, leading to further investigation of the system behaviours in the next chapter.

3.1 VEHICLE DESCRIPTION

The quadrotor is a rotary-wing aircraft which derives its lifting force and controllability from the four identical rotors spaced uniformly around its centre of mass. The fundamental mechanics of the quadrotor are then very simple. Since each of the four rotors is fixed-pitch, the thrust and torque produced is con-

trolled exclusively by changing the rotational speed of the rotor. In adjusting the voltage or PWM signal to each motor, the rotorspeed may be controlled, thus allowing each rotor to produce thrust and torque and induce translational and rotational motion in the aircraft.

The manoeuvrability of the vehicle can result in highly non-linear behaviour arising from cross-coupling in angular velocities and deviations from the hover state (Das et al., 2009). The system is therefore often described by a non-linear rigid-body model, with forces and moments typically informed by either an instantaneous or first-order rotor model.

Figure 3.1 shows the quadrotor in a “plus” configuration. Rotors 1 and 2 are aligned with the x -axis and rotate clockwise, while rotors 3 and 4 are aligned with the y -axis and rotate counter-clockwise. The opposing rotation of each pair of rotors ensures the torques are balanced in hover. Motion of the quadrotor body is induced by manipulating the outputs of the rotors – thrust and torque – via the input PWM. Figure 3.2 demonstrates the effect of this manipulation on the forces and moments of the body. The net thrust T of the quadrotor is determined by the *throttle* of the rotors, changing the thrust of all four rotors equally by some amount ΔT , where ΔT may be either positive or negative. A rolling moment M_x may be excited by adding ΔT to the thrust produced by Rotor 3 and similarly subtracting ΔT from rotor 4. A pitching moment M_y is excited by a similar thrust differential between rotors 1 and 2. Finally, a yawing moment M_z is induced by adding a change in torque ΔQ to rotors 3 and 4, which rotate counter-clockwise, and subtracting the same amount from rotors 1 and 2, which rotate clockwise.

Ignoring complex phenomena such as aero-elastic effects and airframe vibration, the quadrotor can be considered a rigid body. As with a typical rigid body, the quadrotor has both translational freedom, described by the position $\mathbf{r} = [x, y, z]^T \in \mathbb{R}^3$, and rotational freedom, which may be described by the attitude vector of Euler angles $\boldsymbol{\eta} = [\phi, \theta, \psi]^T \in \mathbb{R}^3$, the direction cosine matrix $\mathbf{R}_B^{\mathcal{W}} \in \text{SO}(3)$ or the quaternion vector $\mathbf{q} \in \text{SU}(2)$. The system therefore has six degrees of freedom and only four inputs, making it under-actuated. This must be taken into consideration when designing control algorithms for the quadrotor.

3.2 FRAMES OF REFERENCE AND KINEMATICS

Quadrotor reference frames and kinematics are detailed by Beard (2008) and are adapted in this section for use in modelling the Qball-X4. The position \mathbf{r} and attitude $\boldsymbol{\eta}$ of the quadrotor are described in an inertially-fixed, or “world”, frame of reference, denoted by \mathcal{W} . Phenomena such as the forces and moments acting upon the vehicle are, however, described with respect to a frame of reference fixed on the vehicle body, denoted by \mathcal{B} . The direction cosine matrix $\mathbf{R}_B^{\mathcal{W}}$ describes \mathcal{B} with respect to \mathcal{W} and may be used to transform phenomena

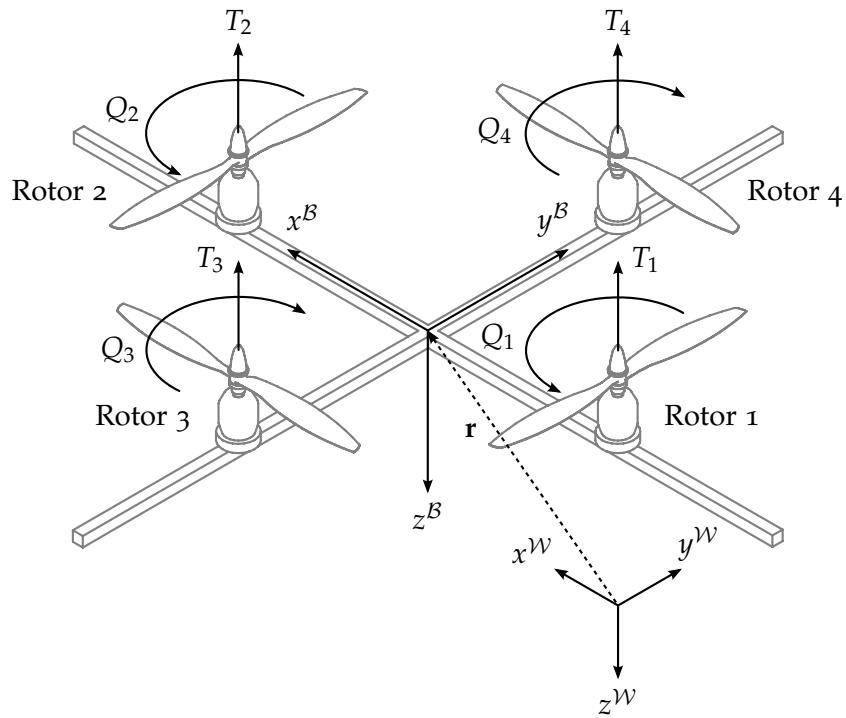


FIGURE 3.1: QUADROTOR BODY FRAME OF REFERENCE WITH RESPECT TO WORLD FRAME AND VEHICLE FORCES AND MOMENTS. THE THRUST OF EACH ROTOR ACTS ALONG THE AXIS OF ROTATION, WHILE THE TORQUE OPPOSES THE DIRECTION OF ROTATION.

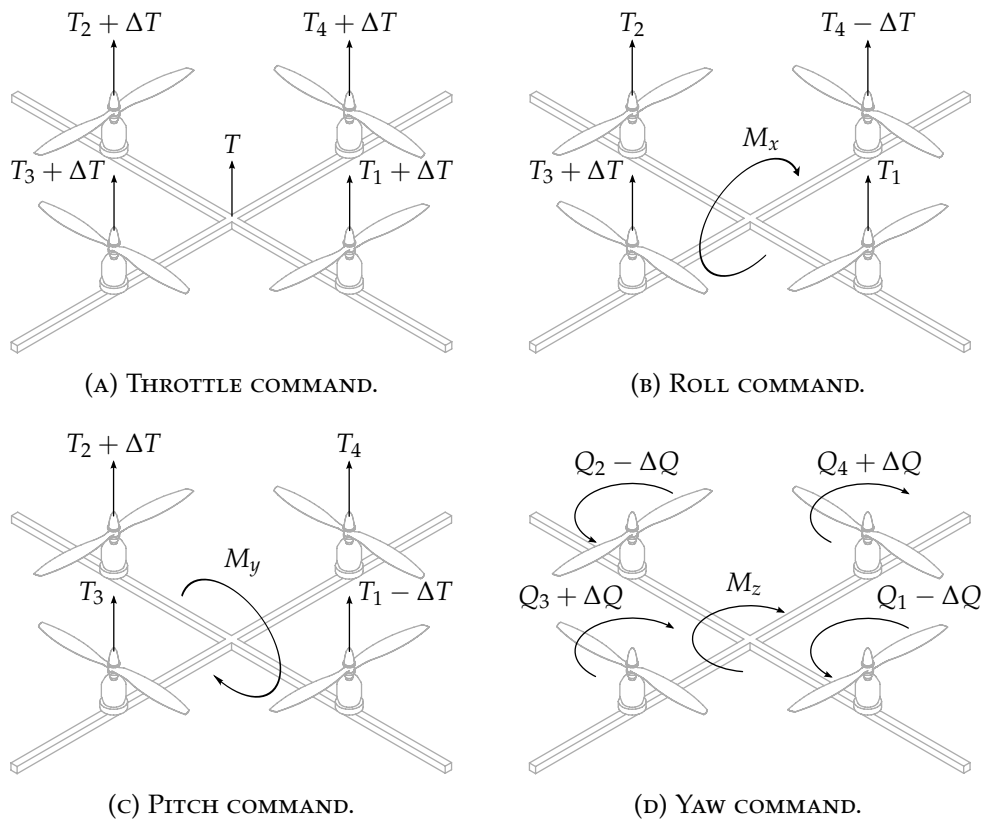


FIGURE 3.2: DEMONSTRATION OF ROTOR OUTPUTS ON RIGID-BODY FORCES.

described in \mathcal{B} to the world frame. Both reference frames and the kinematic relationships between them are detailed in this section.

3.2.1 CHOOSING AN APPROPRIATE KINEMATIC REPRESENTATION

The rotational kinematics of the quadrotor may be described by one of several methods. The most popular method highlighted by the literature and illustrated by Bouabdallah (2007), Voos (2009) and Das et al. (2009), among others, is the use of Euler angles. While this is arguably the most intuitive approach to describing attitude, it has disadvantages which are absent in the alternative approaches of quaternions (Fresk and Nikolakopoulos, 2013) and Direction Cosines Matrices (DCM) (Mellinger, 2012). The choice of kinematic representation for the quadrotor models described in this chapter is justified here.

The primary effect that the choice of kinematic representation has is on the evolution of the vehicle attitude, described by its relationship with the angular velocity of the vehicle $\boldsymbol{\omega}$. The Euler angles describe this relationship by

$$\dot{\boldsymbol{\eta}} = \mathbf{J}_{\boldsymbol{\eta}}^{-1} \boldsymbol{\omega} \quad (3.1)$$

where the inverted Jacobian matrix $\mathbf{J}_{\boldsymbol{\eta}}^{-1}$ is given by

$$\mathbf{J}_{\boldsymbol{\eta}}^{-1} = \begin{bmatrix} 1 & \sin \phi \tan \theta & \cos \phi \tan \theta \\ 0 & \cos \phi & -\sin \phi \\ 0 & \sin \phi \sec \theta & \cos \phi \sec \theta \end{bmatrix}$$

with its full derivation described in Section 3.2.3. The primary advantage of this approach is that the vector of Euler angles $\boldsymbol{\eta}$ provides a description of the vehicle attitude which is very simple to interpret and arguably more intuitive than other methods. The primary drawback is the presence of singularities for the condition $\theta = \pi/2$, resulting from the $\tan \theta$ terms in $\mathbf{J}_{\boldsymbol{\eta}}^{-1}$.

The quaternions describe the attitude response by the relationship (Saripalli, 2009)

$$\dot{\mathbf{q}} = \frac{1}{2} \mathbf{Q}(\mathbf{q}) \boldsymbol{\omega} \quad (3.2)$$

where $\mathbf{q} = [q_0, q_1, q_2, q_3]^T$ and the matrix $\mathbf{Q}(\mathbf{q})$ is given by

$$\mathbf{Q}(\mathbf{q}) = \begin{bmatrix} -q_1 & -q_2 & -q_3 \\ q_0 & q_3 & -q_2 \\ -q_3 & q_0 & q_1 \\ q_2 & -q_1 & q_0 \end{bmatrix} \quad (3.3)$$

This solution avoids singularities and is less computationally complex than the Euler angle approach, as evidenced by the lack of trigonometric terms. However, the solution to this relationship, the quaternion \mathbf{q} , is far less intuitive to interpret and requires a greater state space to solve.

Finally, the attitude may be described by the direction cosine matrix \mathbf{R} (Mellinger et al., 2010a), which is related to the angular velocity by

$$\dot{\mathbf{R}}_{\mathcal{B}}^{\mathcal{A}} = \mathbf{R}_{\mathcal{B}}^{\mathcal{A}} \boldsymbol{\omega} \quad (3.4)$$

where \mathbf{R} describes the rotation from some inertially-fixed frame of reference \mathcal{A} to the vehicle body-fixed frame of reference \mathcal{B} . The advantage of this approach is again the lack of singularities in the solution, while another is that $\mathbf{R}_{\mathcal{B}}^{\mathcal{A}}$ may be directly used in describing the position response without the need to reconstruct it from Euler angles, as described in Equation (3.7). The disadvantage of this approach is again the storage required to handle the state transition, and the lack of intuitive meaning in the solution.

Noting the advantages and disadvantages of each approach to describing the attitude kinematics, a suitable representation may be selected. The quadrotor is not designed to operate near the condition under which singularities occur in Euler angle representation, $\theta = \pi/2$, except under particularly aggressive manoeuvres. As the investigations in this thesis does not consider flights under such conditions, the presence of a singularity in the attitude kinematics has no effect on the quadrotor response. Next, an intuitive means of describing the vehicle attitude is preferred in order to compare the responses of models of different resolution. While it is possible to obtain Euler angles from both quaternions and DCMs, this represents a further calculation beyond the solution of the attitude kinematics state transition. Thus, given the smaller storage requirements of the Euler angle representation and the lack of need to convert the solution to another format, the Euler angles are chosen to represent the attitude kinematics of the quadrotor.

3.2.2 FRAMES OF REFERENCE

The world frame \mathcal{W} is a right-handed orthogonal axes system and is inertially-fixed with respect to a point on the Earth's surface. The NED (north-east-down) convention is satisfied, in that the x -axis is positive in the direction of north, the y -axis is positive in the direction of east and the z -axis is positive in the direction of the local gravity vector (Carrillo et al., 2012).

The quadrotor body-fixed frame \mathcal{B} is a right-handed orthogonal axes system and has origin at the quadrotor centre of mass. The x -axis is positive in the nominal forward direction of the vehicle, the y -axis is positive in the nominal starboard direction and the z -axis is positive downwards and normal to the x - and y -axis, satisfying the condition $\mathbf{z} = \mathbf{x} \times \mathbf{y}$.

Vector properties in \mathcal{W} may be described in \mathcal{B} by rotating through each of the rotational degrees of freedom of the quadrotor in sequence. If the World-fixed frame \mathcal{W} is transformed to the body-fixed frame \mathcal{B} using the rotation

sequence yaw-pitch-roll, the direction cosine matrix describing \mathcal{W} in \mathcal{B} is

$$\begin{aligned} \mathbf{R}_{\mathcal{W}}^{\mathcal{B}} &= \begin{bmatrix} 1 & 0 & 0 \\ 0 & \cos \phi & \sin \phi \\ 0 & -\sin \phi & \cos \phi \end{bmatrix} \begin{bmatrix} \cos \theta & 0 & -\sin \theta \\ 0 & 1 & 0 \\ \sin \theta & 0 & \cos \theta \end{bmatrix} \begin{bmatrix} \cos \psi & \sin \psi & 0 \\ -\sin \psi & \cos \psi & 0 \\ 0 & 0 & 1 \end{bmatrix} \\ &= \begin{bmatrix} c_{\theta}c_{\psi} & c_{\theta}s_{\psi} & -s_{\theta} \\ s_{\phi}s_{\theta}c_{\psi} - c_{\phi}s_{\psi} & s_{\phi}s_{\theta}s_{\psi} + c_{\phi}c_{\psi} & s_{\phi}c_{\theta} \\ c_{\phi}s_{\theta}c_{\psi} + s_{\phi}s_{\psi} & c_{\phi}s_{\theta}s_{\psi} - s_{\phi}c_{\psi} & c_{\phi}c_{\theta} \end{bmatrix} \end{aligned} \quad (3.5)$$

The orientation of \mathcal{B} , and therefore the attitude of quadrotor, is then described in \mathcal{W} by the reverse transformation

$$\begin{aligned} \mathbf{R}_{\mathcal{B}}^{\mathcal{W}} &= \mathbf{R}_{\mathcal{W}}^{\mathcal{B}T} \\ &= \begin{bmatrix} c_{\theta}c_{\psi} & s_{\phi}s_{\theta}c_{\psi} - c_{\phi}s_{\psi} & c_{\phi}s_{\theta}c_{\psi} + s_{\phi}s_{\psi} \\ c_{\theta}s_{\psi} & s_{\phi}s_{\theta}s_{\psi} + c_{\phi}c_{\psi} & c_{\phi}s_{\theta}s_{\psi} - s_{\phi}c_{\psi} \\ -s_{\theta} & s_{\phi}c_{\theta} & c_{\phi}c_{\theta} \end{bmatrix} \end{aligned} \quad (3.6)$$

3.2.3 KINEMATIC RELATIONSHIPS

Given the reference frame definitions provided by Equations (3.5) and (3.6), it is possible to define the kinematics of the quadrotor as follows. For a velocity vector \mathbf{v} described in \mathcal{B} , the position response in \mathcal{W} is given by

$$\dot{\mathbf{r}} = \mathbf{R}_{\mathcal{B}}^{\mathcal{W}} \mathbf{v} \quad (3.7)$$

The angular velocity $\boldsymbol{\omega}$ in \mathcal{B} may be similarly described in \mathcal{W} . The angular velocity may also be related to the rates of change of the attitude angles $\boldsymbol{\eta}$ by

$$\begin{aligned} \boldsymbol{\omega} &= \begin{bmatrix} \dot{\phi} \\ 0 \\ 0 \end{bmatrix} + \begin{bmatrix} 1 & 0 & 0 \\ 0 & \cos \phi & \sin \phi \\ 0 & -\sin \phi & \cos \phi \end{bmatrix} \begin{bmatrix} 0 \\ \dot{\theta} \\ 0 \end{bmatrix} \\ &\quad + \begin{bmatrix} 1 & 0 & 0 \\ 0 & \cos \phi & \sin \phi \\ 0 & -\sin \phi & \cos \phi \end{bmatrix} \begin{bmatrix} \cos \theta & 0 & -\sin \theta \\ 0 & 1 & 0 \\ \sin \theta & 0 & \cos \theta \end{bmatrix} \begin{bmatrix} 0 \\ 0 \\ \dot{\psi} \end{bmatrix} \end{aligned} \quad (3.8)$$

This provides the Jacobian matrix \mathbf{J}_{η} which relates the body angular velocities to the Euler rates by

$$\boldsymbol{\omega} = \mathbf{J}_{\eta} \dot{\boldsymbol{\eta}} \quad (3.9)$$

and is expressed by

$$\mathbf{J}_{\eta} = \begin{bmatrix} 1 & 0 & -\sin \theta \\ 0 & \cos \phi & \sin \phi \cos \theta \\ 0 & -\sin \phi & \cos \phi \cos \theta \end{bmatrix} \quad (3.10)$$

The reverse transformation then provides the attitude response as a function of the quadrotor's angular velocity

$$\dot{\boldsymbol{\eta}} = \mathbf{J}_{\boldsymbol{\eta}}^{-1} \boldsymbol{\omega}$$

$$\text{where } \mathbf{J}_{\boldsymbol{\eta}}^{-1} = \begin{bmatrix} 1 & \sin \phi \tan \theta & \cos \phi \tan \theta \\ 0 & \cos \phi & -\sin \phi \\ 0 & \sin \phi \sec \theta & \cos \phi \sec \theta \end{bmatrix} \quad (3.11)$$

3.3 RIGID BODY DYNAMICS

A rigid body model is used to describe the translational and rotational response of the quadrotor to a force \mathbf{F} and moment \mathbf{M} . The rigid body model may be derived from both Newton-Euler and Euler-Lagrange formalisms, producing identical results. Both approaches are employed here – the results are then discussed and a single model chosen for the quadrotor model family. The full derivations from both formalisms are described in Appendix D.

3.3.1 DERIVATION FROM NEWTON-EULER FORMALISM

The translational and rotational dynamics of a rotating rigid body are derived using Newton-Euler formalism. This approach considers the linear and angular momentum of the body. The translational and rotational components of the response are easily separated and are described as such here.

TRANSLATIONAL RESPONSE

Consider a body represented by a point of mass m . The translational response of the body is obtained by considering its linear momentum, described in the inertially-fixed World frame \mathcal{W} by

$$\mathbf{p} = m\dot{\mathbf{r}} \quad (3.12)$$

The force in \mathcal{W} is the rate of change of linear momentum with time, giving the simple solution

$$\mathbf{F}^{\mathcal{W}} = m \frac{d\dot{\mathbf{r}}}{dt} = m\ddot{\mathbf{r}} \quad (3.13)$$

Alternatively, the force in the body-fixed frame \mathcal{B} may be described by noting the kinematic relationship $\dot{\mathbf{r}} = \mathbf{R}_{\mathcal{B}}^{\mathcal{W}} \mathbf{v}$. The force in \mathcal{W} is now

$$\mathbf{F}^{\mathcal{W}} = m \frac{d}{dt} \left(\mathbf{R}_{\mathcal{B}}^{\mathcal{W}} \mathbf{v} \right)$$

Noting the relationship $\dot{\mathbf{R}} = \mathbf{R}[\boldsymbol{\omega}]_{\times}$, the force in \mathcal{B} is found to be

$$\mathbf{F}^{\mathcal{B}} = m(\dot{\mathbf{v}} + \boldsymbol{\omega} \times \mathbf{v}) \quad (3.14)$$

ROTATIONAL RESPONSE

The rotational response is obtained similarly. The inertia matrix \mathbf{I} of a body is constant when described in the body-fixed frame \mathcal{B} . The time-dependent inertia matrix in \mathcal{W} is then given by the relationship $\mathbf{I}^{\mathcal{W}} = \mathbf{R}_{\mathcal{B}}^{\mathcal{W}} \mathbf{I}^{\mathcal{B}}$.

The angular momentum of a body with inertia matrix \mathbf{I} is therefore described in the World frame \mathcal{W} by

$$\mathbf{L} = \mathbf{I}^{\mathcal{W}} \boldsymbol{\omega}^{\mathcal{W}} \quad (3.15)$$

The moment in \mathcal{W} is then the rate of change of angular momentum with time, giving

$$\mathbf{M}^{\mathcal{W}} = \frac{d}{dt} (\mathbf{I}^{\mathcal{W}} \boldsymbol{\omega}^{\mathcal{W}})$$

which results in Euler's equation, with the form

$$\mathbf{M}^{\mathcal{W}} = \mathbf{I}^{\mathcal{W}} \dot{\boldsymbol{\omega}}^{\mathcal{W}} + \boldsymbol{\omega}^{\mathcal{W}} \times \mathbf{I}^{\mathcal{W}} \boldsymbol{\omega}^{\mathcal{W}} \quad (3.16)$$

Noting the transformations of the moment $\mathbf{M}^{\mathcal{W}} = \mathbf{R}_{\mathcal{B}}^{\mathcal{W}} \mathbf{M}^{\mathcal{B}}$, angular velocity $\boldsymbol{\omega}^{\mathcal{W}} = \mathbf{R}_{\mathcal{B}}^{\mathcal{W}} \boldsymbol{\omega}^{\mathcal{B}}$ and angular acceleration $\dot{\boldsymbol{\omega}}^{\mathcal{W}} = \mathbf{R}_{\mathcal{B}}^{\mathcal{W}} \dot{\boldsymbol{\omega}}^{\mathcal{B}}$, Euler's equation may be described in the body-fixed frame to provide the rotational response

$$\mathbf{I} \dot{\boldsymbol{\omega}} = \mathbf{M} - \boldsymbol{\omega} \times \mathbf{I} \boldsymbol{\omega} \quad (3.17)$$

where the superscripts are dropped for brevity, giving $\mathbf{M}^{\mathcal{B}} = \mathbf{M}$ and $\boldsymbol{\omega}^{\mathcal{B}} = \boldsymbol{\omega}$.

3.3.2 DERIVATION FROM EULER-LAGRANGE FORMALISM

The translational and rotational dynamics of a rotating rigid body are derived using Euler-Lagrange formalism. This approach considers the potential and kinetic energy of the system, the latter of which is composed of translational and rotational components.

Consider the generalised coordinate vector

$$\mathbf{q} = \begin{bmatrix} \mathbf{r} \\ \boldsymbol{\eta} \end{bmatrix}$$

composed of a translational component \mathbf{r} and rotational component $\boldsymbol{\eta}$.

The Lagrangian of the rigid body is the difference between the kinetic energy of the system and its potential energy. The kinetic energy is composed of translational and rotational components, giving

$$L = T_{\text{trans}} + T_{\text{rot}} - V \quad (3.18)$$

The total translational kinetic energy of the system is given by

$$T_{\text{trans}} = \frac{1}{2} m \dot{\mathbf{r}}^T \dot{\mathbf{r}}$$

while the total rotational kinetic energy is given by

$$T_{\text{rot}} = \frac{1}{2} \boldsymbol{\omega}^T \mathbf{I} \boldsymbol{\omega}$$

and the gravitational potential energy by

$$V = mgz$$

Recall the relationship between angular velocity and Euler rates described by Equation (3.9). The rotational kinetic energy may then be described in terms of the generalised coordinates

$$T_{\text{rot}} = \frac{1}{2} \dot{\boldsymbol{\eta}}^T \mathbf{J}_{\eta}^T \mathbf{I} \mathbf{J}_{\eta} \dot{\boldsymbol{\eta}}$$

The Lagrangian is then

$$L = \frac{1}{2} m \dot{\mathbf{r}}^T \dot{\mathbf{r}} + \frac{1}{2} \dot{\boldsymbol{\eta}}^T \mathbf{J}_{\eta}^T \mathbf{I} \mathbf{J}_{\eta} \dot{\boldsymbol{\eta}} - mgz$$

The generalised force vector \mathbf{Q} is composed of the forces and moments described in the body frame \mathcal{B} of the quadrotor

$$\mathbf{Q} = \begin{bmatrix} \bar{\mathbf{F}}^{\mathcal{B}} \\ \mathbf{J}_{\eta}^T \mathbf{M}^{\mathcal{B}} \end{bmatrix}$$

The system dynamics are then derived using the described Lagrangian and the Euler-Lagrange equation, given by Goldstein et al. (2001) as

$$\frac{d}{dt} \left(\frac{\partial L}{\partial \dot{\mathbf{q}}} \right) - \frac{\partial L}{\partial \mathbf{q}} = \mathbf{Q} \quad (3.19)$$

The resulting solution describes the translational motion with

$$m \ddot{\mathbf{r}} - mg \hat{\mathbf{z}} = \mathbf{R}_{\mathcal{B}}^{\mathcal{W}} \bar{\mathbf{F}}^{\mathcal{B}} \quad (3.20)$$

where $\bar{\mathbf{F}}^{\mathcal{B}}$ describes the non-gravitational force, as the gravitational contribution is already present due to consideration of the gravitational potential.

The rotational dynamics have the more complex solution

$$\mathbb{J} \ddot{\boldsymbol{\eta}} + C(\boldsymbol{\eta}, \dot{\boldsymbol{\eta}}) \dot{\boldsymbol{\eta}} = \mathbf{J}_{\eta}^T \mathbf{M} \quad (3.21)$$

where $\mathbb{J} = \mathbb{J}(\boldsymbol{\eta}) = \mathbf{J}_{\eta}^T \mathbf{I} \mathbf{J}_{\eta}$ and $C(\boldsymbol{\eta}, \dot{\boldsymbol{\eta}})$ describes the Coriolis component of the response. Using the small angle approximation, the rotational dynamics then

simplify to

$$\mathbf{I}\dot{\boldsymbol{\eta}} = \mathbf{M} - \dot{\boldsymbol{\eta}} \times \mathbf{I}\dot{\boldsymbol{\eta}} \quad (3.22)$$

3.3.3 LINEARISED MODEL

A linear rigid-body model may be obtained by linearising about the states

$$\begin{aligned} \mathbf{r}_0 &= [x, y, z]^T & \boldsymbol{\eta}_0 &= [0, 0, \psi]^T \\ \dot{\mathbf{r}}_0 &= [0, 0, 0]^T & \boldsymbol{\omega}_0 &= \dot{\boldsymbol{\eta}}_0 = [0, 0, 0]^T \end{aligned}$$

Assuming the presence of a gravitational force, the linear rigid-body model is described by

$$\ddot{\mathbf{r}} = \frac{1}{m} \begin{bmatrix} \cos \psi & -\sin \psi & 0 \\ \sin \psi & \cos \psi & 0 \\ 0 & 0 & 1 \end{bmatrix} \bar{\mathbf{F}}^{\mathcal{B}} + g \begin{bmatrix} -\sin \psi & -\cos \psi \\ \cos \psi & -\sin \psi \\ 0 & 0 \end{bmatrix} \begin{bmatrix} \phi \\ \theta \end{bmatrix} + \begin{bmatrix} 0 \\ 0 \\ g \end{bmatrix} \quad (3.23)$$

$$\dot{\boldsymbol{\eta}} = \mathbf{I}^{-1}\mathbf{M}$$

3.4 QUADROTOR FORCES AND MOMENTS

The described rigid body models relate the translational and rotational responses of the quadrotor to a force \mathbf{F} and moment \mathbf{M} , the compositions of which must be determined. Contributions to the force and moment include standard considerations such as the gravitational force and rotor response and more complex phenomena, described here.

3.4.1 GRAVITATIONAL FORCE

The gravitational force, already highlighted by the Euler-Lagrange derivation, acts exclusively in the z -axis of the world frame. Described in \mathcal{B} , it is

$$\mathbf{F}_{\text{grav}} = \mathbf{R}_{\mathcal{W}}^{\mathcal{B}} \begin{bmatrix} 0 \\ 0 \\ mg \end{bmatrix} \quad (3.24)$$

3.4.2 PROPULSIVE FORCE AND MOMENT

The majority of rotor models described by the literature assume that the thrust and torque produced by each rotor act exclusively in the z -axis of the body-fixed frame. The net propulsive force is therefore in the direction of $z^{\mathcal{B}}$ only, giving

$$\mathbf{F}_{\text{prop}} = \begin{bmatrix} 0 \\ 0 \\ -(T_1 + T_2 + T_3 + T_4) \end{bmatrix} \quad (3.25)$$

where T_i is the thrust generated by rotor $i \in \{1, 2, 3, 4\}$.

The propulsive moment arises from the thrusting action of each rotor about the centre of mass, which induces rolling and pitching motion. Additionally, the reactive torque of the rotors on the airframe produces a yaw response. The moment vector is therefore

$$\mathbf{M}_{\text{prop}} = \begin{bmatrix} L(T_3 - T_4) \\ L(T_2 - T_1) \\ -Q_1 - Q_2 + Q_3 + Q_4 \end{bmatrix} \quad (3.26)$$

where L is the distance of the rotor hubs from the centre of mass and Q_i is the torque generated by rotor i .

3.4.3 GYROSCOPIC TORQUE

The rotation of the rotor blades in combination with the body rotation results in a gyroscopic torque (Voos, 2009). If each rotor $i \in \{1, 2, 3, 4\}$ has rotational velocity Ω_i and moment of inertia I_r about the axis of rotation, the gyroscopic torque is

$$\mathbf{M}_{\text{gyro}} = I_r (\boldsymbol{\omega} \times \hat{\mathbf{z}}^B) (\Omega_1 + \Omega_2 + \Omega_3 + \Omega_4) \quad (3.27)$$

3.4.4 AERODYNAMIC DRAG

Aerodynamic drag on the quadrotor airframe can be approximated by the non-linear model

$$\mathbf{F}_{\text{drag}} = \frac{1}{2} A_c \rho \begin{bmatrix} c_x \dot{x} |\dot{x}| \\ c_y \dot{y} |\dot{y}| \\ c_z \dot{z} |\dot{z}| \end{bmatrix} \quad (3.28)$$

where c_x, c_y, c_z are drag coefficients, A_c is the effective body surface area and ρ is the atmospheric density. Linearising about a constant velocity provides the linear model

$$\mathbf{F}_{\text{drag}} = \frac{1}{2} A_c \rho \begin{bmatrix} \bar{c}_x \dot{x} \\ \bar{c}_y \dot{y} \\ \bar{c}_z \dot{z} \end{bmatrix} \quad (3.29)$$

where $\bar{c}_x, \bar{c}_y, \bar{c}_z$ are the linearised drag coefficients.

The majority of quadrotor models in the literature neglect aerodynamic drag, due to its negligible effect at low airspeeds. Inclusion of a drag model in description of the quadrotor has the useful property of allowing the vehicle to be trimmed about non-zero horizontal velocities.

3.5 ROTOR MODEL

Control of the quadrotor is achieved by adjusting the performance of each rotor such that the net force and moment in or about each axis produces the desired motion. The thrust and torque produced by a single rotor is related to its rotational speed. This is controlled by a pulse width modulation or voltage signal.

While the literature highlighted the tendency of some models to employ the rotorspeed Ω of each motor as the system input, the true input to the motor driving each rotor is either pulse width modulation or voltage. The former is used by the Qball-X4 quadrotor, while the latter is described in literature. Description of the thrust and torque response to the motor input therefore requires either: mapping of thrust and torque to rotorspeed; or direct mapping of thrust and torque to the motor input. The former approach employs separate models of the propeller and motor, described here, while the latter requires an empirical approach to modelling and is described in Chapter 4.

3.5.1 PROPELLER MODEL

From Prouty (1990), the thrust T and torque Q produced by a rotor can be related to its rotational speed Ω by

$$\begin{aligned} T &= C_T \rho A R^2 \Omega^2 \\ Q &= C_Q \rho A R^3 \Omega^2 \end{aligned} \quad (3.30)$$

where A is the rotor disk area and R is the rotor radius. The thrust and torque coefficients, C_T and C_Q respectively, are obtained either from empirical data or analytically, using the relationships described by Fay (2001)

$$\begin{aligned} \frac{C_T}{\sigma a} &= \left(\frac{1}{6} + \frac{1}{4} \mu^2 \right) \theta_0 - (1 + \mu^2) \frac{\theta_{tw}}{8} - \frac{1}{4} \lambda \\ \frac{C_Q}{\sigma a} &= \frac{1}{8a} (1 + \mu^2) \bar{C}_d + \lambda \left(\frac{1}{6} \theta_0 - \frac{1}{8} \theta_{tw} - \frac{1}{4} \lambda \right) \end{aligned} \quad (3.31)$$

where, for the quadrotor, the root pitch θ_0 and blade twist θ_{tw} are fixed. The advance ratio μ changes with vertical flight, resulting in a decrease in both thrust and torque with velocity increase in $-z^B$. Brandt and Selig (2011) demonstrate the loss of performance as advance ratio increases. The losses associated with the relatively small advance ratios of quadrotor are flight are negligible, however. The inflow ratio λ is roughly constant for the same reason.

Constant values of C_T and C_Q , obtained experimentally, describe the rotor behaviour in static flow, a valid assumption for the quadrotor, which normally operates around the hover state. Variable rotor coefficients are useful in more precise analysis of rotor behaviours, as exemplified by Pounds et al. (2010), who examine the effects of rotor flex on quadrotor control.

Bouabdallah (2007) also describes a *hub force* produced by the propeller, which acts normal to the axis of rotation and is similarly described by

$$\begin{aligned} H &= C_H \rho A R^2 \Omega^2 \\ \frac{C_H}{\sigma a} &= \frac{1}{4a} \mu \bar{C}_d + \frac{1}{4} \lambda \mu \left(\theta_0 - \frac{\theta_{tw}}{2} \right) \end{aligned} \quad (3.32)$$

and a rolling moment resulting from asymmetrical lift distribution over the rotor disk during forward flight, described by

$$\begin{aligned} R_m &= C_{R_m} \rho A R^3 \Omega^2 \\ \frac{C_{R_m}}{\sigma a} &= -\mu \left(\frac{1}{6} \theta_0 - \frac{1}{8} \theta_{tw} - \frac{1}{8} \lambda \right) \end{aligned} \quad (3.33)$$

The propeller model is often simplified in literature to the linear relationship

$$\begin{aligned} T &= K_T \Omega^2 \\ Q &= K_Q \Omega^2 \end{aligned} \quad (3.34)$$

where the gains K_T and K_Q are determined through system identification. This model is typically used in controller and trajectory design as it sufficiently describes the performance of the rotors around hover.

3.5.2 MOTOR MODEL

Motor models related in the literature exclusively describe the behaviour of a DC motor driven by a voltage signal. While the three-phase motor employed by the Qball may be modelled empirically, the DC motor model is included here for future consideration. As described by Bresciani (2008), by incorporating rotor and gearbox models, the dynamics of the full rotor system may be described by

$$J_{TR} \dot{\Omega} = -\frac{K_E K_M}{R_M} \eta_E N^2 \Omega - d \Omega^2 + \frac{K_M}{R_M} \eta N u \quad (3.35)$$

where J_{TR} is the moment of inertia of the rotor, K_E and K_M are electrical and mechanical constants, η_E is the efficiency of the system, N is the gearbox ratio and R_M is the resistance in the motor. The input u is a voltage signal in this instance.

Linearising about a nominal operating condition, the rotational speed at hover Ω_h , the rotational response of the rotor is given by

$$\dot{\Omega} = A_R \Omega + B_R u + C_R \quad (3.36)$$

where the coefficients are

$$\begin{aligned} A_R &= -\frac{K_E K_M \eta N^2}{J_{TR} R_M} - \frac{2d}{J_{TR}} \Omega_h \\ B_R &= \frac{K_M \eta N}{J_{TR} R_M} \\ C_R &= \frac{d}{J_{TR}} \Omega_h^2 \end{aligned}$$

and the parameters comprising them are dependent on the properties of the motor and rotor blades.

3.6 INPUTS AND PSEUDO-INPUTS

Denoting the input to a rotor $i = \{1, 2, 3, 4\}$ as u_i , the input vector to the quadrotor system is then

$$\mathbf{u} = [u_1, u_2, u_3, u_4]^T \quad (3.37)$$

Pseudo-inputs are often used in lieu of the true motor inputs to simplify controller design and stability analyses. Note the effect of the rotor thrusts and torques on the quadrotor forces and moments as described by Figure 3.2. Consider only the propulsive forces on the quadrotor. A linear relationship is assumed between the thrust T and torque Q generated by a rotor and its input u . Thus, for a rotor i , its thrust and torque models are described by

$$T_i = K_T u_i \quad Q_i = K_Q u_i \quad (3.38)$$

Defining the net thrust

$$T = \sum_{i=1}^4 T_i$$

and noting Equation (3.26), the net thrust and moments acting on the quadrotor are then related to the input \mathbf{u} by

$$\begin{bmatrix} T \\ M_x \\ M_y \\ M_z \end{bmatrix} = \begin{bmatrix} T_1 + T_2 + T_3 + T_4 \\ L(T_3 - T_4) \\ L(T_2 - T_1) \\ -Q_1 - Q_2 + Q_3 + Q_4 \end{bmatrix} = \begin{bmatrix} K_T(u_1 + u_2 + u_3 + u_4) \\ K_T L(u_3 - u_4) \\ K_T L(u_2 - u_1) \\ K_Q(-u_1 - u_2 + u_3 + u_4) \end{bmatrix}$$

The net thrust and moments are demonstrated by these equations to have linear relationships with the inputs. Thus, the four-pseudo inputs may be defined by normalising the thrust and moments with respect to the input \mathbf{u} . The resulting pseudo-input vector is denoted

$$\mathbf{u}^* = [u_{\text{col}}, u_{\text{lat}}, u_{\text{long}}, u_{\text{yaw}}]^T \quad (3.39)$$

and is related to the quadrotor thrust and moments, and hence the true input \mathbf{u} , by

$$\begin{bmatrix} u_{\text{col}} \\ u_{\text{lat}} \\ u_{\text{long}} \\ u_{\text{yaw}} \end{bmatrix} = \begin{bmatrix} T/K_T \\ M_x/K_T L \\ M_y/K_T L \\ M_z/K_Q \end{bmatrix} = \begin{bmatrix} 1 & 1 & 1 & 1 \\ 0 & 0 & 1 & -1 \\ -1 & 1 & 0 & 0 \\ -1 & -1 & 1 & 1 \end{bmatrix} \begin{bmatrix} u_1 \\ u_2 \\ u_3 \\ u_4 \end{bmatrix} \quad (3.40)$$

Thus, the pseudo-input is related to the true input by the relationship $\mathbf{u}^* =$

$\mathbf{C}\mathbf{u}$ where the Jacobian \mathbf{C} is

$$\mathbf{C} = \begin{bmatrix} 1 & 1 & 1 & 1 \\ 0 & 0 & 1 & -1 \\ -1 & 1 & 0 & 0 \\ -1 & -1 & 1 & 1 \end{bmatrix}$$

Use of pseudo-inputs provides a more intuitive approach to controlling the quadrotor, as each input can be considered to induce motion in a specific direction. The collective input u_{col} drives linear motion in the z^B direction, the lateral input u_{lat} controls rolling motion about x^B , the longitudinal input u_{long} similarly controls pitching motion about y^B and the yaw input u_{yaw} controls yawing motion about z^B . Employing pseudo-inputs has the added benefit of allowing the quadrotor system to be described as a series of single-input, single-output systems.

The inverse relationship may be employed to allow pseudo-inputs specified by the vehicle controller to be translated into true system inputs, that is

$$\mathbf{u} = \mathbf{C}^{-1}\mathbf{u}^*$$

For the case where the relationship of thrust and torque with input is not linear, the above simplification does not apply.

3.7 ADDITIONAL PHENOMENA

Additional phenomena which do not contribute directly to the force and moment acting on the quadrotor are described here.

3.7.1 GROUND EFFECT

Ground effect results in thrust augmentation at altitudes of approximately half the rotor diameter. Bouabdallah (2007) describes the ground effect as

$$\begin{aligned} T_{\text{IGE}} &= C_{T,\text{IGE}}\rho AR^2\Omega^2 \\ \frac{C_{T,\text{IGE}}}{\sigma a} &= \frac{C_{T,\text{OGE}}}{\sigma a} + \frac{\delta v_i}{4\Omega R} \end{aligned} \quad (3.41)$$

where the *in ground effect* thrust coefficient C_{IGE} is related to the out of ground effect coefficient C_{OGE} and a variation in the rotor inflow velocity δv_i which is induced by the image of the rotor, as described by Cheeseman and Bennett (1955). The inflow variation may be described by the function of height z and inflow velocity v_i

$$\delta v_i = v_i \left(\frac{R}{4z} \right)^2$$

Modelling of ground effect thus requires an inflow model is included in the description of rotor behaviour.

3.7.2 AIRFRAME BLOCKAGE AND DRAG

The performance of the rotors in isolation is known as the *free-air* performance (ESDU, 1985, 2006). The typical operating thrust and torque is reduced in comparison to free-air thrust and torque. This is due to airflow blockage caused by the surrounding structure. The rotors on a typical quadrotor are mounted on arms extending out from the centre of mass – these can cause some blockage. Additionally, some vehicles such as the Qball-X4 have protective cages which can affect the airflow through the rotors both upstream and downstream. The rotors can also create a drag force on the airframe, which opposes the direction of thrust and thus reduces performance further.

The rotors of the quadrotor are typically mounted on arms extending out from the centre of the vehicle. This can cause blockage of airflow through the rotors, resulting in a reduction in performance. Additionally, aircraft such as the Qball-X4 have protective cages which can cause a further reduction in performance.

3.7.3 ATMOSPHERIC TURBULENCE

Atmospheric turbulence impacts the quadrotor behaviour both as a disturbance force acting on the aircraft body and as a contribution to the inflow velocity on each rotor. The impact of the former may be modelled by substituting the inertial velocities in Equation (3.28) for the local airspeed components. The latter requires a model of the inflow effects on rotor performance. Description of the gust field itself is achieved either through a stochastic model with realistic bounds or using computational fluid dynamics to generate a velocity field, as described in Murray et al. (2014). This latter approach is yet another example of resolution increase, as well as an expansion of the model scope.

3.7.4 PROCESS NOISE

The state of a dynamic system is subject to process noise. This noise typically describes such phenomena as those detailed in this section. Combining disturbances such as gusts and vehicle vibration into a single noise vector is an yet another example of abstraction. Algorithms such as the Kalman Filter (Kalman, 1960) require knowledge of the covariance of the process noise in order to accurately estimate the system state. The process noise may also be included in models of the system to more accurately reflect its stochastic nature.

A non-linear controllable system with process noise \mathbf{w} has the general form

$$\dot{\mathbf{x}}(t) = f(\mathbf{x}(t), \mathbf{u}(t), \mathbf{w}(t))$$

where \mathbf{w} has covariance \mathbf{Q} and normal probability distribution

$$\mathbf{w}(t) \sim N(0, \mathbf{Q}(t))$$

CHAPTER 4

SYSTEM IDENTIFICATION OF THE QBALL-X4 QUADROTOR

System identification is used to provide data for the properties and models described in Chapter 3. Several approaches are available to determine system constants, including analytical and experimental methods. The results presented here are obtained primarily from experimental tests conducted on the Qball-X4 quadrotor in the University of Glasgow’s Micro Air Systems Technologies (MAST) Laboratory. A complete summary of the identified properties is provided in Appendix G.

The Qball-X4 quadrotor, shown in Figure 1.2, is the primary platform for investigation of autonomous systems in the MAST Laboratory. The primary purpose of the Qball in this project is to provide accurate values for the properties of the mechanistic models described in Chapter 3 and to provide empirical models of subsystems such as the rotors. The Qball is capable of autonomous flight using the MAST Laboratory’s Optitrack motion capture system, which supplies position and attitude measurements to the Qball’s control system. The setup and calibration of the Optitrack system are detailed in Appendix C. The Qball’s rotors are driven by brushless outrunner motors supplied by a constant voltage and variable Pulse-Width Modulation (PWM) signal. The on-board hardware allows direct control of the PWM signal supplied to the Electronic Speed Controller (ESC) of each motor. For the purposes of controlling the Qball and its derived model, the system input \mathbf{u} is a vector of inputs of the form

$$u_i = \bar{u}_i - \bar{u}_0 \tag{4.1}$$

where \bar{u}_i is the PWM signal to motor $i = \{1, 2, 3, 4\}$ and \bar{u}_0 is the PWM value corresponding to zero throttle.

4.1 THE MAST LABORATORY

The MAST Laboratory, shown in Figure 4.1, is used to design, build and test micro air vehicles, enabling rapid prototyping and allowing the full system design process to be undertaken. The MAST Laboratory employs an OptitrackTM motion capture system, supplied by Natural Point, Inc (2014), to provide position and attitude tracking of rigid bodies to a ground station computer. The QUARC[®] real-time control software, supplied with the Qball-X4 by Quanser, Inc (2014), provides toolboxes which facilitate control of the Qball. System controllers may be developed in Simulink[®] (The MathWorks, Inc, 2014a), using the QUARC toolboxes to received position and attitude data via Optitrack and send PWM commands to the Qball-X4 via a wifi connection.

The primary role of the MAST Laboratory in the investigations described in this thesis is to supply empirical data relating to the Qball-X4 for use in the described models. To enable this, a major part of this project has been the installation and setup of the hardware and software which gives the MAST Laboratory its capabilities. For the sake of brevity, the major accomplishments may be summarised as:

- Installation of QUARC interface software and ground station hardware for the Qball-X4 quadrotor.
- Testing and trouble-shooting of Qball-X4 manual flight controllers.
- Optimisation of camera placement using a model of the Optitrack camera system, described in Appendix C.
- Supervision of camera system installation and iterative refinement of camera positions and orientations.
- Calibration of camera system and testing of Qball-X4 in autonomous flight mode.
- Development and testing of prototype micro air vehicles, including a hexrotor and an octocopter.

4.2 BASIC PROPERTIES

Basic properties of the quadrotor and environment are easily obtained. Mass is measured using a digital scale, accurate to 0.001 kg. Table 4.1 provides the mass of the Qball, absent the photovoltaic sensor. With consideration of the position of the centre of mass (Section 4.3), the rotor moment arms are found to be of equal distance from the z^B axis. The rotor radius and disk area are based on measurements taken from the Qball's four APC 10x4.7 slow flyer propellers. Finally, standard values of the acceleration due to gravity and atmospheric density at sea level are used.



FIGURE 4.1: THE UNIVERSITY OF GLASGOW'S MAST LABORATORY, SHOWING THE OPTITRACK MOTION CAPTURE SYSTEM AND ONE OF SEVERAL QUADROTOR MAVS.

TABLE 4.1: BASIC QBALL-X4 PROPERTIES.

PROPERTY	SYMBOL	VALUE	UNIT
Mass	m	1.512	kg
Acceleration due to gravity	g	9.81	m s^{-2}
Atmospheric density	ρ	1.225	kg m^{-3}
Rotor moment arm	L	0.2	m
Rotor radius	R	0.127	m
Rotor disk area	A	0.051	m^2

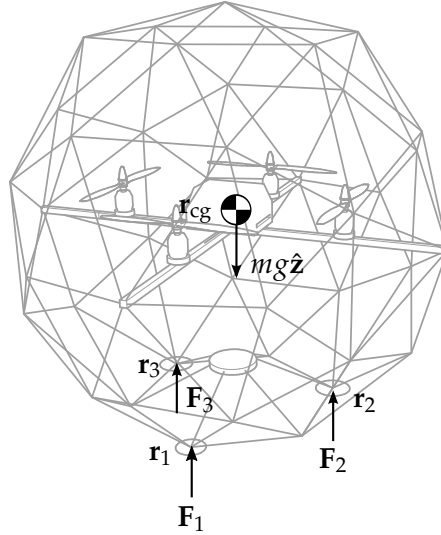


FIGURE 4.2: LOCATION OF AND FORCES AT THE CENTRE OF MASS OF THE QUADROTOR AND THE THREE SUPPORT POINTS AT THE VERTICES OF THE PROTECTIVE CAGE.

4.3 CENTRE OF MASS

The centre of mass is required in order to determine the moments of inertia of the vehicle body and the moment arms of the rotors.

4.3.1 METHODOLOGY

LOCATING THE CENTRE OF MASS IN A SINGLE PLANE

The quadrotor is supported at three points which form a plane, normal to the weight vector of the vehicle, as shown in Figure 4.2. The vehicle weight is distributed amongst the supports, each of which is subject to a resultant force, dependent on the position of the point with respect to the centre of mass. Thus, the structure may be described by

$$\mathbf{M} = (\mathbf{r}_1 - \mathbf{r}_{cg}) \times \mathbf{F}_1 + (\mathbf{r}_2 - \mathbf{r}_{cg}) \times \mathbf{F}_2 + (\mathbf{r}_3 - \mathbf{r}_{cg}) \times \mathbf{F}_3 = \mathbf{0} \quad (4.2)$$

where each point $i = \{1, 2, 3\}$ has position \mathbf{r}_i and is subject to force \mathbf{F}_i , and \mathbf{r}_{cg} is the position of the centre of mass.

Alternatively, since the moments arising from the forces on each point are known to balance the weight acting through \mathbf{r}_{cg} , the net moment may be described by

$$\mathbf{r}_{cg} \times (mg\hat{\mathbf{z}}) = \mathbf{r}_1 \times \mathbf{F}_1 + \mathbf{r}_2 \times \mathbf{F}_2 + \mathbf{r}_3 \times \mathbf{F}_3 \quad (4.3)$$

The position of the centre of mass in the horizontal plane formed by the three support points is then obtained from

$$\mathbf{r}_{cg}^* = \frac{1}{mg} \hat{\mathbf{z}} \times (\mathbf{r}_1 \times \mathbf{F}_1 + \mathbf{r}_2 \times \mathbf{F}_2 + \mathbf{r}_3 \times \mathbf{F}_3) \quad (4.4)$$

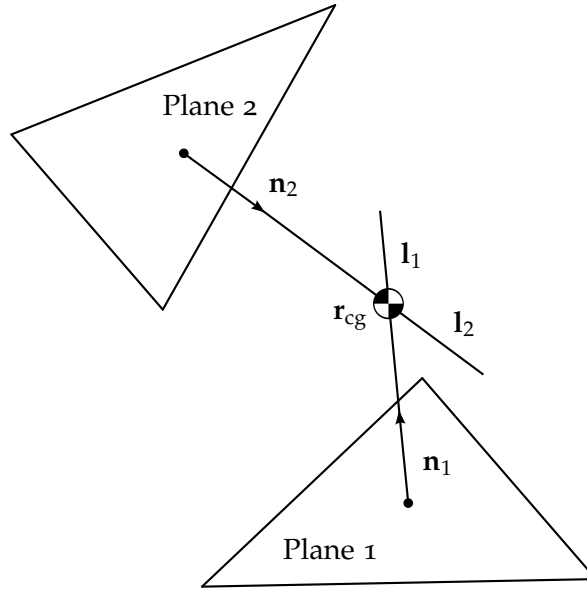


FIGURE 4.3: THE CENTRE OF MASS EXISTS AT THE INTERSECTION OF THE TWO LINES l_1 AND l_2 . THE LINES ARE NORMAL TO THE PLANES DEFINED BY THE SUPPORT POINTS OF EACH ORIENTATION.

Thus, the centre of mass is known to lie along a line, normal to the horizontal plane, which passes through point \mathbf{r}_{cg} .

Selecting three new support points, the vehicle is then positioned such that the weight vector acts in a different direction in the body-fixed frame. In repeating the above operations for this new orientation, the position of the centre of mass in a second plane is found. The CG is then known to exist at the intersection of the lines passing through the two planes at points $\mathbf{r}_{cg,1}^*$ and $\mathbf{r}_{cg,2}^*$.

LINE INTERSECTION

Figure 4.3 shows the intersection of the two lines at the centre of mass. The line normal to plane 1 and passing through $\mathbf{r}_{cg,1}^*$ is described by the equation

$$l_1 = \mathbf{r}_{cg,1}^* + t_1 \mathbf{n}_1 \quad (4.5)$$

with the line normal to plane 2 similarly described by

$$l_2 = \mathbf{r}_{cg,2}^* + t_2 \mathbf{n}_2 \quad (4.6)$$

where \mathbf{n}_1 and \mathbf{n}_2 are the surface normals for each plane.

It is assumed that a unique solution exists for the intersection of the two lines. The centre of mass thus lies at this intersection point, given by

$$\begin{aligned} \mathbf{r}_{cg} &= \mathbf{r}_{cg,1}^* + t_1 \mathbf{n}_1 \\ &= \mathbf{r}_{cg,2}^* + t_2 \mathbf{n}_2 \end{aligned} \quad (4.7)$$

where t_1 and t_2 are parameters describing the distance of the CG along each

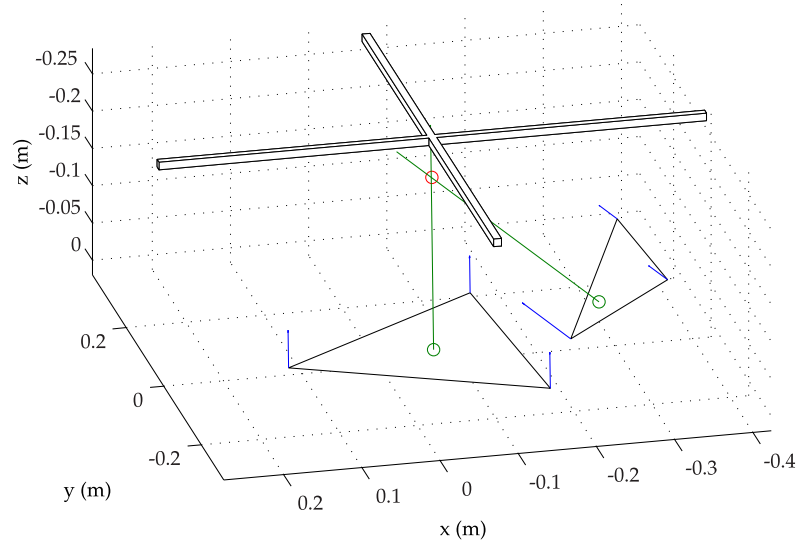


FIGURE 4.4: EXPERIMENTAL DATA PROVIDES THE RESULTANT FORCES AND POSITIONS OF EACH POINT, ALLOWING TWO PLANES TO BE DEFINED. THE POSITION OF THE CENTRE OF MASS IN EACH PLANE THEN PROVIDES THE THREE-DIMENSIONAL POSITION AT THE INTERSECTION OF EACH LINE.

line from the points $\mathbf{r}_{cg,1}^*$ and $\mathbf{r}_{cg,2}^*$, respectively.

The intersection of the two lines is then found by equating the components of the lines in two axes and solving for t_1 and t_2 . Thus, for the equations

$$\begin{aligned} x_{cg,1}^* + t_1 n_{1,x} &= x_{cg,2}^* + t_2 n_{2,x} \\ z_{cg,1}^* + t_1 n_{1,z} &= z_{cg,2}^* + t_2 n_{2,z} \end{aligned} \quad (4.8)$$

have the solutions

$$\begin{aligned} t_1 &= \frac{n_{2,x}(z_{cg,1}^* - z_{cg,2}^*) - n_{2,z}(x_{cg,1}^* - x_{cg,2}^*)}{n_{1,x}n_{2,z} - n_{2,x}n_{1,z}} \\ t_2 &= \frac{n_{1,x}(z_{cg,1}^* - z_{cg,2}^*) - n_{1,z}(x_{cg,1}^* - x_{cg,2}^*)}{n_{1,x}n_{2,z} - n_{2,x}n_{1,z}} \end{aligned} \quad (4.9)$$

4.3.2 EXPERIMENTAL RESULTS

The Optitrack motion capture system, typically employed to track MAVs in the MAST Laboratory, was used to record the position of the support points, relative to the reference frame used in the lab. The Qball was supported on its side and the weight acting on each point recorded. It was then oriented as normal, with the weight through three of the supporting feet recorded. The Optitrack system then provided the positions of the six points comprising the two horizontal planes.

The normals of each plane then provide the direction vector along which the supporting forces act. Applying the methodology presented in the previous section, the equations of the lines are described in the Optitrack reference frame

by

$$\mathbf{l}_1 = \begin{bmatrix} -0.0757 \\ 0.0300 \\ 0.0174 \end{bmatrix} + t_1 \begin{bmatrix} 0 \\ 0 \\ -1 \end{bmatrix} \quad (4.10)$$

$$\mathbf{l}_2 = \begin{bmatrix} -0.2892 \\ 0.0377 \\ -0.0252 \end{bmatrix} + t_2 \begin{bmatrix} 0.7491 \\ -0.0392 \\ -0.6613 \end{bmatrix} \quad (4.11)$$

The intersection of these lines in the x - z plane provides the solutions $t_1 = 0.2311$ and $t_2 = 0.2850$. Substituting into equations (4.10) and (4.11) then provide two solutions for the position of the centre of mass,

$$\mathbf{r}_{\text{cg},1} = \begin{bmatrix} -0.0757 \\ 0.0300 \\ -0.2137 \end{bmatrix}$$

$$\mathbf{r}_{\text{cg},2} = \begin{bmatrix} -0.0757 \\ 0.0266 \\ -0.2137 \end{bmatrix}$$

The existence of two solutions is due to the two lines not intersecting in three-dimensional space, but rather passing within millimetres of one another. This error can be attributed to the resolution of the Optitrack system and differences between the positions of the markers used to denote the support points and the true positions of the support points.

The position of the centre of mass is thus taken as the centroid of the two calculated positions,

$$\mathbf{r}_{\text{cg}} = \begin{bmatrix} -0.0757 \\ 0.0286 \\ -0.2137 \end{bmatrix}$$

which corresponds to a point directly below the geometric centre of the quadrotor airframe, as shown in Figure 4.4. Denoting the geometric centre as point p , the centre of mass thus has relative position

$$\mathbf{r}_{\text{cg}/p}^{\mathcal{B}} = \begin{bmatrix} 0.00 \\ 0.00 \\ 0.05 \end{bmatrix}$$

described in the body-fixed frame.

4.4 MOMENTS OF INERTIA

The moments of inertia of the quadrotor are required to accurately model its attitude dynamics. While it is possible to derive the moments of inertia about

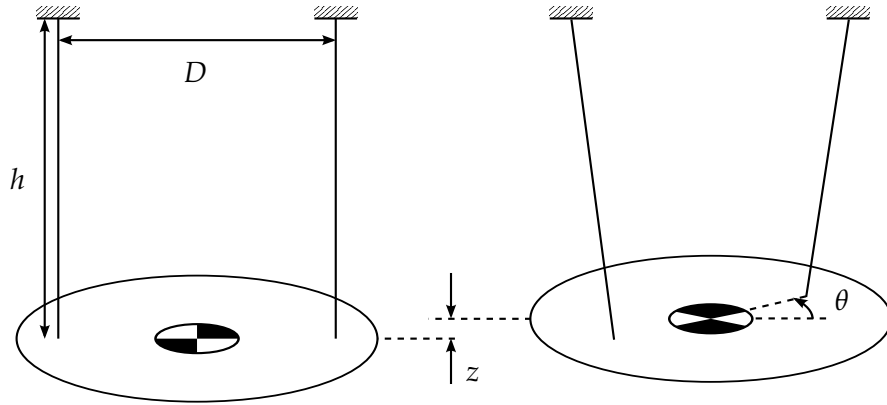


FIGURE 4.5: THE BIFILAR TORSIONAL PENDULUM. THE BODY IS SUSPENDED AT TWO POINTS ON EITHER SIDE OF THE CENTRE OF MASS. BY ROTATING THROUGH ANGLE θ , THE BODY GAINS HEIGHT z . THE MOMENT WHICH DRIVES THE ROTATIONAL RESPONSE OF THE SYSTEM IS THEN PROVIDED BY THE WEIGHT OF THE BODY.

each of the principle axes analytically through consideration of the mass and positions of the vehicle components (Bresciani, 2008), an experimental approach is employed here. Due to the cross configuration of the aircraft, it is assumed that off-axis inertias are negligible. The bifilar pendulum method is used to determine the principle moments of inertia of the quadrotor.

4.4.1 THE BIFILAR TORSIONAL PENDULUM

The bifilar pendulum test described by Jardin and Mueller (2009) involves suspending the vehicle with two wires of length h , separated by distance D (Figure 4.5). If the centre of the quadrotor-body-fixed frame of reference \mathcal{B} is located at the centre of mass, then the vehicle is positioned such that the axis of interest is located at the halfway point between the suspending wires and is parallel to them.

The vehicle is then rotated through angle θ about the axis of interest such that it rises through height z . The weight of the vehicle then provides the restoring torque which drives the rotational response of the system. The moment of inertia about the axis of interest may then be obtained from the natural frequency of the response. The relationship between moment of inertia and natural frequency is determined by first deriving the equation of motion of the rotational response using Euler-Lagrange formalism.

Recalling the Euler-Lagrange equation, and considering the single generalised coordinate θ , the response of the system to a moment M is described by

$$\frac{d}{dt} \left(\frac{\partial L}{\partial \dot{\theta}} \right) - \frac{\partial L}{\partial \theta} = M \quad (4.12)$$

As before, the Lagrangian is the difference between the kinetic energy of the system, composed of rotational and translational components and given by

$$T = \frac{1}{2}I\dot{\theta}^2 + \frac{1}{2}m\dot{z}^2 \quad (4.13)$$

and the gravitational potential energy, given by

$$V = mgz \quad (4.14)$$

The frequency of the rotational response of the pendulum is the property of interest; the vertical displacement z is thus described in terms of θ . The resulting relationship, derived by considering the geometry of the system, is

$$z = h \left(1 - \sqrt{1 - \frac{D^2}{2h^2}(1 - \cos \theta)} \right) \quad (4.15)$$

The translational kinetic energy is negligible in comparison to the rotational kinetic energy, thus the Lagrangian is simplified and Equation (4.15) substituted to obtain

$$\begin{aligned} L &= \frac{1}{2}I\dot{\theta}^2 - mgz \\ &= \frac{1}{2}I\dot{\theta}^2 - mgh \left(1 - \sqrt{1 - \frac{D^2}{2h^2}(1 - \cos \theta)} \right) \end{aligned} \quad (4.16)$$

Assuming both aerodynamic drag and viscous damping are opposing the motion of the pendulum, the moment M is expressed by

$$Q = -K_D\dot{\theta}|\dot{\theta}| - C_D\dot{\theta} \quad (4.17)$$

The equation of motion describing the rotational response is then obtained by substituting the expressions for kinetic energy, potential energy and generalised force in Equation (4.12):

$$\ddot{\theta} + \frac{K_D}{I}\dot{\theta}|\dot{\theta}| + \frac{C_D}{I}\dot{\theta} + \frac{mgD^2}{4Ih} \frac{\sin \theta}{\sqrt{1 - \frac{D^2}{2h^2}(1 - \cos \theta)}} = 0 \quad (4.18)$$

A linear approximation is obtained by describing the aerodynamic damping term with a linear function and using the small angle assumption, resulting in

$$\ddot{\theta} + \frac{1}{I} \left(\frac{8A}{3\pi}K_D + C_D \right) \dot{\theta} + \frac{mgD^2}{4Ih} \theta = 0 \quad (4.19)$$

Comparing to the equation of motion for a simple harmonic oscillator,

$$\ddot{\theta} + 2\zeta\omega_n\dot{\theta} + \omega_n^2\theta = 0 \quad (4.20)$$

the moment of inertia may be related to the natural frequency of the response by

$$I = \frac{mgD^2}{4I\omega_n^2} \quad (4.21)$$

TABLE 4.2: MEASURED MOMENTS OF INERTIA, COMPARED WITH VALUES SUPPLIED BY THE VENDOR OF THE QBALL.

PROPERTY	SYMBOL	VALUE	VENDOR	UNIT
Moment of inertia about x^B	I_x	0.032	0.03	kg m ²
Moment of inertia about y^B	I_y	0.033	0.03	kg m ²
Moment of inertia about z^B	I_z	0.041	0.04	kg m ²

For Equation (4.21) to provide accurate results, the linear approximation of the system response must accurately describe the system dynamics. The initial rotational displacement of the vehicle body must therefore be small. For an error of less than 1%, θ must be in the range $-14^\circ \leq \theta \leq 14^\circ$.

4.4.2 EXPERIMENTAL RESULTS

The quadrotor is oriented such that the x -axis of the quadrotor is aligned with the vertical axis and the centre of mass positioned midway between the suspension wires. A small initial angular displacement about the vertical axis then results in a damped oscillatory response. The rotation of the system is captured on video and the period of ten oscillations determined. The natural frequency of the system is then

$$\omega_n = \frac{2\pi}{T} \quad (4.22)$$

where T is the period of a single oscillation.

The experiment is repeated for rotation about the x -axis with slight variations on the initial displacement. The same process is then repeated for the y - and z -axes in the quadrotor body-fixed frame. The average natural frequency of the response in each axis then provides the moments of inertia as given in Table 4.2.

4.5 ROTOR PROPERTIES AND DYNAMICS

The behaviour of the Qball's rotors may be described either mechanistically or empirically. Section 3.5 describes a rotor model composed of an actuator disk in static flow and a simple motor model. For this model to accurately predict the response of the Qball's rotors, it is necessary to determine the constant properties of the models. Alternately, an empirical model of the rotor response may be obtained by identifying the steady-state and dynamic relationships of the rotors.

4.5.1 METHODOLOGY

Each of the four propeller and motor pairs are attached to a transducer as shown in Figure 4.6. The transducer measures the axial force and torque of the rotor, which it outputs as two voltage signals. The voltage signals are received

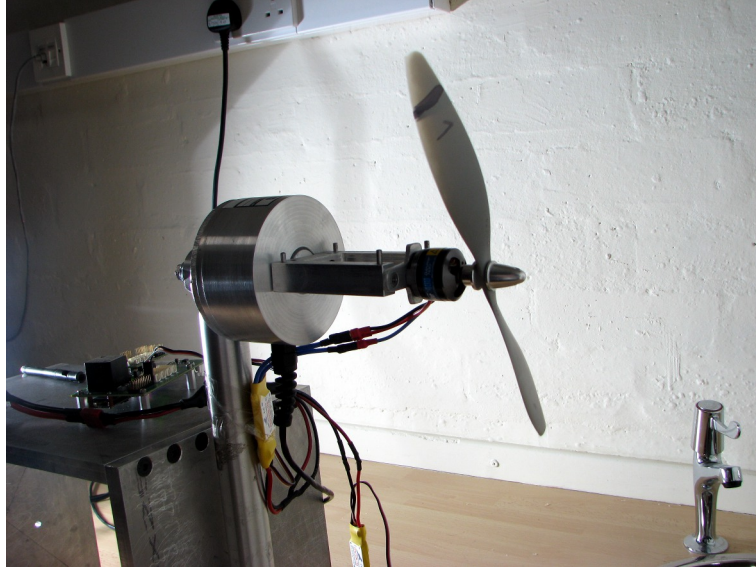


FIGURE 4.6: EXPERIMENTAL RIG FOR ROTOR CHARACTERISATION.

in LabVIEW and converted to thrust and torque using the calibration data detailed in Appendix E. A variable-frequency strobe light is used to measure the rotorspeed. The PWM command to the motor is supplied using a custom controller deployed on the Qball's autopilot hardware. The PWM command \bar{u} is increased incrementally in the range $[0.05, 0.1]$ and the rotorspeed, thrust and torque are recorded. The voltage level of the motor's power supply is also recorded. The complete set of data obtained during system identification of the rotors is described in Appendix E.

4.5.2 IDENTIFYING PROPERTIES OF A MECHANISTIC ROTOR MODEL

A mechanistic rotor model is described in Section 3.5. The propeller model described by Equation (3.30) requires identification of the atmospheric density at the aircraft's operating altitude, the rotor radius and the thrust and torque coefficients of the rotor disk. Using the properties described in Section 4.2, identifying the relationship between thrust T , torque Q and rotorspeed Ω can provide the thrust and torque coefficients, C_T and C_Q , respectively. The thrust and torque measurements taken by the transducer are compared to the rotor-speed measurements across the given range of PWM values. The resulting relationships are shown in Figure 4.7. From the experimental data, the thrust and torque of the Qball in static flow may be approximated by the relationships

$$T = 1.7 \times 10^{-5} \Omega^2 \qquad Q = 2.6 \times 10^{-7} \Omega^2$$

The identified thrust and torque coefficients are then given in Table 4.3. The values are shown to be consistent with those described by Brandt and Selig (2011) for an identical propeller in static flow.

The motor model described by Equation (3.36) is composed of several con-

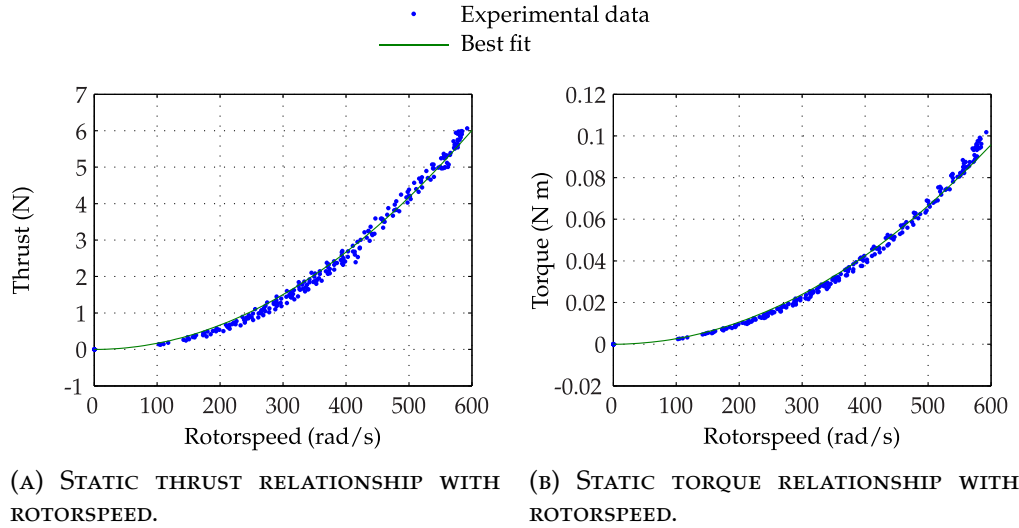


FIGURE 4.7: MEASURED THRUST AND TORQUE RELATIONSHIPS WITH ROTORSPEED AT STEADY-STATE.

TABLE 4.3: IDENTIFIED THRUST AND TORQUE COEFFICIENTS, COMPARED TO VALUES PROVIDED BY BRANDT AND SELIG (2011) FOR IDENTICAL PROPELLER AT COMPARABLE ROTORSPEED.

PROPERTY	SYMBOL	VALUE	BRANDT & SELIG
Thrust coefficient	C_T	0.0170	0.0155
Torque coefficient	C_Q	0.0026	0.0021

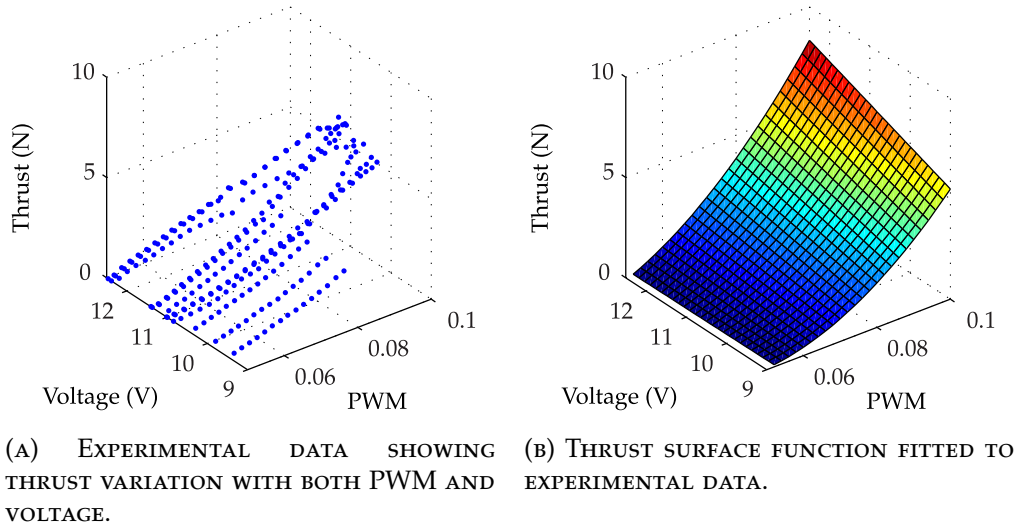


FIGURE 4.8: THRUST CHARACTERISATION RESULTS.

starts related to the configuration of the motor. The motor model describes a DC motor driven by a voltage signal, while the Qball uses three-phase motors driven by a constant voltage and PWM signal. An empirical approach to modelling the rotor behaviour is therefore taken.

4.5.3 AN EMPIRICAL MODEL OF ROTOR BEHAVIOUR

An empirical model of the rotors may be developed by identifying both steady-state and dynamic relationships.

STEADY-STATE RELATIONSHIPS

The thrust and torque of each rotor is measured across the range of PWM values given previously. Successive iterations of the experiment indicated a loss in thrust and torque with a decrease in the voltage supply to the motor. The results of the rotor system identification therefore describe the relationship of thrust and torque with both PWM and the supplied voltage. MATLAB's Curve Fitting Tool is used to fit the experimental data to a quadratic polynomial surface. This approach employs a linear least squares algorithm with robustness provided by the least absolute residual. Figures 4.8 and 4.9 show the captured data from several iterations of the experiment, across a range of PWM and voltage values. The thrust and torque relationships with zeroed PWM u and voltage V are then

$$\begin{aligned} T &= k_{T1}u + k_{T2}u^2 + k_{T3}uV \\ Q &= k_{Q1}u + k_{Q2}u^2 + k_{Q3}uV \end{aligned} \quad (4.23)$$

where the coefficients of each polynomial are given in Table 4.4.

The nominal operating voltage of the Qball's lithium-polymer batteries is 11.1 V. Assuming a constant voltage level during flight, a linear thrust and

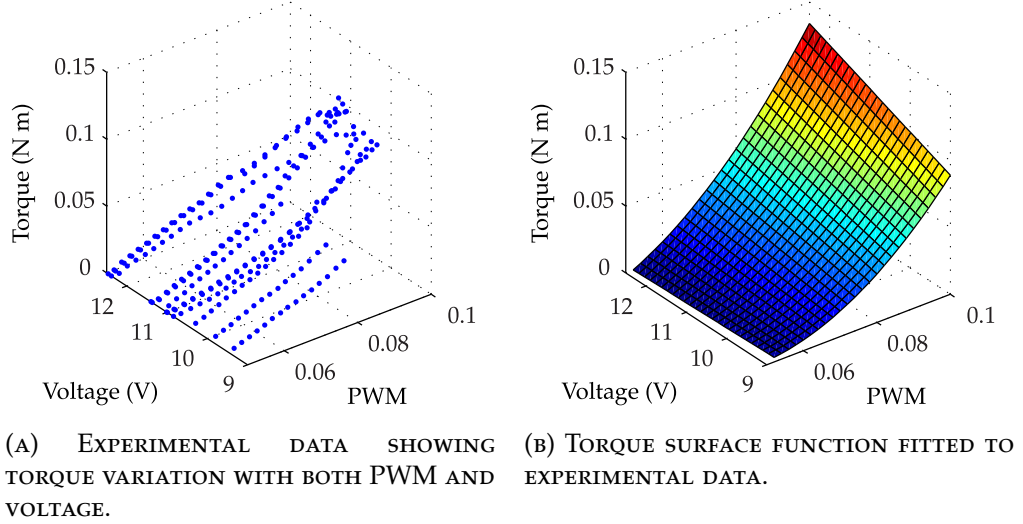


FIGURE 4.9: TORQUE CHARACTERISATION RESULTS.

TABLE 4.4: COEFFICIENTS OF POLYNOMIALS RELATING THRUST AND TORQUE TO PWM AND VOLTAGE.

PROPERTY	SYMBOL	VALUE	UNIT
Thrust gains	k_{T1}	-115.0404	N
	k_{T2}	1671.4069	N
	k_{T3}	16.4609	N V^{-1}
Torque gains	k_{Q1}	-1.6911	Nm
	k_{Q2}	27.2730	Nm
	k_{Q3}	0.2491	N m V^{-1}

TABLE 4.5: GAINS OF LINEAR MODELS RELATING THRUST AND TORQUE TO ZEROED PWM COMMAND.

PROPERTY	SYMBOL	VALUE	UNIT
Thrust gains	K_T	119.6	N
	K_T^*	171.3	N
Torque gains	K_Q	1.919	N m
	K_Q^*	2.764	N m

torque model may be found by considering the thrust and torque relationships at hover and rest. The resulting model is simply

$$T = K_T u \qquad Q = K_Q u \qquad (4.24)$$

An alternative approach to deriving the linear model is to linearise Equation (4.23) for perturbations about the hover state. This results in the linear model

$$T = K_T^* \Delta u + T_h \qquad Q = K_Q^* \Delta u + Q_h \qquad (4.25)$$

where Δu is the perturbation in input about the value for hover u_h , T_h and Q_h are the thrust and torque at hover. The calculated gains for each model are given in Table 4.5.

A comparison of the identified steady-state thrust and torque models is given in Figure 4.10. The linear relationship described by (4.24) is shown to be closer to the non-linear model between rest and hover, while the model linearised around hover is more representative of the true relationship for thrust and torque at values greater than those at hover. Using a linear model rather than the non-linear model described by Equation (4.23) affords the quadrotor system model useful properties with regards to control, such as a *control-affine* form.

DYNAMIC RELATIONSHIPS

The dynamic response of the motors is determined by recording the response in thrust and torque to a series of step inputs. MATLAB's System Identification Tool is used to identify the dynamics of the thrust and torque signals with respect to the PWM input. The magnitudes of the respective signals are neglected by identifying the response of thrust T and torque Q to set-points T_d and Q_d , which are related to the PWM input by the steady-state models described previously.

The thrust response is determined to be a 2nd-order system, described by

$$\frac{T(s)}{T_d(s)} = \frac{c_{T1}}{s^2 + c_{T2}s + c_{T1}} \qquad (4.26)$$

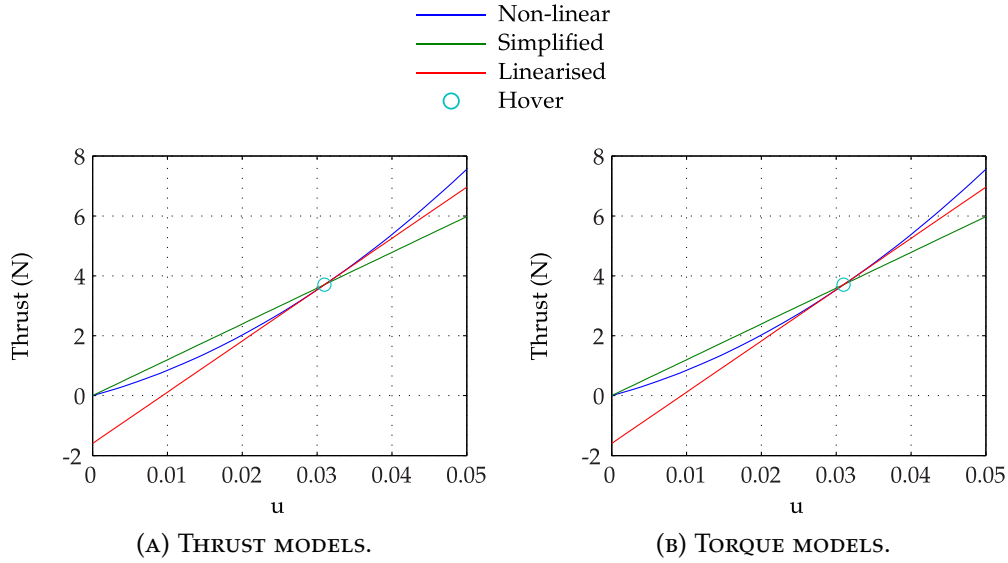


FIGURE 4.10: IDENTIFIED STEADY-STATE THRUST AND TORQUE MODELS OF QBALL-X4 QUADROTOR.

TABLE 4.6: COEFFICIENTS OF THE TRANSFER FUNCTIONS DESCRIBING THRUST AND TORQUE RESPONSE.

PROPERTY	SYMBOL	VALUE
Thrust coefficients	c_{T1}	198.8
	c_{T1}	24.81
	c_{Q1}	2.191×10^4
Torque coefficients	c_{Q2}	2425
	c_{Q3}	67.23
	c_{Q4}	6.793×10^3

while the torque response is found to be a 3rd-order system, described by

$$\frac{Q(s)}{Q_d(s)} = \frac{c_{Q4}s + c_{Q1}}{s^3 + c_{Q3}s^2 + c_{Q2}s + c_{Q1}} \quad (4.27)$$

where the coefficients of each transfer function are given in Table 4.6.

Both the thrust and torque responses may be approximated by the first-order model

$$\frac{T(s)}{T_d(s)} = \frac{Q(s)}{Q_d(s)} = \frac{\omega_R}{s + \omega_R} \quad (4.28)$$

which is sufficient to represent the lag in rotor response in many applications. For the Qball's rotor system, the actuator frequency of the first-order approximation is

$$\omega_R = 10 \text{ rad s}^{-1}$$

The first-order and higher-order models are compared to the experimental measurements in Figure 4.11. While the 2nd- and 3rd-order models accurately

represent the response in thrust and torque respectively, the 1st-order model is sufficient to represent the lag between input and steady-state in the response of both thrust and torque.

FULL ROTOR MODEL

Noting the steady-state and dynamic relationships described in this section, the full rotor model as determined through black box system identification is

$$\begin{aligned}\dot{T} &= c_{T1} (k_{T1}u + k_{T2}u^2 + k_{T3}uV - T) - c_{T2}\dot{T} \\ \ddot{Q} &= c_{Q4} (k_{Q1}u + k_{Q2}u^2 + k_{Q3}uV) + q_Q \\ \dot{q}_Q &= (c_{Q1} - c_{Q3}c_{Q4}) (k_{Q1}u + k_{Q2}u^2 + k_{Q3}uV) - c_{Q1}Q - c_{Q2}\dot{Q} - c_{Q3}q_Q\end{aligned}\tag{4.29}$$

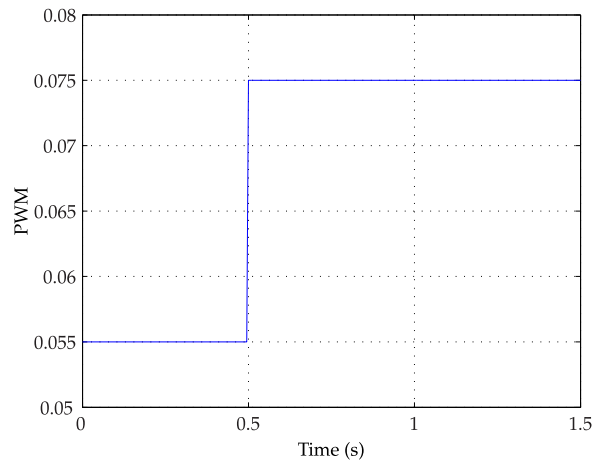
where q_Q is an arbitrary state used to describe the zero in the torque response and the coefficients are as previously defined. This model is based on the characterisation of each of the four rotors separately. Phenomena which may affect the rotor performance in flight but are not present during system identification include blockage from the airframe, ground effect and flow interaction with other rotors.

4.6 VALIDATION OF QUADROTOR MODELS

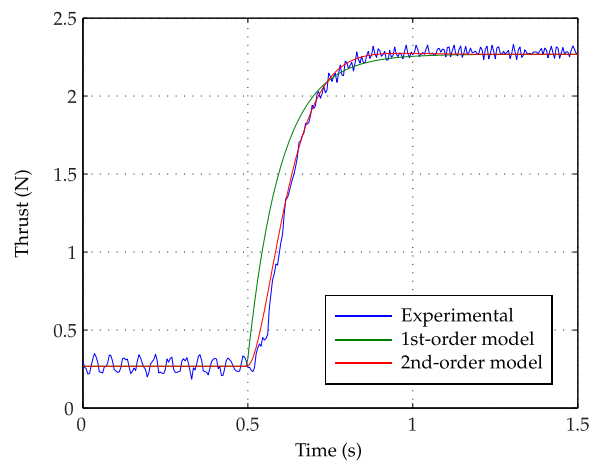
Data from several flights of the Qball is used to validate the rotor and rigid-body models described in this chapter and Chapter 3. The Qball's Inertial Measurement Unit (IMU) employs accelerometers and gyroscopes to measure specific force and angular velocity, respectively, while the Optitrack motion capture system (Figure 4.1) measures the position and attitude of the aircraft. These sensors are detailed in Appendix B. From these measurements, the translational and rotational accelerations of the aircraft may be determined and compared to expected results from simulation. This is a form of behaviour pattern testing, as described by Barlas (1994).

4.6.1 METHODOLOGY

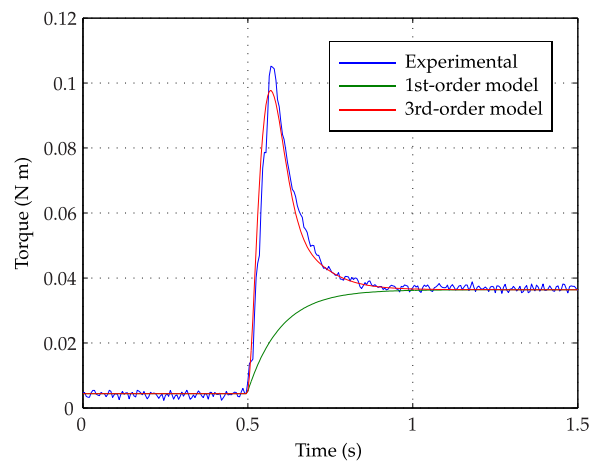
The translational acceleration $\ddot{\mathbf{r}}_{\text{exp}}$ of the Qball during a flight is obtained by differentiating the position history measured by the Optitrack system. The rotational acceleration $\dot{\omega}_{\text{exp}}$ during the flight is obtained through differentiation of the gyroscope measurements. These sensor outputs are chosen to avoid unnecessary frame transformations which could introduce additional noise into the measurements. The acceleration history of the Qball is then compared to simulation results obtained using a model of the system. The criteria for model selection is that it is of high resolution and all properties have been identified and given values. Further discussion of model selection criteria is detailed in



(A) STEP INPUT SIGNAL.



(B) THRUST RESPONSE TO STEP INPUT.



(C) TORQUE RESPONSE TO STEP INPUT.

FIGURE 4.11: DATA SAMPLE FROM ROTOR DYNAMICS IDENTIFICATION. EXPERIMENTAL DATA IS COMPARED TO THE RESULTS OF APPLYING A STEP INPUT TO THE DESCRIBED THRUST AND TORQUE TRANSFER FUNCTIONS.

Chapter 5. The validation model is then

$$\begin{aligned} \dot{\mathbf{r}}_{\text{sim}} &= \begin{bmatrix} 0 \\ 0 \\ g \end{bmatrix} + \frac{1}{m} \mathbf{R}_B^W \begin{bmatrix} 0 \\ 0 \\ -(T_1 + T_2 + T_3 + T_4) \end{bmatrix} \\ \dot{\boldsymbol{\omega}}_{\text{sim}} &= \mathbf{I}^{-1} \begin{bmatrix} L(T_3 - T_4) \\ L(T_2 - T_1) \\ -Q_1 - Q_2 + Q_3 + Q_4 \end{bmatrix} \end{aligned} \quad (4.30)$$

$$\begin{aligned} \text{where } \ddot{T}_i &= c_{T1} (k_{T1}u_i + k_{T2}u_i^2 + k_{T3}u_iV - T) - c_{T2}\dot{T} \\ \ddot{Q} &= c_{Q4} (k_{Q1}u_i + k_{Q2}u_i^2 + k_{Q3}u_iV) + q_{Q,i} \\ \dot{q}_{Q,i} &= (c_{Q1} - c_{Q3}c_{Q4}) (k_{Q1}u_i + k_{Q2}u_i^2 + k_{Q3}u_iV) \\ &\quad - c_{Q1}Q - c_{Q2}\dot{Q} - c_{Q3}q_Q \end{aligned}$$

where u_i is the input to each motor $i = \{1, 2, 3, 4\}$. The properties of the constants are detailed in this chapter and described in full in Appendix G. The transformation matrix \mathbf{R}_B^W is informed by attitude data capture by the Optitrack system. Note that the rotational response of the modelled system has been simplified to avoid systematic drift errors caused by integration of the estimated accelerations. This abstraction is valid for the small angular velocities which occurred during the experimental flight tests.

4.6.2 RESULTS

Comparisons of the empirical and simulation results are shown in Figures 4.12 and 4.13. The simulated accelerations are shown to follow the general trend of the empirical results, with an approximately constant bias in \ddot{z} and variable biases in the rotational velocities. The Qball was operated primarily at the hover condition, with small deviations to produce identifiable perturbations for the validation. This is indicated in the experimental acceleration signals, which have means of approximately zero. Assuming negligible bias or magnitude error in the experimental accelerations, the given results demonstrate an error in the validation model.

The sustained bias error in prediction of \ddot{z} indicates either miscalculation of the system constants or the presence of unmodelled dynamics. A rigorous approach to testing reduces the likelihood of the former source, thus the latter is considered. The rotor model described in Equation (4.30) represents the free-air rotor behaviour in static flow. Additional phenomena which affect the rotor performance are described in Chapter 3. Since ground effect improves rotor performance, its effects on the quadrotor during the test flights are either minimal or are negated by detrimental system behaviour. Likely candidates include blockage and propeller-off airframe drag.

Errors in the prediction of rotational acceleration indicate either: miscalculation of centre of mass; random disturbances; or differences in the performance

of each rotor. Characterisation of the rotors demonstrated uniform performance in the rotors, thus a reduction in thrust could be again be attributed to effects such as airframe blockage or drag.

4.6.3 DISCUSSION OF VALIDATION RESULTS

The validation experiment performed in this section highlights the deficit of confidence in the model described by Equation (4.30), despite the validity of its constituent parts. This provides valuable potential for further investigation in the validity of high-resolution models. The validity could be improved through the introduction of additional behaviours such as those described in Chapter 3 and further empirical testing. For the purposes of the simulation investigations presented in this thesis, the model described by Equation (4.30) is assumed to be sufficiently valid. Extension of the investigations in the following chapters to empirical testing would require a model of higher confidence, although not necessarily higher resolution.

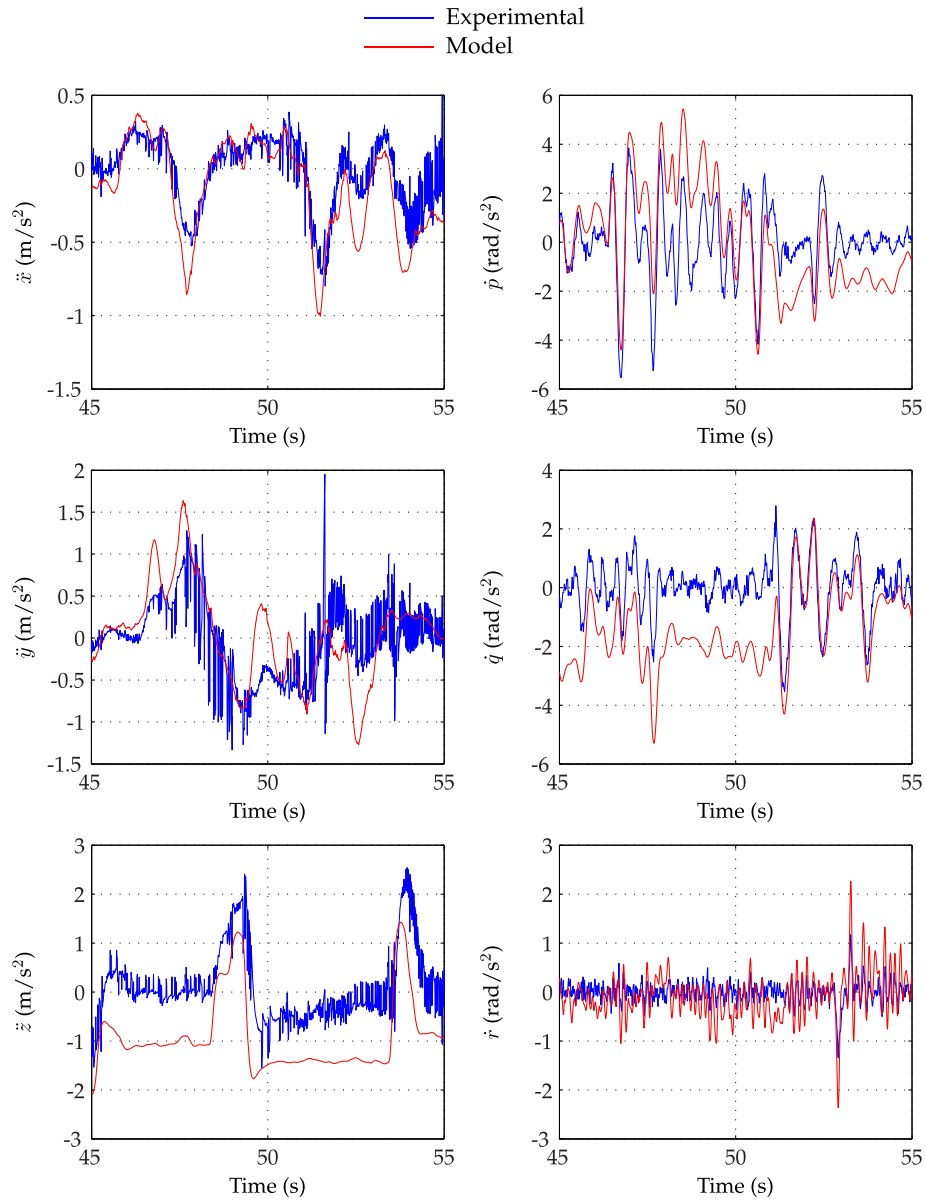


FIGURE 4.12: TRANSLATIONAL AND ROTATIONAL ACCELERATIONS FROM AN EMPIRICAL TEST ARE COMPARED WITH EXPECTED RESULTS FROM SIMULATION. THE SIMULATION MODEL IS DRIVEN BY THE INPUT SIGNALS RECORDING DURING EMPIRICAL TESTING.

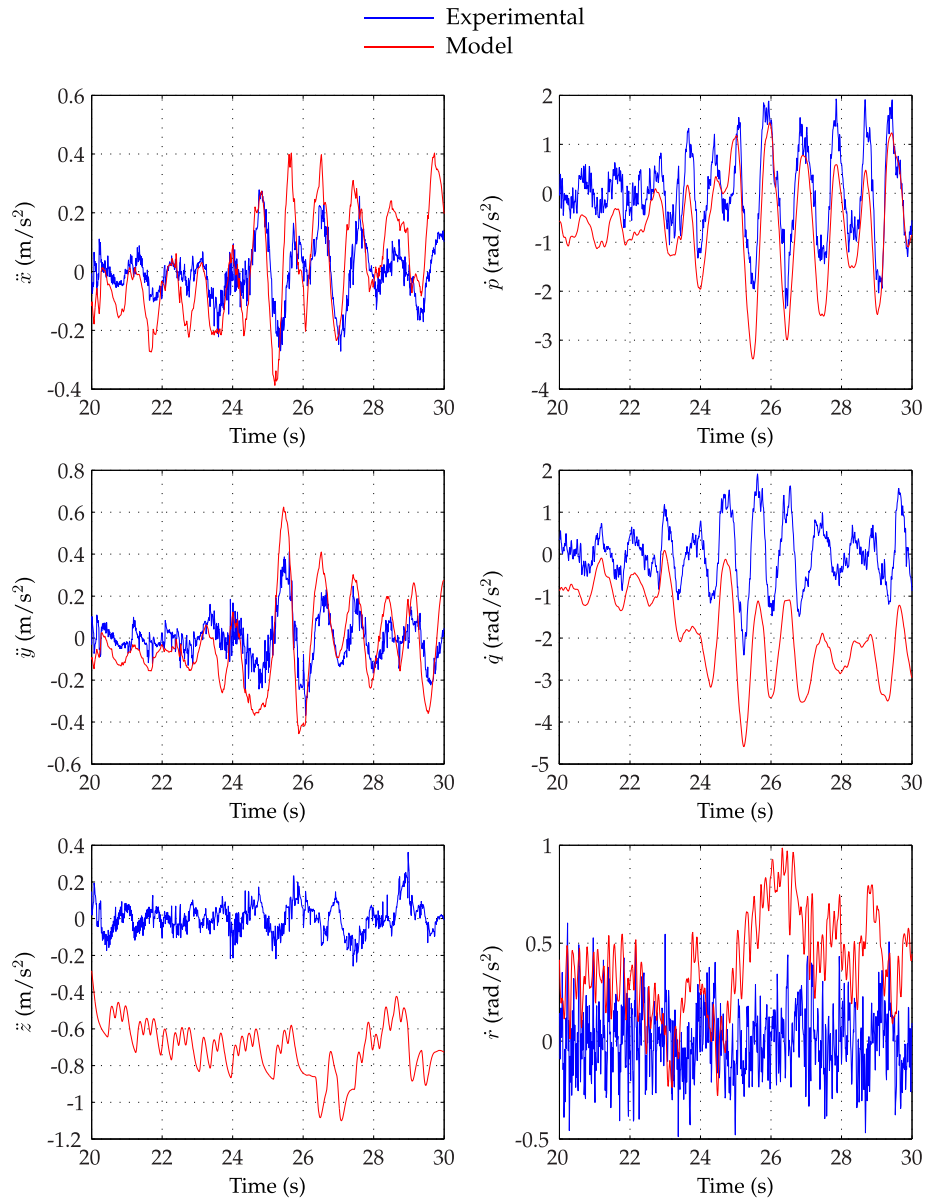


FIGURE 4.13: TRANSLATIONAL AND ROTATIONAL ACCELERATIONS FROM AN ADDITIONAL EMPIRICAL TEST ARE COMPARED WITH EXPECTED RESULTS FROM SIMULATION.

CHAPTER 5

A MULTI-RESOLUTION FAMILY OF QUADROTOR MODELS

Investigations of the effects of model resolution on controller design and trajectory optimisation require a family of quadrotor models of varying resolution. Chapters 3 and 4 present a number of models of the quadrotor system and subsystems as well as brief descriptions of additional unmodelled phenomena. Some of these models may be abstracted to provide lower-resolution relationships. This results in a range of models, each describing different subsystems of the quadrotor and exhibiting different properties in resolution, description and form. A multi-resolution family of models is developed by considering the models described in previous chapters and defining a succession of models which feature a clear progression in resolution.

To best describe the multi-resolution model family, some concepts and generalities must be presented. The model family is composed of several *levels*, each describing the quadrotor system at a specific resolution. The levels are numbered such that lowest-numbered level indicates the lowest resolution, while the highest-numbered describes the level of highest resolution. Each level of the model family describes the same system, with the same extents. The scope of the model is thus consistent between levels. A model in the model family therefore has the general solution

$$\begin{aligned}\dot{\mathbf{x}}(t) &= f(\mathbf{x}(t), \mathbf{u}(t), t) \\ \mathbf{y}(t) &= h(\mathbf{x}(t), \mathbf{u}(t), t)\end{aligned}\tag{5.1}$$

where the input \mathbf{u} and output \mathbf{y} are identical in each level. The difference between levels lies in the size and composition of the state \mathbf{x} and the structure of the process and measurement models, f and h respectively.

The choice of which models to employ for each level of the model family is determined by considering the results of the previous two chapters. Consistency across the model family is desired, ensuring the same system is described

with only the level of abstraction changing. The various models previously described are analysed to determine which of the properties highlighted by the literature review they exhibit. Discussion of these properties then aids the definition of the model family. Each level in the model family is then described in full, detailing the justification for the model employed and the primary differences/additions with respect to the previous levels. Where appropriate, alternative models are described and their exclusions explained. Finally, a number of candidates for higher-still resolution models are presented.

5.1 PROPERTIES OF THE IDENTIFIED QUADROTOR MODELS

The models described in Chapters 3 and 4 may be discussed with reference to the findings of the literature review. Properties such as linearity, resolution and type are applied to each model. Identification of these properties aids development of the model family.

5.1.1 LINEARITY OF MODELS

Linear models are typically used in tasks such as controller or observer design as they are far easier to analyse and provide more predictable results than non-linear models. The rigid-body dynamics of the quadrotor are strongly non-linear, with coupling of attitude and position. A linear model of the rigid body response is described by Equation (3.23). This is sufficient to describe the response of the quadrotor at small deviations from the hover state and is thus used extensively in controller design.

Similarly, while the identified rotor behaviour is shown to be non-linear, it is popularly approximated by a linear relationship in the majority of applications. Non-linear rotor models are typically used in either comprehensive quadrotor simulations, where all phenomena are modelled, or investigations into rotor performance.

Quadrotor behaviour may be described by a combination of linear and non-linear models. The rigid-body dynamics of the system are described by non-linear models derived using both Newton-Euler (Equations (3.13) and (3.17)) and Euler-Lagrange (Equations (3.20) and (3.22)) formalisms. Linearisation of either non-linear rigid body model provides the linear system described by Equation (3.23).

Models of the rotor range from the most basic linear relationship, described by Equation (4.24) to highly non-linear systems, such as those described in Section 3.5. The linear model describes the thrust and torque of the rotor in relation to its input and is generally applicable to the hover or static flow condition. This is sufficient for control applications where deviation from the hover state is minimal and short-term. The non-linear model also relates thrust and torque to input but includes relationships with rotorspeed, aircraft velocities

and blade geometry, increasing the complexity of the model significantly. Non-linear propeller models are employed where the behaviour of the rotor is of particular interest or the intent to develop a comprehensive model of the system. Non-linear motor models are employed for similar reasons.

Inclusion of additional phenomena can further increase the non-linearity of the system. The aerodynamic drag model described by Equation (3.28) relates drag force to the square of the aircraft velocity, while Equation (3.29) describes drag force as a linear function of velocity. The non-linear model is more representative of the true behaviour, but cannot be used directly in roles such as linear stability analysis or Kalman Filter design.

5.1.2 MECHANISTIC AND EMPIRICAL MODELS

The difference between mechanistic and empirical modelling Bokil (2009) is best demonstrated by the rotor models described in the preceding chapters. Section 3.5 describes a number of rotor models defined with reference to the mechanisms and properties of the propeller and motor. This approach has several advantages. First, individual properties may be altered if the system changes, without having to redefine the entire model. Second, as the model is derived from the known mechanics of the system, it describes the system behaviour for the entirety of its operating state, with consideration of any assumptions or abstractions made in its definition. This allows the model to predict behaviour beyond that which has been demonstrated in practice. Finally, the individual properties of the model may be substituted with additional relationships, allowing greater resolution or accuracy in the model. This is evident in the model described by Equation (3.30), where the thrust and torque coefficients may be either constant or non-linear functions of the blade geometry and rotor conditions. A disadvantage of this approach is that each property must be identified accurately to ensure validity in the model. A greater number of properties increases the likelihood of an imprecise model, due to cumulative errors.

Section 4.5 describes the rotor behaviour using empirical models, identified by testing of the rotors within their operational extents. The model is derived from identification of the relationships between the variables of interest: thrust, torque, rotorspeed and pulse width modulation. The benefit of this approach is that the model is fitted to the available data using as few parameters as necessary to ensure validity. The disadvantage of an empirical model is that it is only valid within the extents of the measured data. Behaviour beyond these limits is inherently unpredictable. A model such as that described by Equation (4.29) leaves no scope for increase in resolution, as it directly maps the thrust and torque to input without consideration of additional phenomena. It is thus only valid for the static flow case, while a mechanistic model may be augmented with more complex relationships by substitution of its parameters. However,

an empirical relationship is easily abstracted by fitting a simpler relationship to the model, while a mechanistic model may face loss of its individual parameters in doing so. Additionally, empirical models are often faster to design and implement, due to their basis in observations of the system inputs and outputs only. Mechanistic models typically require separate tests to identify each of the different properties, which can be time-consuming.

5.1.3 DIFFERING FORMALISMS

The quadrotor is assumed to be a rigid body, the dynamics of which are derived from both Newton-Euler and Euler-Lagrange formalisms. Each approach derives the mechanics of the system from different principles. The Newton-Euler method considers the linear and angular momentum of the body to obtain the dynamics of the body in a rotating frame of reference, described by Equations (3.13) and (3.17). The rotational response is then related to the attitude evolution of the vehicle by the kinematic relationship described in Equation (3.11). The forces and moments on the vehicle are thus related to the position \mathbf{r} and attitude $\boldsymbol{\eta}$. The Euler-Lagrange method begins with the kinetic and potential energy of the system and then uses the Lagrangian to determine the evolution of the generalised coordinates $\mathbf{q} = [\mathbf{r}^T, \boldsymbol{\eta}^T]^T$ directly, described by Equations (3.20) and (3.21).

Both approaches relate the same coordinates, \mathbf{r} and $\boldsymbol{\eta}$, to the same forces, \mathbf{F} and \mathbf{M} . The rotation of the body is accounted for in both cases without simplification and both models are highly non-linear. Additionally, with appropriate substitutions, both models are analytically demonstrated to be identical. The primary difference then lies in the derivations themselves, of which the Newton-Euler approach is far more trivial to implement.

5.1.4 RESOLUTION

As highlighted in the literature review, there is no universal measure of complexity or resolution. In some cases, however, identification of relative resolutions is intuitive. The abstraction of the non-linear empirical rotor model described by Equation (4.29) to a linear and/or lower-order system is a clear reduction in resolution. Conversely, the substitution of a constant thrust coefficient in the mechanistic rotor model described by (3.30) with a non-linear function of the blade geometry and inflow velocity represents an obvious increase in resolution. This correlates with the notion that the resolution of a model is related to the number of elements in its composition, particularly the number of states in a dynamic system.

The differing approaches to deriving the rotor model of the Qball highlight the methods by which a model of a given resolution may be obtained from another. The non-linear empirical rotor model is based on observed behaviour of the source system and thus cannot be increased in resolution without sac-

rificing validity. Abstraction of this model is, however, trivial, as the use of arbitrary properties in its composition means the relationship may be simplified without discarding meaningful parameters. This is apparent in the linear rotor relationship described by Equation (4.24) and the non-linear relationship described by Equation (4.23). Both models describe the relationship of thrust and torque with PWM command using arbitrary parameters with no specific property. Conversely, a mechanistic model has greater predictive capabilities and may be augmented by substituting various properties with more complex relationships, as previously stated. Abstraction of such a model may result in a loss of information, although abstractions such as linearised models can retain distinct properties, as demonstrated by Equation (3.36), which describes the linearised model of the motor dynamics described in full by Equation (3.35).

In the absence of a general metric for complexity or resolution, the identified properties of the models described in the previous chapters are used to highlight some obvious relationships of resolution. First, resolution may be related to the size of the state of the system. A larger state indicates a larger number of equations which describe the system and thus implies greater resolution. This is evident in the empirical rotor model, which closely describes the observed thrust response of the rotor with a second-order model but may approximate it with a first-order model – a clear abstraction and reduction in resolution. The first rule is thus identified: increasing the size of a model's state increases its resolution.

Next, model resolution can be related to its linearity. The non-linear rigid body models described in Chapter 3.3 have identical state size to the linear model described by Equation (3.23), but are obviously more complex in their description and involve more elements. Also, a linearised system such as that described by Equation (3.23) is clearly an abstraction of the non-linear model and therefore has lower resolution. The second rule is thus identified: linearisation of a model reduces the resolution.

Finally, a more general rule is described by Simon (1962). The complexity of a model is related to the number of elements in its composition. For models of equal scope, the one with a greater number of elements has greater resolution. This relationship is implicit in the two previous rules, where additional elements are introduced by way of increasing the state size or non-linear relationships. For models with identical order and which are both either linear or non-linear, this rule is useful in identifying the comparative resolution of each model.

Note that these are very general rules applicable specifically to the quadrotor system identified in this thesis. A more general discussion of the results is provided in Chapter 8. The rules may then be applied in specification of an example model family.

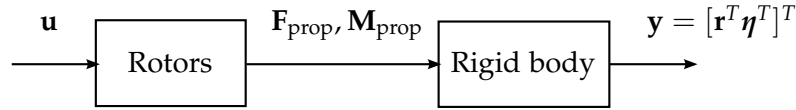


FIGURE 5.1: BLOCK DIAGRAM OF MINIMUM INFORMATION REQUIRED FOR INPUT-OUTPUT MAPPING.

5.2 DEFINING THE MODEL FAMILY

Each level in the multi-resolution model family describes the same system with consistent scope. In the context of a dynamic system such as the quadrotor, this means that the input \mathbf{u} and output \mathbf{y} are the same for each level. Basing the models specifically on the Qball-X₄ system, the input is defined as the zeroed PWM input to each rotor i , where $i = \{1, 2, 3, 4\}$ and is thus

$$\mathbf{u} = [u_1, u_2, u_3, u_4]^T$$

while the output is defined as the displacement of the system in each degree of freedom and is therefore simply related to the states by

$$\mathbf{y} = [x, y, z, \phi, \theta, \psi]^T$$

Any model describing the behaviour of the system must, at the very least, describe the mapping between the specified input and output. In the case of the quadrotor, each model must therefore describe the four rotors and the rigid body response of the system, as demonstrated by Figure 5.1.

The logic for defining the quadrotor model family is thus as follows. The Level 1 model is characterised as a near-linear model with the minimum number of states required to map the output of the system to its input. Successive levels increase in resolution from this baseline by either: increasing the size of the state; substituting linear models with non-linear relationships; or adding some other elements such as static properties. Each level of the model family is described by the general state-space equation

$$\dot{\mathbf{x}}_i(t) = f_i(\mathbf{x}_i(t), \mathbf{u}(t)) \quad (5.2)$$

where the subscript i denotes Level i , the assigned identifier. Models which describe *control-affine* systems may be described in the form

$$\dot{\mathbf{x}}_i(t) = f_i(\mathbf{x}_i(t)) + g_i(\mathbf{x}_i(t)) \mathbf{u}(t) \quad (5.3)$$

As the output of each level is the same, the measurement model is described by

$$\mathbf{y}(t) = h(\mathbf{x}_i(t), t) \quad (5.4)$$

where only the state changes between levels.

5.3 A CANDIDATE MULTI-RESOLUTION MODEL FAMILY

A multi-resolution quadrotor model family is defined using the models presented in Chapters 3 and 4. The choice of models is informed by the concepts presented previously in this chapter and dependent on the data available to populate the model properties. The Qball-X₄ is used as the basis for the model family, thus each level in the model family is required to describe the behaviour of the Qball at a different resolution. It is therefore required that the relationships in each level are populated with empirical data from system identification of the Qball.

The previous chapters highlighted models of several phenomena associated with the quadrotor. Some of these models clearly describe the same phenomena at different resolutions, while others describe the same system with roughly equivalent resolutions but mathematically-distinct relationships. Some models, such as the gyroscopic torques, describe behaviour which is otherwise unconsidered by the quadrotor model. The wealth of models describing the behaviour of the quadrotor and its subsystems with varying resolution, including those not described in this thesis, result in a large number of possible combinations which could inform a multi-resolution model family. This is indicated in Figure 5.2, which describes a non-exhaustive hierarchy of the models which could be used to describe the quadrotor behaviour.

The candidate model family is thus limited to describing the rigid body and rotor behaviours of the quadrotor, which allows a clear increase in resolution between levels. The possibility for inclusion of additional phenomena or the substitution of a model of one type for one of another type is discussed at the end of this chapter.

The candidate model family consists of five levels, with the successive increases in resolution defined as

Level 1 A near-linear rigid-body model and instantaneous, linear rotor model.

Level 2 The rigid-body response is described by a non-linear model.

Level 3 The rotor behaviour is described by a linear, first-order model.

Level 4 The order of the rotor dynamic model is increased.

Level 5 The rotor response is described by a non-linear model.

The following sections describe each level in greater detail and justify the choice of models in its composition.

5.3.1 LEVEL 1

The Level 1 model is characterised by a near-linear rigid body model and an instantaneous, linear rotor model. The system state thus describes the rigid

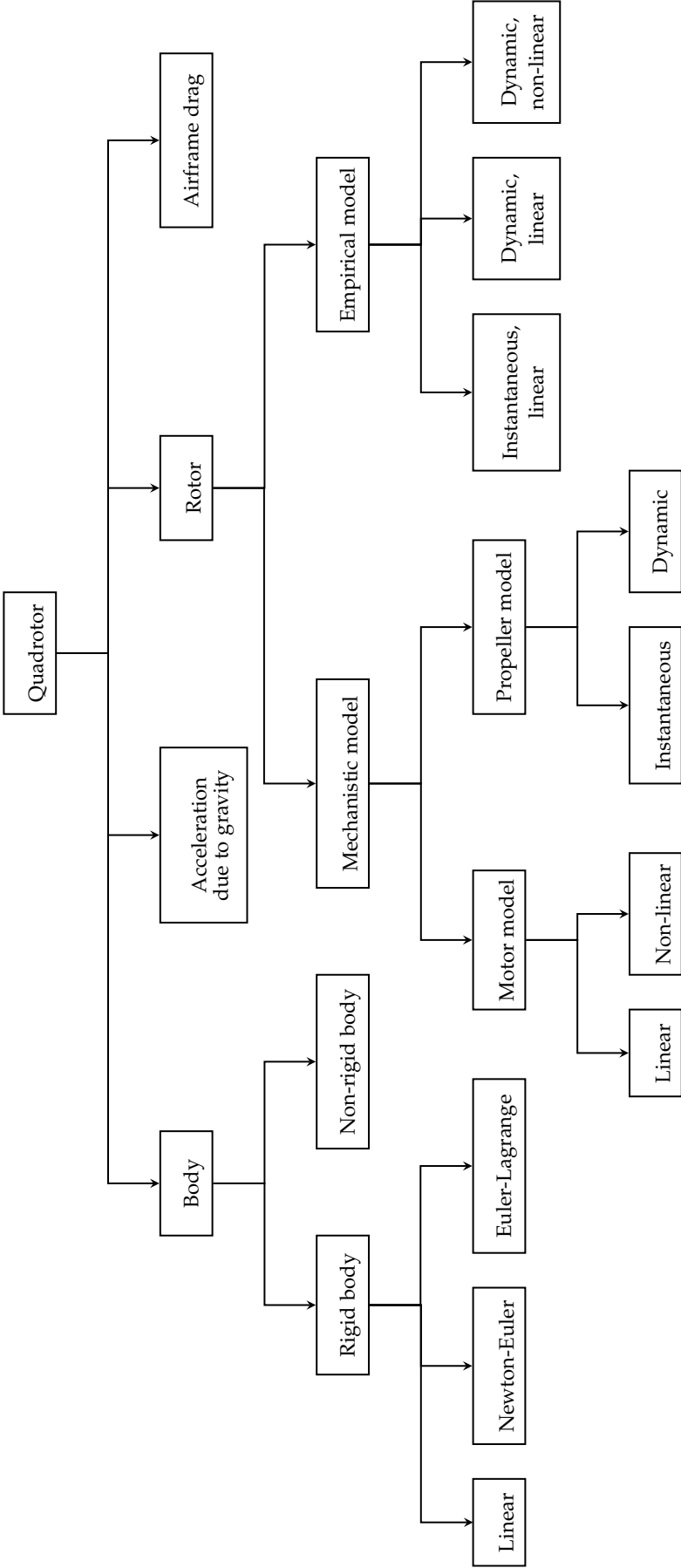


FIGURE 5.2: EXAMPLE OF MODELS AVAILABLE TO DESCRIBE THE QUADROTOR SYSTEM.

body states of the system only, and is given by

$$\mathbf{x}_1 = [x, y, z, \phi, \theta, \psi, \dot{x}, \dot{y}, \dot{z}, \dot{\phi}, \dot{\theta}, \dot{\psi}]^T$$

The Level 1 rigid body model is obtained by linearising the non-linear rigid body models described in Section 3.3, resulting in the relationship described by Equation (3.23). Full yaw displacement is retained, thus the model is not truly non-linear. The force and moment acting on the rigid body is composed of the gravitational contribution and the axial thrust and torque from each rotor. Each rotor is described with the simplest possible model, with thrust and torque described as instantaneous, linear responses to the input \mathbf{u} , related by a single parameter each. The Level 1 model may be described in the control-affine form

$$\dot{\mathbf{x}}_1(t) = f_1(\mathbf{x}_1(t)) + g_1(\mathbf{x}_1)\mathbf{u}(t)$$

The Level 1 model is thus described in full by

$$\begin{aligned} \ddot{\mathbf{r}} &= \begin{bmatrix} -g(\phi \sin \psi + \theta \cos \psi) \\ g(\phi \cos \psi - \theta \sin \psi) \\ g - \frac{K_T}{m} u_{\text{col}} \end{bmatrix} \\ \ddot{\mathbf{j}} &= \begin{bmatrix} \frac{K_T L}{I_x} u_{\text{lat}} \\ \frac{K_T L}{I_y} u_{\text{long}} \\ \frac{K_Q}{I_z} u_{\text{yaw}} \end{bmatrix} \end{aligned} \quad (5.5)$$

where, as stated in Section 3.6, the pseudo-inputs are related to the true system inputs by $\mathbf{u}^* = \mathbf{C}\mathbf{u}$, or in full

$$\begin{bmatrix} u_{\text{col}} \\ u_{\text{lat}} \\ u_{\text{long}} \\ u_{\text{yaw}} \end{bmatrix} = \begin{bmatrix} 1 & 1 & 1 & 1 \\ 0 & 0 & 1 & -1 \\ -1 & 1 & 0 & 0 \\ -1 & -1 & 1 & 1 \end{bmatrix} \begin{bmatrix} u_1 \\ u_2 \\ u_3 \\ u_4 \end{bmatrix}$$

5.3.2 LEVEL 2

Level 2 retains the same rotor model as Level 1, but describes the rigid body response of the quadrotor with the translational model described by Equation (3.20) and the simplified rotational model described by Equation (3.22). The increase in resolution from Level 1 thus comes from the addition of further non-linearities in both the translational and rotational responses. Since the size of the state has not changed, it is again described by

$$\mathbf{x}_2 = [x, y, z, \phi, \theta, \psi, \dot{x}, \dot{y}, \dot{z}, \dot{\phi}, \dot{\theta}, \dot{\psi}]^T$$

The Level 2 model is representative of that which is typically used in investigations in control and trajectory generation. It may be described as differen-

tially flat, where the input can be expressed in terms of the state and output, and control-affine, with the form

$$\dot{\mathbf{x}}_2(t) = f_2(\mathbf{x}_2(t)) + g_2(\mathbf{x}_2(t))\mathbf{u}(t) \quad (5.6)$$

The Level 2 model is then described in full by

$$\begin{aligned} \ddot{\mathbf{r}} &= \begin{bmatrix} 0 \\ 0 \\ g \end{bmatrix} + \frac{1}{m} \mathbf{R}_B^{\mathcal{W}} \begin{bmatrix} 0 \\ 0 \\ -K_T u_{\text{col}} \end{bmatrix} \\ \dot{\mathbf{j}} &= \mathbf{I}^{-1} \left(\begin{bmatrix} K_T L u_{\text{lat}} \\ K_T L u_{\text{long}} \\ K_Q u_{\text{yaw}} \end{bmatrix} - \dot{\mathbf{j}} \times \mathbf{I} \dot{\mathbf{j}} \right) \end{aligned} \quad (5.7)$$

where $\mathbf{u}^* = \mathbf{C}\mathbf{u}$

5.3.3 LEVEL 3

Level 3 again employs the rigid body model described by Equations (3.20) and (3.22). The increase in resolution now comes from an expansion of the state, achieved by substituting the instantaneous rotor model with dynamic relationships. The rotor dynamics are described by Equations (4.24) and (4.28). Following the ethos of making the system as simple as possible, the model does not describe the response of each rotor individually. Rather, the additive property of the linear rotor model permits the definition of net thrust

$$\begin{aligned} T &= T_1 + T_2 + T_3 + T_4 \\ &= K_T \frac{\omega_r}{s + \omega_r} (u_1 + u_2 + u_3 + u_4) \\ &= K_T \frac{\omega_r}{s + \omega_r} u_{\text{col}} \end{aligned}$$

Defining the net moment vector similarly, the state of the Level 3 model may be given as

$$\mathbf{x}_3 = [x, y, z, \phi, \theta, \psi, \dot{x}, \dot{y}, \dot{z}, \dot{\phi}, \dot{\theta}, \dot{\psi}, T, M_x, M_y, M_z]^T$$

The Level 3 model is indicative of the type of model used in aggressive quadrotor control, where the poles of the closed-loop system are sufficiently fast for the rotor dynamics to affect the closed-loop response. The Level 3 model is also control-affine, with the form

$$\dot{\mathbf{x}}_3(t) = f_3(\mathbf{x}_3(t)) + g_3(\mathbf{x}_3(t))\mathbf{u}(t)$$

and is described by

$$\begin{aligned} \dot{\mathbf{r}} &= \begin{bmatrix} 0 \\ 0 \\ g \end{bmatrix} + \frac{1}{m} \mathbf{R}_B^W \begin{bmatrix} 0 \\ 0 \\ -T \end{bmatrix} \\ \ddot{\mathbf{r}} &= \mathbf{I}^{-1} (\mathbf{M} - \dot{\mathbf{r}} \times \mathbf{I} \dot{\mathbf{r}}) \\ \begin{bmatrix} \dot{T} \\ \dot{\mathbf{M}} \end{bmatrix} &= \omega_r \left(\begin{bmatrix} K_T u_{\text{col}} \\ K_T L u_{\text{lat}} \\ K_T L u_{\text{long}} \\ K_Q u_{\text{yaw}} \end{bmatrix} - \begin{bmatrix} T \\ \mathbf{M} \end{bmatrix} \right) \end{aligned} \quad (5.8)$$

where $\mathbf{u}^* = \mathbf{C}\mathbf{u}$

5.3.4 LEVEL 4

The increase in resolution in Level 4 again comes from an increase in state size. This is achieved by increasing the order of the rotor system model. The thrust and torque gains are again linear relationships, described by Equation (4.24), while the dynamics are described by Equations (4.26) and (4.27), respectively. An additional increase in resolution is introduced by employing the rotational rigid body model described by Equation (3.17), which requires the attitude kinematics described by Equation (3.11). The state of the Level 4 model is therefore

$$\mathbf{x}_4 = [x, y, z, \phi, \theta, \psi, \dot{x}, \dot{y}, \dot{z}, p, q, r, T, \dot{T}, M_x, \dot{M}_x, M_y, \dot{M}_y, M_z, \dot{M}_z, q_Q]^T$$

Models such as this are uncommon in literature. While a first-order response is often used when consideration of the rotor dynamics is required, more complex models invariably use a rotor model derived mechanistically, as their typical application is in investigations of rotor behaviours. In this case, the higher-order empirical rotor model is employed specifically because it represents a clear increase in resolution from the first-order model, while retaining the same steady-state gain. The Level 4 model is control-affine of the form

$$\dot{\mathbf{x}}_4(t) = f_4(\mathbf{x}_4(t)) + g_4(\mathbf{x}_4(t))\mathbf{u}(t)$$

and is described in full by

$$\begin{aligned}
\dot{\mathbf{r}} &= \begin{bmatrix} 0 \\ 0 \\ g \end{bmatrix} + \frac{1}{m} \mathbf{R}_B^W \begin{bmatrix} 0 \\ 0 \\ -T \end{bmatrix} \\
\dot{\boldsymbol{\eta}} &= \mathbf{J}_\eta^{-1} \boldsymbol{\omega} \\
\dot{\boldsymbol{\omega}} &= \mathbf{I}^{-1} \left(\begin{bmatrix} M_x \\ M_y \\ M_z \end{bmatrix} - \boldsymbol{\omega} \times \mathbf{I} \boldsymbol{\omega} \right) \\
\begin{bmatrix} \ddot{T} \\ \ddot{M}_x \\ \ddot{M}_y \end{bmatrix} &= c_{T1} \begin{bmatrix} K_T u_{\text{col}} - T \\ K_T L u_{\text{lat}} - M_x \\ K_T L u_{\text{long}} - M_y \end{bmatrix} - c_{T2} \begin{bmatrix} \dot{T} \\ \dot{M}_x \\ \dot{M}_y \end{bmatrix} \\
\ddot{M}_z &= c_{Q4} K_Q u_{\text{yaw}} + x_Q \\
\dot{x}_Q &= (c_{Q1} - c_{Q3} c_{Q4}) K_Q u_{\text{yaw}} - c_{Q1} M_z - c_{Q2} \dot{M}_z - c_{Q3} x_Q
\end{aligned} \tag{5.9}$$

where $\mathbf{u}^* = \mathbf{C} \mathbf{u}$

5.3.5 LEVEL 5

The Level 5 model represents a deviation from the format of the previous four levels in that it is not control-affine. This occurs due to the use of a non-linear rotor model, described by Equation (4.29). It is therefore necessary to individually describe the response of each rotor in both thrust and torque. The increase in resolution thus comes from both the introduction of non-linearities and an expansion of the state, which is now given by

$$\begin{aligned}
\mathbf{x} &= [x, y, z, \dot{x}, \dot{y}, \dot{z}, \phi, \theta, \psi, p, q, r, T_1, T_2, T_3, T_4, \dot{T}_1, \dot{T}_2, \dot{T}_3, \dot{T}_4, \dots \\
&\quad \dots Q_1, Q_2, Q_3, Q_4, \dot{Q}_1, \dot{Q}_2, \dot{Q}_3, \dot{Q}_4, x_{Q,1}, x_{Q,2}, x_{Q,3}, x_{Q,4}]^T
\end{aligned}$$

The choice of an empirical rotor model over a mechanistic one is justified by the clear increase in resolution from the models in Levels 3 and 4. As the Level 5 model is not control-affine, it is described by the general model of a non-linear system, with the form

$$\dot{\mathbf{x}}_5(t) = f_5(\mathbf{x}_5(t), \mathbf{u}(t))$$

and may be described in full by

$$\begin{aligned}
\ddot{\mathbf{r}} &= \begin{bmatrix} 0 \\ 0 \\ g \end{bmatrix} + \frac{1}{m} \mathbf{R}_B^W \begin{bmatrix} 0 \\ 0 \\ -(T_1 + T_2 + T_3 + T_4) \end{bmatrix} \\
\begin{bmatrix} \dot{\phi} \\ \dot{\theta} \\ \dot{\psi} \end{bmatrix} &= \begin{bmatrix} 1 & \sin \phi \tan \theta & \cos \phi \tan \theta \\ 0 & \cos \phi & -\sin \phi \\ 0 & \sin \phi \sec \theta & \cos \phi \sec \theta \end{bmatrix} \boldsymbol{\omega} \\
\dot{\boldsymbol{\omega}} &= \mathbf{I}^{-1} \left(\begin{bmatrix} L(T_3 - T_4) \\ L(T_2 - T_1) \\ -Q_1 - Q_2 + Q_3 + Q_4 \end{bmatrix} - \boldsymbol{\omega} \times \mathbf{I} \boldsymbol{\omega} \right) \\
\dot{T}_i &= c_{T1}(f(u_i, V) - T_i) - c_{T2} \dot{T}_i \\
\dot{Q}_i &= c_{Q4} f(u_i, V) + x_{Q,i} \\
\dot{x}_{Q,i} &= (c_{Q1} - c_{Q3} c_{Q4}) f(u_i, V) - c_{Q1} Q_i - c_{Q2} \dot{Q}_i - c_{Q3} x_{Q,i}
\end{aligned} \tag{5.10}$$

The lack of a linear rotor model results in the pseudo-input \mathbf{u}^* being unsuitable for use with a system described by this model.

5.4 BEYOND THE DESCRIBED MODEL FAMILY

The described model family is chosen according to the availability of accurate data to populate it and a necessary and clear increase in resolution between levels. The model family uses a small selection of the models described in Chapters 3 and 4. It is therefore possible to provide some alternative model combinations for the levels of the model family. Additionally, higher-resolution levels beyond the presented five may be defined to facilitate further investigations. Some possibilities for the models comprising these levels are presented.

5.4.1 ALTERNATIVES TO THE PRESENTED MODELS

Some obvious substitutions may be made for the models comprising the multi-resolution family. The rigid-body model employed by Levels 3 and 4 is derived from Newton-Euler formalism. This model may be substituted with the the rigid body model obtained from Euler-Lagrange formalism, described by Equations (3.20) and (3.21). Both models employ an identical number of states and describe the response of an identical output, position and attitude, to an identical input, force and moment. Both models are similarly non-linear, although the Euler-Lagrange-derived rotational dynamics demonstrate greater *opacity*, as described by Ward (1989).

The rotor dynamics may be similarly substituted with a mechanistic model. A logical progression in rotor model resolution would be:

1. Thrust and torque described by Equation (3.30) with constant coefficients.
The rotorspeed described by an instantaneous model derived from the

steady-state of the model described by Equation (3.36).

2. The rotorspeed dynamics are introduced, using the first-order linear model described by Equation (3.36). This represents an expansion of the state.
3. Variable thrust and torque coefficients, described by Equation (3.31), are introduced to the propeller model described by Equation (3.30). This represents both an expansion of the state and the introduction of non-linearities in the thrust and torque coefficient relationships with aircraft velocity and additional rotor airflow properties.
4. The linear motor model is substituted with the non-linear model described by Equation (3.35), thus introducing further non-linear behaviour into the system.

The motor models described by Equations (3.35) and (3.36) represent an example of what could be used in an alternative model family. They are not applicable to models of the Qball, due to the use of three-phase motors, rather than DC motors.

5.4.2 EXTENDING THE MODEL FAMILY

The model family may be extended beyond the described five levels by introducing additional behaviours to the quadrotor model. These behaviours may increase the resolution of the model in a number of ways. First, the introduction of any additional relationships clearly increases the number of elements comprising the model. Second, the introduced phenomenon may have non-linear behaviours or additional dynamics. Finally, certain phenomena may require that other system behaviours or properties are present in the model, the inclusion of which again increases resolution. Some examples of these behaviours are described in Table 5.1.

TABLE 5.1: CONTRIBUTIONS OF ADDITIONAL PHENOMENA TO THE RESOLUTION OF THE MODEL FAMILY, AND ANY PREREQUISITES WHICH ARE REQUIRED BY A MODEL OF THE PHENOMENON.

PHENOMENON	INFLUENCE	PREREQUISITES
Gyroscopic torques	Additional non-linearities	Rotorspeed model
Aerodynamic drag	Additional non-linearities	-
Higher-resolution rotor model	Additional non-linearities, dynamics	Rotorspeed model, propeller model, inflow model
Process noise	Additional elements	-
Ground effect	Additional non-linearities	Inflow and rotorspeed models
Blockage	Unknown	Inflow model

CHAPTER 6

AN INVESTIGATION OF THE EFFECTS OF MODEL RESOLUTION ON NON-LINEAR DYNAMIC INVERSION CONTROLLER DESIGN AND TESTING

A variety of approaches to quadrotor control are found in the literature, including both linear and non-linear methods. A key consideration in controller design is the ability to handle uncertainties in the system which are not present in simulation testing. The merits of optimal linear techniques such as H_∞ have been and continue to be contrasted with those of non-linear control methods such as backstepping. The simplicity of the quadrotor system and its stability and agility under closed-loop control have led it to be a popular platform for non-linear techniques such as *dynamic inversion*. Also known as input-output linearisation or feedback linearisation, dynamic inversion involves derivation of a feedback law which, when placed in loop with the non-linear system, results in a linear closed-loop system. It is also applicable to linear systems, resulting in a simplified system model which aids selection of controller gains. Use of such an approach requires an accurate model of the system even when employing an additional linear feedback to stabilise the linearised system. The goal is to provide the majority of the control effort through the linearising feedback loop, thus reducing the need to compensate for uncertainties and non-linearities in the linear state feedback. This approach is heavily dependent on the model, therefore allows the effects of resolution on the closed-loop system response to be studied. A multi-resolution model is thus an ideal test platform. An additional benefit of employing dynamic inversion is then the ability to derive consistent linear feedbacks for each level in the model family, providing similar responses in closed loop.

The quadrotor models described in the multi-resolution model family of Chapter 5 are representative of the type used in controller design, where the rotor behaviour is described by an empirical model. Levels 1 and 2 describe the rotor behaviour with a linear, instantaneous model. This is sufficient to predict

the thrust and torque around the operating condition, hover, and is therefore popularly used in basic controller design. Level 3 introduces consideration of the rotor dynamics. A model such as this is typically used to test controllers, while controllers derived from it are rare. Levels 4 and 5 describe further increases in resolution, beyond that typically demonstrated by the literature.

Using dynamic inversion, linearising feedbacks are derived from the models described in Levels 1 to 3 of the model family. The resulting linearised systems are then controlled using state feedback laws which are tuned using pole placement. The derived controllers are then tested on models resolution equal to or greater than the source model. The models described by Levels 4 and 5 are not used to define complementary controllers, as the control bandwidth is limited in practice and these levels described dynamics of very high frequencies. Additionally, the Level 5 model is not control-affine, which is a requirement for dynamic inversion.

6.1 THEORY OF DYNAMIC INVERSION

Dynamic inversion is a popular control strategy for the quadrotor, as demonstrated by its use in Voos (2009), Das et al. (2009) and Mistler et al. (2001). Glad and Ljung (2000) describe the theory of dynamic inversion, also known as input-output linearisation, and apply it to a general SISO system as follows.

To be inverted, the system must be described in the control-affine form

$$\dot{\mathbf{x}} = f(\mathbf{x}) + g(\mathbf{x})u \quad (6.1)$$

$$y = h(\mathbf{x}) \quad (6.2)$$

where f , g and h are infinitely differentiable, smooth functions.

The output y is not explicitly dependent on the input u , but rather is affected by it through the state \mathbf{x} . To invert the system, it is necessary to determine the explicit relationship between input and output. This is achieved by differentiating the output until an expression containing the input is obtained. Differentiating Equation (6.2) and substituting Equation (6.1) gives

$$\begin{aligned} \dot{y} &= h_{\mathbf{x}}(\mathbf{x})\dot{\mathbf{x}} \\ &= h_{\mathbf{x}}(f(\mathbf{x}) + g(\mathbf{x})u) \end{aligned} \quad (6.3)$$

where $h_{\mathbf{x}}$ is the gradient of $h(\mathbf{x})$ with respect to \mathbf{x} and the matrix of partial differentials described by

$$h_{\mathbf{x}} = \left[\frac{\partial h}{\partial x_1}, \dots, \frac{\partial h}{\partial x_n} \right]$$

where n is the the length of the state vector \mathbf{x} .

Equation (6.3) may be expanded into the components

$$\dot{y} = h_x f(\mathbf{x}) + h_x g(\mathbf{x})u \quad (6.4)$$

The *Lie derivatives* (Ślebodziński, 1931) of the system are introduced, where L_f and L_g are the Lie derivatives in the direction of f and g respectively. They are then described by the relationships

$$L_f = f_1 \frac{\partial}{\partial x_1} + \cdots + f_n \frac{\partial}{\partial x_n}$$

$$L_g = g_1 \frac{\partial}{\partial x_1} + \cdots + g_n \frac{\partial}{\partial x_n}$$

Equation (6.4) may then be rewritten as

$$\dot{y} = L_f h(\mathbf{x}) + L_g h(\mathbf{x})u \quad (6.5)$$

For the condition where $L_g h(\mathbf{x}) \neq 0$, the expression for the first derivative of the output contains the input, thus \dot{y} is explicitly dependent on u . In this case, the system has *relative degree* 1. For the case where $L_g h(\mathbf{x}) \equiv 0$, it is necessary to differentiate the output again, giving

$$\ddot{y} = L_f^2 h(\mathbf{x}) + L_g L_f h(\mathbf{x})u \quad (6.6)$$

Then, for the conditions $L_g h(\mathbf{x}) \equiv 0$, $L_g L_f h(\mathbf{x}) \neq 0$, the expression for the second derivative of the output contains the input, thus \ddot{y} is explicitly dependent on u . In this case, the system has relative degree 2. On the conditions of $L_g h(\mathbf{x}) \equiv 0$, $L_g L_f h(\mathbf{x}) \equiv 0$, the output is differentiated again until it is explicitly dependent on the input. The relative degree ν is then the ν th derivative of the output which is explicitly dependent on the output. The resulting system is described by

$$y^{(\nu)} = L_f^\nu h(\mathbf{x}) + L_g L_f^{\nu-1} h(\mathbf{x})u, \quad L_g L_f^{\nu-1} h(\mathbf{x}) \neq 0 \quad (6.7)$$

Describing the output in this form allows the introduction of the feedback

$$u = \frac{1}{L_g L_f^{\nu-1} h(\mathbf{x})} \left(\hat{u} - L_f^\nu h(\mathbf{x}) \right) \quad (6.8)$$

which, when substituted into Equation (6.7), results in the linear relationship

$$y^{(\nu)} = \hat{u} \quad (6.9)$$

which maps the output to the reference signal \hat{u} .

For a system with multiple outputs of identical relative degree, Equation (6.7) may also be employed to describe an output vector $\mathbf{y} = h(\mathbf{x})$ with respect

to an input vector \mathbf{u} , yielding the relationship

$$\mathbf{y}^{(v)} = L_f^v h(\mathbf{x}) + L_g L_f^{v-1} h(\mathbf{x}) \mathbf{u}, \quad L_g L_f^{v-1} h(\mathbf{x}) \neq 0 \quad (6.10)$$

where, for an output and input of dimension m , $L_f^v h(\mathbf{x})$ is a vector of length m and $L_g L_f^{v-1}$ is a square matrix of dimensions $m \times m$. The corresponding feedback is then

$$\mathbf{u} = \left(L_g L_f^{v-1} h(\mathbf{x}) \right)^{-1} \left(\hat{\mathbf{u}} - L_f^v h(\mathbf{x}) \right) \quad (6.11)$$

where $\hat{\mathbf{u}}$ is the reference signal vector of length m .

The linearised system is controlled by a state feedback law which acts on y and its derivatives up to the $(v-1)$ th. The new input \hat{u} is then essentially the desired v th derivative of y . The state feedback law may therefore be described generally by

$$\hat{u} = y_d^{(v)} = -\mathbf{K} \begin{bmatrix} y - y_d \\ \dot{y} \\ \vdots \\ y^{(v-1)} \end{bmatrix} \quad (6.12)$$

where the state feedback gain is $\mathbf{K} = [K_1, K_2, \dots, K_v]$.

6.2 QUADROTOR CONTROLLER DESIGN AND STRUCTURE

Dynamic inversion is applicable to systems which may be described in control-affine form, such as the quadrotor models in Levels 1 to 4 of the multi-resolution model family. The quadrotor is an under-actuated system, with four inputs and six degrees of freedom. This impacts the ability to feedback linearise the system and requires the use of a nested-loop structure in the controller, shown in Figure 6.1. To invert the quadrotor system, it is necessary to define two separate outputs. Das et al. (2009) describe a *tracking output* $\mathbf{y}_t = h_t(\mathbf{x}) = [x, y, z, \psi]^T$ and a *flat output* $\mathbf{y}_f = h_f(\mathbf{x}) = [z, \phi, \theta, \psi]^T$. The flat outputs may be related to the pseudo-inputs $\mathbf{u}^* = [u_{\text{col}}, u_{\text{lat}}, u_{\text{long}}, u_{\text{yaw}}]^T$ by a series of SISO systems. It is then possible to invert each system such that linear relationships are obtained between the flat output and new pseudo-input $\hat{\mathbf{u}}^*$. A state feedback law then allows the system to be controlled by specifying a desired flat output $\mathbf{y}_{f,d}$.

The consequence of employing a multi-resolution family of models is the resulting disparity in system order between levels. Levels 1 and 2 describe the flat outputs as second-order systems, while Level 3 describes a third-order system and Levels 4 and 5 describe higher-order systems. Thus, the flat outputs

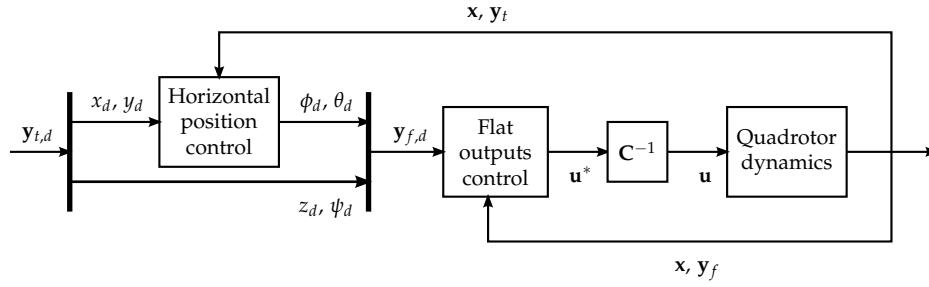


FIGURE 6.1: NESTED LOOP STRUCTURE OF QUADROTOR CONTROLLER WITH LINEARISING FEEDBACK BLOCKS.

are related to the pseudo-inputs by the general relationships

$$\begin{aligned}
 z^{(\nu)} &= a_z(\mathbf{x}) + b_z(\mathbf{x})u_{\text{col}} \\
 \phi^{(\nu)} &= a_\phi(\mathbf{x}) + b_\phi(\mathbf{x})u_{\text{lat}} \\
 \theta^{(\nu)} &= a_\theta(\mathbf{x}) + b_\theta(\mathbf{x})u_{\text{long}} \\
 \psi^{(\nu)} &= a_\psi(\mathbf{x}) + b_\psi(\mathbf{x})u_{\text{yaw}}
 \end{aligned} \tag{6.13}$$

where a_i and b_i , for $i = \{z, \phi, \theta, \psi\}$, are equivalent to the Lie derivatives of the flat outputs at the ν th derivative.

To ensure station-keeping trajectory control of the quadrotor, it is necessary to stabilise the zero dynamics of the system (Das et al., 2009). This is accomplished by controlling the tracking output. While height z_d and yaw ψ_d commands may be directly supplied to the inner loop controller, the horizontal position commands x_d and y_d must be used to determine the roll ϕ_d and pitch θ_d commands. This is achieved by inverting the relationship

$$\begin{bmatrix} \dot{x} \\ \dot{y} \end{bmatrix} = f_{xy}(\phi, \theta, \mathbf{x}, \mathbf{u}) \tag{6.14}$$

which is demonstrated to be invertible in the next section. A state feedback controller then allows the tracking of the desired horizontal position. The dynamics of the inner loop must be sufficiently fast that the outer loop is able to accurately track trajectory commands.

6.3 DYNAMIC INVERSION OF QUADROTOR MODELS

Dynamic inversion is applied to the quadrotor models described by Levels 1 to 3 of the multi-resolution model family. The flat outputs of each model are then related to new pseudo-inputs by linear systems of order ν , where ν is the relative degree of the system. The horizontal position dynamics of each model are inverted to provide a mapping between the tracking outputs and the desired trajectory, which is assumed to be linear for a sufficiently fast attitude response.

6.3.1 LEVEL 1

The dynamics of the flat outputs of the Level 1 model are linear, thus application of dynamic inversion only simplifies the system. The system has relative degree 2. The Level 1 quadrotor model relates the flat outputs $\mathbf{y}_f = [z, \phi, \theta, \psi]^T$ to the pseudo-inputs \mathbf{u}^* by the linear relationships

$$\begin{aligned} \ddot{z} &= g - \frac{K_T}{m} u_{\text{col}} \\ \ddot{\phi} &= \frac{K_T L}{I_x} u_{\text{lat}} \\ \ddot{\theta} &= \frac{K_T L}{I_y} u_{\text{long}} \\ \ddot{\psi} &= \frac{K_Q}{I_z} u_{\text{yaw}} \end{aligned} \quad (6.15)$$

It is clear that this system may be represented using the general form described by Equation (6.10), where the Lie derivatives are

$$L_f^2 h_f(\mathbf{x}) = \begin{bmatrix} g \\ 0 \\ 0 \\ 0 \end{bmatrix} \quad L_g L_f h_f(\mathbf{x}) = \begin{bmatrix} -\frac{K_T}{m} & 0 & 0 & 0 \\ 0 & \frac{K_T L}{I_x} & 0 & 0 \\ 0 & 0 & \frac{K_T L}{I_y} & 0 \\ 0 & 0 & 0 & \frac{K_Q}{I_z} \end{bmatrix}$$

Dynamic inversion is applied to this system using the formula described by Equation (6.11). Since the flat outputs are already linear functions of the inputs, the derived feedbacks are also linear but have the advantage of simplifying the closed-loop system and providing consistency with the linearised higher-resolution models. The resulting feedbacks are then

$$\begin{aligned} u_{\text{col}} &= \frac{m}{K_T} (g - \hat{u}_{\text{col}}) \\ u_{\text{lat}} &= \frac{I_x}{K_T L} \hat{u}_{\text{lat}} \\ u_{\text{long}} &= \frac{I_y}{K_T L} \hat{u}_{\text{long}} \\ u_{\text{yaw}} &= \frac{I_z}{K_Q} \hat{u}_{\text{yaw}} \end{aligned} \quad (6.16)$$

Applying the derived feedbacks to each pseudo-input, the closed-loop system satisfies Equation (6.9) and relates the flat outputs to the new inputs by

$$\begin{aligned} \ddot{z} &= \hat{u}_{\text{col}} \\ \ddot{\phi} &= \hat{u}_{\text{lat}} \\ \ddot{\theta} &= \hat{u}_{\text{long}} \\ \ddot{\psi} &= \hat{u}_{\text{yaw}} \end{aligned} \quad (6.17)$$

where the new inputs $\hat{\mathbf{u}}^*$ may be intuitively related to the desired accelerations

of the flat outputs by

$$\hat{\mathbf{u}}^* = \begin{bmatrix} \hat{u}_{\text{col}} \\ \hat{u}_{\text{lat}} \\ \hat{u}_{\text{long}} \\ \hat{u}_{\text{yaw}} \end{bmatrix} = \begin{bmatrix} \ddot{z}_d \\ \ddot{\phi}_d \\ \ddot{\theta}_d \\ \ddot{\psi}_d \end{bmatrix} \quad (6.18)$$

The trajectories of the linearised flat output systems are then controlled by state feedback laws acting on the flat outputs and their first derivatives, as per the general law described by Equation (6.12).

The inner loop is stabilised by inverting the horizontal position dynamics of the quadrotor to obtain roll and pitch commands as functions of the desired acceleration in x and y . The Level 1 model relates the horizontal position response to the roll and pitch displacements by the non-linear relationships

$$\begin{aligned} \ddot{x} &= -g(\phi \sin \psi + \theta \cos \psi) \\ \ddot{y} &= g(\phi \cos \psi - \theta \sin \psi) \end{aligned} \quad (6.19)$$

Taking the attitude angles ϕ and θ to be the inputs to this system and the outputs to be $\mathbf{y}_{xy} = h_{xy}(\mathbf{x}) = [x, y]^T$, the Lie derivatives of the horizontal position dynamics are found to be

$$L_f^2 h_{xy}(\mathbf{x}) = \begin{bmatrix} 0 \\ 0 \end{bmatrix} \quad L_g L_f h_{xy}(\mathbf{x}) = \begin{bmatrix} -g \sin \psi & -g \cos \psi \\ g \cos \psi & -g \sin \psi \end{bmatrix}$$

Employing the formula described by Equation (6.11), the horizontal position dynamics are inverted to obtain roll and pitch commands, ϕ_d and θ_d respectively, in terms of the desired horizontal accelerations

$$\begin{aligned} \phi_d &= -\frac{1}{g}(\ddot{x}_d \sin \psi - \ddot{y}_d \cos \psi) \\ \theta_d &= -\frac{1}{g}(\ddot{x}_d \cos \psi + \ddot{y}_d \sin \psi) \end{aligned} \quad (6.20)$$

where \ddot{x}_d and \ddot{y}_d are the desired accelerations in x and y respectively.

The roll and pitch responses of the quadrotor are required to be sufficiently fast such that the roll and pitch dynamics are near-instantaneous with respect to the horizontal position dynamics. Thus, for the assumptions $\phi(t) \approx \phi_d(t)$ and $\theta(t) \approx \theta_d(t)$, the Laplace transform yields the transfer function

$$\frac{\Phi(s)}{\Phi_d(s)} = \frac{\Theta(s)}{\Theta_d(s)} \approx 1$$

it is clear that the closed-loop horizontal position dynamics may be described by

$$\begin{aligned} \ddot{x} &= \ddot{x}_d \\ \ddot{y} &= \ddot{y}_d \end{aligned} \quad (6.21)$$

where the inputs \dot{x}_d and \dot{y}_d to the horizontal position feedback are subject to state feedback control.

6.3.2 LEVEL 2

The Level 2 model is highly non-linear. The flat outputs are therefore also related to the inputs by the non-linear relationships

$$\begin{aligned}\ddot{z} &= g - \frac{K_T}{m} u_{\text{col}} \cos \phi \cos \theta \\ \ddot{\phi} &= \frac{K_T L}{I_x} u_{\text{lat}} + \frac{I_y - I_z}{I_x} \dot{\theta} \dot{\psi} \\ \ddot{\theta} &= \frac{K_T L}{I_y} u_{\text{long}} + \frac{I_z - I_x}{I_y} \dot{\phi} \dot{\psi} \\ \ddot{\psi} &= \frac{K_Q}{I_z} u_{\text{yaw}} + \frac{I_x - I_y}{I_z} \dot{\phi} \dot{\theta}\end{aligned}\tag{6.22}$$

which yield the Lie derivatives

$$L_f^2 h_f(\mathbf{x}) = \begin{bmatrix} g \\ \frac{I_y - I_z}{I_x} \dot{\theta} \dot{\psi} \\ \frac{I_z - I_x}{I_y} \dot{\phi} \dot{\psi} \\ \frac{I_x - I_y}{I_z} \dot{\phi} \dot{\theta} \end{bmatrix} \quad L_g L_f h(\mathbf{x}) = \begin{bmatrix} -\frac{K_T}{m} \cos \phi \cos \theta & 0 & 0 & 0 \\ 0 & \frac{K_T L}{I_x} & 0 & 0 \\ 0 & 0 & \frac{K_T L}{I_y} & 0 \\ 0 & 0 & 0 & \frac{K_T L}{I_z} \end{bmatrix}$$

Dynamic inversion is then applied to the system. The derived feedbacks are also non-linear and are then described by the relationships

$$\begin{aligned}u_{\text{col}} &= \frac{m(g - \hat{u}_{\text{col}})}{K_T \cos \phi \cos \theta} \\ u_{\text{lat}} &= \frac{1}{K_T L} (I_x \hat{u}_{\text{lat}} + (I_z - I_y) \dot{\theta} \dot{\psi}) \\ u_{\text{long}} &= \frac{1}{K_T L} (I_y \hat{u}_{\text{long}} + (I_x - I_z) \dot{\phi} \dot{\psi}) \\ u_{\text{yaw}} &= \frac{1}{K_Q} (I_z \hat{u}_{\text{yaw}} + (I_y - I_x) \dot{\phi} \dot{\theta})\end{aligned}\tag{6.23}$$

The feedbacks are applied to each pseudo-input, resulting in linear closed loop systems equivalent to those of the feedback-linearised Level 1 quadrotor model:

$$\begin{aligned}\ddot{z} &= \hat{u}_{\text{col}} \\ \ddot{\phi} &= \hat{u}_{\text{lat}} \\ \ddot{\theta} &= \hat{u}_{\text{long}} \\ \ddot{\psi} &= \hat{u}_{\text{yaw}}\end{aligned}$$

The inner loop is again stabilised by inverting the horizontal position dy-

namics, which the Level 2 model describes by

$$\begin{aligned}\ddot{x} &= -\frac{K_T}{m}u_{\text{col}}(\sin\phi\sin\psi + \cos\phi\sin\theta\cos\psi) \\ \ddot{y} &= \frac{K_T}{m}u_{\text{col}}(\sin\phi\cos\psi - \cos\phi\sin\theta\sin\psi)\end{aligned}\quad (6.24)$$

Taking the expressions $\sin\phi$ and $\sin\theta$ to be the inputs to this system and the outputs again as $\mathbf{y}_{xy} = [x, y]^T$, comparison with Equation (6.10) yields the Lie derivatives

$$L_f^2 h_{xy}(\mathbf{x}) = \begin{bmatrix} 0 \\ 0 \end{bmatrix} \quad L_g L_f h_{xy}(\mathbf{x}) = \begin{bmatrix} -\frac{K_T}{m}u_{\text{col}}\sin\psi & -\frac{K_T}{m}u_{\text{col}}\cos\phi\cos\psi \\ \frac{K_T}{m}u_{\text{col}}\cos\psi & -\frac{K_T}{m}u_{\text{col}}\cos\phi\sin\psi \end{bmatrix}$$

Employing Equation (6.11), the linearising feedback is found to be

$$\begin{aligned}\sin\phi_d &= \frac{m(\dot{y}_d\cos\psi - \dot{x}_d\sin\psi)}{K_T u_{\text{col}}} \\ \sin\theta_d &= -\frac{m(\dot{x}_d\cos\psi + \dot{y}_d\sin\psi)}{K_T u_{\text{col}}\cos\phi}\end{aligned}$$

which then maps the feedback explicitly to the attitude commands, assuming ϕ_d and θ_d are in the interval $[-\frac{\pi}{2}, \frac{\pi}{2}]$. The final feedback is then

$$\begin{aligned}\phi_d &= \arcsin\left(\frac{m(\dot{y}_d\cos\psi - \dot{x}_d\sin\psi)}{K_T u_{\text{col}}}\right) \\ \theta_d &= -\arcsin\left(\frac{m(\dot{x}_d\cos\psi + \dot{y}_d\sin\psi)}{K_T u_{\text{col}}\cos\phi}\right)\end{aligned}\quad (6.25)$$

which linearises the horizontal position dynamics for the case $\phi = \phi_d, \theta = \theta_d$.

Again assuming near-instantaneous response in the roll and pitch inner-loop dynamics, the feedback-linearised horizontal position dynamics are described by the linear relationships

$$\begin{aligned}\ddot{x} &= \ddot{x}_d \\ \ddot{y} &= \ddot{y}_d\end{aligned}$$

6.3.3 LEVEL 3

The Level 3 model is also non-linear and involves an increase in order in each of the flat output relationships, due to the introduction of a first-order rotor

model. The Level 3 model describes the dynamics of the flat outputs by

$$\begin{aligned}
 \ddot{z} &= g - \frac{1}{m}T \cos \phi \cos \theta \\
 \ddot{\phi} &= \frac{1}{I_x}M_x + \frac{I_y - I_z}{I_x}\dot{\theta}\dot{\psi} \\
 \ddot{\theta} &= \frac{1}{I_y}M_y + \frac{I_z - I_x}{I_y}\dot{\phi}\dot{\psi} \\
 \ddot{\psi} &= \frac{1}{I_z}M_z + \frac{I_x - I_y}{I_z}\dot{\phi}\dot{\theta}
 \end{aligned} \tag{6.26}$$

The pseudo-inputs are not described in these relationships. The system therefore has relative degree greater than 2. Differentiating each output again provides the results

$$\begin{aligned}
 z^{(3)} &= \frac{1}{m} (T(\dot{\phi} \sin \phi \cos \theta + \dot{\theta} \cos \phi \sin \theta) - \dot{T} \cos \phi \cos \theta) \\
 \phi^{(3)} &= \frac{1}{I_x} \dot{M}_x + \frac{I_y - I_z}{I_x} (\dot{\theta}\ddot{\psi} + \ddot{\theta}\dot{\psi}) \\
 \theta^{(3)} &= \frac{1}{I_y} \dot{M}_y + \frac{I_z - I_x}{I_y} (\dot{\phi}\ddot{\psi} + \ddot{\phi}\dot{\psi}) \\
 \psi^{(3)} &= \frac{1}{I_z} \dot{M}_z + \frac{I_x - I_y}{I_z} (\dot{\phi}\ddot{\theta} + \ddot{\phi}\dot{\theta})
 \end{aligned} \tag{6.27}$$

The Level 3 model describes the rotor dynamics by the relationships

$$\begin{aligned}
 \dot{T} &= \omega_R(K_T u_{\text{col}} - T) \\
 \dot{M}_x &= \omega_R(K_T L u_{\text{lat}} - M_x) \\
 \dot{M}_y &= \omega_R(K_T L u_{\text{long}} - M_y) \\
 \dot{M}_z &= \omega_R(K_Q u_{\text{yaw}} - M_z)
 \end{aligned} \tag{6.28}$$

These may be substituted into Equation (6.27) to provide the required mappings between input and output. The system therefore has relative degree 3 and is described by

$$\begin{aligned}
 z^{(3)} &= \frac{1}{m} (T(\dot{\phi} \sin \phi \cos \theta + \dot{\theta} \cos \phi \sin \theta + \omega_R \cos \phi \cos \theta) \\
 &\quad - \omega_R K_T u_{\text{col}} \cos \phi \cos \theta) \\
 \phi^{(3)} &= \frac{\omega_R}{I_x} (K_T L u_{\text{lat}} - M_x) + \frac{I_y - I_z}{I_x} (\dot{\theta}\ddot{\psi} + \ddot{\theta}\dot{\psi}) \\
 \theta^{(3)} &= \frac{\omega_R}{I_y} (K_T L u_{\text{long}} - M_y) + \frac{I_z - I_x}{I_y} (\dot{\phi}\ddot{\psi} + \ddot{\phi}\dot{\psi}) \\
 \psi^{(3)} &= \frac{\omega_R}{I_z} (K_Q u_{\text{yaw}} - M_z) + \frac{I_x - I_y}{I_z} (\dot{\phi}\ddot{\theta} + \ddot{\phi}\dot{\theta})
 \end{aligned} \tag{6.29}$$

which, by comparison with Equation (6.10), yield the Lie derivatives

$$L_f^3 h_f(\mathbf{x}) = \begin{bmatrix} \frac{T}{m} (\omega_R \cos \phi \cos \theta + \dot{\phi} \sin \phi \cos \theta + \dot{\theta} \cos \phi \sin \theta) \\ \frac{1}{I_x} ((I_y - I_z)(\dot{\theta}\ddot{\psi} + \ddot{\theta}\dot{\psi}) - M_x \omega_R) \\ \frac{1}{I_y} ((I_z - I_x)(\dot{\phi}\ddot{\psi} + \ddot{\phi}\dot{\psi}) - M_y \omega_R) \\ \frac{1}{I_z} ((I_x - I_y)(\dot{\phi}\ddot{\theta} + \ddot{\phi}\dot{\theta}) - M_z \omega_R) \end{bmatrix}$$

$$L_g L_f^2 h_f(\mathbf{x}) = \begin{bmatrix} -\frac{K_T \omega_R}{m} \cos \phi \cos \theta & 0 & 0 & 0 \\ 0 & \frac{K_T L \omega_R}{I_x} & 0 & 0 \\ 0 & 0 & \frac{K_T L \omega_R}{I_y} & 0 \\ 0 & 0 & 0 & \frac{K_Q \omega_R}{I_z} \end{bmatrix}$$

Dynamic inversion is then applied to the flat output models. The derived feedbacks are non-linear and are described by the relationships

$$\begin{aligned} u_{\text{col}} &= \frac{1}{K_T \omega_R \cos \phi \cos \theta} (T(\dot{\phi} \sin \phi \cos \theta + \dot{\theta} \cos \phi \sin \theta) - m \hat{u}_{\text{col}}) + \frac{T}{K_T} \\ u_{\text{lat}} &= \frac{1}{K_T L} \left(\frac{I_x}{\omega_R} \hat{u}_{\text{lat}} - \frac{I_y - I_z}{\omega_R} (\dot{\theta}\ddot{\psi} + \ddot{\theta}\dot{\psi}) + M_x \right) \\ u_{\text{long}} &= \frac{1}{K_T L} \left(\frac{I_y}{\omega_R} \hat{u}_{\text{long}} - \frac{I_z - I_x}{\omega_R} (\dot{\phi}\ddot{\psi} + \ddot{\phi}\dot{\psi}) + M_y \right) \\ u_{\text{yaw}} &= \frac{1}{K_Q} \left(\frac{I_z}{\omega_R} \hat{u}_{\text{yaw}} - \frac{I_x - I_y}{\omega_R} (\dot{\phi}\ddot{\theta} + \ddot{\phi}\dot{\theta}) + M_z \right) \end{aligned} \quad (6.30)$$

The feedbacks are applied to each pseudo-input, resulting in linear closed-loop systems of order 3. The flat outputs are then related to the new inputs by

$$\begin{aligned} z^{(3)} &= \hat{u}_{\text{col}} \\ \phi^{(3)} &= \hat{u}_{\text{lat}} \\ \theta^{(3)} &= \hat{u}_{\text{long}} \\ \psi^{(3)} &= \hat{u}_{\text{yaw}} \end{aligned} \quad (6.31)$$

where the new inputs are again intuitively related to the desired ν th derivative of the flat outputs. For a system of relative degree 3, the new inputs describe the desired *jerk* of each flat output, or

$$\hat{\mathbf{u}}^* = \begin{bmatrix} \hat{u}_{\text{col}} \\ \hat{u}_{\text{lat}} \\ \hat{u}_{\text{long}} \\ \hat{u}_{\text{yaw}} \end{bmatrix} = \begin{bmatrix} z_d^{(3)} \\ \phi_d^{(3)} \\ \theta_d^{(3)} \\ \psi_d^{(3)} \end{bmatrix} \quad (6.32)$$

The flat output trajectories are then controlled by state feedback laws which now act on the flat outputs and their first and second derivatives, as per the general law described by Equation (6.12).

The Level 3 quadrotor model describes the horizontal position dynamics by

the non-linear relationships

$$\begin{aligned}\ddot{x} &= -\frac{1}{m}T(\sin\phi\sin\psi + \cos\phi\sin\theta\cos\psi) \\ \ddot{y} &= \frac{1}{m}T(\sin\phi\cos\psi - \cos\phi\sin\theta\sin\psi)\end{aligned}\quad (6.33)$$

Again taking $\sin\phi$ and $\sin\theta$ as the inputs to horizontal position dynamics, comparison with Equation (6.10) yields the Lie derivatives

$$L_f^2 h_{xy}(\mathbf{x}) = \begin{bmatrix} 0 \\ 0 \end{bmatrix} \quad L_g L_f h_{xy}(\mathbf{x}) = \begin{bmatrix} -\frac{T}{m}\sin\psi & -\frac{T}{m}\cos\phi\cos\psi \\ \frac{T}{m}\cos\psi & -\frac{T}{m}\cos\phi\sin\psi \end{bmatrix}$$

which ultimately provides the linearising feedbacks

$$\begin{aligned}\phi_d &= \arcsin\left(\frac{m(\dot{y}_d\cos\psi - \dot{x}_d\sin\psi)}{T}\right) \\ \theta_d &= -\arcsin\left(\frac{m(\dot{x}_d\cos\psi + \dot{y}_d\sin\psi)}{T\cos\phi}\right)\end{aligned}\quad (6.34)$$

where ϕ_d and θ_d are again assumed to be in the interval $[-\frac{\pi}{2}, \frac{\pi}{2}]$.

Assuming near-instantaneous response in the roll and pitch dynamic of the inner-loop, the horizontal position dynamics are once again approximated by the linear relationships

$$\begin{aligned}\ddot{x} &= \ddot{x}_d \\ \ddot{y} &= \ddot{y}_d\end{aligned}$$

6.4 STATE FEEDBACK CONTROL FOR MULTIPLE RESOLUTIONS

The previous section described linearising feedbacks for the models in Levels 1 to 3 of the quadrotor multi-resolution model family. Applying these feedbacks to the system inputs \mathbf{u}^* linearises and simplifies the relationship between the flat outputs and a new input $\hat{\mathbf{u}}^*$. The resulting linearised systems may be described generally in terms of the flat outputs by

$$\begin{aligned}z^{(\nu)} &= \hat{u}_{\text{col}} = z_d^{(\nu)} \\ \phi^{(\nu)} &= \hat{u}_{\text{lat}} = \phi_d^{(\nu)} \\ \theta^{(\nu)} &= \hat{u}_{\text{long}} = \theta_d^{(\nu)} \\ \psi^{(\nu)} &= \hat{u}_{\text{yaw}} = \psi_d^{(\nu)}\end{aligned}\quad (6.35)$$

where the relative degree ν of the system is dependent on the Level of the model family, as described by

$$\nu = \begin{cases} 2 & \text{for Levels 1 and 2} \\ 3 & \text{for Level 3} \end{cases}$$

The remaining tracking outputs are consistently described for each Level by

$$\left. \begin{array}{l} \ddot{x} = \ddot{x}_d \\ \ddot{y} = \ddot{y}_d \end{array} \right\} \text{ if } \frac{\Phi(s)}{\Phi_d(s)} = \frac{\Theta(s)}{\Theta_d(s)} \approx 1$$

The linearised output relationships are controlled by state feedback laws of the form described by Equation (6.12), resulting in linear transfer functions of the form

$$\frac{Y(s)}{Y_d(s)} = \frac{K_1}{s^\nu + K_\nu s^{\nu-1} + \dots + K_2 s + K_1} \quad (6.36)$$

the poles of which may be specified in order to obtain a desired system response. Since the minimum relative degree demonstrated by the multi-resolution model family is 2, two of the poles specified for the response of a given output must remain consistent between levels. Any additional poles are then chosen to be significantly faster than these two poles. This ensures a consistent closed-loop response for the model-controller pair derived from each level of the model family.

6.4.1 HEIGHT CONTROL

The linearised dynamics of the quadrotor are described by the relationship

$$z^{(\nu)} = \hat{u}_{\text{col}} = z_d^{(\nu)}$$

where ν is the relative degree of the system. A state feedback control law is then employed, with the form

$$\hat{u}_{\text{col}} = -\mathbf{K}_z \begin{bmatrix} z - z_d \\ \dot{z} \\ \ddot{z} \\ \vdots \\ z^{(\nu-1)} \end{bmatrix} \quad (6.37)$$

where \mathbf{K}_z is a row vector of length $(\nu - 1)$ for a ν th-order single-input single-output system such as the feedback-linearised height model. Choosing optimal values of \mathbf{K}_z is then trivial. The height response is selected by specifying first the poles of the 2nd-order systems described the feedback-linearised models of Levels 1 and 2. The Level 3 model introduces an additional pole, which is chosen such that the closed-loop response of the system is consistent with Levels 1 and 2.

RESPONSE TUNING OF LEVELS 1 AND 2 HEIGHT DYNAMICS

The feedback-linearised height dynamics for Levels 1 and 2 are identically described by

$$\ddot{z} = \hat{u}_{\text{col}}$$

and have relative degree 2. The general state feedback law described by Equation (6.12) is applied to the linearised system, in the form

$$\hat{u}_{\text{col}} = - \begin{bmatrix} K_{z1} & K_{z2} \end{bmatrix} \begin{bmatrix} z - z_d \\ \dot{z} \end{bmatrix} \quad (6.38)$$

The closed-loop response to an input z_d is then described by the linear transfer function

$$\frac{Z(s)}{Z_d(s)} = \frac{K_{z1}}{s^2 + K_{z2}s + K_{z1}} \quad (6.39)$$

The state feedback gains for a desired height response are obtained by comparing the poles of Equation (6.39) with the roots of the standard characteristic equation

$$s^2 + 2\zeta\omega_n s + \omega_n^2 = 0 \quad (6.40)$$

which are the complex conjugate pair

$$s = -\zeta\omega_n \pm \sqrt{\zeta^2 - 1}\omega_n$$

The state feedback gains are then related to the desired system properties by

$$\begin{aligned} K_{z1} &= \omega_{n,z}^2 \\ K_{z2} &= 2\zeta_z\omega_{n,z} \end{aligned} \quad (6.41)$$

where the subscript z signifies system properties specific to the height response. The response of the system is thus dictated by the selection of a desired damping ratio ζ_z and settling time $\tau_{s,z}$ which determine the natural frequency of the system through the relationship

$$\omega_n = -\frac{\ln(0.02)}{\zeta\tau_s}$$

RESPONSE TUNING OF LEVEL 3 HEIGHT DYNAMICS

The feedback-linearised height dynamics for Level 3 are described by the third-order system

$$z^{(3)} = \hat{u}_{\text{col}}$$

which has relative degree 3. The general state feedback law described by Equation (6.12) is applied to the linearised system, in the form

$$\hat{u}_{\text{col}} = - \begin{bmatrix} K_{z1} & K_{z2} & K_{z3} \end{bmatrix} \begin{bmatrix} z - z_d \\ \dot{z} \\ \ddot{z} \end{bmatrix} \quad (6.42)$$

The closed-loop response to an input z_d is then described by the linear transfer function

$$\frac{Z(s)}{Z_d(s)} = \frac{K_{z1}}{s^3 + K_{z3}s^2 + K_{z2}s + K_{z1}} \quad (6.43)$$

The increase in relative degree of the height model and the corresponding change in the state feedback controller result in an additional pole in the closed-loop response described by Equation (6.43). To ensure a consistent response between the closed-loop height dynamics described by Levels 1, 2 and 3, the state feedback gains are determined by comparison with the characteristic equation

$$0 = (s^2 + 2\zeta\omega_n + \omega_n^2)(s + p) \quad (6.44)$$

where the specified damping ratio and natural frequency and therefore the dominant poles are identical to those chosen for Levels 1 and 2 and the additional pole p is sufficiently fast such that the closed-loop response is identical to that of Levels 1 and 2. The state feedback gains are then given by

$$\begin{aligned} K_{z1} &= p_z \omega_{n,z}^2 \\ K_{z2} &= \omega_{n,z}^2 + 2p_z \zeta_z \omega_{n,z} \\ K_{z3} &= 2\zeta_z \omega_{n,z} + p_z \end{aligned} \quad (6.45)$$

COMPARISON OF CLOSED-LOOP HEIGHT RESPONSE

The closed-loop responses of the height models described by Levels 1 to 3 are compared, as shown in Figure 6.2. The trajectory of the Level 3 model becomes identical to those of the Levels 1 and 2 models as the speed of the additional pole p_z reaches infinity. Computational considerations limit the magnitude of p_z in practice, thus it is chosen to be $p_z = 20\omega_{n,z}$, determined through simulation testing.

6.4.2 YAW CONTROL

The yaw controllers of the quadrotor model family are tuned similarly. The linearised yaw dynamics are generally described by the relationship

$$\psi^{(v)} = \hat{u}_{\text{yaw}} = \psi_d^{(v)}$$

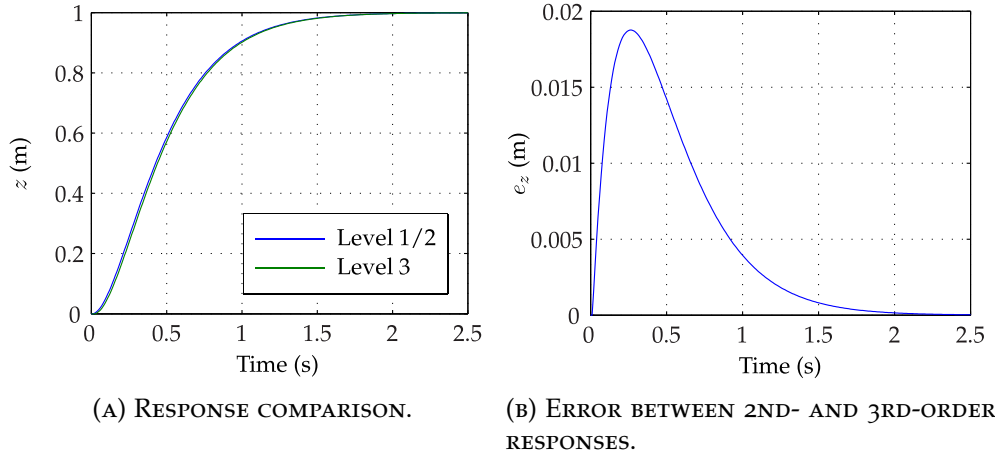


FIGURE 6.2: COMPARISON OF THE CLOSED-LOOP RESPONSES IN HEIGHT FOR LEVELS 1 TO 3, WHERE THE ADDITIONAL POLE IN THE LEVEL 3 RESPONSE IS SPECIFIED TO BE $p_z = 20\omega_{n,z}$. THE ERROR e_z IS DEFINED BY $e_z = z_{1/2} - z_3$, WHERE z_i DENOTES THE RESPONSE AT LEVEL i .

where ν is the relative degree of the system. The state feedback law for yaw control is then

$$\hat{u}_{\text{yaw}} = -\mathbf{K}_\psi \begin{bmatrix} \psi - \psi_d \\ \dot{\psi} \\ \ddot{\psi} \\ \vdots \\ \psi^{(\nu-1)} \end{bmatrix} \quad (6.46)$$

For the second-order yaw model described by Levels 1 and 2, the closed-loop system is described by the transfer function

$$\frac{\Psi(s)}{\Psi_d(s)} = \frac{K_{\psi 1}}{s^2 + K_{\psi 2}s + K_\psi} \quad (6.47)$$

which, through comparison with Equation (6.40) gives the state feedback gain relationships as

$$\begin{aligned} K_{\psi 1} &= \omega_{n,\psi}^2 \\ K_{\psi 2} &= 2\zeta_\psi \omega_{n,\psi} \end{aligned} \quad (6.48)$$

Similarly, the third-order yaw model described by Level 3 has the closed-loop transfer function

$$\frac{\Psi(s)}{\Psi_d(s)} = \frac{K_{\psi 1}}{s^3 + K_{\psi 3}s^2 + K_{\psi 2}s + K_\psi} \quad (6.49)$$

which, through comparison with Equation (6.44) gives the state feedback gain

relationships as

$$\begin{aligned} K_{\psi 1} &= p_{\psi} \omega_{n,\psi}^2 \\ K_{\psi 2} &= \omega_{n,\psi}^2 + 2p_{\psi} \zeta_{\psi} \omega_{n,\psi} \\ K_{\psi 3} &= p_{\psi} + 2\zeta_{\psi} \omega_{n,\psi} \end{aligned} \quad (6.50)$$

6.4.3 HORIZONTAL POSITION CONTROL

As stated previously, control of the quadrotor's position in the horizontal plane is achieved by rolling and pitching the vehicle to induce motion in the desired direction. The horizontal position response is thus described by a system of order $(\nu + 2)$, where ν is the relative degree of the roll and pitch dynamics described by the model. The position response may be tuned by assuming that the poles of the roll and pitch response are sufficiently faster than those of the position response such that the approximation

$$\frac{\Phi(s)}{\Phi_d(s)} = \frac{\Theta(s)}{\Theta_d(s)} \approx 1$$

is applicable. The closed-loop stability of the horizontal position response is then ensured by specifying a roll/pitch response which is sufficiently fast.

TUNING OF POSITION RESPONSE

Assuming a near-instantaneous roll and pitch response, the feedback-linearised horizontal position dynamics may be described by the relationships

$$\ddot{x} = \ddot{x}_d \qquad \ddot{y} = \ddot{y}_d$$

where the desired accelerations in x and y are determined by the state feedback laws

$$\ddot{x}_d = - \begin{bmatrix} K_{p1} & K_{p2} \end{bmatrix} \begin{bmatrix} x - x_d \\ \dot{x} \end{bmatrix}, \quad \ddot{y}_d = - \begin{bmatrix} K_{p1} & K_{p2} \end{bmatrix} \begin{bmatrix} y - y_d \\ \dot{y} \end{bmatrix} \quad (6.51)$$

The closed-loop response in x and y is then described by the transfer function

$$\frac{X(s)}{X_d(s)} = \frac{Y(s)}{Y_d(s)} = \frac{K_{p1}}{s^2 + K_{p2}s + K_{p1}} \quad (6.52)$$

where the state feedback gains are once again determined by comparison with Equation (6.40), giving

$$\begin{aligned} K_{p1} &= \omega_{n,p}^2 \\ K_{p2} &= 2\zeta_p \omega_{n,p} \end{aligned} \quad (6.53)$$

TUNING OF ROLL AND PITCH RESPONSE

The linearised roll and pitch dynamics of the quadrotor are described by the relationships

$$\phi^{(v)} = \hat{u}_{\text{lat}} \qquad \theta^{(v)} = \hat{u}_{\text{long}}$$

where the inputs \hat{u}_{lat} and \hat{u}_{long} are determined by the state feedback laws

$$\ddot{\phi}_d = -\mathbf{K}_a \begin{bmatrix} \phi - \phi_d \\ \dot{\phi} \\ \ddot{\phi} \\ \vdots \\ \phi^{(v-1)} \end{bmatrix}, \quad \ddot{\theta}_d = -\mathbf{K}_a \begin{bmatrix} \theta - \theta_d \\ \dot{\theta} \\ \ddot{\theta} \\ \vdots \\ \theta^{(v-1)} \end{bmatrix} \quad (6.54)$$

As with the height and yaw dynamics, Levels 1 and 2 of the model family describe the roll and pitch dynamics as 2nd-order systems, while Level 3 describes a 3rd-order system. The attitude response is thus specified similarly. Levels 1 and 2 describe the closed-response by

$$\frac{\Phi(s)}{\Phi_d(s)} = \frac{\Theta(s)}{\Theta_d(s)} = \frac{K_{a1}}{s^2 + K_{a2}s + K_{a1}} \quad (6.55)$$

with the corresponding gains

$$\begin{aligned} K_{a1} &= \omega_{n,a}^2 \\ K_{a2} &= 2\zeta_a \omega_{n,a} \end{aligned} \quad (6.56)$$

while Level 3 describes the closed-loop response by

$$\frac{\Phi(s)}{\Phi_d(s)} = \frac{\Theta(s)}{\Theta_d(s)} = \frac{K_{a1}}{s^3 + K_{a3}s^2 + K_{a2}s + K_{a1}} \quad (6.57)$$

with the corresponding gains

$$\begin{aligned} K_{a1} &= p_a \omega_{n,a}^2 \\ K_{a2} &= \omega_{n,a}^2 + p_a 2\zeta_a \omega_{n,a} \\ K_{a3} &= 2\zeta_a \omega_{n,a} + p_a \end{aligned} \quad (6.58)$$

STABILITY OF HORIZONTAL POSITION RESPONSE

The stability of the closed-loop response in x and y is determined by considering the horizontal position dynamics without assuming instantaneous roll and pitch response. The horizontal position is then described by the models in

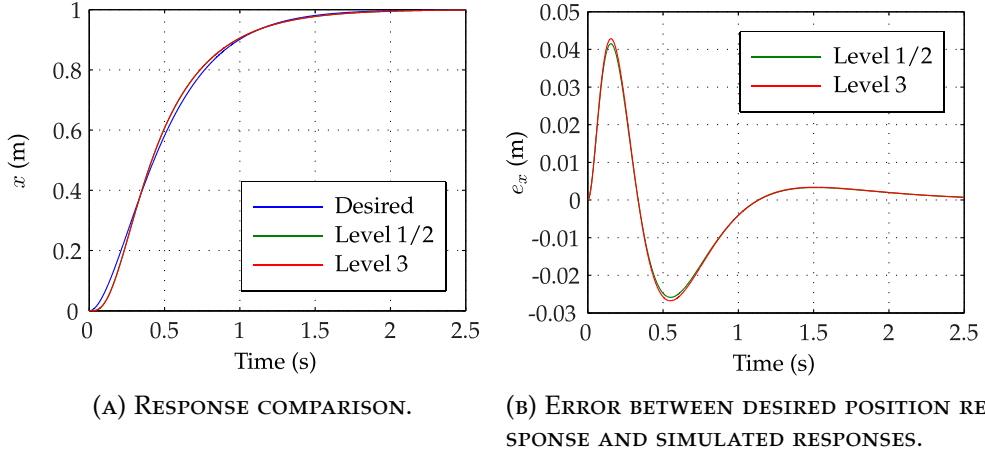


FIGURE 6.3: COMPARISON OF THE CLOSED-LOOP RESPONSES IN HORIZONTAL POSITION FOR LEVELS 1 TO 3, WITH ATTITUDE RESPONSE NATURAL FREQUENCY $\omega_{n,a} = 10\omega_{n,p}$. THE ERROR e_x IS DEFINED BY $e_x = x_{\text{DES}} - x_i$, WHERE x_{DES} IS THE DESIRED RESPONSE AND x_i DENOTES THE RESPONSE AT LEVEL i .

Levels 1 and 2 as

$$\frac{X(s)}{X_d(s)} = \frac{Y(s)}{Y_d(s)} = \frac{K_{a1}K_{p1}}{s^4 + K_{a2}s^3 + K_{a1}s^2 + K_{a1}K_{p2}s + K_{a1}K_{p1}} \quad (6.59)$$

It is assumed that the desired damping ratio of both the position and attitude responses is $\zeta = 1$. The natural frequency of the roll and pitch response is then parameterised by $\omega_{n,a} = k\omega_{n,p}$. Applying the Routh-Hurwitz stability criterion to the system described by Equation (6.59), the position response is found to be stable for all values of natural frequency $\omega_{n,a}$ where $k > 2$. This analysis is presented in greater detail in Appendix F.

Similarly, the linearised horizontal position dynamics are described by the Level 3 model by

$$\frac{X(s)}{X_d(s)} = \frac{Y(s)}{Y_d(s)} = \frac{K_{a1}K_{p1}}{s^5 + K_{a3}s^4 + K_{a2}s^3 + K_{a1}s^2 + K_{a1}K_{p2}s + K_{a1}K_{p1}} \quad (6.60)$$

Using numerical analysis, the Level 3 position response is found to be stable for the all values of natural frequency $\omega_{n,a} = k\omega_{n,p}$ where $k > k_{\min}$. The minimum constant k_{\min} is dependent on the placement of the additional pole p_a , via the relationship

$$\lim_{p_a \rightarrow \infty} k_{\min} = 2$$

Since p_a is limited in magnitude in practice, k is required to be much greater than 2 to ensure stability. Additionally, the attitude dynamics are ideally significantly faster than the position dynamics in order to eliminate oscillatory motion in the position response. Figure 6.3 demonstrates the effect the relative speed of the attitude response has on the position response.

6.4.4 STABILITY OF CLOSED-LOOP FLAT OUTPUT DYNAMICS

SECOND-ORDER SYSTEM

The stability of the flat output is verified using Lyapunov's second method. For the case as described by Levels 1 and 2 of the model family, the linearised closed-loop response of the flat outputs is described by

$$\ddot{\mathbf{y}}_f = \mathbf{K}_1(\mathbf{y}_{f,d} - \mathbf{y}_f) - \mathbf{K}_2\dot{\mathbf{y}}_f$$

where the matrices \mathbf{K}_i describe state feedback gains for the flat output controllers, given by

$$\mathbf{K}_i = \begin{bmatrix} K_{zi} & 0 & 0 & 0 \\ 0 & K_{\phi i} & 0 & 0 \\ 0 & 0 & K_{\theta i} & 0 \\ 0 & 0 & 0 & K_{\psi i} \end{bmatrix}$$

Defining the operating conditions $\mathbf{y}_f = [z_d, \phi_d, \theta_d, \psi_d]^T$ and $\dot{\mathbf{y}}_f = [0, 0, 0, 0]^T$, the stability of the flat outputs is determined by defining an appropriate Lyapunov function

$$V = \frac{1}{2} \left((\mathbf{y}_f - \mathbf{y}_{f,d})^T \mathbf{K}_1 (\mathbf{y}_f - \mathbf{y}_{f,d}) + \dot{\mathbf{y}}_f^T \dot{\mathbf{y}}_f \right) \quad (6.61)$$

which provides the time derivative

$$\dot{V} = -\dot{\mathbf{y}}_f^T \mathbf{K}_2 \dot{\mathbf{y}}_f \quad (6.62)$$

The Lyapunov function V is then positive definite for the condition $\mathbf{K}_1 > 0$. The derivative is negative definite for the condition $\mathbf{K}_2 > 0$. The closed-loop flat output dynamics described by the linearised second-order system are thus asymptotically stable under these conditions for all values of \mathbf{y}_f and $\dot{\mathbf{y}}_f$.

Consider the definition of the state feedback gains for the second-order system

$$\begin{aligned} K_1 &= \omega_n^2 \\ K_2 &= 2\zeta\omega_n \end{aligned}$$

The stability criteria is then described in terms of the chosen tuning parameters by

$$\omega_n^2 > 0, \quad 2\zeta\omega_n > 0$$

The system is therefore stable for all positive definite values of ω_n and ζ , as expected.

THIRD-ORDER SYSTEM

The closed-loop system resulting from applying state feedback control to the linearised Level 3 model is described by

$$\mathbf{y}_f^{(3)} = \mathbf{K}_1 (\mathbf{y}_{f,d} - \mathbf{y}_f) - \mathbf{K}_2 \dot{\mathbf{y}}_f - \mathbf{K}_3 \ddot{\mathbf{y}}_f \quad (6.63)$$

With the additional operating condition $\ddot{\mathbf{y}}_f = [0, 0, 0, 0]^T$, the Lyapunov function is define to be

$$\begin{aligned} V = \frac{1}{2} & \left((\mathbf{y}_f - \mathbf{y}_{f,d})^T (\mathbf{K}_2 \mathbf{K}_3 - \mathbf{K}_1) \mathbf{K}_1 \mathbf{K}_2^{-1} (\mathbf{y}_f - \mathbf{y}_{f,d}) \right. \\ & + (\mathbf{K}_2 \dot{\mathbf{y}}_f + \mathbf{K}_1 (\mathbf{y}_f - \mathbf{y}_{f,d}))^T \mathbf{K}_2^{-1} (\mathbf{K}_2 \dot{\mathbf{y}}_f + \mathbf{K}_1 (\mathbf{y}_f - \mathbf{y}_{f,d})) \\ & \left. + (\mathbf{K}_3 \dot{\mathbf{y}}_f + \ddot{\mathbf{y}}_f)^T (\mathbf{K}_3 \dot{\mathbf{y}}_f + \ddot{\mathbf{y}}_f) \right) \end{aligned} \quad (6.64)$$

which provides the time derivative

$$\dot{V} = \dot{\mathbf{y}}_f^T (\mathbf{K}_1 - \mathbf{K}_2 \mathbf{K}_3) \dot{\mathbf{y}}_f \quad (6.65)$$

The Lyapunov function V and is then positive definite and \dot{V} is negative definite for the conditions $\mathbf{K}_1 > 0$, $\mathbf{K}_2 > 0$, $\mathbf{K}_3 > 0$, $\mathbf{K}_2 \mathbf{K}_3 - \mathbf{K}_1 > 0$. The closed-loop flat output dynamics described by the linearised third-order system are thus asymptotically stable under these conditions for all values of \mathbf{y}_f , $\dot{\mathbf{y}}_f$ and $\ddot{\mathbf{y}}_f$.

Consider the definition of the state feedback gains for the third-order system

$$\begin{aligned} K_1 &= p\omega_n^2 \\ K_2 &= \omega_n^2 + 2p\zeta\omega_n \\ K_3 &= p + 2\zeta\omega_n \end{aligned}$$

The stability criteria is then described in terms of the chosen tuning parameters by

$$\begin{aligned} p\omega_n^2 &> 0, \quad \omega_n^2 + 2p\zeta\omega_n > 0, \quad p + 2\zeta\omega_n > 0 \\ 2\zeta\omega_n(\omega_n^2 + p^2 + p\zeta\omega_n) &> 0 \end{aligned}$$

The system is therefore stable for all positive definite values of ω_n , p and ζ , as expected.

6.5 CONTROLLER TESTING ON MODEL FAMILY

It is useful at this stage to introduce some standard notation to the model family and the derived controllers. As described in Chapter 5, each model in the multi-resolution family is described by the general state-space equation

$$\dot{\mathbf{x}}_i(t) = f_i(\mathbf{x}_i(t), \mathbf{u}(t))$$

where $i = \{1, 2, 3, 4, 5\}$ denotes the level in the model family. The non-linear controllers derived in this chapter may be described by the general model

$$\begin{aligned}\mathbf{u}(t) &= \mathbf{C}^{-1}\mathbf{u}^*(t) \\ \mathbf{u}^*(t) &= c_j(\mathbf{x}(t), \mathbf{y}_{t,d}(t))\end{aligned}\tag{6.66}$$

where the closed-loop system inputs are $\mathbf{y}_{t,d} = [x_d, y_d, z_d, \psi_d]^T$ and $j = \{1, 2, 3\}$ denotes the level from which the controller is derived and the control matrix \mathbf{C} is

$$\mathbf{C} = \begin{bmatrix} 1 & 1 & 1 & 1 \\ 0 & 0 & 1 & -1 \\ -1 & 1 & 0 & 0 \\ -1 & -1 & 1 & 1 \end{bmatrix}$$

The closed-loop system of any quadrotor-controller pair is therefore described by

$$\dot{\mathbf{x}}_i(t) = f_i\left(\mathbf{x}_i(t), \mathbf{C}^{-1}[c_j(\mathbf{x}_i(t), \mathbf{y}_{t,d}(t))]\right)$$

The state feedback gains are determined for each pair $i = j = \{1, 2, 3\}$. These systems have been demonstrated to be stable through a combination of linear stability analysis and Lyapunov's second method. For the condition $j \neq i$, the closed-loop system is highly non-linear and its stability unknown. This is representative of controller design and testing in practice. The controller is derived from a model of the system, ensuring the closed-loop system behaves as desired in simulation. In practice unmodelled dynamics or non-linearities result in an unexpected or undesirable response.

Such effects are investigated in simulation by applying the derived controllers to models of higher resolution, simulating the application of controllers in practice. This approach allows differences in the response of each level to be discussed with reference to the behaviours described by the level. Each non-linear controller c_j , where $j = \{1, 2, 3\}$ is therefore applied to the model f_i described by each level $i = \{1, 2, 3, 4, 5\}$ in the model family, subject to the condition $i \geq j$. A unit step input is applied to each of the desired tracking outputs $\mathbf{y}_{t,d} = [x_d, y_d, z_d, \psi_d]^T$ and the responses analysed. Finally, a typical trajectory is defined and each controller-model combination commanded to follow it. The results of these simulation experiments are then discussed.

6.5.1 STEP CHANGE IN HEIGHT RESPONSE

A step input is supplied to the controller input z_d to induce a change in height in the quadrotor models. The response of each model f_i to an input to each controller c_j , subject to the condition $i \geq j$, is presented. For each model-controller pair, the desired settling time $\tau_{s,z}$ of the closed-loop height response

is varied to change the performance of the controller. The specified damping ratio is set constant at $\zeta_z = 1$ for each test, while the additional pole specifying the performance of the Level 3 controller is parameterised by $p_z = 20 \omega_{n,z}$.

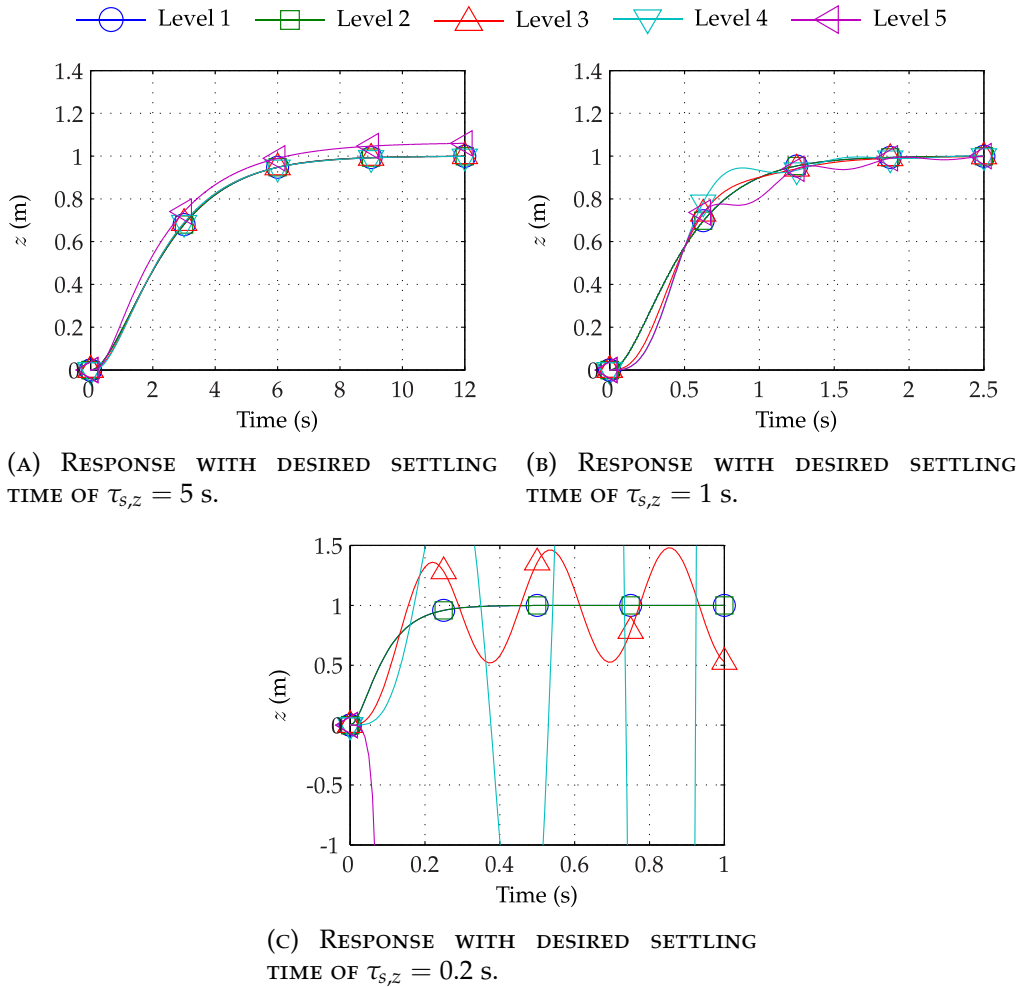


FIGURE 6.4: UNIT STEP RESPONSE IN HEIGHT FOR LEVEL 1 CONTROLLER APPLIED TO MODEL FAMILY.

Figure 6.4 shows the response of each model in the multi-resolution family to a step input in z_d , supplied to the Level 1 controller c_1 . This gives the closed-loop system

$$\dot{\mathbf{x}}_i(t) = f_i \left(\mathbf{x}_i(t), \mathbf{C}^{-1} [c_1(\mathbf{x}_i(t), \mathbf{y}_{t,d}(t))] \right), \quad i = \{1, 2, 3, 4, 5\} \quad (6.67)$$

where $\mathbf{y}_{t,d} = [0, 0, 1, 0]^T$. A chosen settling time of $\tau_{s,z} = 5$ s is shown to result in a stable response in each level. The trajectories followed by the models in Levels 1 to 4 is shown to be almost identical, while the Level 5 model demonstrates a steady-state error, due to the non-linearity in the rotor model. This result emphasises the need for integral action when accurately tracking trajectories in practice. Decreasing the specified settling time to $\tau_{s,z} = 1$ s results in oscillatory behaviour in the response of the Level 4 and Level 5 models. The higher frequency of the rotor dynamics described by these models and the lack

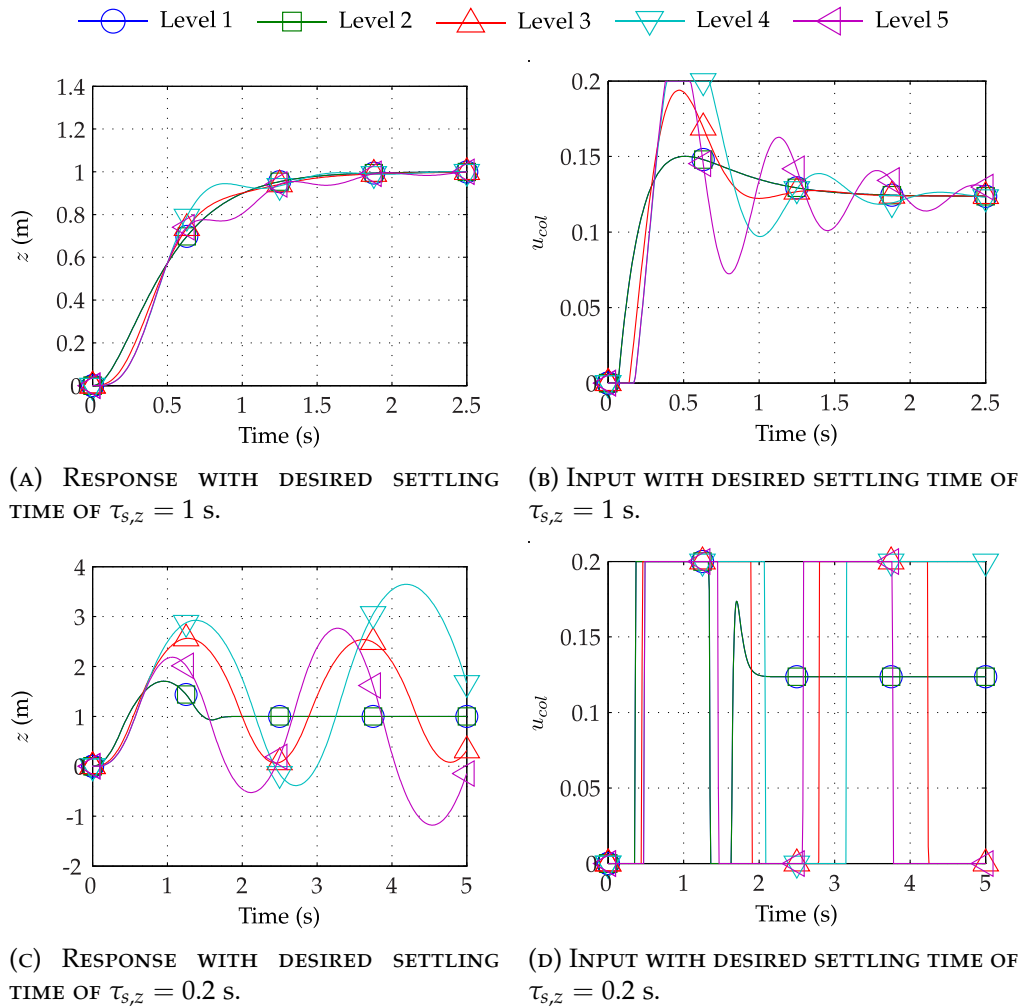


FIGURE 6.5: UNIT STEP RESPONSE IN HEIGHT FOR LEVEL 1 CONTROLLER APPLIED TO MODEL FAMILY, WITH LIMITS ON MAGNITUDE OF CONTROL INPUTS.

of compensation for this by the controller results in the poles of the closed-loop system tending towards the imaginary axis. This is further evident when decreasing the specified settling time to $\tau_{s,z} = 0.2$ s. The height response described by Levels 4 and 5 is now completely unstable. The response of the Level 3 model demonstrates slightly unstable oscillatory behaviour, again due to the poles uncompensated-for rotor dynamics crossing the imaginary axis.

These results highlight the impact of unmodelled dynamics on the response of the closed-loop system. As the natural frequency of the closed-loop system is increased, the dynamics of the rotors become non-negligible. Without compensating for the additional states in the system, the response then becomes unstable. It must be noted that for desired settling times of $\tau_{s,z} = 1$ s and $\tau_{s,z} = 0.2$ s, the actuator limits $0 \leq u_i \leq 0.05$ of the system are exceeded in the simulation, which is not possible in reality. Limiting the system input \mathbf{u} to this range, Figure 6.5 demonstrates results which are more representative of those in practice. Imposing limits is shown to have negligible impact on the closed-loop system for $\tau_{s,z} = 1$ s, but alters the response characteristics for the

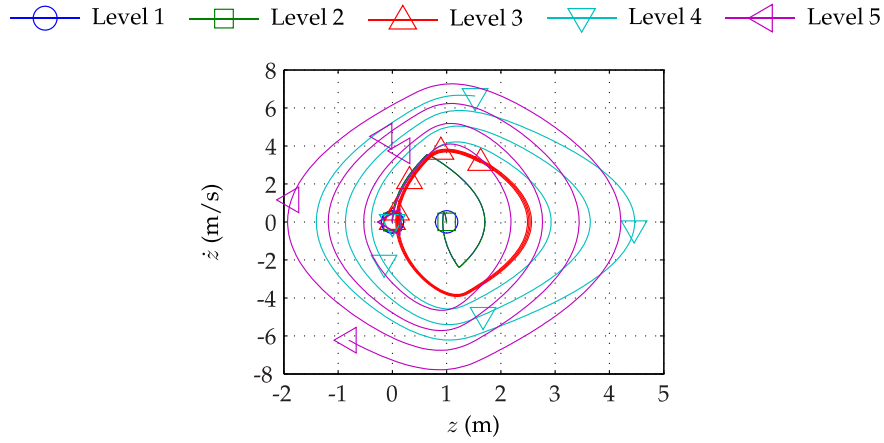


FIGURE 6.6: PHASE PLANE PLOT OF z AND \dot{z} FOR LEVEL 1 CONTROLLER APPLIED TO MODEL FAMILY, WITH LIMITED INPUT RANGE AND DESIRED SETTLING TIME $\tau_{s,z} = 0.2$ s.

system with $\tau_{s,z} = 0.2$ s considerably. While the models described by Levels 1 and 2 quickly reach an equilibrium, the Level 3 model displays a stable but oscillatory response. The systems described by Levels 4 and 5 are unstable but not exponentially so. Figure 6.6 demonstrates these results.

The controller derived from Level 2 of the model family, c_2 , is then applied to the models described by each Levels 2 to 5, giving the closed-loop system

$$\dot{\mathbf{x}}_i(t) = f_i(\mathbf{x}_i(t), \mathbf{C}^{-1}[c_2(\mathbf{x}_i(t), \mathbf{y}_{t,d}(t))]), \quad i = \{2, 3, 4, 5\} \quad (6.68)$$

$\mathbf{y}_{t,d} = [0, 0, 1, 0]^T$. Figure 6.7 shows the results of applying a step input in z_d for chosen values of $\tau_{s,z}$. The results are shown to be similar to those for c_1 as expected. This is due to the similarities in the height dynamics of Levels 1 and 2 when the quadrotor is level. The observations made on the behaviour of the closed-loop systems with the controller c_1 can therefore also be attributed to c_2 .

Next, the controller derived from Level 3 of the model family, c_3 , is applied to the models described by each Levels 3 to 5, giving the closed-loop system

$$\dot{\mathbf{x}}_i(t) = f_i(\mathbf{x}_i(t), \mathbf{C}^{-1}[c_3(\mathbf{x}_i(t), \mathbf{y}_{t,d}(t))]), \quad i = \{3, 4, 5\} \quad (6.69)$$

where $\mathbf{y}_{t,d} = [0, 0, 1, 0]^T$. Figure 6.8 shows the results of applying a step input in z_d to each closed-loop system. The dynamics of the rotors are now accounted for by the controller through the first-order model described by Level 3. For desired closed-loop settling times of $\tau_{s,z} = 5$ s and $\tau_{s,z} = 1$ s, the height dynamics of Levels 4 and 5 is shown to respond as desired. For $\tau_{s,z} = 1$ s, the Level 5 height model is shown to respond in the opposite direction from desired. This is due to the simulated input exceeding the limits of the physical input signal, resulting in unpredictable behaviour in the non-linear rotor model of Level 5. Once again, limiting the input signal ensures the model behaves as predicted and produces a more desirable response, as shown in Figure 6.9. This

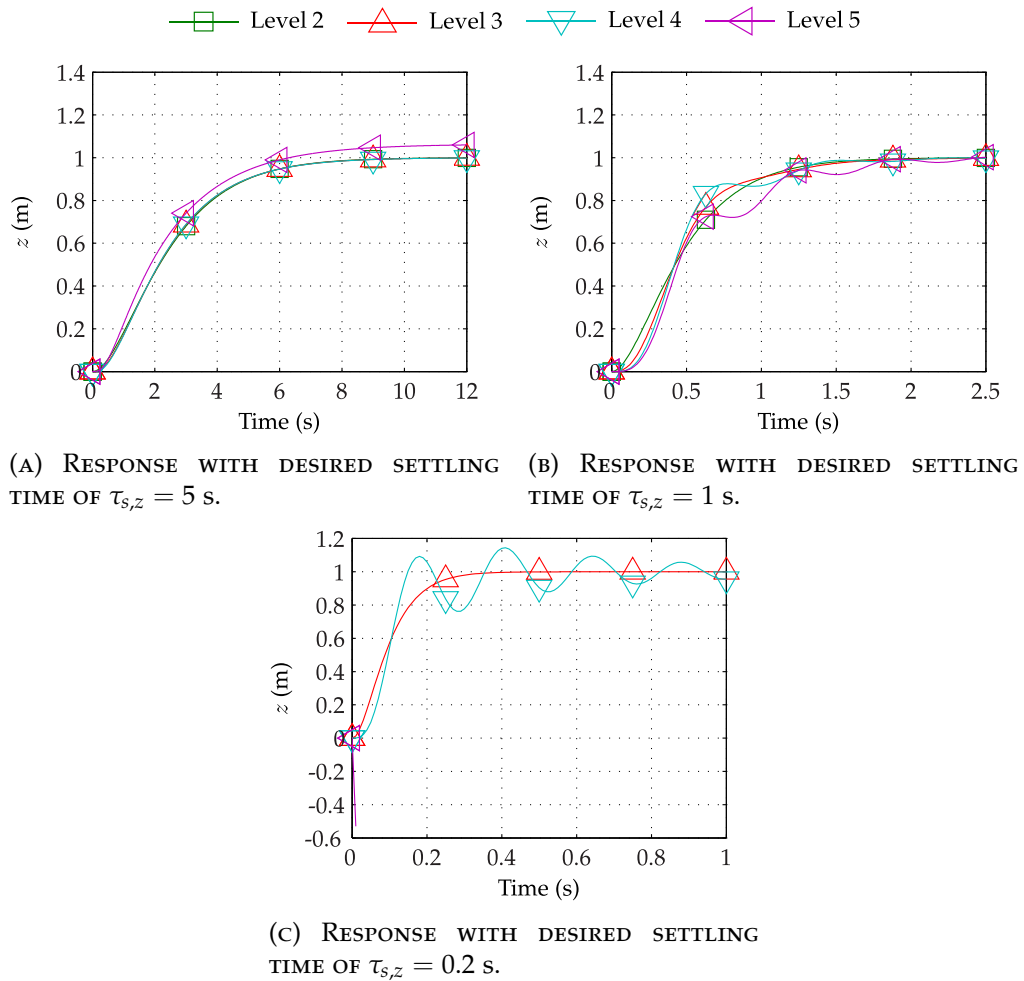


FIGURE 6.7: UNIT STEP RESPONSE IN HEIGHT FOR LEVEL 2 CONTROLLER APPLIED TO LEVELS 2 TO 5 OF THE MODEL FAMILY.

is further evidenced in the height response of the Level 5 model for $\tau_{s,z} = 0.2$ s, where the system is shown to be exponentially unstable, while the Level 4 model is oscillatory and stable. The frequency of the closed-loop system has now increased sufficiently such that the additional poles of the rotor dynamics cause oscillatory behaviour in the response. Thus, while the rotor dynamics *have* been accounted for by the control system, increasing the closed-loop frequency of the system highlights the effects of further unmodelled dynamics.

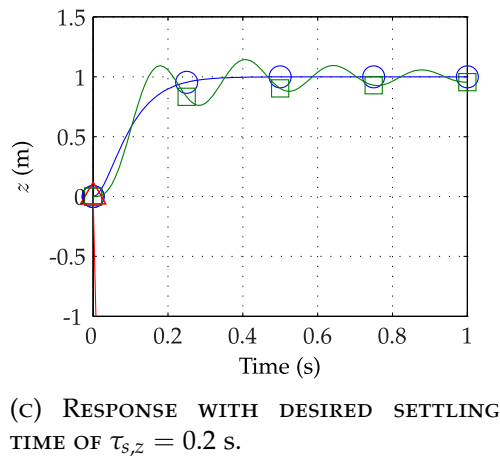
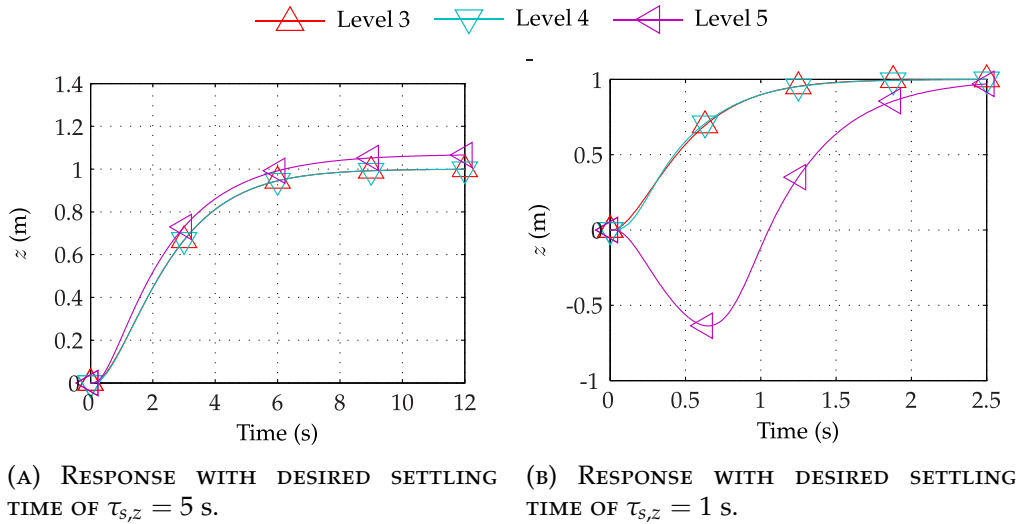


FIGURE 6.8: UNIT STEP RESPONSE IN HEIGHT FOR LEVEL 3 CONTROLLER APPLIED TO LEVELS 3 TO 5 OF THE MODEL FAMILY.

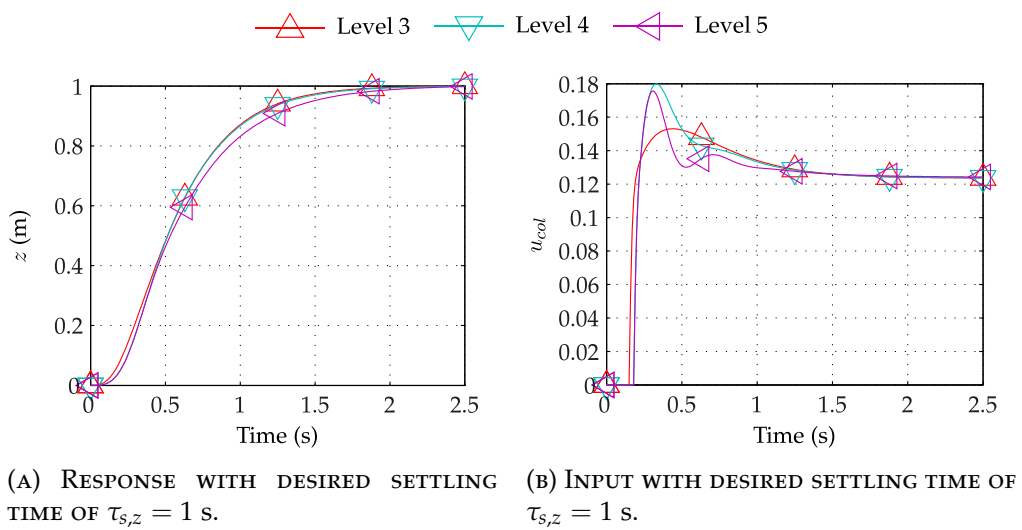


FIGURE 6.9: UNIT STEP RESPONSE IN HEIGHT FOR LEVEL 3 CONTROLLER APPLIED TO LEVELS 3 TO 5 OF THE MODEL FAMILY, WITH LIMITS ON MAGNITUDE OF CONTROL INPUTS.

6.5.2 STEP INPUT IN YAW DIRECTION

A step input is supplied to the controller input ψ_d to induce a change in yaw displacement in the quadrotor models. Again, the response of each model f_i to an input to each controller c_j , subject to the condition $i \geq j$, is presented. For each model-controller pair, the desired settling time $\tau_{s,\psi}$ of the closed-loop yaw response is varied to change the performance of the controller. The specified damping ratio is set constant at $\zeta_\psi = 1$ for each test, while the additional pole parameterising the performance of the Level 3 controller is placed at $p_\psi = 20\omega_{n,\psi}$.

Figure 6.10 shows the response of each model in the multi-resolution family to a step input in ψ_d , supplied to the Level 1 controller c_1 . The resulting closed-loop system is described by Equation (6.67), where $\mathbf{y}_{t,d} = [0, 0, 0, 1]^T$. A desired closed-loop settling time of $\tau_{s,\psi} = 5$ s is shown to produce a similar yaw response for each level, as expected. A value of $\tau_{s,\psi} = 1$ s increases the natural frequency of the closed-loop system, resulting in the additional poles of the models in Levels 3 to 5 moving toward the imaginary axis and impacting

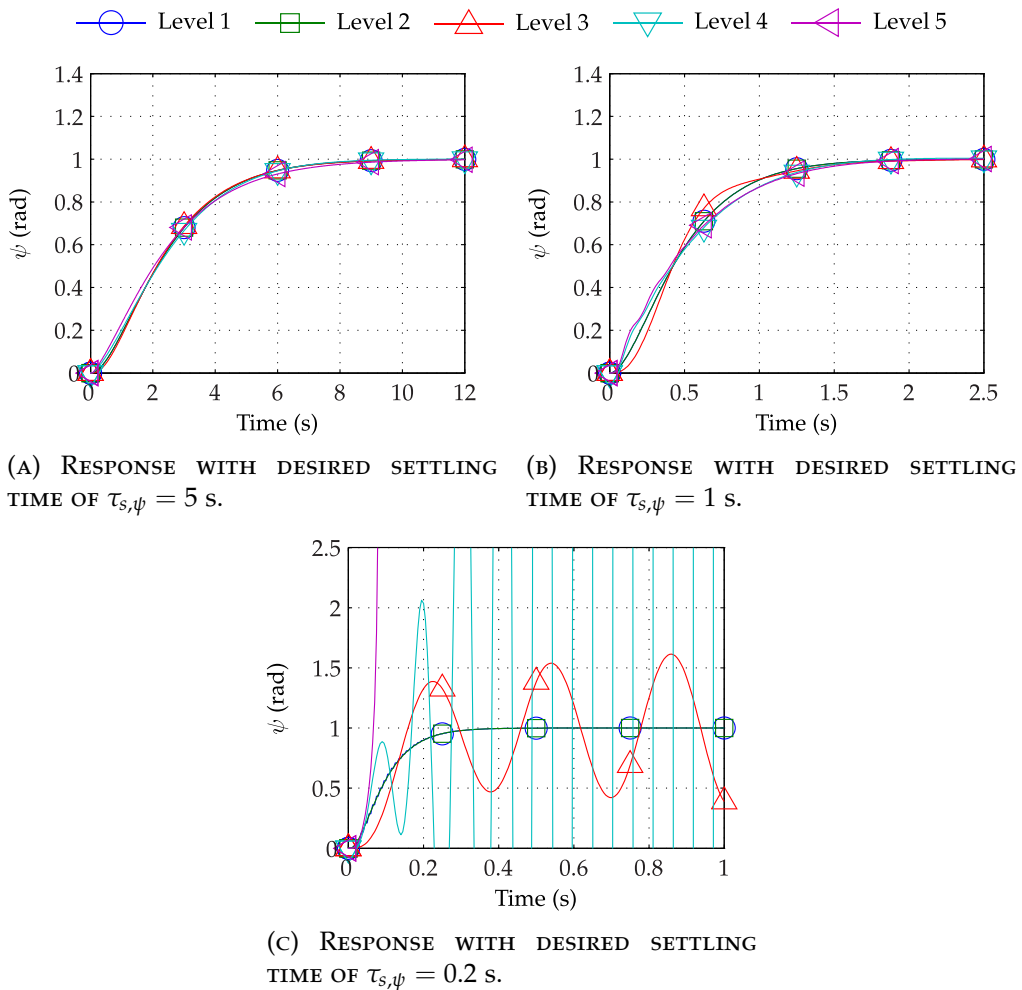


FIGURE 6.10: UNIT STEP RESPONSE IN YAW DISPLACEMENT FOR LEVEL 1 CONTROLLER APPLIED TO MODEL FAMILY.

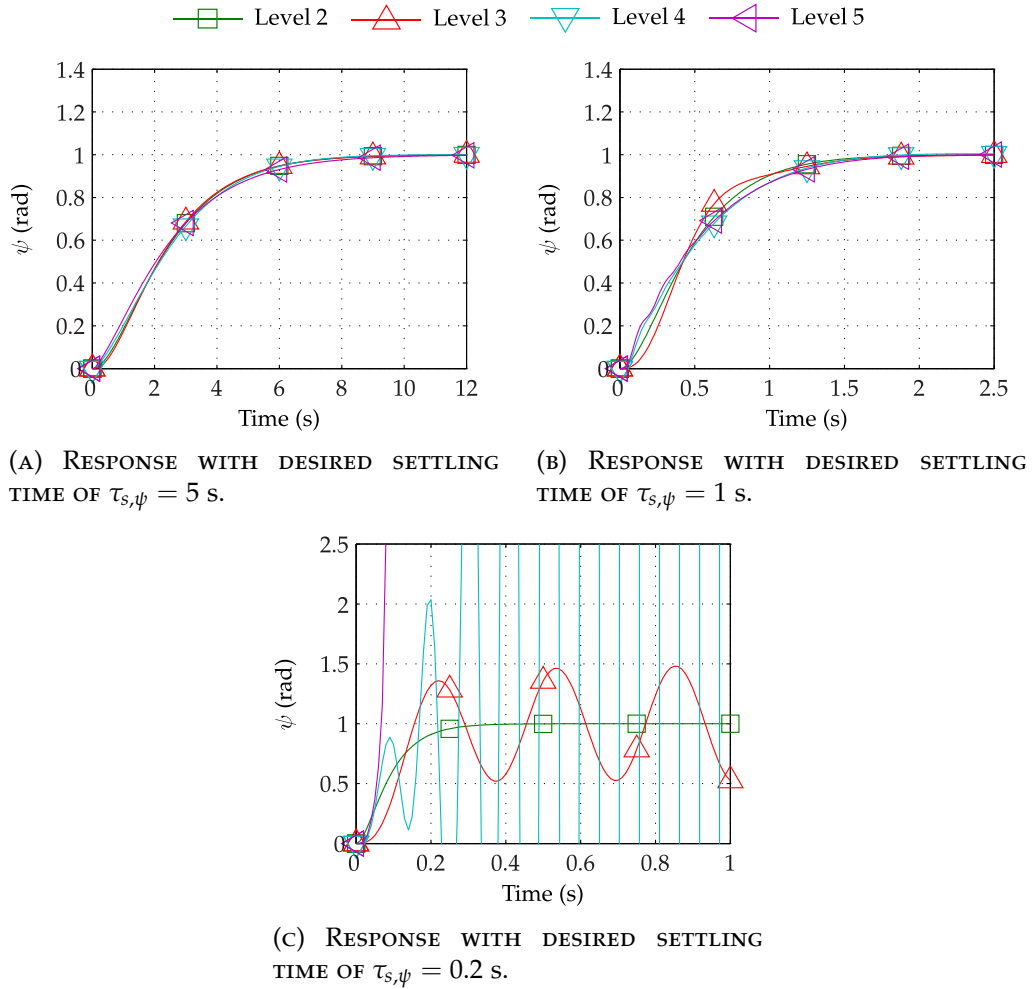


FIGURE 6.11: UNIT STEP RESPONSE IN YAW DISPLACEMENT FOR LEVEL 2 CONTROLLER APPLIED TO LEVELS 2 TO 5 OF THE MODEL FAMILY.

the response. Finally, a value of $\tau_{s,\psi} = 0.2$ s results in unstable behaviour in the models described by Levels 3 to 5, due to the presence of closed-loop poles in the positive real axis of the complex plane. The systems inputs \mathbf{u} again exceed the limits of the physical system in the latter two cases. For the case of $\tau_{s,\psi} = 1$ s, the magnitude of the inputs are not sufficient to cause unstable behaviour in the Level 5 model. For the case of $\tau_{s,\psi} = 0.2$ s, the inputs are sufficiently far out-with the limits of predictable behaviour that the Level 5 model is exponentially unstable.

The controller c_2 is then applied to Levels 2 to 5 of the model family, giving the closed-loop system described by Equation (6.68), with input $\mathbf{y}_{t,d} = [0, 0, 0, 1]^T$. The results of applying a unit step input in ψ_d are shown in Figure 6.11. As expected, the results of applying c_2 to each quadrotor model are similar to those when using the controller c_1 . In level, hovering flight, the yaw dynamics of the Levels 1 and 2 models are identical, thus the derived yaw controllers are also identical.

The controller c_3 is then applied to Levels 3 to 5 of the model family,

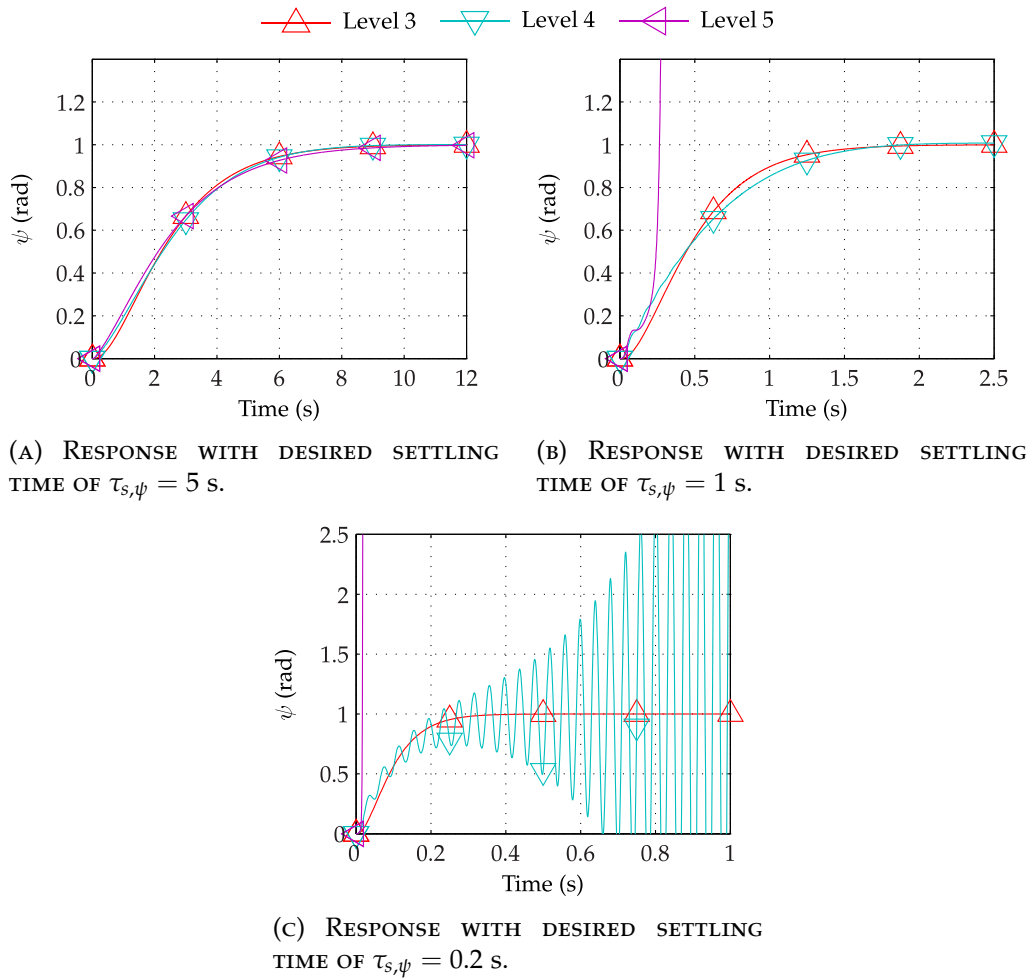


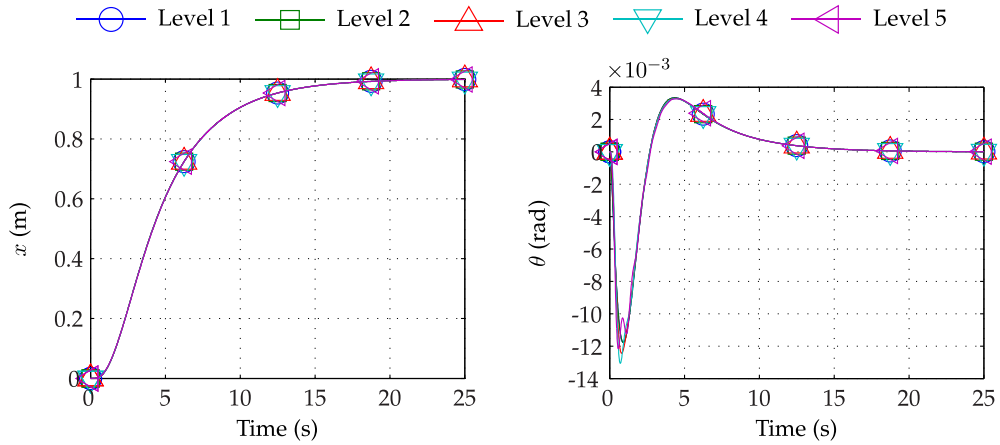
FIGURE 6.12: UNIT STEP RESPONSE IN YAW DISPLACEMENT FOR LEVEL 3 CONTROLLER APPLIED TO LEVELS 3 TO 5 OF THE MODEL FAMILY.

giving the closed-loop system described by Equation (6.69), with the input $\mathbf{y}_{t,d} = [0, 0, 0, 1]^T$. Figure 6.12 shows the results of applying a unit step input in ψ_d to the controller. For a desired settling time of $\tau_{s,\psi} = 5$ s, the closed-loop response in yaw is slow enough to ensure that the model described by each level is stable. Increasing the natural frequency of the closed-loop system by specifying $\tau_{s,\psi} = 1$ s, the Level 5 model is shown to be exponentially unstable. This is again due to the control inputs exceeding the physical limits of the system, resulting in rotor behaviour which is unpredictable with respect to the controller. Decreasing the closed-loop settling time further to $\tau_{s,\psi} = 0.2$ s, the Level 4 model is shown to become unstable also, as the frequency of the closed-loop system approaches the natural frequency of the uncompensated rotor dynamics.

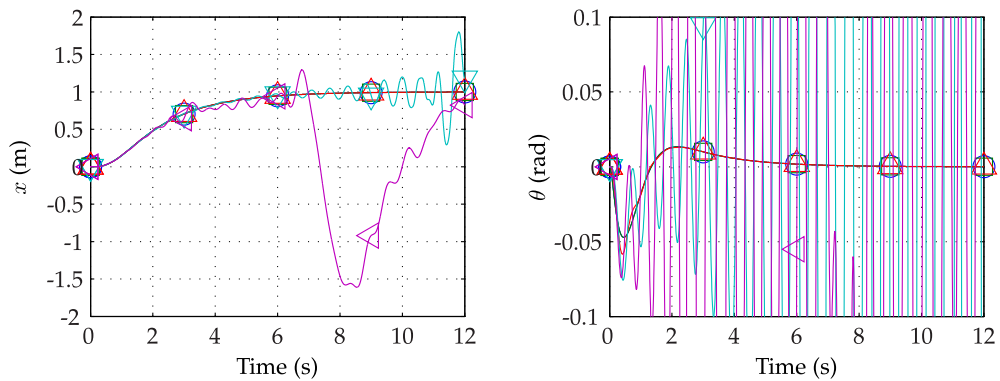
6.5.3 STEP INPUT IN HORIZONTAL POSITION

The response of the quadrotor in horizontal position is investigated by applying a step input in the controller command x_d to induce a change in x . For each

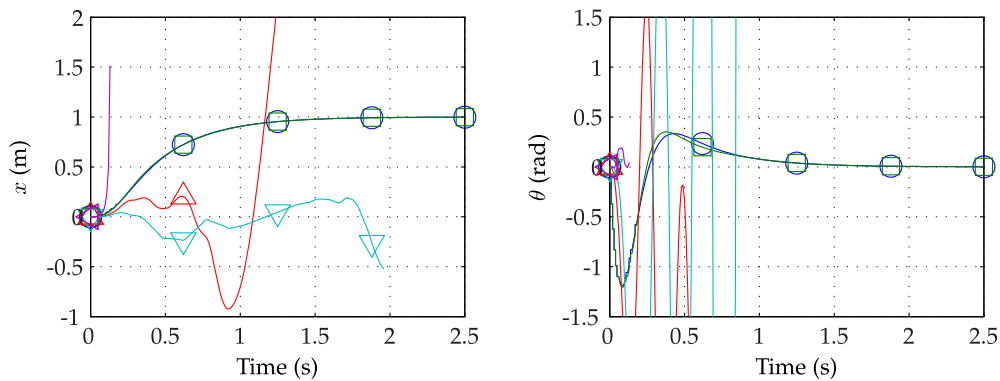
model f_i the step command is input to the controller c_j , where $i \geq j$. For each model-controller pair, the desired settling time $\tau_{s,p}$ of the closed-loop position response is varied to change the performance of the controller. The natural frequency of the desired closed-loop attitude response is related to the natural frequency of the closed-loop attitude response by $\omega_{n,a} = k\omega_{n,p}$, where $k = 10$ is used to ensure a desirable response in the outer loop. The specified damping ratios of both the inner and outer loops are $\zeta_a = \zeta_p = 1$, while the additional pole parameterising the Level 3 controller is placed at $p_a = 20\omega_{n,a}$.



(A) RESPONSE WITH DESIRED SETTLING TIME OF $\tau_{s,p} = 10$ s.



(B) RESPONSE WITH DESIRED SETTLING TIME OF $\tau_{s,p} = 5$ s.



(C) RESPONSE WITH DESIRED SETTLING TIME OF $\tau_{s,p} = 1$ s.

FIGURE 6.13: UNIT STEP RESPONSE IN HORIZONTAL POSITION FOR LEVEL 1 CONTROLLER APPLIED TO MODEL FAMILY.

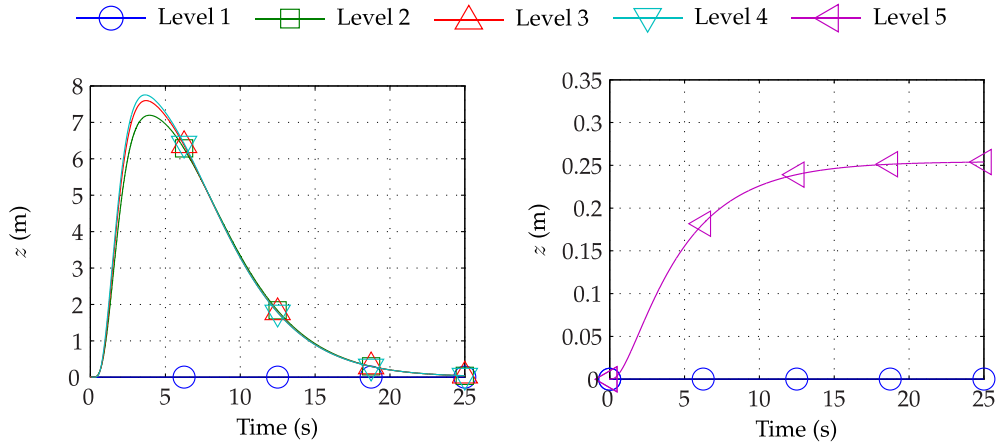


FIGURE 6.14: HEIGHT RESPONSE TO UNIT STEP INPUT IN x_d . THE DIFFERENCE IN BEHAVIOUR BETWEEN THE LEVEL 1 MODEL AND HIGHER-RESOLUTION LEVELS BECOMES APPARENT WHEN ROLLING OR PITCHING THE QUADROTOR. THE LEVEL 5 MODEL IS SHOWN TO HAVE A STEADY-STATE ERROR DUE TO THE NON-LINEAR ROTOR MODEL.

Figure 6.13 shows the response of each level in the multi-resolution model family to a step input in x_d , supplied to the Level 1 controller c_1 . This gives the closed-loop system described by Equation (6.67), with the input $\mathbf{y}_{t,d} = [1, 0, 0, 0]^T$. A specified settling time of $\tau_{s,p} = 10$ s is shown to produce an identical position response for each level. This is expected, as the linear system described by Equation (6.52) is identical for each level. The pitch response is shown to be of low frequency and magnitude, thus the dynamics and non-linearities of the higher-resolution models do not impact the closed-loop response significantly. For a settling time of $\tau_{s,p} = 5$ s the position and attitude responses of the models described by Levels 4 and 5 are shown to be unstable. The higher frequency of the inner loop which controls the roll and pitch response of the system results in instabilities with a position response much lower than that of the height dynamics. Increasing the natural frequency of the closed-loop system further, $\tau_{s,p} = 1$ s also results in unstable behaviour in the Level 3 model, as the frequency approaches that of the rotor dynamics without compensating for it.

Figure 6.14 shows the response in height for a step input in x_d to the Level 1 controller. The difference between the Level 1 and Level 2 models becomes apparent here, as the linear controller is not sufficient to ensure accurate tracking of height in the non-linear models. Additionally, the non-linear rotor model of the Level 5 quadrotor causes a steady-state error in z .

The Level 2 controller c_2 is applied to the model family in Figure 6.15, giving the closed-loop system described by Equation (6.68) with the input x_d . As expected, the responses in x and θ for a desired settling time of $\tau_{s,p} = 10$ s are similar to those for the Level 1 controller, since the quadrotor is in approximately level flight. Increasing the frequency of the system by setting $\tau_{s,p} = 5$ s, the

differences between the controllers c_1 and c_2 become apparent, although the responses in Levels 4 and 5 are still unstable. Further increasing the frequency of the system by setting $\tau_{s,p} = 1$ s, the Level 3 model is shown to become unstable also, as the rotor dynamics become non-negligible. The system does, however, remain stable for slightly longer than when using the Level 1 controller.

Finally, applying again the Level 3 controller c_3 to the model family results in the closed-loop system described by Equation (6.69). Application of a

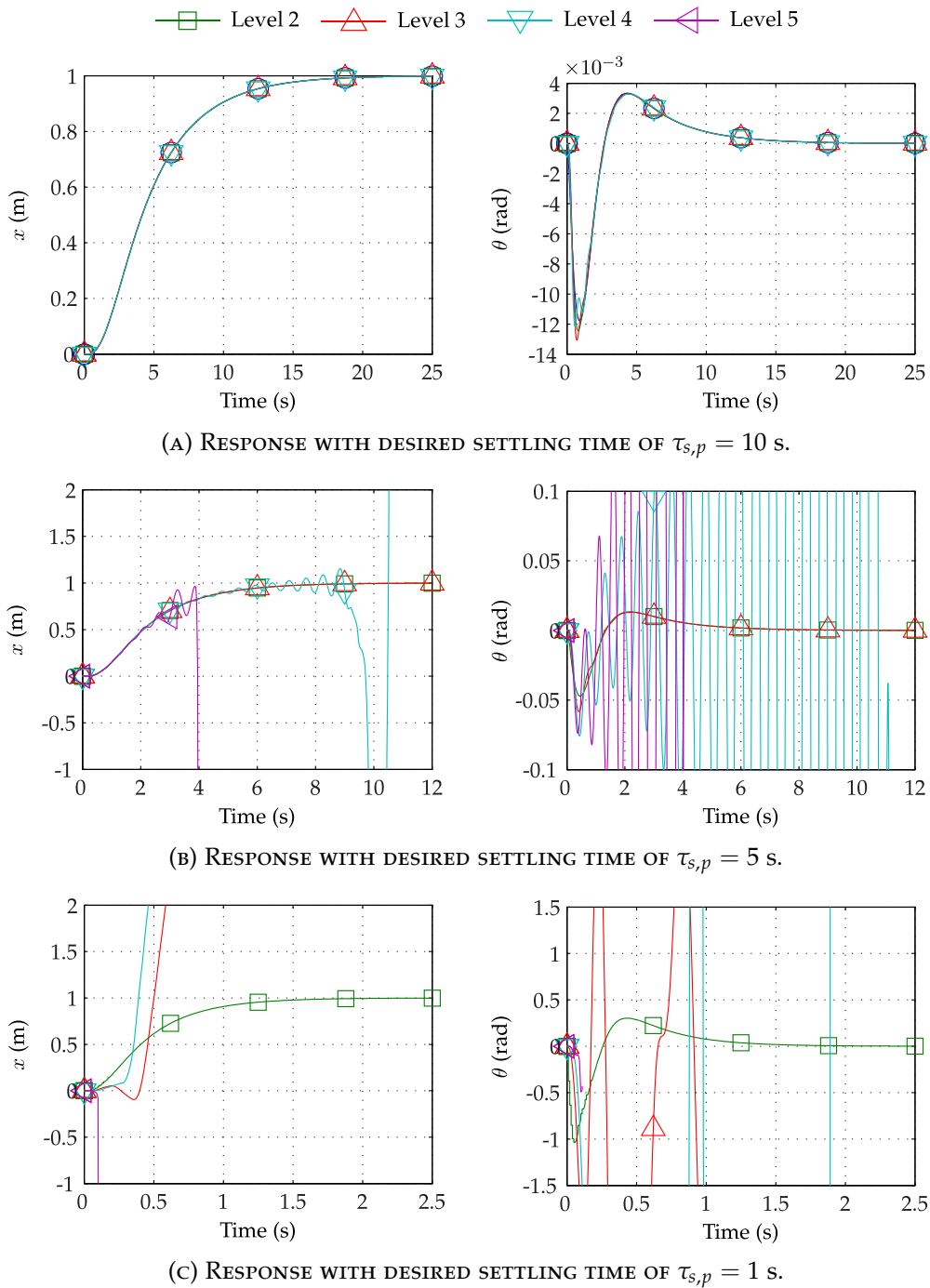


FIGURE 6.15: UNIT STEP RESPONSE IN HORIZONTAL POSITION FOR LEVEL 2 CONTROLLER APPLIED TO LEVELS 2 TO 5 OF THE MODEL FAMILY.

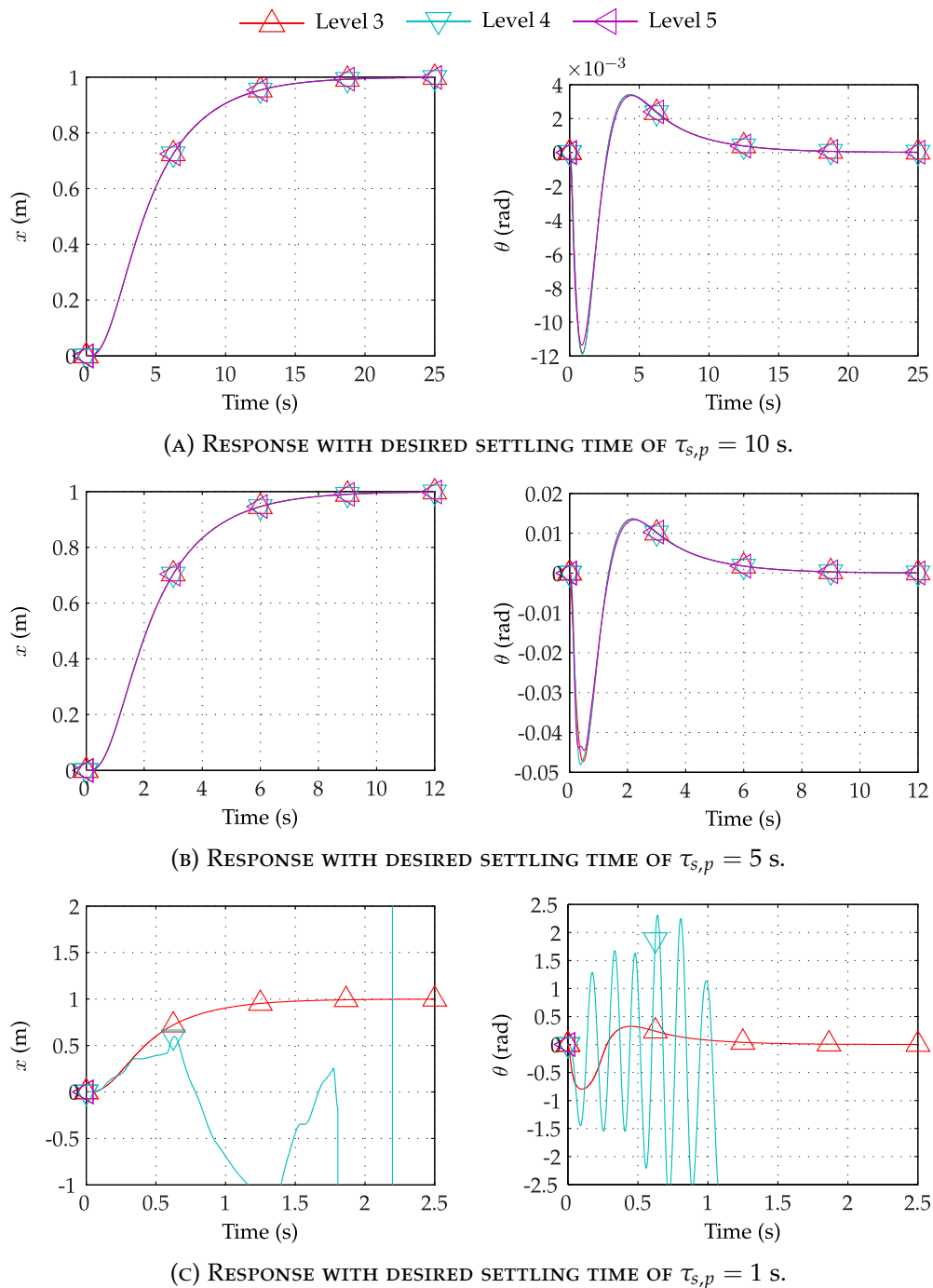


FIGURE 6.16: UNIT STEP RESPONSE IN HORIZONTAL POSITION FOR LEVEL 2 CONTROLLER APPLIED TO LEVELS 2 TO 5 OF THE MODEL FAMILY.

step input in x_d provides the results shown in Figure 6.16. Again, for a low frequency closed-loop response parameterised by $\tau_{s,p} = 10$ s, the quadrotor system is asymptotically stable at all levels. Increasing the frequency by setting $\tau_{s,p} = 5$ s, the system remains stable, as the rotor dynamics are sufficiently damped by the controller. Further increasing the frequency by setting $\tau_{s,p} = 1$ s, the position response described by the Level 3 model is stable as expected. The models described by Levels 4 and 5 are unstable at this frequency, again

due to additional dynamics in the rotor response. The Level 5 model is shown to be highly unstable, due to the control inputs far exceeding the limits of the physical system.

6.5.4 FOLLOWING A TRAJECTORY

As described in Chapter 2, the problem presented by the actuator limits range on the system input \mathbf{u} may be solved to some degree by designing suitable trajectories. An example trajectory is employed to demonstrate the behaviour of each quadrotor when commanded to follow a smooth path rather than a discontinuous step input. The approach to trajectory design is detailed in Chapter 7, but an example derived from it may be employed and is described by

$$\begin{aligned} x_d(t) &= 0.004t^3 - 0.0002t^4 \\ y_d(t) &= 0.01t^3 - 0.0015t^4 + 0.00006t^5 \\ z_d(t) &= -0.018t^3 + 0.0029t^4 - 0.00012t^5 \\ \psi_d(t) &= 0.0314t^3 - 0.00472t^4 + 0.000189t^5 \end{aligned} \quad (6.70)$$

which provides the reference trajectory shown in Figure 6.17.

The desired flat output $\mathbf{y}_{t,d}(t) = [x_d(t), y_d(t), z_d(t), \psi_d(t)]^T$ is supplied to each controller-quadrotor pair, giving the results shown in Figures 6.18, 6.19 and 6.20. These results demonstrate the benefit of smooth trajectory design, as the Level 5 model is shown to remain stable for values of $\tau_{s,p}$ and $\tau_{s,\psi}$ where supplying a step input under these conditions rendered the system unstable. Instabilities caused by the dynamics of the rotors in Levels 3 to 5 when supplying a step input are also present when inputting a smooth trajectory command.

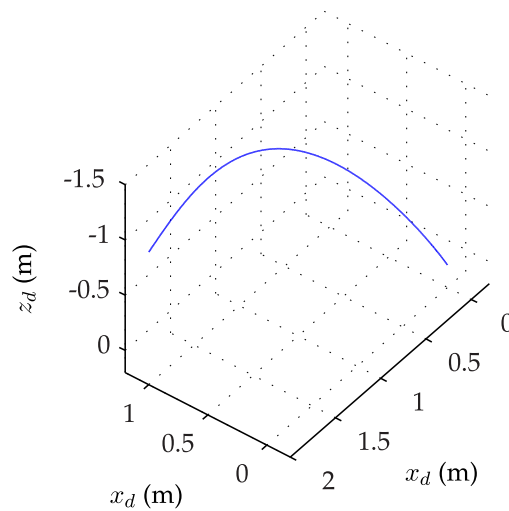
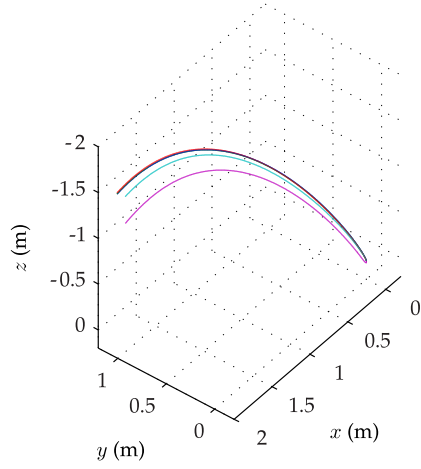
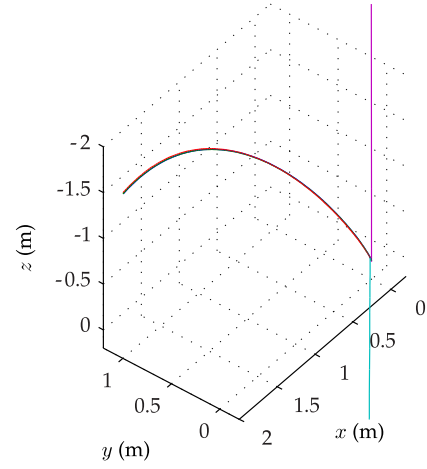


FIGURE 6.17: REFERENCE TRAJECTORY FOR MODEL COMPARISON.

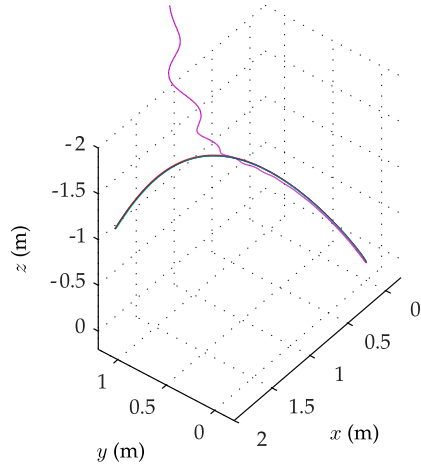
— Level 1 — Level 2 — Level 3 — Level 4 — Level 5



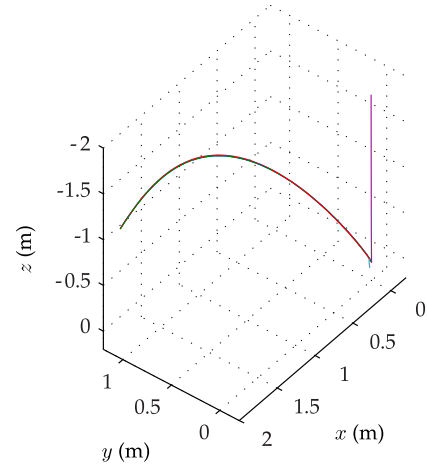
(A) TRAJECTORY WITH CONTROLLER PROPERTIES $\tau_{s,p} = \tau_{s,z} = 10$ s, $\tau_{s,\psi} = 1$ s.



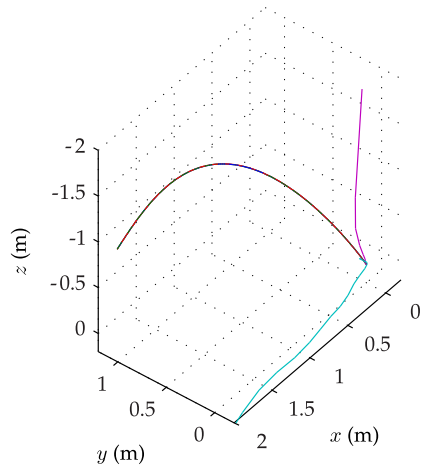
(B) TRAJECTORY WITH CONTROLLER PROPERTIES $\tau_{s,p} = \tau_{s,z} = 10$ s, $\tau_{s,\psi} = 0.2$ s.



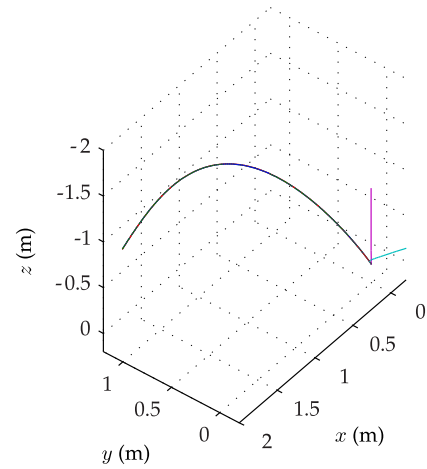
(C) TRAJECTORY WITH CONTROLLER PROPERTIES $\tau_{s,p} = \tau_{s,z} = 5$ s, $\tau_{s,\psi} = 1$ s.



(D) TRAJECTORY WITH CONTROLLER PROPERTIES $\tau_{s,p} = \tau_{s,z} = 5$ s, $\tau_{s,\psi} = 0.2$ s.

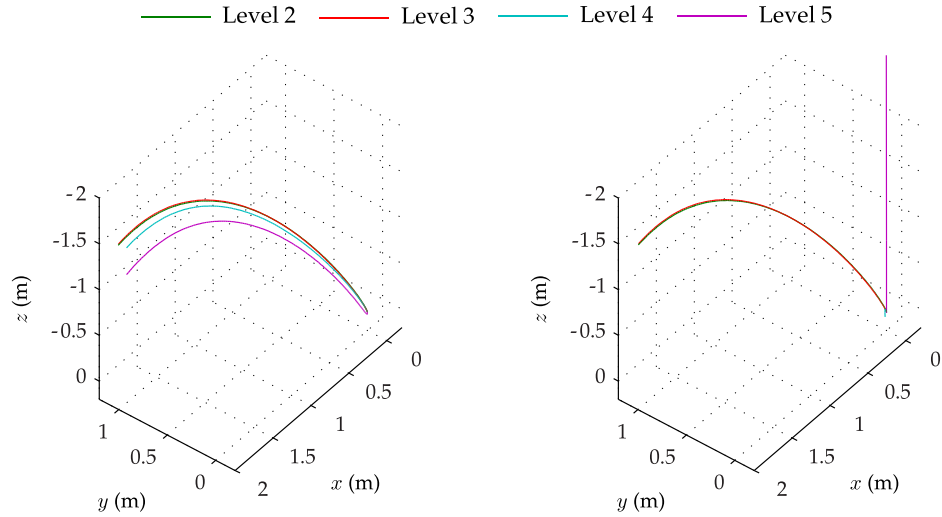


(E) TRAJECTORY WITH CONTROLLER PROPERTIES $\tau_{s,p} = \tau_{s,z} = 2$ s, $\tau_{s,\psi} = 1$ s.



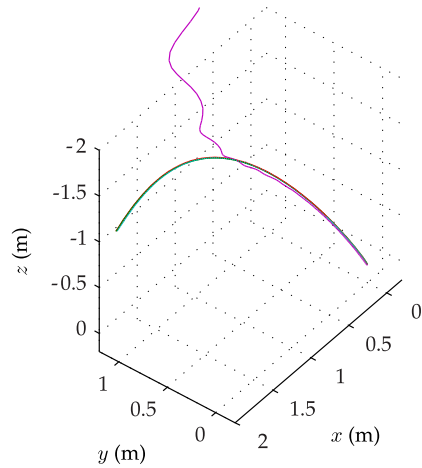
(F) TRAJECTORY WITH CONTROLLER PROPERTIES $\tau_{s,p} = \tau_{s,z} = 2$ s, $\tau_{s,\psi} = 0.2$ s.

FIGURE 6.18: RESPONSE OF EACH MODEL f_i , WHERE $i = \{1, 2, 3, 4, 5\}$, TO A SMOOTH TRAJECTORY COMMAND $\mathbf{y}_{t,d}(t)$ SUPPLIED TO CONTROLLER c_1 .

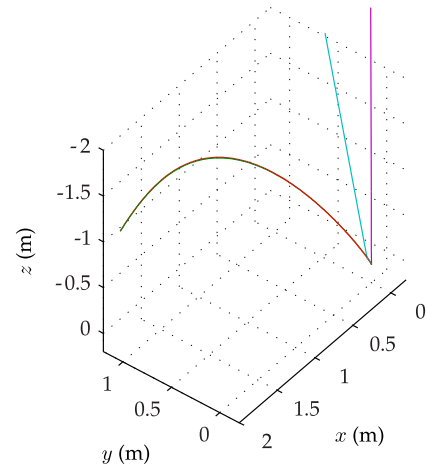


(A) TRAJECTORY WITH CONTROLLER PROPERTIES $\tau_{s,p} = \tau_{s,z} = 10$ s, $\tau_{s,\psi} = 1$ s.

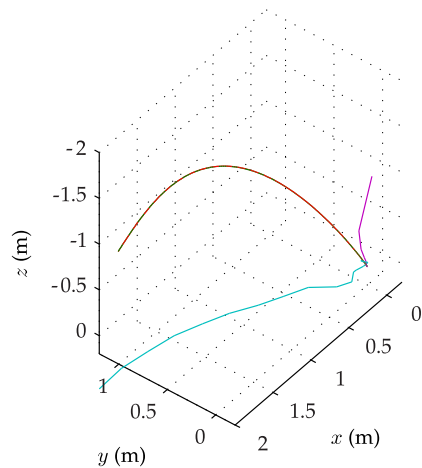
(B) TRAJECTORY WITH CONTROLLER PROPERTIES $\tau_{s,p} = \tau_{s,z} = 10$ s, $\tau_{s,\psi} = 0.2$ s.



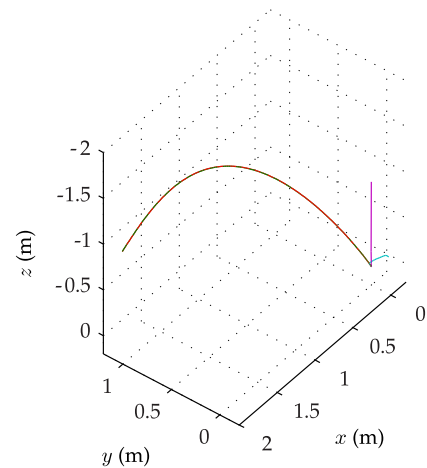
(C) TRAJECTORY WITH CONTROLLER PROPERTIES $\tau_{s,p} = \tau_{s,z} = 5$ s, $\tau_{s,\psi} = 1$ s.



(D) TRAJECTORY WITH CONTROLLER PROPERTIES $\tau_{s,p} = \tau_{s,z} = 5$ s, $\tau_{s,\psi} = 0.2$ s.

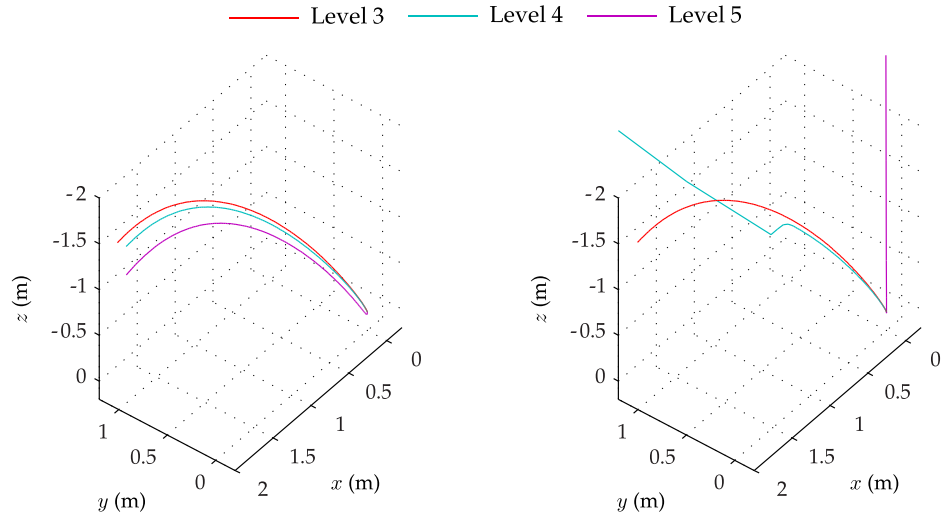


(E) TRAJECTORY WITH CONTROLLER PROPERTIES $\tau_{s,p} = \tau_{s,z} = 2$ s, $\tau_{s,\psi} = 1$ s.



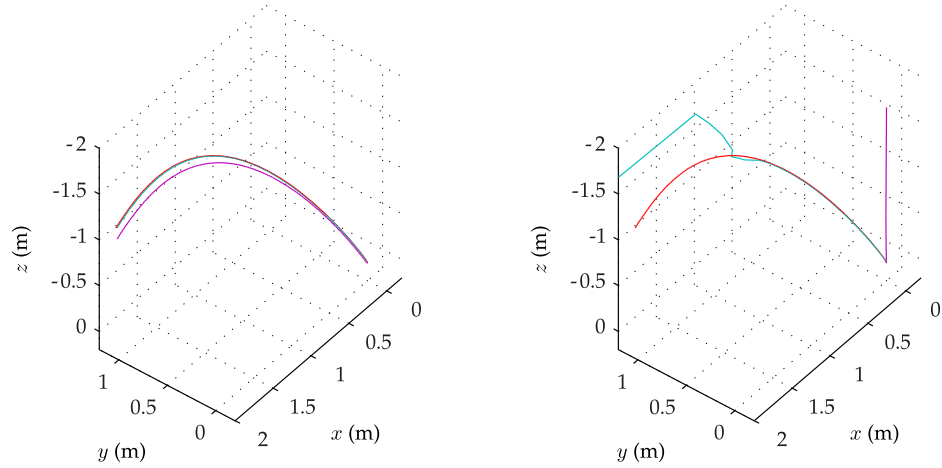
(F) TRAJECTORY WITH CONTROLLER PROPERTIES $\tau_{s,p} = \tau_{s,z} = 2$ s, $\tau_{s,\psi} = 0.2$ s.

FIGURE 6.19: RESPONSE OF EACH MODEL f_i , WHERE $i = \{2, 3, 4, 5\}$, TO A SMOOTH TRAJECTORY COMMAND $\mathbf{y}_{t,d}(t)$ SUPPLIED TO CONTROLLER c_2 .



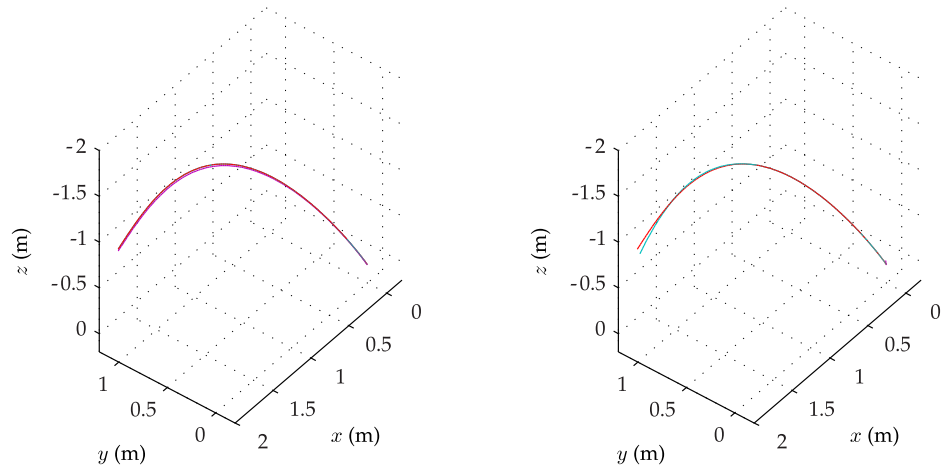
(A) TRAJECTORY WITH CONTROLLER PROPERTIES $\tau_{s,p} = \tau_{s,z} = 10$ s, $\tau_{s,\psi} = 1$ s.

(B) TRAJECTORY WITH CONTROLLER PROPERTIES $\tau_{s,p} = \tau_{s,z} = 10$ s, $\tau_{s,\psi} = 0.2$ s.



(C) TRAJECTORY WITH CONTROLLER PROPERTIES $\tau_{s,p} = \tau_{s,z} = 5$ s, $\tau_{s,\psi} = 1$ s.

(D) TRAJECTORY WITH CONTROLLER PROPERTIES $\tau_{s,p} = \tau_{s,z} = 5$ s, $\tau_{s,\psi} = 0.2$ s.



(E) TRAJECTORY WITH CONTROLLER PROPERTIES $\tau_{s,p} = \tau_{s,z} = 2$ s, $\tau_{s,\psi} = 1$ s.

(F) TRAJECTORY WITH CONTROLLER PROPERTIES $\tau_{s,p} = \tau_{s,z} = 2$ s, $\tau_{s,\psi} = 0.2$ s.

FIGURE 6.20: RESPONSE OF EACH MODEL f_i , WHERE $i = \{3, 4, 5\}$, TO A SMOOTH TRAJECTORY COMMAND $\mathbf{y}_{t,d}(t)$ SUPPLIED TO CONTROLLER c_3 .

6.6 A COMPARISON OF NON-LINEAR DYNAMIC INVERSION CONTROL AND CONVENTIONAL PID

Simulation testing of the quadrotor with Non-linear Dynamic Inversion (NDI) control has been shown to produce both stable and responsive flight. However, compared to conventional Proportional Integral Derivative (PID) control, design of an NDI controller requires far more information about the system and is therefore more time-consuming to develop in instances where the system has not already been fully identified. In theory, as NDI cancels out non-linearities in the system, it should produce a closed-loop response with minimal overshoot and oscillation, as demonstrated by Voos (2009), Mistler et al. (2001) and the results of the previous section.

The developed NDI controllers are thus compared to a conventional PID controller (Bouabdallah et al., 2004) to examine the benefits of one over the other. The primary focus of this investigation is to determine the difference, if any, in response and control effort of closed-loop systems employing each controller with similar settling times. To limit the scope of this investigation, both control strategies are applied to the Level 5 model described by Equation (5.10) and the NDI controller employed is derived from Level 3 of the model family. The bandwidth of the NDI controller is specified by the desired closed-loop settling time of $\tau_{s,z} = \tau_{s,p} = 5$ s.

6.6.1 STRUCTURE OF THE PID CONTROLLER

The PID controller is structured identically to the NDI controller, as shown in Figure 6.1. The flat outputs controller then consists of a single feedback law, expressed by

$$\mathbf{u}^* = \mathbf{K}_{P,f}(\mathbf{y}_f - \mathbf{y}_{f,d}) + \mathbf{K}_{I,f} \int (\mathbf{y}_f - \mathbf{y}_{f,d}) dt + \mathbf{K}_{D,f} \frac{d}{dt}(\mathbf{y}_f - \mathbf{y}_{f,d}) \quad (6.71)$$

where $\mathbf{y} = [z, \phi, \theta, \psi]^T$ and the gains $\mathbf{K}_{P,f}$, $\mathbf{K}_{I,f}$ and $\mathbf{K}_{D,f}$ are diagonal matrices. The horizontal position is controlled by a similar feedback law which provides the roll and pitch commands

$$\begin{aligned} \begin{bmatrix} \phi_d \\ \theta_d \end{bmatrix} &= \begin{bmatrix} -\sin \psi & \cos \psi \\ -\cos \psi & -\sin \psi \end{bmatrix} \mathbf{u}_{xy} \\ \mathbf{u}_{xy} &= K_{P,xy} (\mathbf{y}_{xy} - \mathbf{y}_{xy,d}) + K_{I,xy} \int (\mathbf{y}_{xy} - \mathbf{y}_{xy,d}) dt \\ &\quad + K_{D,xy} \frac{d}{dt}(\mathbf{y}_{xy} - \mathbf{y}_{xy,d}) \end{aligned} \quad (6.72)$$

where $K_{P,xy}$, $K_{I,xy}$ and $K_{D,xy}$ are scalar gains.

6.6.2 TUNING OF PID GAINS

The PID gains are tuned using MATLAB's SISO Design Tool and the controllers tested in Simulink on linearised models of the quadrotor's height, yaw and horizontal position dynamics, as derived from the Level 4 model. The controllers are then tested in simulation on the Level 5 model to identify issues presented by the additional non-linearities of Level 5 with respect to Level 4.

The attitude response is tuned for a closed-loop bandwidth of 3.9 rad s^{-1} and a phase lag of 60° , providing a similar response profile to that of the NDI controller. The height response is tuned for a bandwidth of 0.39 rad s^{-1} and phase lag of 70° , while the horizontal position is tuned for a bandwidth of 0.39 rad s^{-1} and phase lag of 75° .

A first-order filter of bandwidth 5 rad s^{-1} is used to smooth out step inputs to the PID controller. Without this filter, the control inputs would exceed the measured actuator limits of the Level 5 model, thus resulting in unpredictable behaviour. The filter is not required when smooth trajectories are supplied to the controller.

The roll and pitch controllers are designed as proportional-derivative (PD) only. Thus, the resulting PID gains are

$$\mathbf{K}_{P,f} = \begin{bmatrix} 2.47 \times 10^{-4} & 0 & 0 & 0 \\ 0 & 3.717 \times 10^{-4} & 0 & 0 \\ 0 & 0 & 3.717 \times 10^{-4} & 0 \\ 0 & 0 & 0 & 3.84 \times 10^{-1} \end{bmatrix}$$

$$\mathbf{K}_{I,f} = \begin{bmatrix} 1.42 \times 10^{-6} & 0 & 0 & 0 \\ 0 & 0 & 0 & 0 \\ 0 & 0 & 0 & 0 \\ 0 & 0 & 0 & 4.46 \times 10^{-2} \end{bmatrix}$$

$$\mathbf{K}_{D,f} = \begin{bmatrix} 5.111 \times 10^{-3} & 0 & 0 & 0 \\ 0 & 5.575 \times 10^{-3} & 0 & 0 \\ 0 & 0 & 5.575 \times 10^{-3} & 0 \\ 0 & 0 & 0 & 4.17 \times 10^{-2} \end{bmatrix}$$

$$K_{P,xy} = 2.644 \times 10^{-3}$$

$$K_{I,xy} = 1.583 \times 10^{-5}$$

$$K_{D,xy} = 4.037 \times 10^{-2}$$

6.6.3 COMPARISON OF HEIGHT RESPONSE

The response of the quadrotor to a step input in height is compared for PID and NDI controllers. Figure 6.21 demonstrates the difference in both output and input between the two strategies. Despite being derived from the Level 3 model, the NDI controller handles the additional dynamics and non-linearities

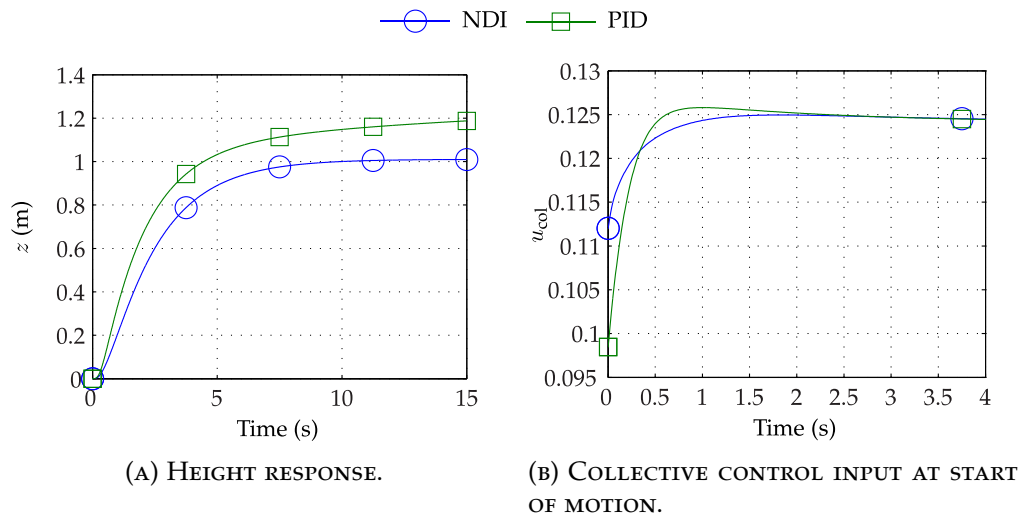


FIGURE 6.21: COMPARISON OF NDI AND PID CONTROLLERS IN HEIGHT RESPONSE AND CORRESPONDING PSEUDO-INPUT.

of the Level 5 model with zero oscillation and negligible steady-state error. Conversely, while the PID controller demonstrated zero steady-state error during tuning on the Level 4 model, an error is readily apparent in the Level 5 height response.

This can be attributed to the non-linear rotor model of the Level 5 model and the increased control effort required by the PID controller versus the NDI algorithm. The steady-state error could be reduced by increasing the integral action in the PID controller, at the cost of increasing overshoot in the response. The NDI controller also demonstrates a reduced control effort in comparison to the PID controller.

6.6.4 COMPARISON OF YAW RESPONSE

The response of the quadrotor to a step input in yaw displacement is compared for both controllers. Figure 6.22 demonstrates the difference in output and input between both strategies. Despite exhibiting a faster rise time than NDI-controlled system, the PID-controlled yaw response is shown to be more stable by the yaw pseudo-input history. Testing of the Level 4 yaw model demonstrated an oscillatory but stable open-loop response. While the NDI controller is designed to cancel out non-linearities in the system, the PID controller is not. The PID controller is therefore capable of utilising positive non-linearities and dynamics in the system, which the Levels 4 and 5 yaw response may represent.

Ultimately, both controllers produce stable yaw responses, reaching the steady-state at the desired settling time. The PID controller is shown to demand significantly less control action.

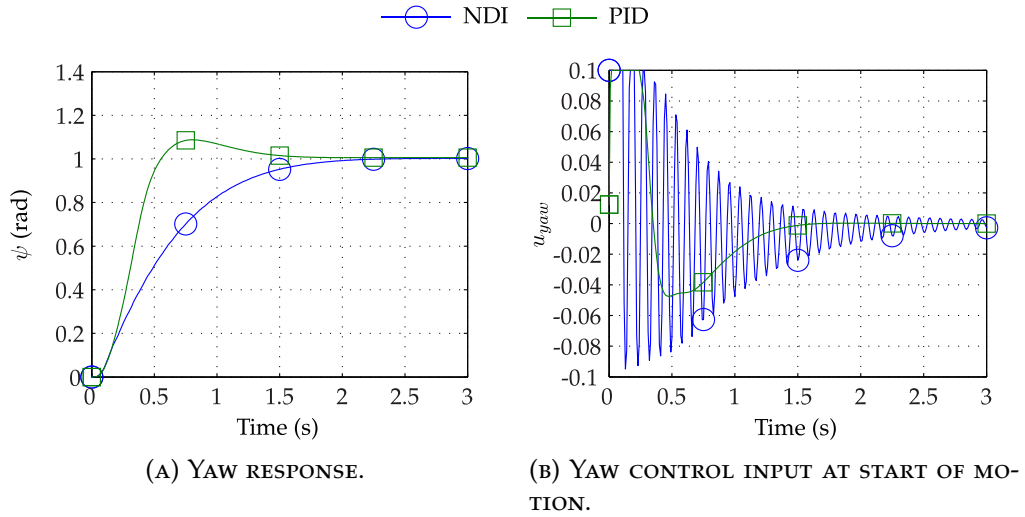


FIGURE 6.22: COMPARISON OF NDI AND PID CONTROLLERS IN YAW RESPONSE AND CORRESPONDING PSEUDO-INPUT.

6.6.5 COMPARISON OF HORIZONTAL POSITION RESPONSE

The response of the quadrotor to a step input in horizontal position is compared for both controllers. Figure 6.23 demonstrates the difference in output and input for each strategy. Simulation testing of the PID horizontal position controller highlighted the need for a first-order filter in the step command. Without the filter, input signals generated by the PID controller far exceeded the actuator limits of the system and produced highly unpredictable behaviour.

With the filter in place, the PID controller is shown to demand less control effort than the NDI controller, but produces an inferior response in the position.

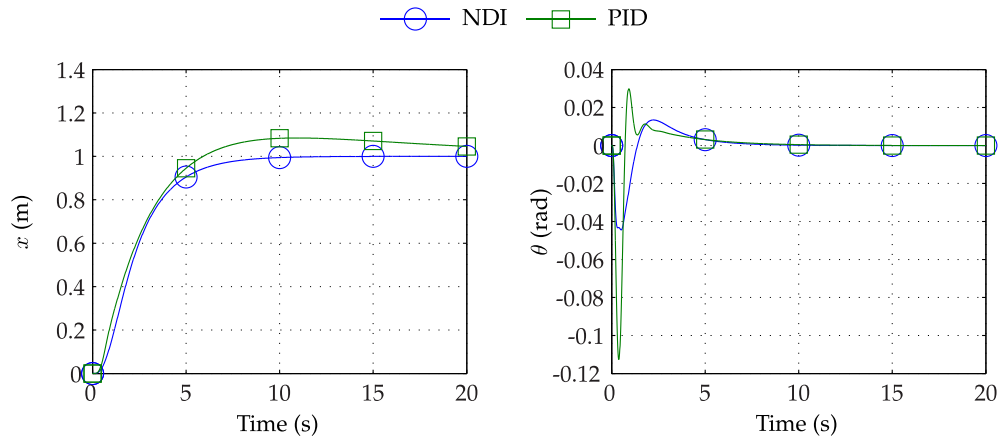
6.6.6 COMPARISON OF TRAJECTORY FOLLOWING

Each controller is applied to the Level 5 quadrotor model and commanded to follow a trajectory specified by the polynomials

$$\begin{aligned}
 x_d(t) &= 0.00296t^3 - (2.963 \times 10^{-4})t^4 + (7.901 \times 10^{-6})t^5 \\
 y_d(t) &= 0 \\
 x_d(t) &= -0.00296t^3 + (2.963 \times 10^{-4})t^4 - (7.901 \times 10^{-6})t^5 \\
 \psi_d(t) &= 0
 \end{aligned} \tag{6.73}$$

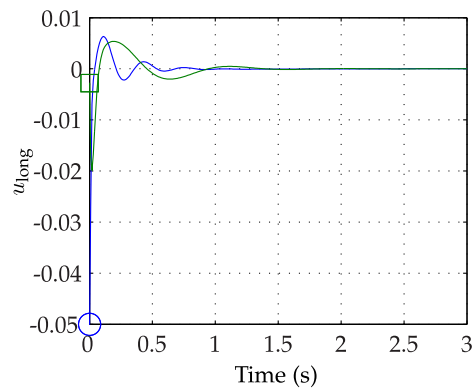
which takes the aircraft from $\mathbf{r} = [0, 0, 0]^T$ to $\mathbf{r} = [1, 0 - 1]^T$ via a smooth path. As Figure 6.24 shows, the NDI controller tracks the commanded path perfectly as expected, while the PID controller is shown to have a small initial error which increases near the end of the trajectory.

Figure 6.25 compares the relevant input and output histories of the quadrotor for each controller during the trajectory following. Again, the NDI controller is shown to demand more control effort than the PID controller, but with the



(A) HORIZONTAL POSITION RESPONSE.

(B) ATTITUDE RESPONSE.



(C) LONGITUDINAL CONTROL INPUT AT START OF MOTION.

FIGURE 6.23: COMPARISON OF NDI AND PID CONTROLLERS IN HORIZONTAL POSITION RESPONSE AND CORRESPONDING PSEUDO-INPUT.

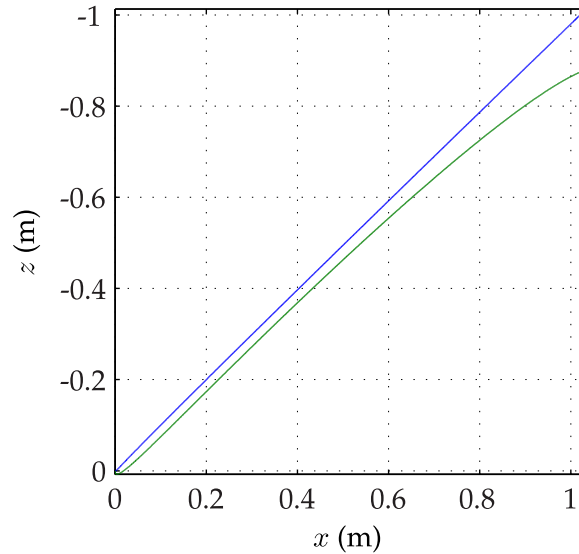


FIGURE 6.24: COMPARISON OF TRAJECTORIES FOLLOWED BY QUADROTORS UNDER NDI AND PID CONTROL.

advantage of superior trajectory-tracking. In both systems, the control signals are well within the measured actuator limits of the system.

6.6.7 DISCUSSION OF RESULTS

The primary benefit of PID control, the ability to govern a system with little-to-no information about the system properties, is rendered redundant here by comprehensive models of system processes. While the differences between the Level 3 and Level 5 quadrotor models might have resulted in poor performance by the Level 3 NDI controller, it has been demonstrated that this is not the case for the chosen controller bandwidths. PID control may provide greater benefits when introducing further phenomena into the quadrotor model, which the NDI controller may not have accounted for.

6.7 DISCUSSION AND CONCLUSIONS

6.7.1 DISCUSSION OF CONTROLLER DESIGN AND RESULTS

The results presented in this chapter demonstrate a potential benefit of a multi-resolution model of a system. The models described by Levels 1 and 2 of the model family are typical of those used in controller design, while use of the Level 3 model allows the rotor dynamics to be compensated for by the controller. The controllers derived from these models are designed such that they ensure a stable closed-loop response, with Lyapunov's second method verifying this. However, application of the derived controllers to the models described by Levels 4 and 5 demonstrates that the closed-loop system becomes unstable as the gains of the controller are increased. It is thus demonstrated that, while

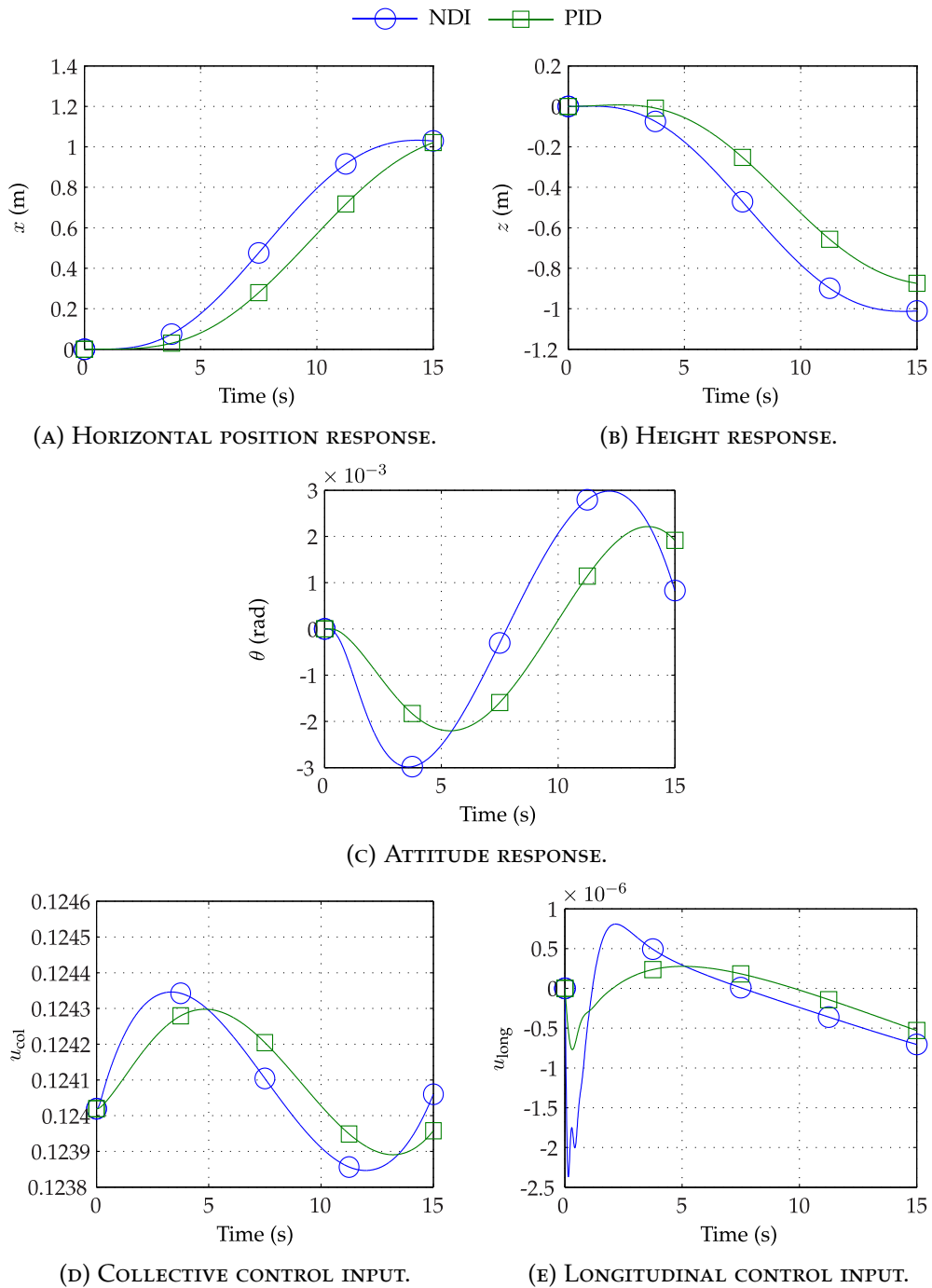


FIGURE 6.25: COMPARISON OF NDI AND PID CONTROLLERS IN FOLLOWING A TRAJECTORY, DEMONSTRATING THE DIFFERENCES IN INPUT AND OUTPUT RESPONSES.

a controller ensures a stable response in theory and simulation, this may not be the case in a higher resolution model or, crucially, in practice. A stiff controller such as that characterised by high values of τ_s is shown to provide a stable response for every quadrotor system in the model family. Increasing the responsiveness of the controller is shown to result in instabilities caused by dynamics or non-linearities which are not considered at lower resolutions. Thus, while it is possible to implement stiff controllers in practice with relatively low risk, the multi-resolution model demonstrates its worth in designing more responsive controllers.

6.7.2 CONCLUSIONS

Dynamic inversion is a popular method for in designing non-linear controllers for the quadrotor platform. Use of this technique requires an accurate model of the system which is then inverted and placed in closed loop with the plant. It has been demonstrated that differences between the inverted model and plant can result in undesirable performance, particularly when a high-bandwidth response is desired. A multi-resolution model aids in the design of such controllers by allowing a dynamic inversion controller derived from a low-resolution model to be tested on a succession of higher-resolution models to better determine its potential performance in reality.

CHAPTER 7

INVESTIGATING THE EFFECTS OF MODEL RESOLUTION ON OPTIMISATION OF TRAJECTORIES FOR WIRELESS POWER TRANSMISSION

The literature review described in Chapter 2 highlighted the recent advancements in Wireless Power Transmission (WPT), or *power beaming*, technology. The technology used to convert electrical energy to electromagnetic energy and vice-versa has improved sufficiently such that wireless powering of unmanned aircraft or recharging of onboard power sources is now feasible, as demonstrated by Achteik et al. (2011). The significant amount of power in the transmitting beam is a cause for concern, although measures to address this are under consideration, as described by Nugent et al. (2011). While a cut-off switch for the laser beam is essential, additional safety concerns may be minimised by ensuring close co-operation between the energy-transmitting ground station and the receiving aircraft.

This chapter presents a case study of one approach to improving the safety and efficiency of wireless power transmission. To ensure that the laser beam always terminates at the intended destination – a photovoltaic sensor on the receiving aircraft – the aircraft trajectory may be optimised to better complement the performance of the tracking and beam steering system which projects the laser. The aims of this study are twofold. First, some insight may be gained into the required performance of an actuated Energy Transmission System (ETS). Second, the effect of model resolution on the solutions of the trajectory optimisation may be investigated, allowing further discussion of the benefits of multi-resolution modelling.

The SiFRe simulation engine's multi-agent functionality is used to model a quadrotor aircraft ETS working in co-operation in a wireless power transmission operation. The quadrotor trajectory is optimised such that the laser spot is always on-target with minimal overspill. The optimisation is performed for each level in the quadrotor model family, with an appropriate controller to

provide accurate trajectory following. The optimisation results are then compared for each level. These comparisons then permit discussion of the impact of model resolution on the results of trajectory optimisation.

7.1 DESCRIPTION OF WIRELESS POWER TRANSMISSION SCENARIO AND THE ENERGY TRANSMISSION SYSTEM

A wireless power transmission and its associated systems can take a number of forms. The experiment detailed by Achteik et al. (2011) employed a near-stationary quadrotor and a fixed laser emitter, with beam steering achieved through use of an actuated mirror. This describes one possible scenario, with the obvious limitation that the quadrotor movement is restricted. The scenario and energy transmission apparatus considered in this case study differ from the aforementioned experiment.

As described in Nugent and Kare (2011) and highlighted in Chapter 2, a wireless power transmission operation can take two forms. The first involves near-continual charging of the UAV, with only brief interruptions in transmission. The aircraft would therefore only require a small energy reserve onboard – an ideal solution for the weight-restricted quadrotor. In this case, the aircraft would be required to continue to its mission while being charged, due to the limited capability for operating on an isolated power supply. The second form involves periodic charging of the UAV. In this case, the aircraft would be able to utilise its own power supply to pursue its mission, returning to the vicinity of the ETS for charging. Alternatively, it could perform its mission for the duration of the flight and be charged periodically by the ETS. This latter scenario has the benefit of allowing the ETS to service multiple aircraft in sequence.

The scenario considered in this study is the charging stage of the latter case, where the quadrotor enters the charging volume of the ETS and receives power while following a flight path which leads it back out of the volume to return to its mission. During this stage, the ETS is required to transmit the laser beam onto the photovoltaic sensor mounted on the underside of the quadrotor with sufficient precision. As the quadrotor and ETS are intended to co-operate in the power transfer, the ETS controller is informed of the quadrotor's relative position, allowing it to seek out the quadrotor as it enters the charging volume. An optical sensor mounted on the actuated component of the ETS allows the photovoltaic sensor, identified by a ring of LEDs, to be tracked. Upon visually acquiring the LEDs, the ETS controller acts to track the centroid of the LED positions in camera space, which corresponds to the geometric centre of the sensor. The laser beam is then projected parallel to the sightline of the camera by an emitter also located on the actuated component of the ETS. Assuming minimal distance between the laser beam and camera sightline, the optical sensor then identifies the location of the laser spot on the sensor and the ETS controller acts to centre it on the photovoltaic sensor.

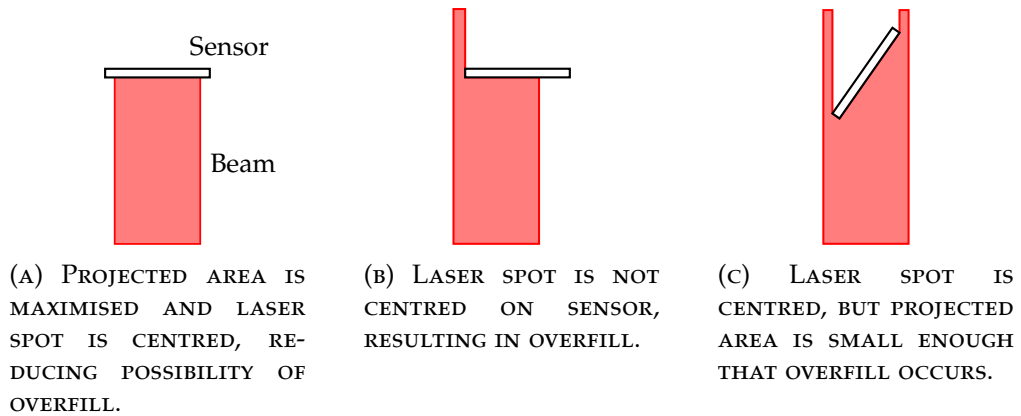


FIGURE 7.1: POOR BEAM STEERING OR INSUFFICIENT PROJECTED SENSOR AREA CAN RESULT IN OVERFILL OF THE SENSOR AND POSE A SAFETY HAZARD.

An energy transmission system of sufficiently high bandwidth would therefore be able to seek, acquire and track the receiving sensor in a short period of time after the quadrotor enters the charging volume. There is, however, the possibility of the beam overflowing or missing the sensor due to either lag in the tracking and beam steering response or the orientation of the sensor with respect to the beam vector. Figure 7.1 demonstrates how an incoming laser beam may *overflow* the sensor due to steering errors or a large angle of incidence. There are a number of reasons the beam might overflow the sensor in both cases. First, the distance between sensor and beam source may be sufficiently large that the beam diameter approaches the diameter of the sensor. Any small error in centring the laser spot then risks overflowing the sensor. Similarly, a large angle of incidence reduces the projected area of the sensor and results in overflow. Second, at both short and long range, noise or *jitter* in the tracking and beam steering (Kim, Nagashima, and Agrawal, 2011) can result in noise in the laser spot position on the receiving sensor. Ensuring it is nominally centred and that the projected sensor surface area is maximised then reduces the likelihood of missing or overflowing the sensor.

While time could be committed to reducing jitter and other errors in the ETS control system, it is possible to optimise the trajectory of the quadrotor such that it works in co-operation with the ETS to minimise any errors. This results in improved operational safety and increases the efficiency of the transmission. As the quadrotor follows a trajectory which takes it in and then back out of the charging volume, its yaw controller ensures that the photovoltaic sensor surface normal is aligned with the laser beam in the horizontal plane, maximising the projected surface area.

The flight dynamics of the quadrotor then impact the performance of the power transmission in the following ways. First, the ability of the ETS to track the quadrotor is dependent on the bandwidth and performance of the closed-loop ETS response and the relative acceleration of the quadrotor. The trajectory followed by the quadrotor must therefore be one which allows the ETS to

accurately centre the laser spot on the photosensitive sensor throughout the transmission. Second, as the quadrotor position and attitude dynamics are strongly coupled in closed loop, the attitude of the quadrotor along the trajectory is dependent on both the translational acceleration of the vehicle and the curvature of the trajectory. The angle of incidence of the sensor normal with the laser beam is therefore related to the defined trajectory and the quadrotor tracking performance in closed loop. Additionally, actuator limits restrict the bandwidth of the quadrotor yaw controller. Optimisation of the trajectory then ensures minimal phase difference between the yaw command and response.

7.2 ADDITIONAL GEOMETRY AND FRAME OF REFERENCE

Recall the kinematics and frames of reference described in Chapter 3. These definitions are extended to include the energy transmission system and its subsystems, shown in Figure 7.2. Assigning the subscript Q to properties relating to the quadrotor, the quadrotor is stated to have position $\mathbf{r}_Q \in \mathbb{R}^3$ and attitude $\boldsymbol{\eta}_Q \in \mathbb{R}^3$ in the World frame \mathcal{W} . The geometric centre of the photosensitive diode, denoted by S, has fixed position $\mathbf{r}_{S/Q}^{\mathcal{B}} \in \mathbb{R}^3$ with respect to the quadrotor. The orientation of the sensor is described by the surface normal $\mathbf{n}_S^{\mathcal{B}} \in \mathbb{R}^3$ and is also fixed in \mathcal{B} . The sensor position and surface normal are therefore described in the World frame by

$$\begin{aligned}\mathbf{r}_S &= \mathbf{r}_Q + \mathbf{R}_B^{\mathcal{W}} \mathbf{r}_{S/Q}^{\mathcal{B}} \\ \hat{\mathbf{n}}_S &= \mathbf{R}_B^{\mathcal{W}} \hat{\mathbf{n}}_S^{\mathcal{B}}\end{aligned}$$

The centre of rotation of the energy transmission system, denoted by E, has fixed position $\mathbf{r}_E \in \mathbb{R}^3$ in \mathcal{W} . The orientation of the ETS's actuated platform is described with respect to \mathcal{W} by $\boldsymbol{\eta}_E = [\theta_E, \psi_E]^T \in \mathbb{R}^2$. Defining a frame of reference \mathcal{E} fixed on this platform as shown in Figure 7.3, the orientation of \mathcal{W} may be described in \mathcal{E} by

$$\mathbf{R}_{\mathcal{W}}^{\mathcal{E}} = \begin{bmatrix} \cos \theta_E & 0 & -\sin \theta_E \\ 0 & 1 & 0 \\ \sin \theta_E & 0 & \cos \theta_E \end{bmatrix} \begin{bmatrix} \cos \psi_E & \sin \psi_E & 0 \\ -\sin \psi_E & \cos \psi_E & 0 \\ 0 & 0 & 1 \end{bmatrix}$$

which provides the direction cosine matrix describing \mathcal{W} in \mathcal{E}

$$\mathbf{R}_{\mathcal{W}}^{\mathcal{E}} = \begin{bmatrix} \cos \theta_E \cos \psi_E & \cos \theta_E \sin \psi_E & -\sin \theta_E \\ -\sin \psi_E & \cos \psi_E & 0 \\ \sin \theta_E \cos \psi_E & \sin \theta_E \sin \psi_E & \cos \theta_E \end{bmatrix} \quad (7.1)$$

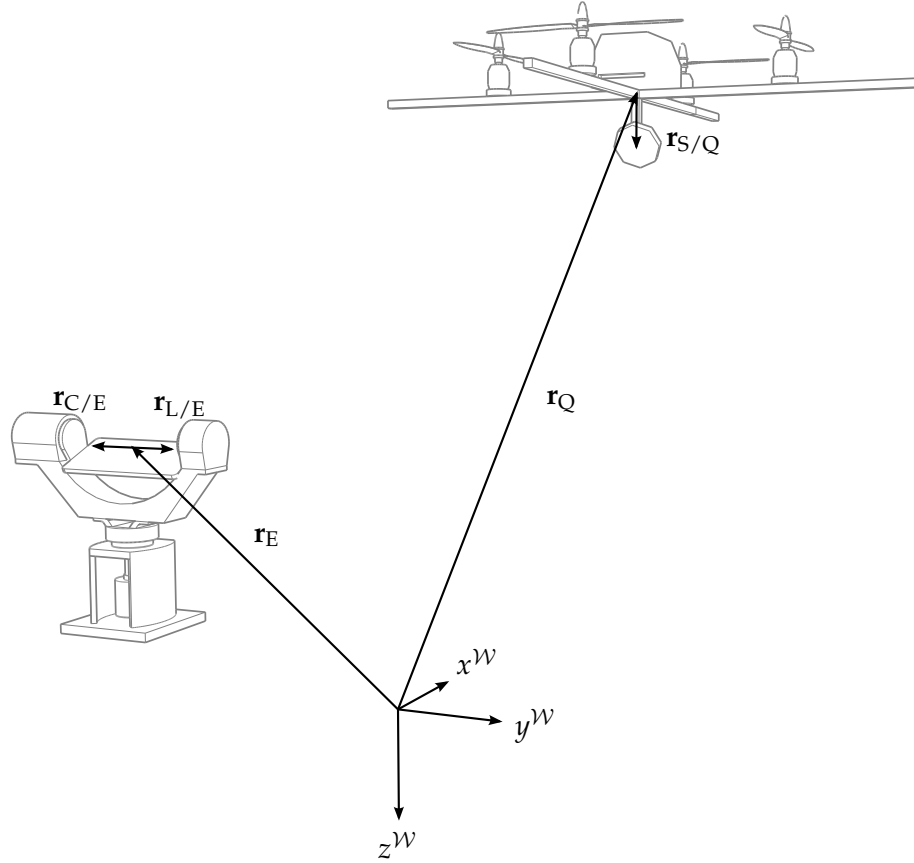


FIGURE 7.2: GEOMETRY OF QUADROTOR AND ETS AGENTS WITH RESPECT TO INERTIAL FRAME \mathcal{W} .

The reverse transformation then describes \mathcal{E} in \mathcal{W} by

$$\mathbf{R}_{\mathcal{E}}^{\mathcal{W}} = \left(\mathbf{R}_{\mathcal{W}}^{\mathcal{E}} \right)^T = \begin{bmatrix} \cos \theta_E \cos \psi_E & -\sin \psi_E & \sin \theta_E \sin \psi_E \\ \cos \theta_E \sin \psi_E & \cos \psi_E & \sin \theta_E \cos \psi_E \\ -\sin \theta_E & 0 & \cos \theta_E \end{bmatrix} \quad (7.2)$$

The ETS's optical camera, denoted by C, and laser emitter, denoted by L, are fixed on the actuated platform at $\mathbf{r}_{C/E}^{\mathcal{E}} \in \mathbb{R}^3$ and $\mathbf{r}_{L/E}^{\mathcal{E}} \in \mathbb{R}^3$ respectively. Their positions are therefore described in \mathcal{W} by

$$\begin{aligned} \mathbf{r}_C &= \mathbf{r}_E + \mathbf{R}_{\mathcal{E}}^{\mathcal{W}} \mathbf{r}_{C/E}^{\mathcal{E}} \\ \mathbf{r}_L &= \mathbf{r}_E + \mathbf{R}_{\mathcal{E}}^{\mathcal{W}} \mathbf{r}_{L/E}^{\mathcal{E}} \end{aligned}$$

The unit direction vectors of the camera line of sight and laser beam are fixed in \mathcal{E} at $\hat{\mathbf{n}}_C^{\mathcal{E}}$ and $\hat{\mathbf{n}}_L^{\mathcal{E}}$, respectively. They are then described in \mathcal{W} by

$$\begin{aligned} \hat{\mathbf{n}}_C &= \mathbf{R}_{\mathcal{E}}^{\mathcal{W}} \hat{\mathbf{n}}_C^{\mathcal{E}} \\ \hat{\mathbf{n}}_L &= \mathbf{R}_{\mathcal{E}}^{\mathcal{W}} \hat{\mathbf{n}}_L^{\mathcal{E}} \end{aligned}$$

These definitions are employed in describing the dynamic and geometric

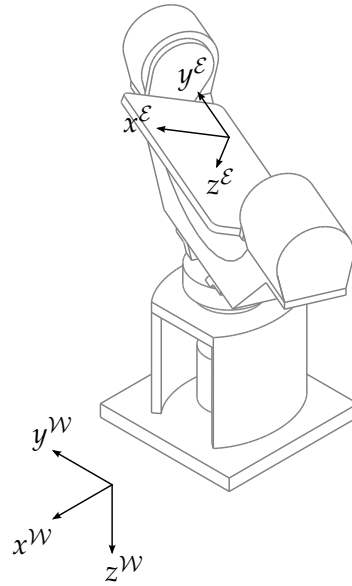


FIGURE 7.3: AXES DEFINITION OF REFERENCE FRAME \mathcal{E} , FIXED ON THE ENERGY TRANSMISSION SYSTEM'S ACTUATED PLATFORM.

models of the ETS and its interactions with the quadrotor.

7.3 MODELLING AND CONTROL OF AN ENERGY TRANSMISSION SYSTEM

The wireless power transmission simulation requires an ETS agent to interact with the quadrotor agent. This agent is comprised of a dynamic model describing the response of the actuated platform, an optical sensor model and a geometry model describing the interaction of the laser beam with the photovoltaic sensor on the quadrotor.

7.3.1 ENERGY TRANSMISSION SYSTEM DESCRIPTION

The ETS model is based on a system built at the University of Glasgow, shown in Figure The ETS consists of three components: a camera which provides visual feedback to the system controller for target tracking; a low-power visible-light laser for simulating the laser pointing accuracy and stabilisation of the system; and an actuated platform which provides two degrees of rotational freedom. The camera and laser emitter are positioned on the platform and aligned such that the camera sightline and laser beam are parallel. Two brushless motors supply the torque which drives the panning and tilting motion of the platform, allowing the camera sight and laser beam to be directed as required. Each motor has an encoder which measures its precise rotational displacement. The motor inputs are determined by a controller which is informed by feedback from the camera.

A photosensitive diode mounted on the underside of the quadrotor works in tandem with the ETS by receiving the power transmitted by the laser. The



FIGURE 7.4: PARTIALLY-CONSTRUCTED ENERGY TRANSFER SYSTEM, LACKING ONLY CAMERA AND LASER EMITTER.

diode is slightly inclined, to favour a laser beam incoming from a lower altitude. A ring of LEDs around the sensor provides increased visibility to the ETS camera. Power received by the diode is transferred electrically to the quadrotor batteries.

7.3.2 SYSTEM MODEL

ACTUATOR DYNAMICS

The rotational displacement of the actuated platform is driven by two brushless motors. The dynamics of the system are described by the first-order model

$$\dot{\eta}_E = \frac{1}{\tau} (\mathbf{u} - \eta_E) \quad (7.3)$$

where the inputs \mathbf{u} to the system are the rotational set-points

$$\mathbf{u} = \eta_{E,d} = [\psi_{E,d}, \theta_{E,d}]^T \quad (7.4)$$

The time constant τ of the model is determined through experimentation with the reference system.

CAMERA MODEL

A simple camera model is employed to describe the feedback of visual data to the ETS tracking control system. The camera is designed to sense the LEDs positioned around the receiving sensor on the quadrotor. The relative positions of the diodes in inertial Euclidean 3-space \mathbb{R}^3 into the camera Euclidean 2-space \mathbb{R}^2 using the pinhole camera model described by Hartley and Zisserman (2003).

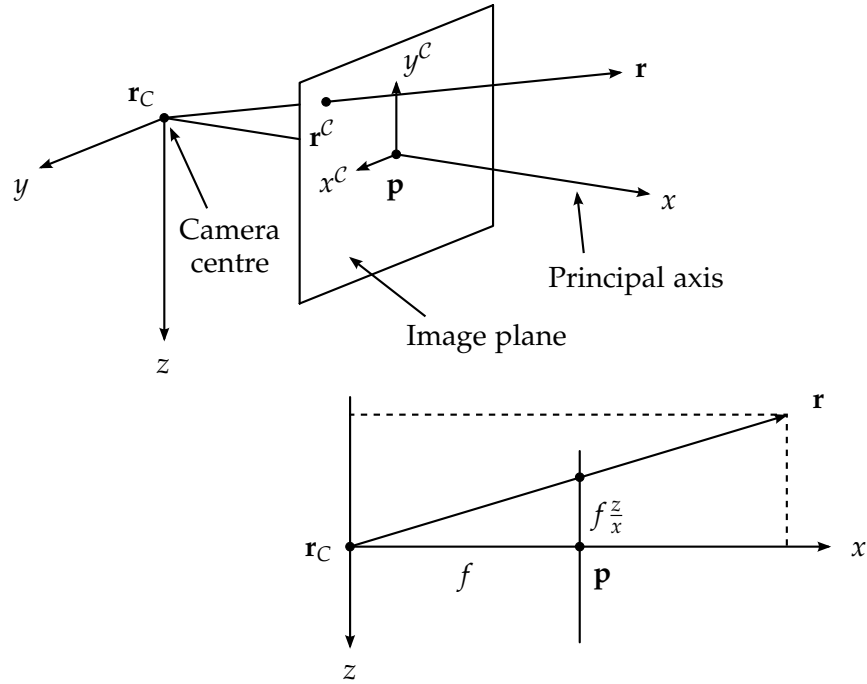


FIGURE 7.5: GEOMETRY OF THE PINHOLE CAMERA MODEL. THE CAMERA CENTRE \mathbf{r}_C IS AT THE CENTRE OF THE COORDINATE SYSTEM. THE COORDINATES OF A POINT WITH POSITION \mathbf{r} IN EUCLIDEAN 3-SPACE ARE MAPPED TO 2-SPACE BY CONSIDERING THE INTERSECTION OF THE POINT WITH THE IMAGE PLANE, FIXED AT THE PRINCIPLE POINT \mathbf{p} ALONG THE PRINCIPLE AXIS x (HARTLEY AND ZISSERMAN, 2003).

A point P , fixed in the quadrotor body-frame \mathcal{B} , has position in \mathcal{W} described by

$$\mathbf{r}_P = \mathbf{r}_Q + \mathbf{R}_B^{\mathcal{W}} \mathbf{r}_{P/Q}^{\mathcal{B}}$$

It is then described relative to the camera position \mathbf{r}_C in \mathcal{E} by

$$\begin{aligned} \mathbf{r}_{P/C}^{\mathcal{E}} &= \mathbf{R}_W^{\mathcal{E}} (\mathbf{r}_P - \mathbf{r}_C) \\ &= \mathbf{R}_W^{\mathcal{E}} \left(\mathbf{r}_Q - \mathbf{r}_E + \mathbf{R}_B^{\mathcal{W}} \mathbf{r}_{P/Q}^{\mathcal{B}} \right) - \mathbf{r}_{C/E}^{\mathcal{E}} \end{aligned}$$

If $\mathbf{r}_{P/C}^{\mathcal{E}} = [x_{P/C}, y_{P/C}, z_{P/C}]^T$ describes the position of P in *object space*, the position in *camera space* is described by

$$\begin{aligned} x_P^c &= f \frac{y_{P/C}}{x_{P/C}} \\ y_P^c &= -f \frac{z_{P/C}}{x_{P/C}} \end{aligned} \tag{7.5}$$

The camera has field of view λ_C and aspect ratio A . For P to be visible to

the camera, it must therefore satisfy the constraints

$$\begin{aligned} -f \tan \lambda_C &\leq x^C \leq f \tan \lambda_C \\ -Af \tan \lambda_C &\leq y^C \leq Af \tan \lambda_C \end{aligned}$$

LASER GEOMETRY MODEL

The laser beam is modelled as a beam of finite length, originating at the point describing the position of the laser emitter \mathbf{r}_L and terminating at the point \mathbf{r}_{LS} , where it intersects the surface plane of the photovoltaic sensor on the quadrotor. The intersection point is determined by first describing the laser beam as a line of length l , with the equation

$$\mathbf{p} = l \hat{\mathbf{n}}_L + \mathbf{r}_L, \quad l \in \mathbb{R} \quad (7.6)$$

where \mathbf{p} is any point along the line. The surface of the photosensitive diode is described by the plane

$$(\mathbf{p} - \mathbf{r}_S) \cdot \hat{\mathbf{n}}_S = 0 \quad (7.7)$$

Equating (7.6) and (7.7) provides the length of the laser beam, subject to conditions imposed by the finite extent of the photodiode surface plane

$$l = \begin{cases} \frac{(\mathbf{r}_S - \mathbf{r}_L) \cdot \hat{\mathbf{n}}_S}{\hat{\mathbf{n}}_L \cdot \hat{\mathbf{n}}_S} & \text{if } \|\mathbf{p} - \mathbf{r}_S\| \leq r_S \\ \infty & \text{if } \|\mathbf{p} - \mathbf{r}_S\| > r_S \end{cases} \quad (7.8)$$

The laser termination point is then given by

$$\mathbf{r}_{LS} = l \hat{\mathbf{n}}_L + \mathbf{r}_L \quad (7.9)$$

7.3.3 TRACKING CONTROLLER

The ETS is designed to search for, acquire and track the photosensitive sensor mounted on the quadrotor. The control system has three modes:

1. Seek – sightline control is used to direct the principle axis of the camera towards the quadrotor using the transmitted position of the quadrotor.
2. LED tracking – visual feedback provides the coordinates of the LEDs in the camera space. The controller then acts to center the centroid of the LEDs, and therefore the sensor, in the camera frame.
3. Laser spot tracking – as the sensor is centred in the camera frame, the laser beam is emitted onto the sensor surface at a slight offset. Visual feedback from the camera then allows the tracking controller to position the laser spot at the centre of the sensor.

SEEKING MODE

The position of the quadrotor in inertial space \mathbf{r}_Q is transmitted to the ETS control system. In directing the camera sight towards the quadrotor position, the LEDs identifying the photosensitive sensor become visible, allowing the visual tracking controller to take over.

The commands to the actuating motors are the desired rotational displacements of the ETS platform. These are provided by the geometric relationships

$$\tan \psi_{E,d} = \frac{y_Q - y_E}{x_Q - x_E} \quad (7.10)$$

$$\tan \theta_{E,d} = -\frac{z_Q - z_E}{\sqrt{(x_Q - x_E)^2 + (y_Q - y_E)^2}} \quad (7.11)$$

LED TRACKING MODE

The LEDs are detected in the camera space and their coordinates transmitted to the tracking controller. If an LED i has position $\mathbf{r}_i^C \in \mathbb{R}^2$ in camera space, the centroid of N_S LEDs, all visible to the camera, has position

$$\mathbf{r}_{\text{centroid}}^C = \frac{1}{N_S} \sum_{i=1}^{N_S} \mathbf{r}_i^C$$

Noting the model of the ETS as described by Equation (7.3), a proportional-integral (PI) controller may be specified, with the form

$$\mathbf{u} = \tau \left(K_p \mathbf{e} + K_i \frac{1}{s} \mathbf{e} \right) + \boldsymbol{\eta}_E \quad (7.12)$$

The centre of the camera image has coordinates $\mathbf{r}_0^C = [0 \ 0]^T$. The feedback error \mathbf{e} is then the coordinates of the target point in the camera space. Using the small approximation, the feedback error may be described by

$$\mathbf{e} = \mathbf{r}_{\text{centroid}}^C \approx f \begin{bmatrix} \theta_{E,d} - \theta_E \\ \psi_{E,d} - \psi_E \end{bmatrix} \quad (7.13)$$

The closed-loop response may therefore be approximated by the function

$$\frac{\Psi_E(s)}{\Psi_{E,d}(s)} = \frac{\Theta_E(s)}{\Theta_{E,d}(s)} = \frac{K_p f s + K_i f}{s^2 + K_p f s + K_i f} \quad (7.14)$$

and can be tuned by relating the controller gains to desired response characteristics

$$K_p = \frac{2\zeta\omega_n}{f}$$

$$K_i = \frac{\omega_n^2}{f}$$

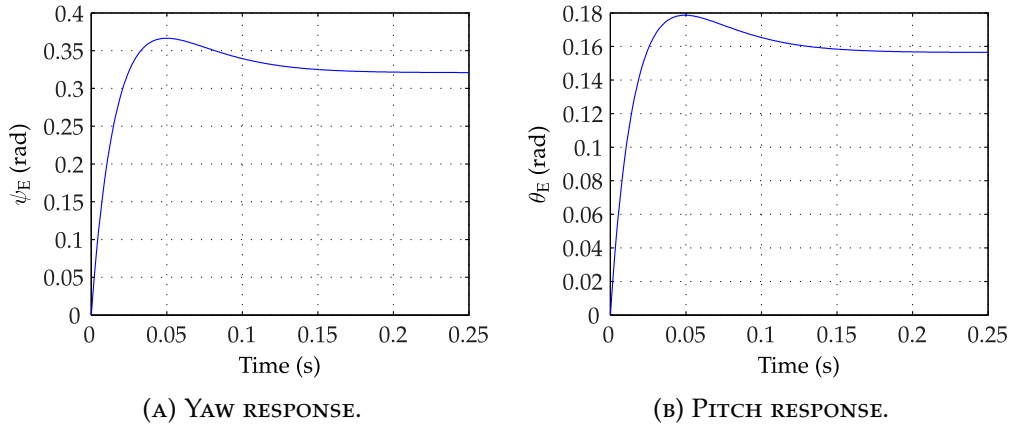


FIGURE 7.6: ETS ROTATIONAL RESPONSE WITH VISUAL FEEDBACK FOR TARGET INITIALLY AT $\mathbf{r}^c = [200, 100]^T$.

LASER SPOT TRACKING MODE

Upon centring the receiving sensor in camera space, the laser beam is emitted and the camera detects the laser spot on the sensor surface. The controller then acts to centre the laser spot on the sensor, using the control law described by Equation (7.12), with the adjusted feedback error

$$\mathbf{e} = \mathbf{r}_{\text{centroid}}^c - \mathbf{r}_L^c \quad (7.15)$$

where \mathbf{r}_L^c is the position of the laser space in camera space.

ETS TRACKING RESPONSE

The response of the ETS to a visual input is required to be fast enough to track a fast-moving object such as the quadrotor. The linear relationship described by Equation (7.14) is used to tune the controller and is compared to the true system response in Figure 7.6.

7.4 TRAJECTORY DEFINITION AND QUADROTOR CONTROLLER REVISION

An example trajectory was used in Chapter 6 to demonstrate the stability and performance of the quadrotor controllers. This trajectory was defined using the approach described by Cowling et al. (2007). This approach is again used to define smooth trajectories for the quadrotor to follow during wireless power transmission. There are two primary benefits to this approach. First, a smooth trajectory permits use of a responsive controller while minimising the possibility of the actuator limits being reached. This is a concern in practical flight, where the actuator limits represent a non-linear discontinuity and can result in unpredictable behaviour or a limit cycle when reached. Second, the trajectory is defined by a number of parameters. These may be varied to optimise the

path for the wireless power transmission. An additional benefit is the versatility of the approach, allowing the generation of smooth paths around obstacles or through multiple waypoints, leaving scope for further investigations in trajectory optimisation.

7.4.1 SMOOTH TRAJECTORY DEFINITION WITH POLYNOMIALS

Recall the tracking outputs $\mathbf{y}_t = [x, y, z, \psi]^T$ of the quadrotor system. For any output in \mathbf{y}_t , boundary conditions for the n th derivative are chosen such that a polynomial of order $m = 2n - 1$ is obtained. Six boundary conditions for a single output are defined: the displacement, velocity and acceleration at both the beginning and end of the trajectory. A polynomial of order $m = 5$ is thus obtained.

The desired trajectory of x is obtained by first expressing the desired acceleration \ddot{x} by the third-order polynomial

$$\ddot{x}_d(t) = a_2 + a_3t + a_4t^2 + a_5t^3 = \sum_{k=2}^5 a_k t^{k-2} \quad (7.16)$$

The desired velocity of x is then found by integrating to obtain the 4th-order polynomial

$$\begin{aligned} \dot{x}_d(t) &= a_1 + a_2t + \frac{1}{2}a_3t^2 + \frac{1}{3}a_4t^3 + \frac{1}{4}a_5t^4 \\ &= \sum_{k=1}^5 \frac{1}{\max(1, k-1)} a_k t^{k-1} \end{aligned} \quad (7.17)$$

Finally, integrating again provides the desired position as a polynomial of order $m = 5$

$$\begin{aligned} x_d(t) &= a_0 + a_1t + \frac{1}{2}a_2t^2 + \frac{1}{6}a_3t^3 + \frac{1}{12}a_4t^4 + \frac{1}{20}a_5t^5 \\ &= \sum_{k=1}^5 \frac{1}{\max(1, k(k-1))} a_k t^k \end{aligned} \quad (7.18)$$

Denoting the time at the beginning of the trajectory t_0 , the n th derivative of x_d at t_0 is expressed by $x_d^{(n)}(t_0) = x_0^{(n)}$. Similarly, the time at the end of the trajectory is denoted t_f and the output denoted $x_d^{(n)}(t_f) = x_f^{(n)}$. The polynomials described by Equations (7.16), (7.17) and (7.18) are then evaluated at t_0 and t_f to provide the relationship

$$\begin{bmatrix} x_0 \\ \dot{x}_0 \\ \ddot{x}_0 \\ x_f \\ \dot{x}_f \\ \ddot{x}_f \end{bmatrix} = \begin{bmatrix} 1 & t_0 & \frac{1}{2}t_0^2 & \frac{1}{6}t_0^3 & \frac{1}{12}t_0^4 & \frac{1}{20}t_0^5 \\ 0 & 1 & t_0 & \frac{1}{2}t_0^2 & \frac{1}{3}t_0^3 & \frac{1}{4}t_0^4 \\ 0 & 0 & 1 & t_0 & t_0^2 & t_0^3 \\ 1 & t_f & \frac{1}{2}t_f^2 & \frac{1}{6}t_f^3 & \frac{1}{12}t_f^4 & \frac{1}{20}t_f^5 \\ 0 & 1 & t_f & \frac{1}{2}t_f^2 & \frac{1}{3}t_f^3 & \frac{1}{4}t_f^4 \\ 0 & 0 & 1 & t_f & t_f^2 & t_f^3 \end{bmatrix} \begin{bmatrix} a_0 \\ a_1 \\ a_2 \\ a_3 \\ a_4 \\ a_5 \end{bmatrix} \quad (7.19)$$

The desired trajectories in y and z are constructed similarly, while the yaw

trajectory is determined by a line-of-sight controller. The three-dimensional trajectory $\mathbf{r}_d(t) \in \mathbb{R}^3$ is therefore determined by selection of the parameters $\mathbf{r}_0, \dot{\mathbf{r}}_0, \ddot{\mathbf{r}}_0, \mathbf{r}_f, \dot{\mathbf{r}}_f, \ddot{\mathbf{r}}_f \in \mathbb{R}^3$.

7.4.2 CONTROLLER REVISION

To improve the tracking performance of the quadrotor controller, the general state feedback law described by Equation (6.12) is augmented with the desired velocity. The state feedback for the linearised height dynamics is then

$$\hat{u}_{\text{col}} = -\mathbf{K}_z \begin{bmatrix} z - z_d \\ \dot{z} - \dot{z}_d \\ \ddot{z} \\ \vdots \\ z^{(v-1)} \end{bmatrix}$$

while feedbacks for horizontal position control are

$$\dot{x}_d = -\mathbf{K}_p \begin{bmatrix} x - x_d \\ \dot{x} - \dot{x}_d \end{bmatrix}, \quad \dot{y}_d = -\mathbf{K}_p \begin{bmatrix} y - y_d \\ \dot{y} - \dot{y}_d \end{bmatrix}$$

The yaw controller is augmented with a line-of-sight autopilot to ensure the photovoltaic sensor is directed towards the laser emitter throughout the transmission. The yaw command is then based on the multi-agent feedback

$$\psi_d = \arctan \frac{y_E - y_Q}{x_E - x_Q} \quad (7.20)$$

7.4.3 CONTROLLER PAIRING

To ensure that the quadrotor system described by each level of the model family is responsive while remaining stable, each model is paired with a suitable controller. Thus, for the remainder of this section, the term Level i refers to the closed-loop system formed by each model-controller pairing. Referring to the definitions of f_i and c_j provided in Chapters 5 and 6, these pairings are defined as

Level 1 Quadrotor model f_1 and controller c_1 .

Level 2 Quadrotor model f_2 and controller c_2 .

Level 3 Quadrotor model f_3 and controller c_3 .

Level 4 Quadrotor model f_4 and controller c_3 .

Level 5 Quadrotor model f_5 and controller c_3 .

The properties of each controller are chosen such that a consistent closed-loop response in each pairing is intended. These properties are detailed in Appendix

G. For the remainder of this chapter, the expression Level i , $i = \{1, 2, 3, 4, 5\}$, refers to either the closed-loop quadrotor system described above, or the multi-agent wireless power transmission simulation employing said level. The distinction between the two is made clear where appropriate.

7.5 PROBLEM DESCRIPTION AND OPTIMISATION SETTINGS

The optimisation problem is formulated as a function of three errors. The errors are described as functions of the relative geometry of the multi-agent system comprising the quadrotor and energy transmission system.

7.5.1 OPTIMISATION PROBLEM

The optimisation problem is formulated as a cost function Φ which is subject to the dynamics, controllers and trajectories of both agents. The problem is therefore posed as

$$\begin{aligned}
 & \min_{\mathbf{X} \subseteq \hat{\mathbf{X}} \in \mathbb{R}^{18}} \Phi(\mathbf{X}) \quad \text{for } t \in [t_0, t_f] \\
 & \text{subject to} \quad \dot{\mathbf{x}}_Q(t) = f_Q(\mathbf{x}_Q(t), \mathbf{r}_{Q,d}(t), \psi_{Q,d}(t)) \\
 & \quad \quad \quad \dot{\mathbf{x}}_E(t) = f_E(\mathbf{x}_E(t), \boldsymbol{\eta}_{E,d}(t)) \\
 & \quad \quad \quad \mathbf{r}_{Q,d}(t) = g_1(\hat{\mathbf{X}}, t_0, t_f) \\
 & \quad \quad \quad \psi_d(t) = g_2(\mathbf{x}_Q(t), \mathbf{x}_E(t)) \\
 & \quad \quad \quad \boldsymbol{\eta}_{E,d}(t) = g_3(\mathbf{x}_Q(t), \mathbf{x}_E(t))
 \end{aligned} \tag{7.21}$$

where f_Q describes the controlled quadrotor system at a given level, f_E the closed-loop ETS dynamics, g_1 and g_2 the relationships specifying the quadrotor output commands and g_3 the ETS displacement commands. The parameter set $\hat{\mathbf{X}}$ describes all possible boundary conditions of the commanded quadrotor trajectory $\mathbf{r}_{Q,d}$

$$\hat{\mathbf{X}} = \left[\mathbf{r}_0^T \quad \dot{\mathbf{r}}_0^T \quad \ddot{\mathbf{r}}_0^T \quad \mathbf{r}_f^T \quad \dot{\mathbf{r}}_f^T \quad \ddot{\mathbf{r}}_f^T \right]^T$$

of which the chosen variables \mathbf{X} are a subset describing any combination of elements from $\hat{\mathbf{X}}$. The cost function is then specified as

$$\Phi(\mathbf{X}) = \int_{t_0}^{t_f} (e_1(t) + e_2(t) + e_3(t)) dt \tag{7.22}$$

where the errors $e_1, e_2, e_3 \geq 0 \in \mathbb{R}$ are dependent on the relative geometry of the multi-agent system.

7.5.2 ERRORS

Each error e_i is scaled by a weight \mathbf{Q}_i and normalised with respect to a nominal maximum M_i .

PROJECTED AREA OF RECEIVING SENSOR

The laser beam intersects the plane of the sensor surface at angle of incidence γ . To ensure maximum projected sensor area in the direction of the laser beam, γ must be minimised. The line-of-sight autopilot employed by the quadrotor yaw controller acts to minimise this angle in the $x - y$ plane.

The angle of incidence is described by

$$\cos \gamma = -\hat{\mathbf{n}}_S, \hat{\mathbf{n}}_L \quad (7.23)$$

The angular error is therefore $(\cos \gamma_d - \cos \gamma)$, where $\gamma_d = 0$. This provides the first error function

$$e_1 = \frac{Q_1}{M_1^2} (1 + \hat{\mathbf{n}}_S^T \hat{\mathbf{n}}_L)^2 \quad (7.24)$$

where $M_1 = 1$ and $Q_1 = 1$.

TRACKING ERROR OF LASER SPOT

The laser beam intersects the sensor surface at a point \mathbf{r}_{LS} . To ensure accurate beam pointing and avoid overfill, the error between the laser spot position and the centroid of the sensor surface must be minimised. The second error function is therefore

$$e_2 = \frac{1}{M_2^2} (\mathbf{r}_{LS} - \mathbf{r}_S)^T \mathbf{Q}_2 (\mathbf{r}_{LS} - \mathbf{r}_S) \quad (7.25)$$

where $M_2 = 0.05$ and

$$\mathbf{Q}_2 = \begin{bmatrix} 1 & 0 & 0 \\ 0 & 1 & 0 \\ 0 & 0 & 1 \end{bmatrix}$$

TARGET RANGE

Finally, laser energy is absorbed by the atmosphere while in transit. It is thus desirable to minimise the distance of the target receiver from the emitter, although not to the detriment of the operation's safety. The third error function is then

$$e_3 = \frac{1}{M_3^2} (\mathbf{r}_S - \mathbf{r}_L)^T \mathbf{Q}_3 (\mathbf{r}_S - \mathbf{r}_L) \quad (7.26)$$

where $M_3 = 50$ and

$$\mathbf{Q}_3 = \begin{bmatrix} 0.001 & 0 & 0 \\ 0 & 0.001 & 0 \\ 0 & 0 & 0.001 \end{bmatrix}$$

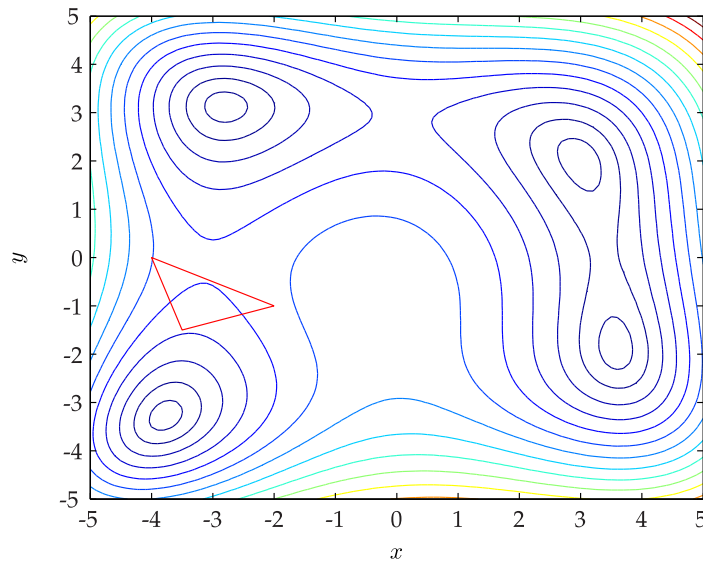


FIGURE 7.7: EXAMPLE OF NELDER-MEAD SIMPLEX OF THREE VERTICES ON THE TWO-DIMENSIONAL HIMMELBLAU FUNCTION (HIMMELBLAU, 1972).

7.5.3 OPTIMISATION ALGORITHMS

MATLAB's Optimization tool is used to identify values of \mathbf{X} which minimise the cost function Φ . Two methods are employed, the unconstrained line-search algorithm `fminsearch` and the simulated annealing algorithm `simulannealbnd`.

LINE-SEARCH

The line-search algorithm `fminsearch` uses the non-linear Nelder-Mead method proposed by Nelder and Mead (1965) and is designed to identify local minima. For an optimisation with k variables, the Nelder-Mead method uses a simplex with $k + 1$ vertices and evaluates the cost function at each of these vertices. For example, a two-dimensional surface would employ a triangle, as shown in Figure 7.7. The vertex of greatest value is discarded and replaced with a new vertex. The simplex morphs in accordance with the landscape of the surrounding manifold. It elongates down inclines, reflects upon encountering valleys and contracts in the neighbourhood of a minimum, thus narrowing the search space. The vertices of the simplex eventually converge upon a local minimum. The algorithm is effective and concise in comparison to more complex solutions. However, the identified minimum is strongly dependent on the initial search location.

The algorithm as used by MATLAB is derived from the work presented by Lagarias, Reeds, Wright, and Wright (1998), which be summarised as follows. The Nelder-Mead algorithm is designed to minimise a function $\Phi(\mathbf{X})$ for $\mathbf{X} \in \mathbb{R}^n$. Coefficients are defined which describe the reflection ρ , expansion χ , contraction γ and shrinkage σ of the simplex. The values typically used for

these coefficients are

$$\rho = 1, \quad \chi = 2, \quad \gamma = \frac{1}{2}, \quad \sigma = \frac{1}{2}$$

For an iteration k in the optimisation, a simplex Δ_k is given, where each of its $n + 1$ vertices are a point in \mathbb{R}^n . The assumption is made that each iteration begins by ordering each vertex $\mathbf{X}_1^{(k)}, \dots, \mathbf{X}_{n+1}^{(k)}$ such that

$$\Phi_1^{(k)} \leq \Phi_2^{(k)} \leq \dots \leq \Phi_{n+1}^{(k)}$$

where $\Phi_i^{(k)} = \Phi(\mathbf{X}_i^{(k)})$. Using this order and dropping the k superscript for brevity, Φ_1 can be considered the *best* function value and Φ_{n+1} the *worst*. Consequently, \mathbf{X}_1 is the best vertex and \mathbf{X}_{n+1} the worst. Each iteration k is designed to generate a new simplex such that $\Delta_{k+1} \neq \Delta_k$. The result of each iteration is then either: a single new vertex which replaces the worst vertex \mathbf{X}_{n+1} in the simplex of the next iteration; or a set of n new points which, together with the best vertex \mathbf{X}_1 , form the new simplex in the next iteration. A single iteration of the Nelder-Mead algorithm is described by Lagarias et al. (1998) as follows:

1. ORDER: The vertices \mathbf{X} are ordered such that $\Phi_1 \leq \Phi_2 \leq \dots \leq \Phi_{n+1}$.
2. REFLECT: The *reflection point* \mathbf{X}_r is calculated from

$$\mathbf{X}_r = \bar{\mathbf{X}} + \rho(\bar{\mathbf{X}} - \mathbf{X}_{n+1}) = (1 + \rho)\bar{\mathbf{X}} - \rho\mathbf{X}_{n+1}$$

where $\bar{\mathbf{X}}$ is the centroid of the best n points of the simplex. The solution $\Phi_r = \Phi(\mathbf{X}_r)$ is then evaluated, and if it satisfies the condition $\Phi_1 \leq \Phi_r < \Phi_n$, \mathbf{X}_r is accepted and the iteration is terminated.

3. EXPAND: If $\Phi_r < \Phi_1$, the *expansion point* \mathbf{X}_e is calculated from

$$\mathbf{X}_e = \bar{\mathbf{X}} + \chi(\mathbf{X}_r - \bar{\mathbf{X}}) = (1 + \rho\chi)\bar{\mathbf{X}} - \rho\chi\mathbf{X}_{n+1}$$

The solution $\Phi_e = \Phi(\mathbf{X}_e)$ is then evaluated, and if it satisfies the condition $\Phi_e < \Phi_r$, \mathbf{X}_e is accepted and the iteration is terminated.

4. CONTRACT: If $\Phi_r \geq \Phi_n$, a *contraction* is performed between $\bar{\mathbf{X}}$ and either \mathbf{X}_r or \mathbf{X}_{n+1} , which are respectively described by

- (a) OUTSIDE: If $\Phi_n \leq \Phi_r < \Phi_{n+1}$, an *outside contraction* is performed, giving the vertex

$$\mathbf{X}_c = \bar{\mathbf{X}} + \gamma(\mathbf{X}_r - \bar{\mathbf{X}}) = (1 + \rho\gamma)\bar{\mathbf{X}} - \rho\gamma\mathbf{X}_{n+1}$$

The solution $\Phi_c = \Phi(\mathbf{X}_c)$ is evaluated, and if $\Phi_c \leq \Phi_r$, \mathbf{X}_c is accepted and the iteration is terminated. If $\Phi_c > \Phi_r$, a *shrink* is performed, as described by step 5.

(b) **INSIDE:** If $\Phi_r \geq \Phi_{n+1}$, an *inside contraction* is performed, giving the vertex

$$\mathbf{X}_{cc} = \bar{\mathbf{X}} - \gamma(\bar{\mathbf{X}} - \mathbf{X}_{n+1}) = (1 - \gamma)\bar{\mathbf{X}} + \gamma\mathbf{X}_{n+1}$$

The solution $\Phi_{cc} = \Phi(\mathbf{X}_{cc})$ is then evaluated, and if $\Phi_{cc} < \Phi_{n+1}$, \mathbf{X}_{cc} is accepted and the iteration is terminated. If $\Phi_{cc} \geq \Phi_{n+1}$, a shrink is performed, as described by step 5.

5. Perform a shrink step: The function Φ is evaluated at the n points $\mathbf{v}_i = \mathbf{X}_1 + \sigma(\mathbf{X}_i - \mathbf{X}_1)$, where $i = 2, \dots, n + 1$. The unordered vertices of the simplex at the next iteration then consist of $\mathbf{X}_1, \mathbf{v}_2, \dots, \mathbf{v}_{n+1}$.

This algorithm reiterates and generates new simplexes until the simplex converges upon the local minimum. For the purposes of the optimisation experiments described in this section, MATLAB's Nelder-Mead algorithm is employed with the following parameters: a maximum number of function evaluations of 2000; a termination tolerance on the cost function value of 2×10^{-4} ; a termination tolerance on the variable value of 2×10^{-4} . The initial search location on the manifold varies with the optimisation problem.

SIMULATED ANNEALING

The simulated annealing algorithm `simulannealbnd` is based on methods published independently by Kirkpatrick, Gelatt Jr, and Vecchi (1983) and Černý (1985). These algorithms were inspired by a mathematical model of annealing which was developed by Metropolis, Rosenbluth, Rosenbluth, Teller, and Teller (1953). Annealing is the process by which a material is heated to alter its physical structure and then cooled to ensure the new structure is retained.

Simulated annealing then emulates this process by employing a temperature variable. The temperature is initially high and gradually decreases as the algorithm progresses. While the temperature is high, the algorithm may jump out of any local minima it encounters, simulating the high energy state of the system. As it "cools", the energy of the system reduces and the search space focuses to a solution which is ideally close to the global minimum. Simulated annealing can be employed to find the global minimum of a cost function for which there are several minima, as is likely to be the case with the multi-variable problem described by Equation (7.21). Since this method is probabilistic, it has the potential to produce different results each time it is employed.

Bertsimas and Tsitsiklis (1993) describe the basic elements of the simulated annealing algorithm, with the symbols adapted here for consistency, as:

1. A finite set \mathbf{X} .
2. A real-valued cost function Φ , defined on \mathbf{X} . Let $\mathbf{X}^* \subset \mathbf{X}$ be the set of global minima of Φ , assumed to be a proper subset of \mathbf{X} .

3. For each $i \in \mathbf{X}$, a set $\mathbf{X}_i \subset \mathbf{X} - \{i\}$ is defined, called the set of neighbours of i .
4. For every i , a collective of positive coefficients q_{ij} is defined, where $j \in \mathbf{X}_i$, such that $\sum_{j \in \mathbf{X}_i} q_{ij} = 1$. It is assumed that $j \in \mathbf{X}_i$ if and only if $i \in \mathbf{X}_j$.
5. A non-increasing function $T : N \rightarrow (0, \infty)$, called the *cooling schedule*. Here N is the set of positive integers, and $T(t)$ is called the *temperature* at time t .
6. An initial state, $\mathbf{x}_0 \in \mathbf{X}$.

The algorithm then consists of a discrete-time inhomogeneous Markov chain $\mathbf{x}(t)$. If the current state $\mathbf{x}(t)$ is equal to i , a neighbour of i , j , is chosen at random. The probability that any $j \in \mathbf{X}_i$ is selected is equal to q_{ij} . Upon choosing j , the next state $\mathbf{x}(t+1)$ is determined by the logical operation

$$\begin{aligned} &\text{if } J_j \leq J_i, \text{ then } \mathbf{x}(t+1) = j \\ &\text{if } J_j > J_i, \text{ then} \\ &\quad \mathbf{x}(t+1) = j \text{ with probability } \exp\left(-\frac{J_j - J_i}{T(t)}\right) \\ &\quad \mathbf{x}(t+1) = i \text{ otherwise} \end{aligned}$$

The cooling schedule $T(t)$ is designed to gradually reduce the rate at which the Markov chain reaches equilibrium. At high temperatures, equilibrium is reached quickly, while at low temperatures, the time taken to reach equilibrium is much longer. This emulates the cooling aspect of the physical annealing process. The probabilistic nature of the algorithm allows the temperature to occasionally increase. It can therefore be considered a local search algorithm with a probabilistic aspect which allows “upward” movements with the goal of escaping from local minima. The algorithm eventually progresses until the state \mathbf{x} is determined to be “good enough” by the termination criteria.

In using simulated annealing to optimise quadrotor trajectories, upper and lower bounds are defined to limit the search space of the optimisation. The identified minimum is therefore not necessarily the global minimum, but a near-optimal solution in the specified search space. MATLAB’s simulated annealing algorithm uses a random number generator to decide which points to evaluate. To ensure a consistent methodology between levels of resolution, the random number generator uses a constant seed of 10 for each optimisation. The initial temperature is set to 100 ; the interval for reannealing is set to 100, the maximum termination tolerance on the optimisation function is set to 1×10^{-6} .

7.6 RESULTS

The multi-agent wireless power transmission model is optimised by minimising the cost function described by Equation (7.21). A number of different scenarios are specified by adjusting which of the parameters in the set \mathbf{X} are varied and which remain constant during the optimisation. Additionally, employing different initial conditions allow investigation of local minima in short- or long-range transmissions and high- or low-speed flight. The Nelder-Mead algorithm `fminsearch` is used primarily, as the local minima around the initial conditions are of greater interest than the global minimum. The simulated annealing method `simulannealbnd` is briefly employed to investigate the effects of resolution on its results. This requires that the algorithm behaviour is drawn from the same random number seed for optimisation of each level.

The optimisation is performed with three different parameter set sizes, each investigating a different aspect of the possible results. The optimisation is first performed on a trajectory with two variables. An example 10 second flight is optimised using the Nelder-Mead method. The optimisation is then repeated for a 20 second flight with different trajectory properties. Next, the trajectory is optimised for four variables. The potential for identifying different local minima in each level of the model family is examined. Finally, the optimisation is performed with six variable properties. Simulated annealing with appropriate boundary conditions is performed on the simulation with the Level 1 quadrotor model to obtain an approximate global minimum. The Nelder-Mead method is then employed to obtain the minima for each level with greater precision. This is contrasted with the results of using the Nelder-Mead with arbitrary initial conditions. It is assumed that, for each set of n parameters, the n -dimensional manifold describing the cost function at each level has the same general shape, with variance in the values of the minima and their corresponding coordinates. Note that, as the ETS agent is described by the same model for each optimisation, the identifier Level i is taken to describe the multi-agent simulation and all of its component agents with a quadrotor model and controller of Level i .

7.6.1 SIMULATION SETUP

The quadrotor is directed to follow a trajectory $\mathbf{y}_d(t)$, starting at $t_0 = 0$ and finishing at t_f . The ETS is placed at the origin of the $x - y$ plane in \mathcal{W} . At t_0 the quadrotor is positioned on the $y - z$ plane in the positive y direction. The trajectory directs the quadrotor to the opposite side of the ETS in y via an arc which allows the wireless power transmission to occur. At t_f , the end of the trajectory is reached. The power transmission is taken to begin at t_0 and finish at t_f , with the initial ETS orientation and quadrotor yaw displacement specified such that the laser spot is incident on the photovoltaic sensor as the simulation starts. This is done to eliminate the significant optimisation errors associated

with the laser spot being off-target. The optimisation is then focussed on the smaller errors which occur due to poor tracking and beam-steering and sub-optimal angle of incidence.

The cost function Φ is minimised for a set of parameters $\mathbf{X} \subseteq \hat{\mathbf{X}}$, which is a subset of all the possible variables describing the trajectory. Different scenarios are presented through selection of specific elements of $\hat{\mathbf{X}}$ as optimisation variables and setting the remainder as constants. To simplify the optimisation, the acceleration parameters remain constant at $\ddot{\mathbf{r}}_0 = \ddot{\mathbf{r}}_f = \mathbf{0}$ for each case. The data used to populate the models in the WPT simulation are described in Appendix G.

The SiFRe engine uses a fourth-order Runge-Kutta algorithm to solve the state transition. Time-steps for each level are chosen such that the simulation run-time is minimised while ensuring stability in the closed-loop system. The time-steps for the ETS and cost function agents are initially consistent in each level. The values of the time-steps for each agent are chosen such that the agent dynamics are adequately capture and are described in Chapter G. The optimisation is performed for the multi-agent system comprising the quadrotor-controller system at each level, as detailed previously, and the energy transmission system. The quadrotor agent co-operates with the ETS agent in the transmission, while a cost function pseudo-agent calculates the errors and determines the cost function.

7.6.2 OPTIMISATION WITH TWO VARIABLES

The trajectory is parameterised by two variables $\mathbf{X} = \{\dot{x}_0, \dot{x}_f\}$, while the remainder of the parameter set, denoted by $\hat{\mathbf{X}} \setminus \mathbf{X}$, is constant. The optimisation is performed for two scenarios. The first is a 10 second flight at short range, while the second is a 20 second flight at a longer range. For both scenarios, the quadrotor trajectory is optimised for each level and the results compared.

CASE 1: 10 SECOND FLIGHT

The quadrotor trajectory definition has fixed initial position $\mathbf{r}_0 = [0, 10, -2]^T$ at $t_0 = 0$ s and fixed final position $\mathbf{r}_f = [0, -10, -2]^T$ at $t_f = 10$ s. The constant velocity properties are fixed at $\{\dot{y}_0, \dot{z}_0, \dot{y}_f, \dot{z}_f\} = 0$. The trajectory is optimised for the two-parameter set $\mathbf{X} = \{\dot{x}_0, \dot{x}_f\}$ over the range $[t_0, t_f]$, with initial values $\mathbf{X}_0 = \{5, -5\}$.

Table 7.1 contains the trajectory properties obtained by optimising each level of the multi-agent simulation for Case 1. The cost function minima for each level are also given. The quadrotor agent described by each level is commanded to follow the optimised trajectory for that level, resulting in the error and cost function histories described by Figure 7.8, where the errors e_1 , e_2 and e_3 are defined by Equations (7.24), (7.25) and (7.26). Figure 7.9 shows the optimised trajectories. The results of the optimisation demonstrate a small variance in the

TABLE 7.1: TRAJECTORY PROPERTIES OBTAINED FROM TWO-PARAMETER OPTIMISATION OF 10 SECOND FLIGHT.

LEVEL	\dot{x}_0	\dot{x}_f	Φ_{\min}
1	4.1119	-7.9288	0.4559
2	4.1045	-8.0230	0.4546
3	4.0759	-8.0803	0.4949
4	4.6392	-8.3791	0.4695
5	4.6392	-8.3017	0.4379
Mean	4.3157	-8.1426	0.4626
Std Dev	0.2957	0.1905	0.0213

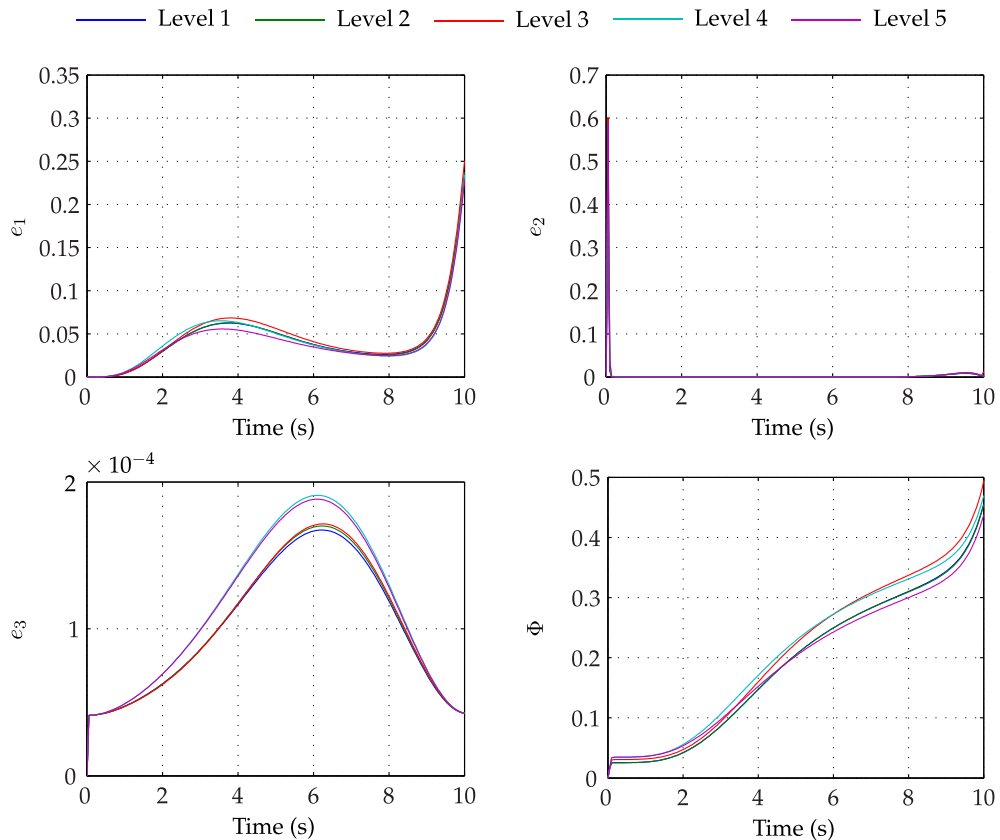


FIGURE 7.8: ERROR AND COST FUNCTION HISTORIES FOR EACH LEVEL DURING FLIGHTS WITH TRAJECTORY PROPERTIES DETERMINED BY TWO-PARAMETER OPTIMISATION OF 10 SECOND FLIGHT.

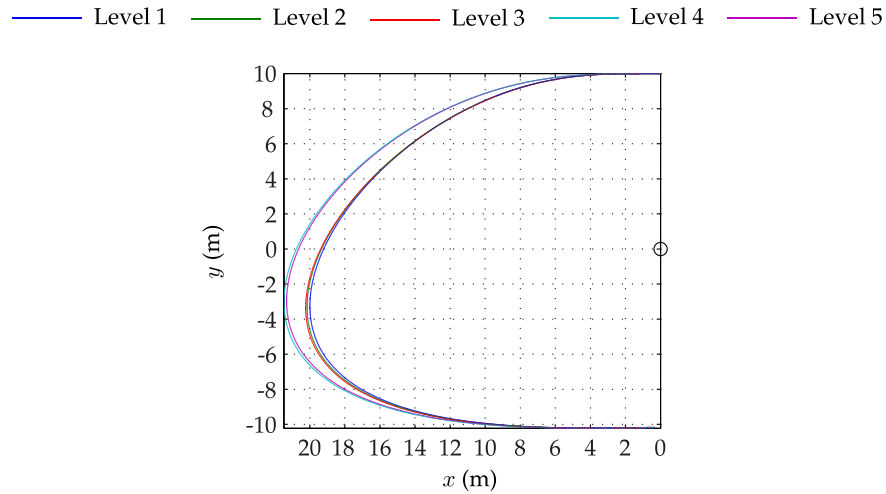
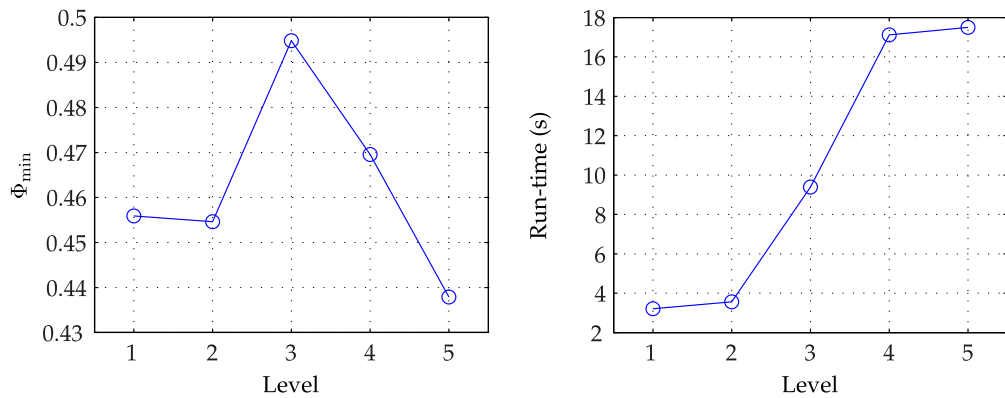


FIGURE 7.9: NEAR-OPTIMAL TRAJECTORIES FOR A 10 SECOND FLIGHT OF THE QUADROTOR AT EACH LEVEL, DETERMINED BY A TWO-PARAMETER OPTIMISATION.



(A) COST FUNCTION MINIMA FOR EACH LEVEL. (B) AVERAGE RUN-TIMES FOR EACH LEVEL.

FIGURE 7.10: COMPARISON OF COST FUNCTION MINIMA AND AVERAGE RUN-TIME PER FUNCTION CALL FOR EACH LEVEL, FOR TWO-PARAMETER OPTIMISATION OF 10 SECOND FLIGHT.

optimised trajectory properties and cost function minima. In defining a trajectory using these properties, the near-optimal paths determined from Levels 1 to 3 are shown to be similar to each other and distinct from the paths determined from optimisation of the Levels 4 and 5 models.

The effect of model and temporal resolution on the optimisation results is more clearly highlighted in Figure 7.10. A linear relationship between model resolution and the minima values is not evident. A decrease in step-size in the non-quadrotor agents is shown to reduce the minima for a given level, although at the expense of simulation run-time.

TABLE 7.2: TRAJECTORY PROPERTIES OBTAINED FROM TWO-PARAMETER OPTIMISATION OF 20 SECOND FLIGHT.

LEVEL	\dot{x}_0	\dot{x}_f	Φ_{\min}
1	4.9242	-4.3382	0.1333
2	4.9242	-4.3381	0.1333
3	4.8125	-4.4050	0.1475
4	2.9047	-5.2531	0.1293
5	2.8532	-5.3832	0.1250
Mean	4.0838	-4.7435	0.1337
Std Dev	1.1009	0.5273	0.0084

CASE 2: 20 SECOND FLIGHT

The optimisation is repeated for a longer transmission at greater range. The quadrotor trajectory definition has fixed initial position $\mathbf{r}_0 = [0, 20, -3]^T$ at $t_0 = 0$ s and fixed final position $\mathbf{r}_f = [0, -20, -3]^T$ at $t_f = 20$ s. The constant velocity properties are fixed at $\{\dot{y}_0, \dot{z}_0, \dot{y}_f, \dot{z}_f\} = 0$. The trajectory is optimised for the two-parameter set $\mathbf{X} = \{\dot{x}_0, \dot{x}_f\}$ over the range $[t_0, t_f]$, with initial values $\mathbf{X}_0 = \{5, -5\}$.

Table 7.2 contains the trajectory properties and cost function minima obtained by optimising each level of the multi-agent simulation for Case 1. Commanding the quadrotor agent of each level to follow the corresponding optimised trajectory provides the error and cost function histories shown in Figure 7.11. The corresponding trajectories are given in Figure 7.12. A greater variance is evident in the results of optimising the 20 second flight, with similarities in the grouping of Levels 1, 2 and 3 and the grouping of Levels 4 and 5.

Figure 7.13 more clearly demonstrates the difference in optimisation results between levels for each case. While Case 1 demonstrates no linear relationship between the resolution and the magnitude of the minimum, Case 2 exhibits a decrease in the minimum as the resolution increases. As with previous results, an increase in temporal resolution is shown to produce a smaller minimum.

The difference in the solutions of each level may be further examined by considering the cost function manifolds in the vicinity of the initial and optimised variables. Figure 7.14 compares the contours of each level, while Figure 7.15 shows the function surface for each level of the optimisation, demonstrating the presence of several minima in the vicinity of the chosen initial variables. Optimisation of the Levels 1 to 3 models results in identification of minima which are not global within the boundaries shown, instead providing solutions which are closer to the initial parameter values. Optimisation of Levels 4 and 5 is shown to provide the apparent global minima, at least in the given boundaries. As the only difference between the optimisations of each level is the definition of the cost function manifold, the disparity in solutions between levels must result from a gradient difference around the initial location.

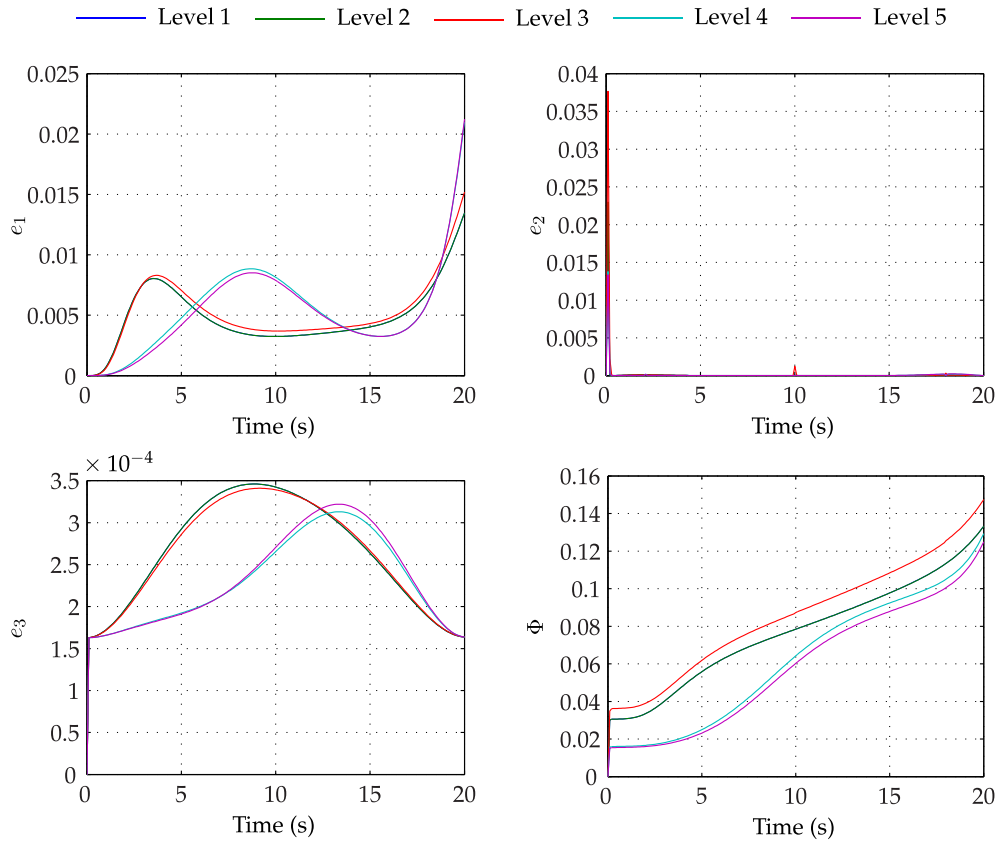


FIGURE 7.11: ERROR AND COST FUNCTION HISTORIES FOR EACH LEVEL DURING FLIGHTS WITH TRAJECTORY PROPERTIES DETERMINED BY TWO-PARAMETER OPTIMISATION OF 20 SECOND FLIGHT.

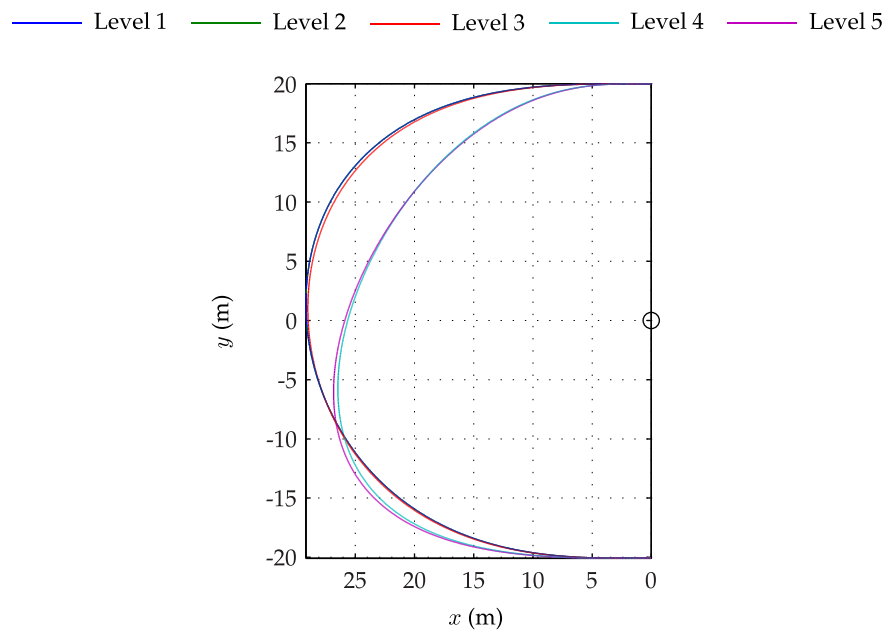
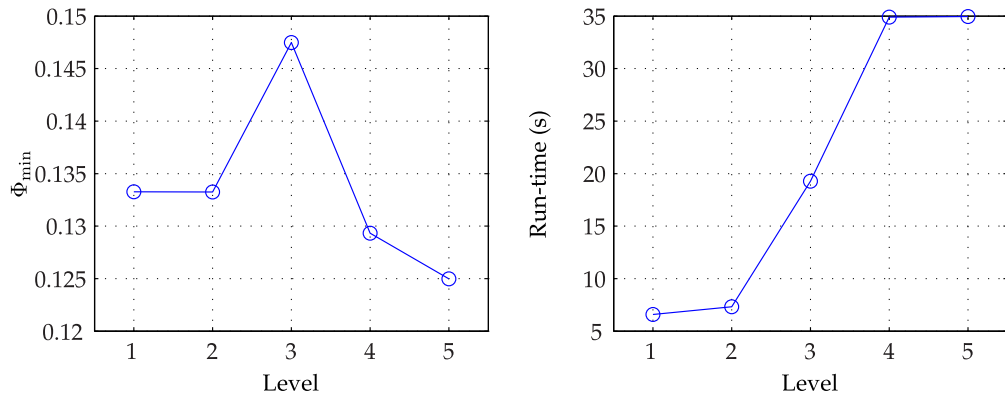


FIGURE 7.12: NEAR-OPTIMAL TRAJECTORIES FOR A 20 SECOND FLIGHT OF THE QUADROTOR AT EACH LEVEL, DETERMINED BY A TWO-PARAMETER OPTIMISATION.



(A) COST FUNCTION MINIMA FOR EACH LEVEL. (B) AVERAGE RUN-TIMES FOR EACH LEVEL.

FIGURE 7.13: COMPARISON OF COST FUNCTION MINIMA AND AVERAGE RUN-TIME PER FUNCTION CALL FOR EACH LEVEL, FOR TWO-PARAMETER OPTIMISATION OF 20 SECOND FLIGHT.

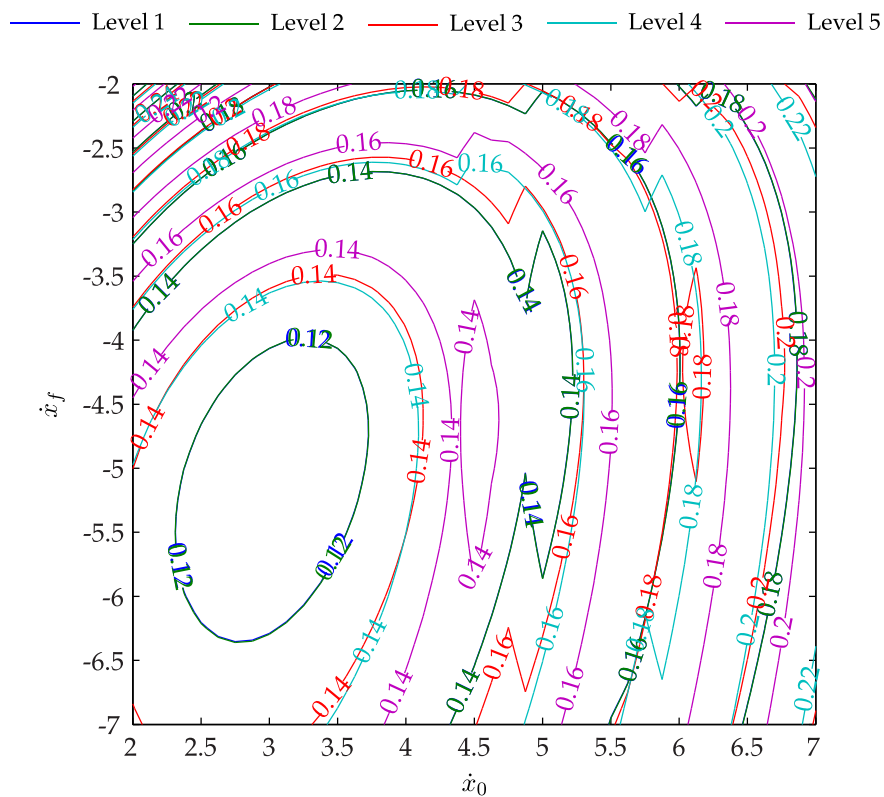


FIGURE 7.14: COMPARISON OF COST FUNCTION SURFACE CONTOURS FOR EACH LEVEL IN TWO-VARIABLE OPTIMISATION OF A 20 SECOND FLIGHT.

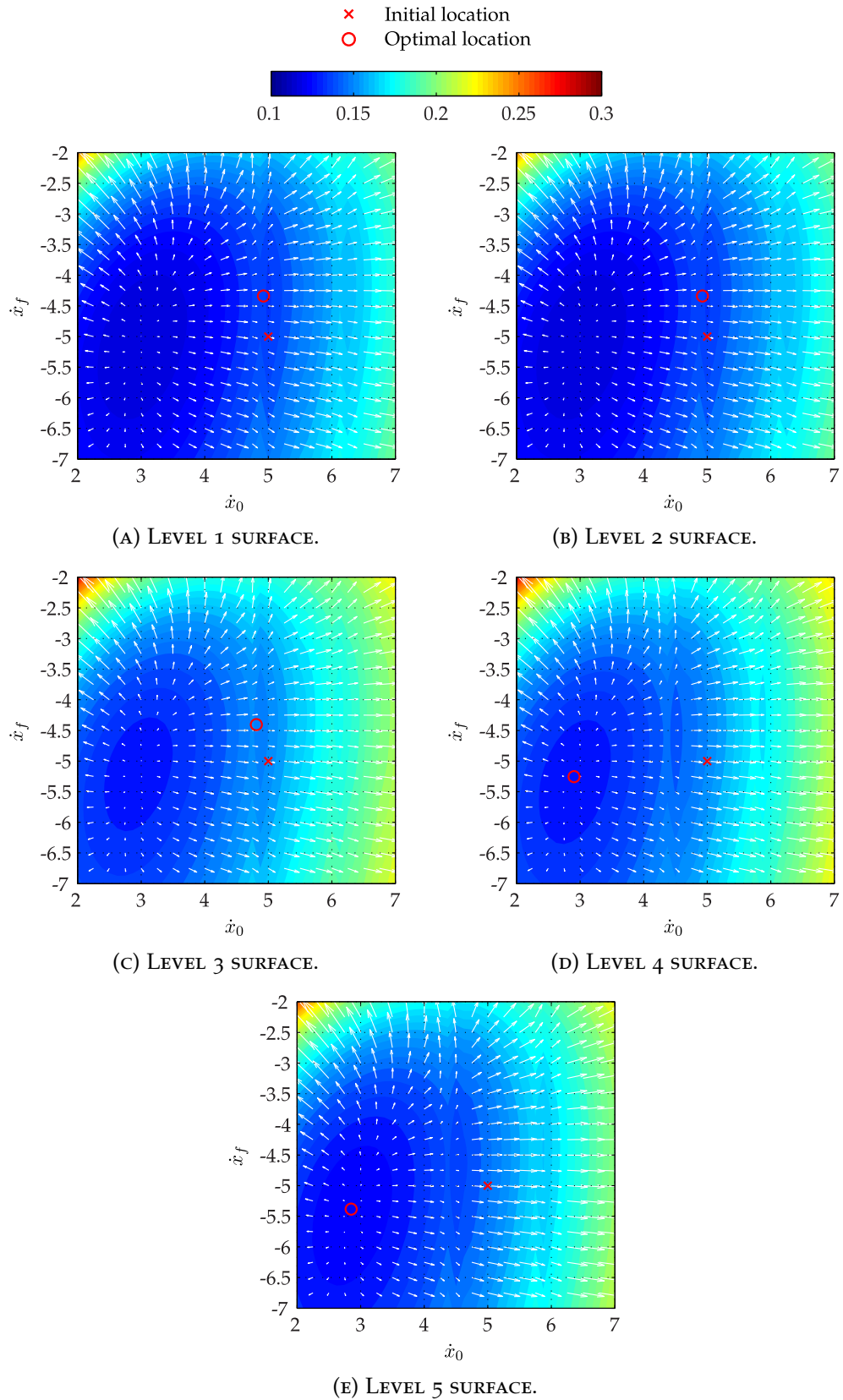


FIGURE 7.15: COST FUNCTIONS MANIFOLDS IN TWO-VARIABLE OPTIMISATION OF 20 SECOND FLIGHT, DEMONSTRATING HOW THE DIFFERENCE IN THE MANIFOLD GRADIENT BETWEEN LEVELS CAN PRODUCE DIFFERENT SOLUTIONS FOR IDENTICAL INITIAL CONDITIONS.

7.6.3 OPTIMISATION WITH FOUR VARIABLES

The trajectory is parameterised by four variables $\mathbf{X} = \{\dot{x}_0, \dot{z}_0, \dot{x}_f, \dot{z}_f\}$, while the remainder of the parameter set, denoted by $\hat{\mathbf{X}} \setminus \mathbf{X}$, is constant. The optimisation is performed twice for the same scenario, a 10 second flight at short range, but with different initial values for the parameter set \mathbf{X} . For each set of initial conditions, the quadrotor trajectory is again optimised for each level and the results compared.

For each set of initial variables, the quadrotor trajectory is specified by the fixed initial position $\mathbf{r}_0 = [0, 10, -2]^T$ at $t_0 = 0$ s and fixed final position $\mathbf{r}_f = [0, -10, -2]^T$ at $t_f = 10$ s. The constant velocity properties are fixed at $\{\dot{y}_0, \dot{y}_f\} = 0$. The trajectory is then optimised for the parameter set $\mathbf{X} = \{\dot{x}_0, \dot{z}_0, \dot{x}_f, \dot{z}_f\}$ over the range $[t_0, t_f]$.

CASE 1: FIRST SET OF INITIAL VARIABLES

The quadrotor trajectory is optimised with the initial parameter values $\mathbf{X}_0 = \{5, 0, -5, 0\}$.

Table 7.3 presents the trajectory properties and cost function minima obtained by optimising each level of the multi-agent simulation for Case 1. Commanding the quadrotor system described by each level to follow the trajectory described by the corresponding optimised properties results in the error and cost function histories given in Figure 7.16. The optimised trajectories are displayed in Figure 7.17. The variance in the near-optimal values of both \dot{z}_0 and \dot{z}_f is shown to be significant, resulting in significantly different trajectories for each level. As demonstrated by the two-parameter optimisations, the presence of several local minima within a relatively small search space is possible. An increase in variables increases the probability of the optimisation algorithm identifying different minima for each level.

TABLE 7.3: TRAJECTORY PROPERTIES OBTAINED FROM EXAMPLE FOUR-PARAMETER OPTIMISATION, WITH INITIAL PARAMETER SET $\mathbf{X}_0 = [5, 0, -5, 0]^T$.

LEVEL	\dot{x}_0	\dot{z}_0	\dot{x}_f	\dot{z}_f	Φ_{\min}
1	5.0875	-1.8207	-8.8086	1.6562	0.3995
2	5.1423	-1.7013	-9.0441	2.3373	0.3940
3	4.5750	-1.4557	-8.1007	-0.4157	0.4725
4	5.2930	-2.1867	-9.1777	1.4426	0.4140
5	4.4633	-0.0557	-10.1561	5.0490	0.3576
Mean	4.9122	-1.4440	-9.0574	2.0139	0.4075
Std Dev	0.3688	0.8196	0.7415	1.9795	0.0418

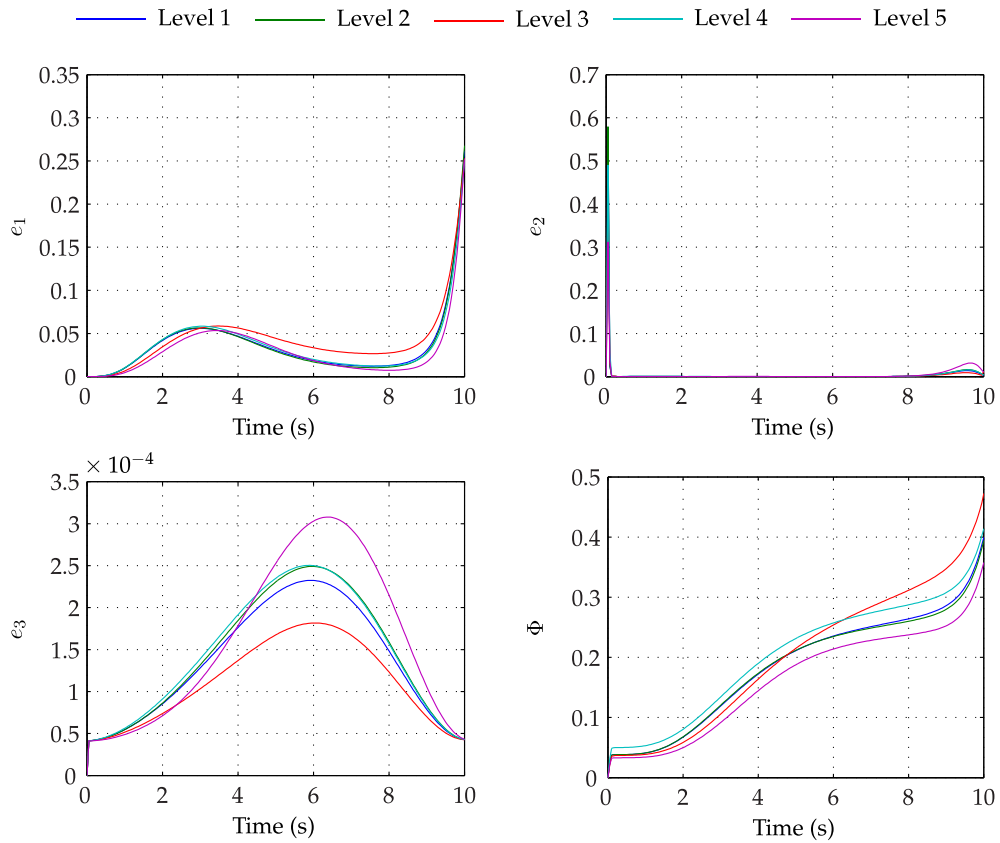


FIGURE 7.16: ERROR AND COST FUNCTION HISTORIES FOR EACH LEVEL DURING FLIGHTS WITH TRAJECTORY PROPERTIES DETERMINED BY FOUR-PARAMETER OPTIMISATION WITH INITIAL PARAMETER SET $\mathbf{X}_0 = [5, 0, -5, 0]^T$.

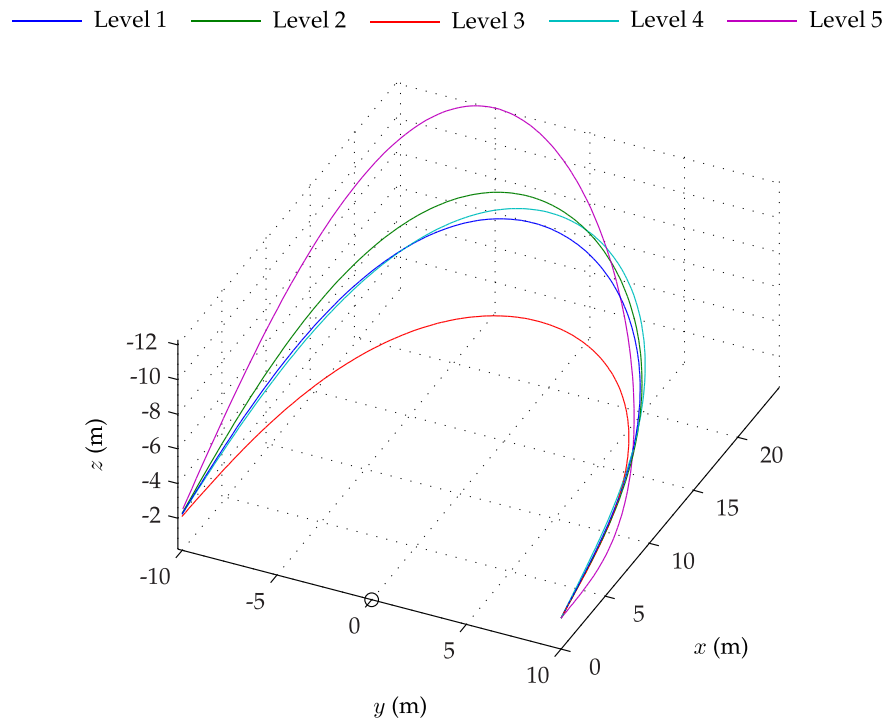


FIGURE 7.17: NEAR-OPTIMAL TRAJECTORIES OF QUADROTOR FLIGHT AT EACH LEVEL, DETERMINED BY A FOUR-PARAMETER OPTIMISATION WITH INITIAL PARAMETER SET $\mathbf{X}_0 = [5, 0, -5, 0]^T$.

TABLE 7.4: TRAJECTORY PROPERTIES OBTAINED FROM EXAMPLE FOUR-PARAMETER OPTIMISATION, WITH INITIAL PARAMETER SET $\mathbf{X}_0 = [5, -1.5, -8, 1.5]^T$.

LEVEL	\dot{x}_0	\dot{z}_0	\dot{x}_f	\dot{z}_f	Φ_{\min}
1	4.8517	-0.6733	-9.5925	3.6503	0.3834
2	4.8614	-0.6033	-9.4834	4.0015	0.3823
3	4.7599	-0.5557	-9.4687	4.0321	0.4181
4	4.4533	-0.3104	-10.1551	4.6959	0.3883
5	4.4633	-0.0559	-10.1551	5.0476	0.3576
Mean	4.6779	-0.4397	-9.7710	4.2855	0.3860
Std Dev	0.2044	0.2544	0.3540	0.5696	0.0216

CASE 2: SECOND SET OF INITIAL VARIABLES

The quadrotor trajectory is optimised with the initial parameter values $\mathbf{X}_0 = \{5, -1.5, -8, 1.5\}$.

Table 7.4 contains the trajectory properties and cost function minima obtained by optimising each level of the simulation for Case 1. In commanding the quadrotor to follow the trajectories specified by these properties, the resulting error and cost function histories are as shown in Figure 7.18. Figure 7.19 gives the optimised trajectories for each level. The variance in the optimised properties is significantly reduced in comparison to those for both cases employing the first set of initial variables. This implies that each level has identified equivalent local minima of each four-dimensional manifold.

COMPARISON OF RESULTS

Figure 7.20 compares the minima and average run-times for each level in all four six-parameter optimisation experiments. Comparing the optimised trajectory properties and minima for each investigation, it is clear that adjusting the initial values of the parameter set has resulted in different minima being found in certain levels, while others identify the same minimum.

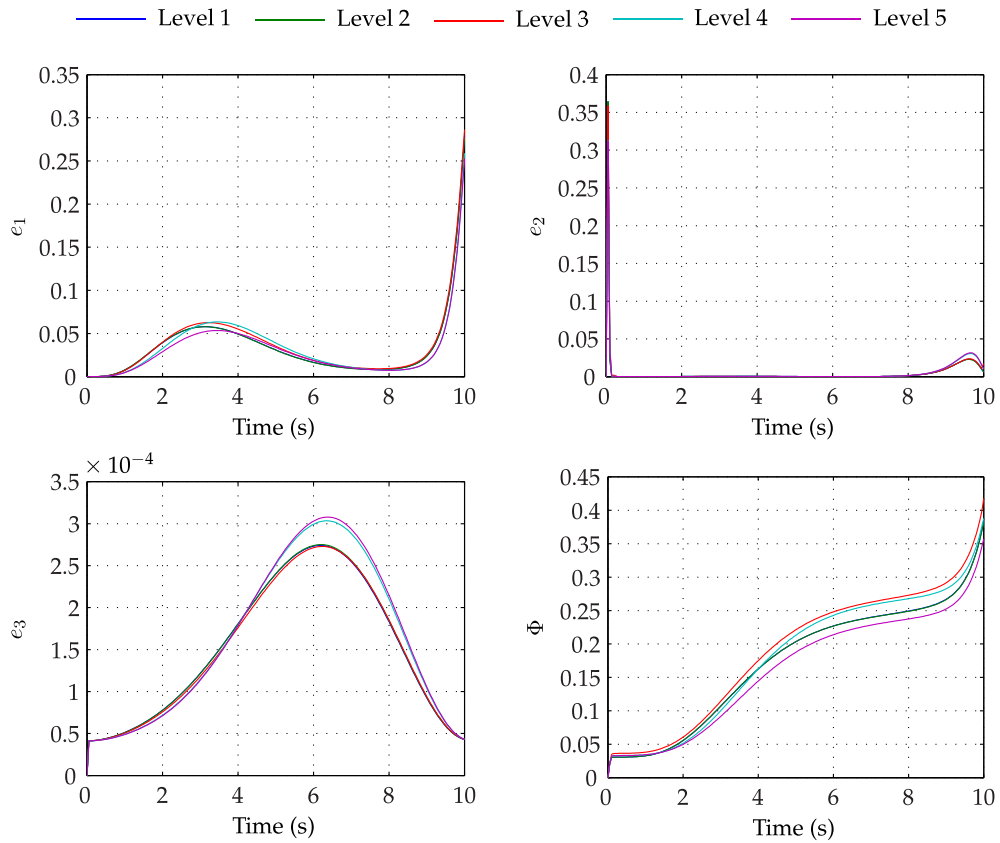


FIGURE 7.18: ERROR AND COST FUNCTION HISTORIES FOR EACH LEVEL DURING FLIGHTS WITH TRAJECTORY PROPERTIES DETERMINED BY FOUR-PARAMETER OPTIMISATION WITH INITIAL PARAMETER SET $\mathbf{X}_0 = [5, -1.5, -8, 1.5]^T$.

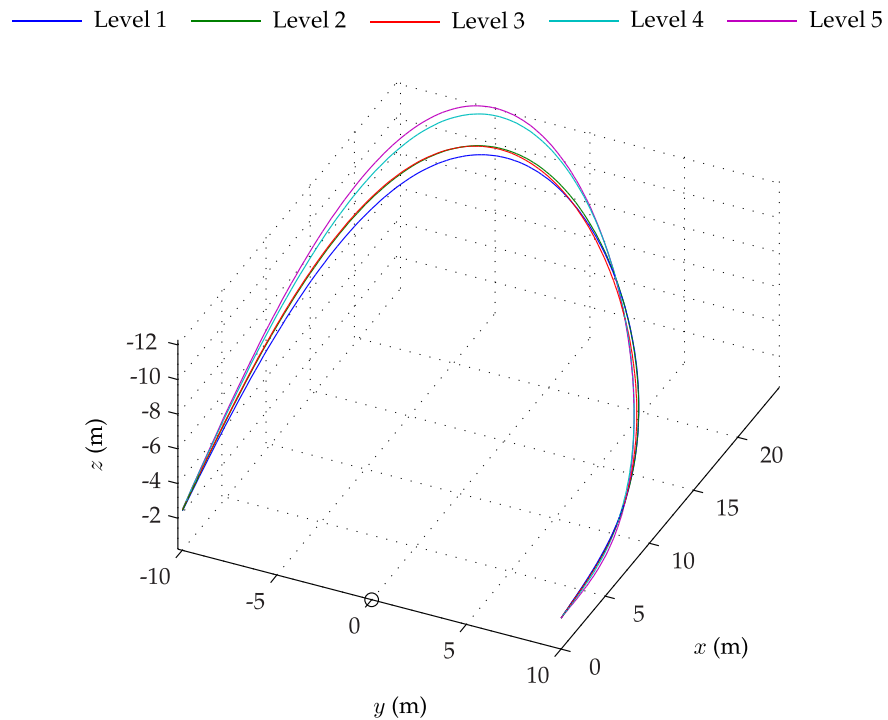


FIGURE 7.19: NEAR-OPTIMAL TRAJECTORIES OF QUADROTOR FLIGHT AT EACH LEVEL, DETERMINED BY A FOUR-PARAMETER OPTIMISATION WITH INITIAL PARAMETER SET $\mathbf{X}_0 = [5, -1.5, -8, 1.5]^T$.

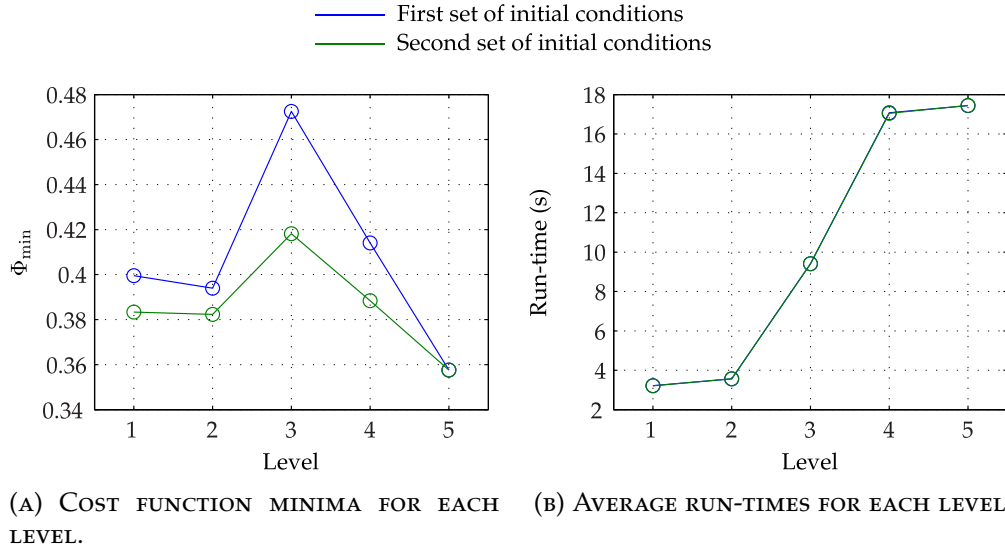


FIGURE 7.20: COMPARISON OF COST FUNCTION MINIMA AND AVERAGE RUN-TIME PER FUNCTION CALL FOR EACH LEVEL, FOR FOUR-PARAMETER OPTIMISATION.

7.6.4 OPTIMISATION WITH SIX VARIABLES

The trajectory is parameterised by six variables $\mathbf{X} = \{\dot{x}_0, \dot{y}_0, \dot{z}_0, \dot{x}_f, \dot{y}_f, \dot{z}_f\}$, allowing full optimisation of the velocity properties describing the trajectory. The remainder of the parameter set, $\hat{\mathbf{X}} \setminus \mathbf{X}$, is constant. The potential for different levels providing inconsistent trajectory properties by identifying different minima has been highlighted in the four-variable optimisations. Recognising the potential for a greater number of local minima in a six-dimensional manifold, simulated annealing is employed to determine the global minimum, using an arbitrary initial parameter set \mathbf{X}_0 . As this method provides only an approximate solution, it is employed in combination with the Level 1 multi-agent model. The parameter set \mathbf{X}_{SA} determined by this optimisation is then employed as the initial location for a line-search optimisation applied to the entire model family. This represents an ideal use for multi-resolution model families, where the low-resolution model is employed to narrow the search space of the optimisation, whereupon higher-resolution models may be utilised to refine the results. The results of the narrowed-search-space optimisation are contrasted with the results of supplying the initial parameter set \mathbf{X}_0 directly to the Nelder-Mead algorithm.

Again, the effects of variation in the temporal resolution are investigated by considering the two cases described previously.

For each optimisation, the quadrotor trajectory is specified by the fixed initial position $\mathbf{r}_0 = [0, 10, -2]^T$ at $t_0 = 0$ s and fixed final position $\mathbf{r}_f = [0, -10, -2]^T$ at $t_f = 10$ s. The trajectory is then optimised for the parameter set $\mathbf{X} \in \mathbb{R}^6$ over the range $[t_0, t_f]$.

TABLE 7.5: TRAJECTORY PROPERTIES OBTAINED FROM OPTIMISATION USING SIX-PARAMETER LINE-SEARCH ALGORITHM WITH ARBITRARY INITIAL SEARCH SPACE.

LEVEL	\dot{x}_0	\dot{y}_0	\dot{z}_0	\dot{x}_f	\dot{y}_f	\dot{z}_f	Φ_{\min}
1	4.7797	1.7700	0.8266	-10.6056	-2.4288	3.0848	0.3954
2	4.7333	1.8921	-2.7571	-9.9531	-0.3834	1.1164	0.3846
3	3.9434	1.5529	0.1031	-10.6632	-0.1782	5.7000	0.3980
4	5.4111	4.7113	-2.8719	-12.7021	-0.0474	5.3021	0.3413
5	5.0905	3.2595	-3.1522	-11.7766	-0.5576	3.7516	0.3329
MEAN	4.7916	2.6372	-1.5703	-11.1401	-0.7191	3.7910	0.3704
STD DEV	0.5468	1.3390	1.8808	1.0917	0.9754	1.8426	0.0310

TABLE 7.6: BOUNDARY CONDITIONS AND NEAR-OPTIMAL SOLUTIONS FOR GLOBAL MINIMISATION OF LEVEL 1 MODEL USING SIMULATED ANNEALING.

	\dot{x}_0	\dot{y}_0	\dot{z}_0	\dot{x}_f	\dot{y}_f	\dot{z}_f	Φ_{\min}
\mathbf{X}_{ub}	0	-10	-10	-30	-10	-10	
\mathbf{X}_{lb}	30	10	10	0	10	10	
\mathbf{X}_{SA}	4.7367	3.2820	-2.6448	-10.2011	-0.2568	3.5407	0.3799

CASE 1: LINE-SEARCH OPTIMISATION WITH ARBITRARY INITIAL VARIABLE SET

The initial parameter set $\mathbf{X}_0 = \{5, 0, 0, -5, 0, 0\}$ is employed in the Nelder-Mead method without boundary conditions. The optimisation is again performed for each level of the multi-agent model family.

Table 7.5 presents the trajectory properties and cost function minima obtained optimising each level. The quadrotor is commanded to follow a trajectory defined by the properties determined for the corresponding level, resulting in the errors shown in Figure 7.21 and the trajectories shown in Figure 7.22. The optimised trajectory properties demonstrate greater variance than those of the previous method, while the resulting trajectories of each level are clearly inconsistent with one another.

CASE 2: LINE-SEARCH OPTIMISATION WITH NARROWED SEARCH SPACE

The simulated annealing algorithm is applied to the Level 1 multi-agent model to narrow the search space around the global minimum within the upper and lower boundary conditions, \mathbf{X}_{ub} and \mathbf{X}_{lb} , respectively. The optimisation is initialised with the parameter set $\mathbf{X}_0 = \{5, 0, 0, -5, 0, 0\}$ which provides the approximate solutions given in Table 7.6. A line-search optimisation then employs each level of the model family with the solution \mathbf{X}_{SA} as a starting point.

Table 7.7 presents the trajectory properties and cost function minima obtained by optimising each level of the model family. In commanding the quadrotor to follow the trajectories specified by these properties, the errors and cost

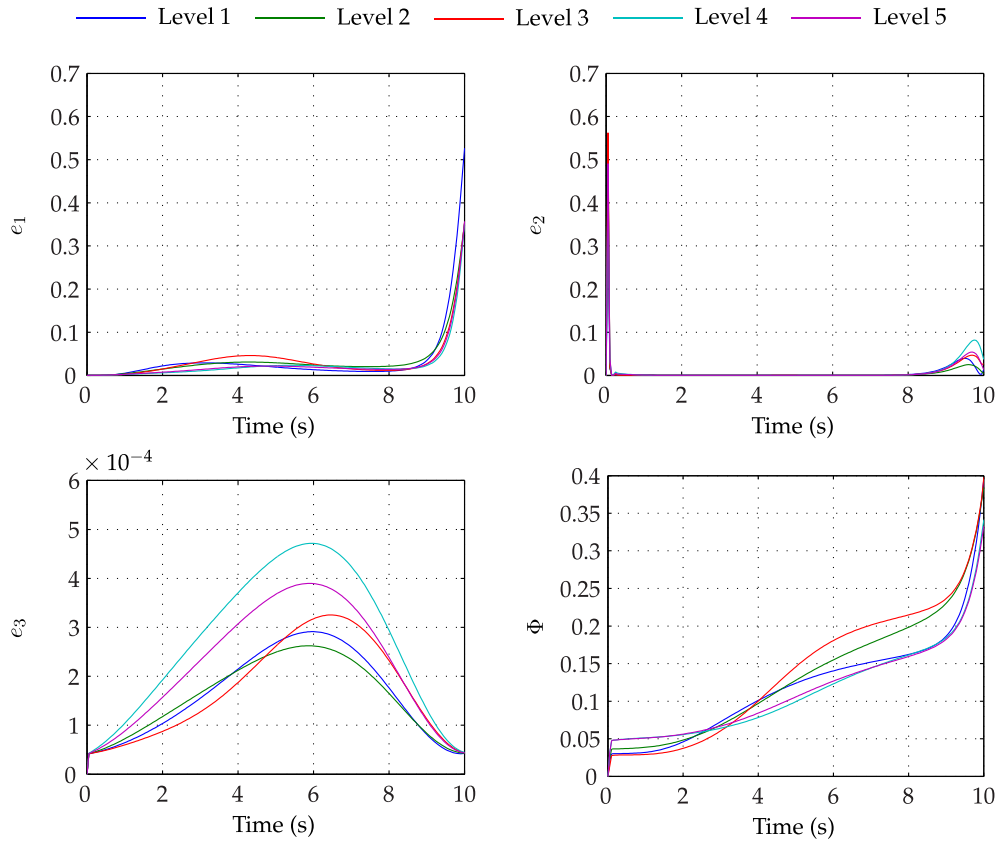


FIGURE 7.21: ERROR AND COST FUNCTION HISTORIES FOR EACH LEVEL DURING FLIGHTS WITH TRAJECTORY PROPERTIES DETERMINED BY SIX-PARAMETER LINE-SEARCH OPTIMISATION WITH ARBITRARY INITIAL SEARCH SPACE.

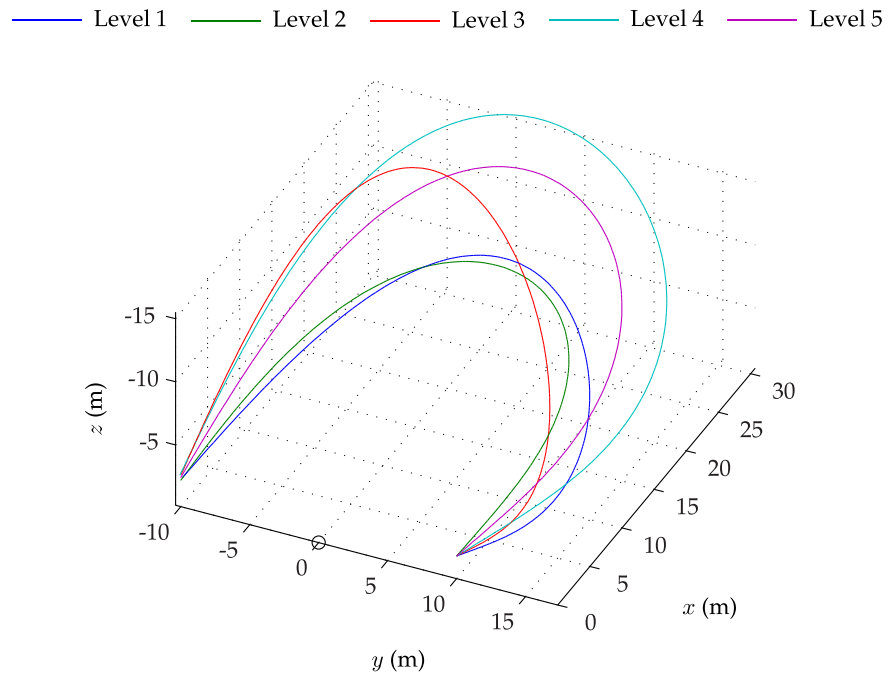


FIGURE 7.22: NEAR-OPTIMAL TRAJECTORIES FOR A FLIGHT OF THE QUADROTOR AT EACH LEVEL, DETERMINED BY A SIX-PARAMETER LINE-SEARCH OPTIMISATION WITH ARBITRARY INITIAL SEARCH SPACE.

TABLE 7.7: TRAJECTORY PROPERTIES OBTAINED FROM OPTIMISATION USING SIX-PARAMETER LINE-SEARCH ALGORITHM WITH NARROWED INITIAL SEARCH SPACE.

LEVEL	\dot{x}_0	\dot{y}_0	\dot{z}_0	\dot{x}_f	\dot{y}_f	\dot{z}_f	Φ_{\min}
1	4.8437	1.9135	-1.1567	-10.9652	-0.3957	4.4408	0.3574
2	4.8621	2.0291	-1.0744	-10.9129	-0.3748	5.0918	0.3550
3	4.7663	1.8501	-0.9578	-10.6817	-0.2511	5.0060	0.3928
4	4.6209	3.9887	-1.1900	-12.7879	-0.8458	7.6321	0.3318
5	4.6307	3.7459	-1.0510	-12.5157	-0.3556	7.7577	0.3149
Mean	4.7447	2.7054	-1.0860	-11.5727	-0.4446	5.9857	0.3504
Std Dev	0.1144	1.0660	0.0917	0.9955	0.2311	1.5808	0.0294

function of the multi-agent model are given the time histories shown in Figure 7.23. The optimised trajectories are provided in Figure 7.24. The optimised trajectories of the Levels 4 and 5 models are shown to be consistent with one another but distinct from those resulting from the models of Levels 1 to 3.

COMPARISON OF RESULTS

Figure 7.25 compares the solutions for each optimisation. By narrowing the initial search space around the global minimum, the Nelder-Mead method is shown to produce more optimised results in comparison to using arbitrary initial conditions in the vicinity of the global minimum. While the possibility remains for the Nelder-Mead method to identify a non-global minimum in any of the cases even after the approximate location of the global minimum has been determined, the results strongly imply that this is not the case. Figure 7.26 contrasts the results of both approaches when the solution derived from one level is applied to the others. It is clear in Figure 7.26b that the optimised trajectory properties for each level are those derived from the optimisation of that level. This is characterised by the black line describing the lower bound of the cost function solutions. Figure 7.26a does not exhibit this property, as the trajectory properties obtained for, for example, the Level 3 model result in a smaller cost function solution when applied to the Levels 1 and 2 models than the properties obtained from those levels. This confirms that the minima identified by optimising at least these two levels are not the global solutions.

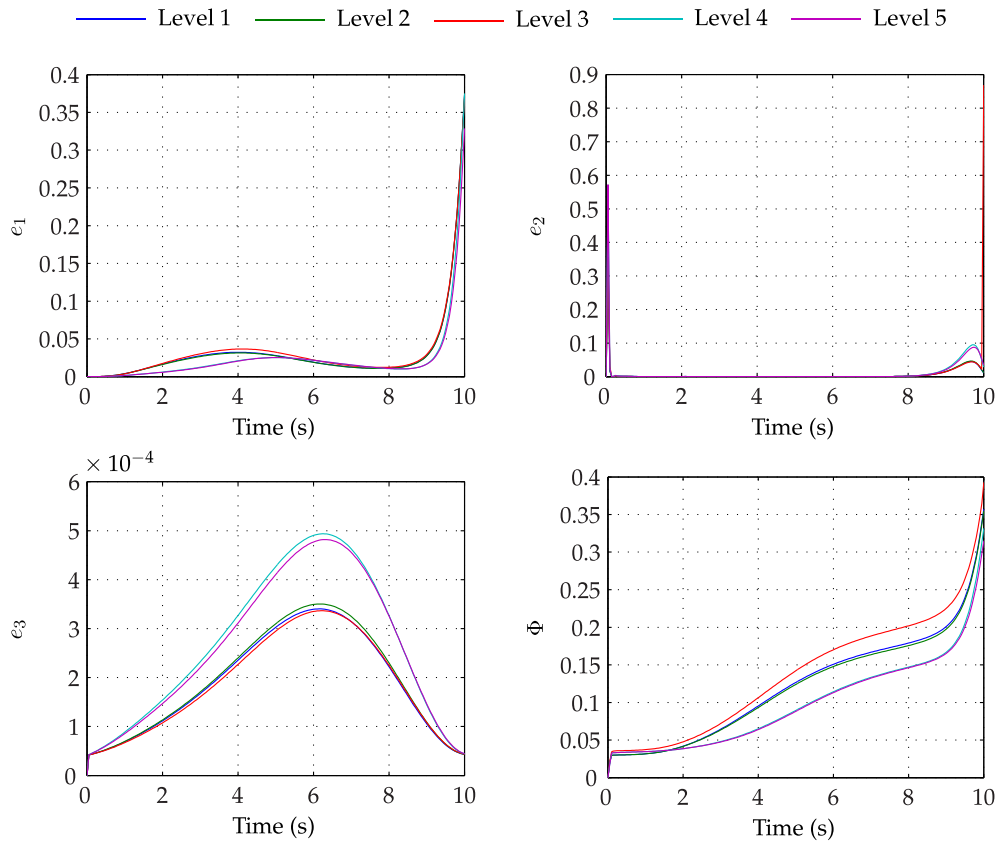


FIGURE 7.23: ERROR AND COST FUNCTION HISTORIES FOR EACH LEVEL DURING FLIGHTS WITH TRAJECTORY PROPERTIES DETERMINED BY SIX-PARAMETER LINE-SEARCH OPTIMISATION WITH NARROWED INITIAL SEARCH SPACE.

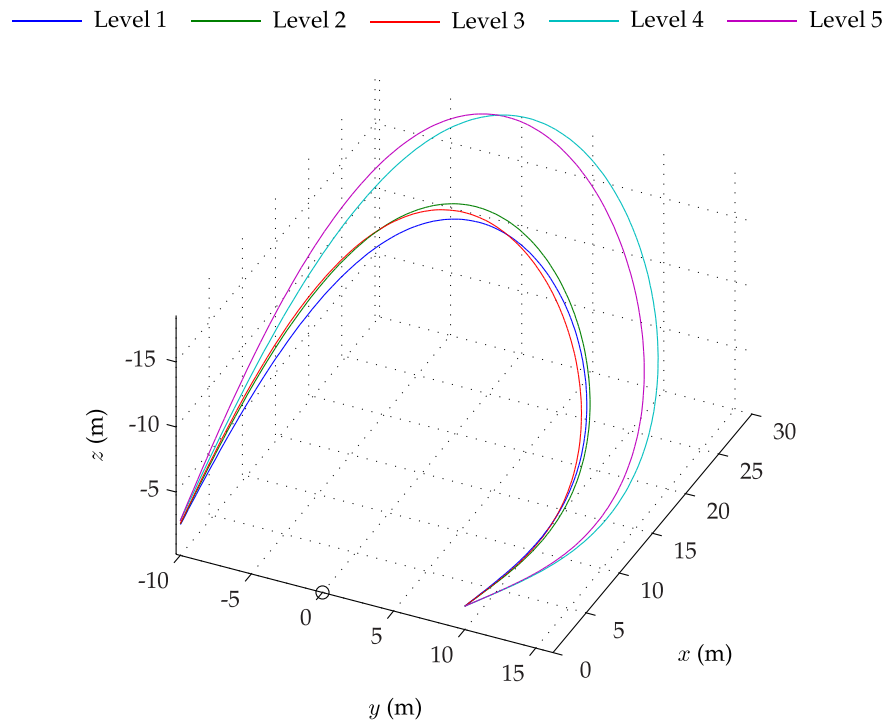
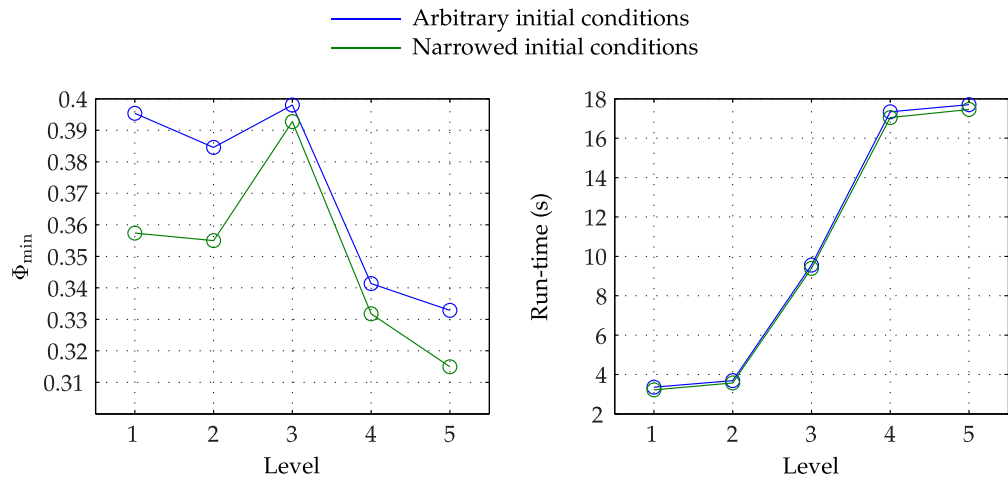
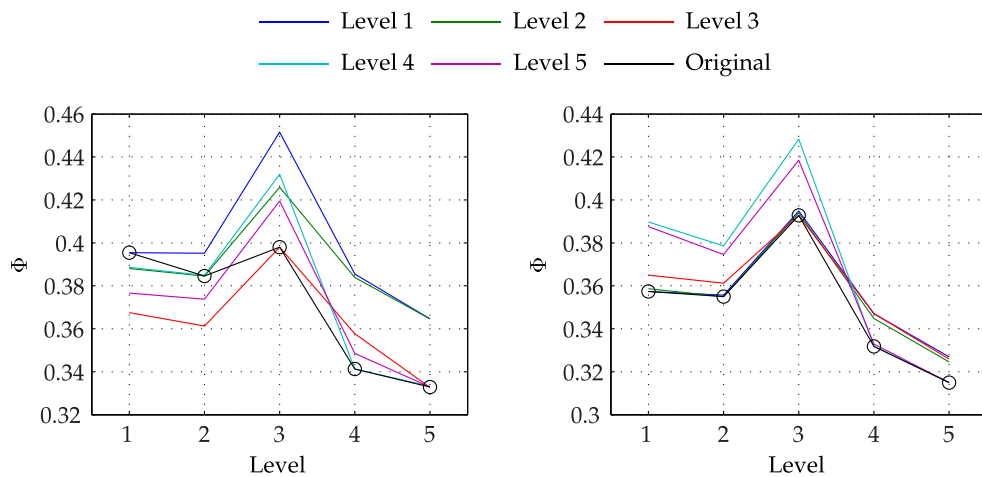


FIGURE 7.24: NEAR-OPTIMAL TRAJECTORIES FOR A FLIGHT OF THE QUADROTOR AT EACH LEVEL, DETERMINED BY A SIX-PARAMETER LINE-SEARCH OPTIMISATION WITH NARROWED INITIAL SEARCH SPACE.



(A) COST FUNCTION MINIMA FOR EACH LEVEL. (B) AVERAGE RUN-TIMES FOR EACH LEVEL.

FIGURE 7.25: COMPARISON OF COST FUNCTION MINIMA AND AVERAGE RUN-TIME PER FUNCTION CALL FOR EACH LEVEL, FOR SIX-PARAMETER OPTIMISATION.



(A) MINIMA IDENTIFIED BY NELDER-MEAD METHOD AFTER NARROWING THE SEARCH SPACE WITH THE SIMULATED ANNEALING ALGORITHM. (B) MINIMA IDENTIFIED BY EMPLOYING NELDER-MEAD METHOD WITH ARBITRARY INITIAL CONDITIONS.

FIGURE 7.26: COMPARISON OF APPLYING THE COST FUNCTION SOLUTIONS RESULTING FROM APPLYING THE OPTIMISED TRAJECTORY PROPERTIES OBTAINED FROM ONE LEVEL TO THE OTHERS.

7.7 DISCUSSION OF RESULTS AND CONCLUSIONS

The results presented in this chapter allow some conclusions to be drawn about the impact of model resolution on trajectory optimisation, and how multi-resolution modelling may be employed in such analyses. Additionally, the results of optimising trajectories for wireless power transmission may be discussed more generally.

7.7.1 OPTIMISING TRAJECTORIES FOR WIRELESS POWER TRANSMISSION

It is clear from the presented trajectories and optimisation errors of the investigations described by this chapter that the quadrotor's trajectory may be optimised to improve the safety of the wireless power transmission technology. The results of the each optimisation, while providing different solutions, are intuitive with regards to their outcomes. The component of the quadrotor's velocity which is normal to the laser beam is sufficiently small throughout the flight that the ETS is able to seek, acquire and accurately track the photovoltaic sensor for the duration of the transmission. The curvature of the trajectory and the velocity of the quadrotor throughout the transmission are such that the quadrotor's inclination from the horizontal plane maximises the projected area of the photovoltaic sensor with respect to the laser beam.

The component error histories of the optimised flights indicate two areas for further investigation. First, the laser spot error e_2 is greatest at the very beginning of the simulation, occurring during the energy transmission system's seeking and acquiring phase. Upon acquiring the target and entering tracking mode, this error becomes negligible. Second, for the remainder of the flight, the greatest error occurs in the project area of the sensor surface with respect to the laser beam, characterised by e_1 . Investigation into the source of this error can focus on two components: the relative heading of the quadrotor, determined by the speed of its yaw response; and the inclination of the quadrotor from the horizontal plane, determined by its acceleration along the trajectory.

7.7.2 EFFECTS OF MODEL RESOLUTION ON OPTIMISATION SOLUTIONS

Differences in the optimised trajectories obtained from each level of the multi-agent model family are evident, particularly in the results of the four- and six-variable optimisations. As the goal of the optimisation is to generate trajectories which maximise the safety of wireless power transmission, the issue is deciding which resolution of model to use in realising this goal.

DIFFERENCES BETWEEN LEVELS

It is clear from the results of each of the presented optimisation studies that models of different resolution provide different results. While some of the

solutions produce completely different trajectories for each level, there is commonality between the trajectories of Levels 1 and 2 in some cases. Similarly, Levels 4 and 5 demonstrate similar solutions in some instances. Additionally, the minima derived from Levels 4 and 5 are consistently the smallest, while Level 3 consistently produces the largest minima.

The variance of the optimised trajectory properties and cost function solution are shown to change with the number of variables in the optimisation. In each optimisation of a given number of variables, Case 1 describes the same initial trajectory properties, some of which remain fixed while the rest are varied by the optimisation. As the number of variables increases, so does the variance between the optimised trajectory properties and the resulting trajectories.

These differences may be explained by the fundamental difference in the cost function at each level. It is assumed, from the presented evidence and the similarities between each level of the multi-agent model, that the general shape of the cost function manifold is similar for each level, with some variance in the magnitude of the local and apparent global minima, their locations on the manifold and the gradient of the manifold at a given location. For a given set of initial variables, the optimisation may therefore identify minima in different locations for each level, resulting in solutions with similar cost function values but vastly different trajectory properties. In cases where the gradient of the manifold at the initial location is more consistent between levels, or where the search space has been narrowed around a known minimum, solution with greater consistency between levels are produced.

Increasing the number of variables in the optimisation is shown to increase the potential for identifying non-global minima when using a simple algorithm such as the Nelder-Mead method. As demonstrated, simulated annealing can be used to identify the smallest minimum within specified boundaries, but is time-consuming and produces imprecise solutions. A faster algorithm such as Nelder-Mead provides more accurate results but, as stated, may identify non-global minima and minima at entirely different locations between levels. A combination of methods is therefore suggested. Simulated annealing is employed with the computationally-efficient Level 1 model to narrow the search space around a near-optimal solution. Then, with the assumption that the corresponding minimum of higher-resolution models, whatever its value, is in the same approximate location, the Nelder-Mead method is used with a higher-resolution model to provide a more precise location and solution of this minimum.

SELECTING THE OPTIMAL RESOLUTION

For the benefit of discussion, it is assumed that the Level 5 multi-agent model describes the true behaviour of the system and that the lower resolution models are abstractions of varying degree. In cases where the equivalent minima for

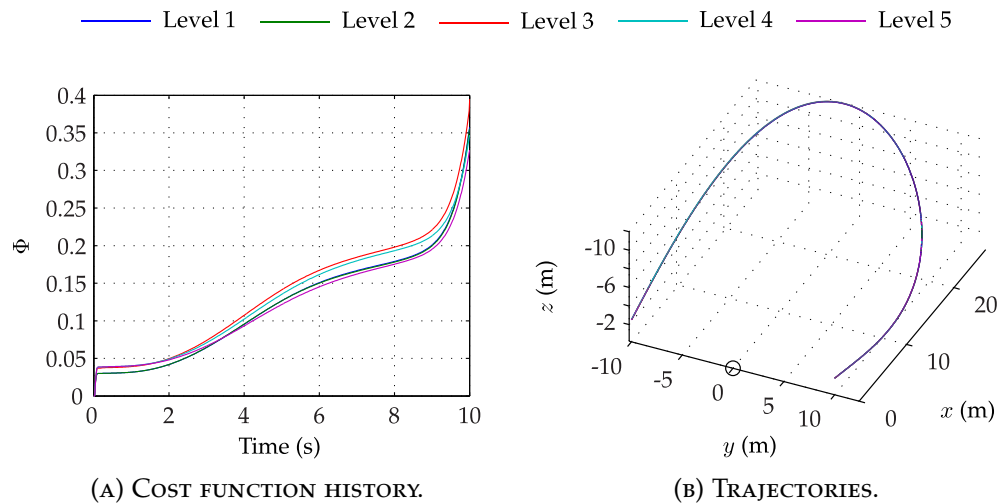


FIGURE 7.27: COST FUNCTION HISTORY AND TRAJECTORIES OF FLIGHT AT EACH LEVEL WHEN FOLLOWING A TRAJECTORY DETERMINED BY OPTIMISATION OF THE LEVEL 1 MULTI-AGENT MODEL.

each level are identified, the optimised trajectories are shown to be similar. The suitability of the solution for a low-resolution model for application to high-resolution model, or the source system in practice, may be investigated. Figure 7.27 shows the cost function histories and trajectories of each level when following a path determined by optimisation of the Level 1 model. Each level is shown to accurately track the specified trajectory, while the variance in the cost function throughout its evolution is shown to be minimal. This suggests that a low-resolution model is sufficient to optimise the trajectories of the system. As they inherently require smaller step-sizes to be solved, higher-resolution models may be useful in optimising the system on shorter time-scales. An example of this would be in the large laser spot position error at the beginning of the transmission.

CHAPTER 8

CONCLUSIONS AND FURTHER WORK

The primary objective of this thesis was to determine the effect, if any, that model resolution has on typical research applications of autonomous systems. Employing the quadrotor as an example, two case studies were investigated: controller design and stability using dynamic inversion, and; trajectory optimisation in a multi-agent scenario. In addition to the focus on multi-resolution modelling, some conclusions may be drawn on wireless power transmission and the benefits of developing predicative models of applications of the technology.

8.1 DEVELOPMENT OF A MULTI-RESOLUTION MODEL

Development of the multi-resolution quadrotor model described in this thesis employed a combination of mechanistic and empirical modelling. This was achieved first by examining modelling precedents in the literature, as described in Chapter 2. In particular, the literature highlighted the lack of high-resolution quadrotor models. With work by Bouabdallah (2007) being a notable exception, the majority of models describe the quadrotor system as a non-linear rigid body with either instantaneous or first-order linear rotor dynamics. Additionally, there was diversity in the methods used to acquire the component models of the system. Rigid-body models were derived from the differing formalisms of Newton-Euler and Euler-Lagrange, which ultimately provide the same end through different means. Rotor models were obtained either empirically through dark grey box system identification or derived analytically and simplified to obtain a first-order response.

The two predominant approaches of mechanistically deriving models and obtaining them empirically through system identification then informed the direction of the succeeding two chapters. Chapter 3 presented the configuration of the quadrotor and introduced the typical system inputs and outputs. This allowed consistency in the structure of the eventual multi-resolution model while

the process models and states of the system could be varied between levels. Opposing approaches to modelling the kinematics and rigid-body dynamics of the quadrotor were presented and discussed. These methods highlighted the differing, but effectively equivalent, approaches one could take to deriving mechanistic models. The forces and moments acting on the rigid body were introduced with reference to the literature. The key contributor in this area was taken to be the thrusts and torques produced by the four rotors, which link the system inputs to the outputs, position and attitude, of the system. Additionally, the variety of approaches to modelling the rotor itself was explored. The concept of pseudo-inputs, a property prevalent in the literature and of great use in control, was introduced and discussed with respect to the quadrotor. Finally, some additional phenomena which affect the quadrotor in ways other than through disturbance forces were discussed.

While Chapter 3 supplied the rigid-body model of the quadrotor, it also introduced several system properties in need of quantification and highlighted the requirement for a rotor model. Chapter 4 thus describes system identification of the Qball-X4 with the goal of completing the model described in the previous chapter. The key contribution of this chapter to the research was the identification of the rotor dynamics, which were found to be represented by a non-linear, multi-order, empirical model. This allowed a high-resolution model to be defined, from which lower resolution models were obtained through abstraction. Validation of this high-resolution model against flight data from the Qball-X4 highlighted the presence of unmodelled dynamics and the possibility of developing higher-still resolution models in future work.

The component models obtained in Chapters 3 and 4 were then discussed in Chapter 5, allowing a multi-resolution family of quadrotor models to be defined. This model family represented a specific case, having selected certain models of the quadrotor over others. A general description of the model family was introduced, relating the consistent system input \mathbf{u} to its output \mathbf{y} through some state \mathbf{x}_i at a level i . Some alternative models for each level were discussed, allowing further exploration of the concept in future work. The definition of the model family thus allowed the two case studies to be explored.

8.2 THE IMPACT OF MODEL RESOLUTION ON SYSTEMS ENGINEERING OBJECTIVES

The multi-resolution model described in Chapter 5 was employed in two case studies with the intention of identifying the impact of model resolution on the outcome of typical systems engineering objectives. Chapter 6 demonstrates the effect resolution has on the design on non-linear dynamic inversion controllers. In such a model-centric approach to controller design, differences in the models are shown to produce inconsistent behaviours in the model family for a given controller resolution. This is as expected. The increase in resolution in the

model family primarily describes two properties. First, additional states are introduced as higher frequencies in the dynamics are included in the model. Second, greater deviations from the trim state are considered, resulting in use of non-linear relationships over linearised models. Thus, for low-speed flight around the hover condition, each model effectively describes the same system. This is evidenced by the identical responses of each closed-loop system when using low bandwidth control action. As the controller becomes more aggressive, the closed-loop dynamics become faster and the aircraft deviates further from the hover state. The resulting differences in the response of each quadrotor model are significant enough to produce an optimal response in one level and an unstable response in another. While models such as those described by Levels 4 and 5 of the model family are unlikely to be used in design of a dynamic inversion controller, specifically because of their resolution, they are ideal for testing of developed controllers before any practical implementation. Although dynamic inversion is particularly popular with the quadrotor when compared to more traditional aircraft, the findings of this investigation are easily transferable to other aircraft of similar configurations, including compound helicopters, multi-copters and ornithopters.

Resolution again has a clear effect on the results of optimising the quadrotor trajectory for wireless power transmission. In this case, the difference is primarily attributed to either a difference in the manifold of the optimisation cost function or identification of minima in significantly different locations. As a result, the trajectories obtained from the optimisation of each level of the multi-agent model vary from similar to wildly different. In this incidence, the identification of which resolution is best is less clear, as the variance in the minima for each case is typically small. While optimisation of Levels 4 and 5 is shown to consistently produce smaller minima, this does not necessarily translate to superior results in practice. Both the wireless power transmission concept and investigation of the effects of resolution on trajectory optimisation in WPT would have great scope for further work and would benefit significantly from it.

Both case studies provide some useful insights in choice of model resolution. In the case of controller design, the choice of resolution is typically made intuitively by the modeller. The results of the case study on dynamic inversion control corroborate this approach, as testing of each controller, model and set of response properties produces typically expected results. While it is then possible, with knowledge of the desired system performance, to intuitively select a single resolution, the multi-resolution concept has its own benefits as described in the next section. The trajectory optimisation is less transparent, as demonstrated by the variety of solutions produced. In this case, further analysis of the agent models would be required to provide some useful relationship between resolution and the optimisation solution.

8.3 BENEFITS OF A MULTI-RESOLUTION MODEL

Chapter 6 employs the concept of dynamic inversion, popularly used to design non-linear control strategies for the quadrotor. The benefit of dynamic inversion lies in the ability of the inverted system model to simplify the system behaviour when placed in closed loop. As the models employed in dynamic inversion in the literature are typically very simple, it is of interest to determine the performance of a typically dynamic inversion controller when applied to a higher-resolution model of the system. The results of Chapter 6 demonstrate the stability and performance of a dynamic inversion controller derived from a model of given resolution when applied to a succession of higher-resolution models. When employing a stiff state feedback law to control the feedback-linearised system, the response of each level in the model family is virtually identical, as expected. Increasing the responsiveness of the controller, the deficiencies of the low-resolution models become clear. The controllers derived from Levels 1 and 2 result in unstable behaviour beyond a certain bandwidth when in closed loop with higher levels, while the controller derived from Level 3 continues to provide stable control at higher bandwidths. The benefit of the multi-resolution approach is thus demonstrated in its ability to more comprehensively test the performance of such model-centric control algorithms in simulation.

Chapter 7 describes a multi-agent model of a wireless power transmission. In addition to providing a platform for investigating behaviours and interactions in a WPT scenario, the multi-resolution capabilities of SiFRE also allow the impact of resolution to be investigated. Optimisation of the quadrotor trajectories in a wireless power transmission improves both the safety and efficiency of the operation, but requires models of the quadrotor, energy transmission system and environment. While the latter two are intentionally described with very simple models, the quadrotor is described at several resolutions. The results of the trajectory optimisation for several cases demonstrate a dependency on the resolution of the model, particularly as the number of variables in the optimisation increases. A multi-resolution model introduces the potential for selecting an optimal resolution in both this case and other optimisations. The resolution and validity of the multi-agent model is balanced with the run-time of the simulation. In optimisations, where the simulation algorithm is executed several dozen times at least, reduction of the lead time on results is crucial.

From the results of these investigations, the primary advantage of employing a multi-resolution model in autonomous systems engineering is clear. By describing a range of models of varying resolution, the model of optimal resolution may be employed for a given objective, balancing resolution and validity with computational efficiency, short lead time and the principle of Ockham's Razor. A simulation engine capable of changing model resolution mid-simulation, such as MAVERIC, provides even finer tuning of this balance. In

investigations such as state estimation or trajectory optimisation, this allows the optimal resolution to be employed at any given time. This ensures that the required precision is employed in certain analyses, while reducing lead time by employing simple models where precision is less important.

8.4 TOWARDS SAFE AND EFFICIENT WIRELESS POWER TRANSMISSION

Aside from consideration of the effects of model resolution, the optimisation of trajectories in wireless power transmission provides some insights into the development of safe and efficient WPT technology. As demonstrated by the results of Chapter 7, the greatest beam-steering error occurs as the energy transmission system visually acquires the photovoltaic sensor to which it must transmit the laser beam. It is crucial to the safety of the operation that the laser beam does not overfill the sensor at any time. The trajectory optimisation is intended to minimise this risk, while safeguards described in the literature are designed to deactivate the laser if overfill is about to occur (or if an object intersects the laser beam). However, as described in the case study, the tracking controller of the ETS requires that the laser spot is visible on the target surface in order to centre it. The remainder of the time, the camera sight is centred on the sensor surface. This introduces the risk of the laser beam overfilling the sensor upon activation. This is dependent on the dimensions of the sensor, beam length and diameter, distance between the laser beam and camera sight vectors and finally any alignment errors in either the camera or laser beam. Miscalculation of any of these introduces the potential for the laser beam to overfill, or miss entirely, the sensor upon activation.

A potential solution to this is to use a low-power beam to ensure an accurate lock on the target sensor. The power transmission beam, aligned with the low-power beam at minimal displacement, is then projected onto the sensor *only after* the target is being accurately tracked. Other approaches, such as slower aircraft flight or beginning the transmission at hover, are less desirable in circumstances such as military operations or search and rescue missions.

8.5 FUTURE WORK

8.5.1 MULTI-RESOLUTION MODELLING

The literature review highlights an absence of multi-resolution modelling in systems engineering, despite its obvious benefits. However, the work described in this thesis highlights some avenues of further investigation.

With regards to the model family described in Chapter 5, areas of expansion or uses of alternative models are obvious. While describing a range of models in an effort to cover several applications, the model family is specifically

oriented to performing analyses in control and navigation. In addition to augmented the model family with levels of higher resolution, it may be of benefit to describe *alternative* models for certain levels, where this alternative model is of greater use in a certain objective than the primary model. An example of this is in investigation of rotor performance, which is shown to be performed with mechanistic rotor models in the literature. Additionally, the impact of using these models in lieu of those employed in the two case studies described in this work is of interest.

As highlighted in previous discussion of results, there is also scope for introducing higher-resolution models in other areas, including the ETS and environment models of the WPT simulation. Additionally, use of on-the-fly variable-resolution models such as those employed in MAVERIC would provide finer tuning of the simulation run-time versus the validity of results.

Finally, to truly test the benefits of a multi-resolution approach to systems engineering and design, the models must be validated and the extents of their validation determined. In doing so, it would be possible to determine how applicable the developed controllers or optimised trajectories are to reality.

8.5.2 WIRELESS POWER TRANSMISSION

FURTHER OPTIMISATION VARIABLES

The optimisations presented in Chapter 7 describe a very specific scenario with the majority of the simulations describing a trajectory with consistent initial and final positions and consistent timespan. Further investigations could explore a greater variety of scenarios, including longer-range transmissions and a greater variety of trajectory curves. Specific properties which could be changed in further efforts include: the number of variables; which properties are varied and which are fixed; boundary conditions; initial conditions; and the values of fixed properties. Additionally, the time properties t_0 and t_f could also be optimised and a time-averaged cost-function minimised.

With regards to the physical systems involved in the power transmission, different configurations may be investigated. Properties such as the position, size and orientation of the photovoltaic sensor, laser emitter and electro-optical sensor may be subject to optimisation. Additionally, an actuated photovoltaic sensor would remove the restrictions on the quadrotor's ability to yaw and is thus worth investigating. These properties and the trajectory of the aircraft may also be optimised with respect to the *efficiency* of the wireless power transmission, which may be investigated either separately or in combination with the safety considerations of the operation. The prospect of using several energy transmission systems and/or optimising power transmission to multiple quadrotors is also fertile ground for research.

As demonstrated by the simulation results, there is a relatively large beam steering error at the beginning of the transmission which occurs due to delay

in the visual tracking response of the ETS. While the beam-steering controller is sufficiently fast for the remainder of the transmission, the sample rate of the camera places a physical limit on the bandwidth of the system. Other solutions that may be explored include feedforward control, allowing the predicted trajectory of the quadrotor to inform the ETS controller, and multi-stage laser beams, where a low-power beam aids target acquisition and tracking and a high-power beam is only projected with the beam-steering error is minimal.

MULTI-RESOLUTION MODELLING

A notable limitation of the SiFRe engine which is not shared by the MAVERIC simulation engine is that a model must maintain the same resolution for the duration of the simulation. As stated previously, the primary error at the beginning of the transmission is the beam-steering error, while the quadrotor attitude becomes the primary concern for the remainder of the flight. A multi-resolution model with mid-simulation “level-switching” would aid in optimisation of the power transmission by considering it in two segments. The first segment, describing the initial target seeking and acquisition, would benefit from a model with higher temporal resolution, while the second segment would describe the remainder of the transmission and employ a low-resolution model.

With regards to continued investigation of the effects of model resolution on optimisation of wireless power transmission, there are several avenues which may be explored. The ETS described in Chapter 7 would be considered a Level 1 model in a multi-resolution ETS model, employing the minimum required relationships to describe the behaviour of the system. As the ETS is driven by two brushless motors, its dynamic model might benefit from a mechanistic model of the motors and consideration of the moments of inertia. The pinhole camera model described in Chapter 7 could be supplanted by a more complex model, describing the effect of lens distortion or framerate on target tracking. Finally, the laser emitter and beam, limited to a geometric model in the given investigations, could be augmented by including radiometric relationships. This would allow the efficiency of the transmission to be determined and allow the impact of optimising the safety of the transmission on its efficiency to be investigated, or vice-versa. Ray-tracing of the laser beam as it diverges would allow over-fill of the photovoltaic sensor to be more accurately modelled. As described in Chapter 5, there is also scope for expanding or augmenting the quadrotor multi-resolution model, permitting the investigation of the effect of specific phenomena, such as ground effect or aerodynamic in sustained forward flight, on the optimisation.

Finally, while the controllers utilised by the quadrotor model at each level are designed to provide consistent responses in closed loop, the controllers employed by the models in Levels 1 and 2 are, by necessity, different from that employed by the remaining models. Further investigations could make use of a

control system which provides responsive and stable control for the quadrotor, independent of resolution.

APPENDIX A

THE SiFRe SIMULATION ENGINE

The SiFRe (Simulation Framework for investigations in Resolution) simulation engine is used to conduct the simulation experiments described in this thesis. The engine uses MATLAB's Object-Oriented Programming (OOP) feature to enable simulation of the behaviours and interaction of several agents simultaneously. These agents may describe: completely different systems; the same system at different levels of resolution; the same system with with different controller or trajectory properties; or any combination of these three. In simulating multiple agents describing a system such as the quadrotor at different resolutions or with different controller properties, SiFRe allows the behaviours of each agent to be quickly compared, using a variety of visual outputs.

This appendix briefly describes the structure and design of the SiFRe engine and presents examples of the visual outputs used to analyse the behaviours of the agents.

A.1 CLASSES

The SiFRe engine is composed of multiple classes, which describe the various agents and the framework of the engine itself.

A.1.1 SIMULATION CLASS

The simulation engine class `cSimEngine` is instantiated as an object which updates the behaviours of each agent and governs the interactions between them. The agent objects and a black box object are input to the simulation engine object upon instantiation. Each agent object has its own time step which is specific to resolution and type. The simulation loop operated by `cSimEngine` updates at a global time step. Each agent is then updated only at its own specific time step, ensuring the agent solver is always running at an optimal step size. The global time step is lower than or equal to the smallest agent time step.

A *blackboard* property is updated with the properties of each agent as the agent itself updates, allowing the behaviours of one agent to depend on those of another. The blackboard property also passes data to the black box object at an additional sample time step, allowing agent outputs to be displayed and analysed after the simulation has ended.

A.1.2 BLACK BOX CLASS

The black box class `cBlackBox` records the properties of each agent at each sample time and allows this data to be presented in a number of formats. Agent inputs, outputs and states are presented both for each agent individually or for all agents simultaneously, allowing comparison of agent behaviours. Geometry models of agents allow animation outputs to be displayed, allowing for a more intuitive representation of agent behaviours and interactions. A switch function allows the user to select the desired output.

A.1.3 AGENT CLASS

The generic agent class `cAgent` describes the properties and methods which are common to all agents, including agent time, agent step size, states, inputs, outputs, the agent type and level of resolution and the integration method used to solve the evolution of the agent dynamics. Both Euler and Runge-Kutta 4th-order solvers are described by the `cAgent` class.

A.1.4 QUADROTOR CLASS

The quadrotor agent class `cQuadrotor` is a subclass of the `cAgent` class and describes all agent properties and methods specific to the quadrotor. This includes models of the system dynamics at multiple levels of resolution, multiple controllers, sensors, subsystems and geometry models.

A.1.5 ETS CLASS

The energy transmission system agent class `cETS` is a subclass of the `cAgent` class and describes all agent properties and methods specific to the ETS. This includes a model of the system dynamics, a multiple-mode controller, a camera sensor model and a geometry model.

A.1.6 OPTIMISER CLASS

The optimiser class `cOptimiser` is a pseudo-agent which is used to determine the weighted error of the wireless power transmission optimisation. Each error is considered an input to the agent. The single agent state is then the cumulative cost over the duration of the simulation.

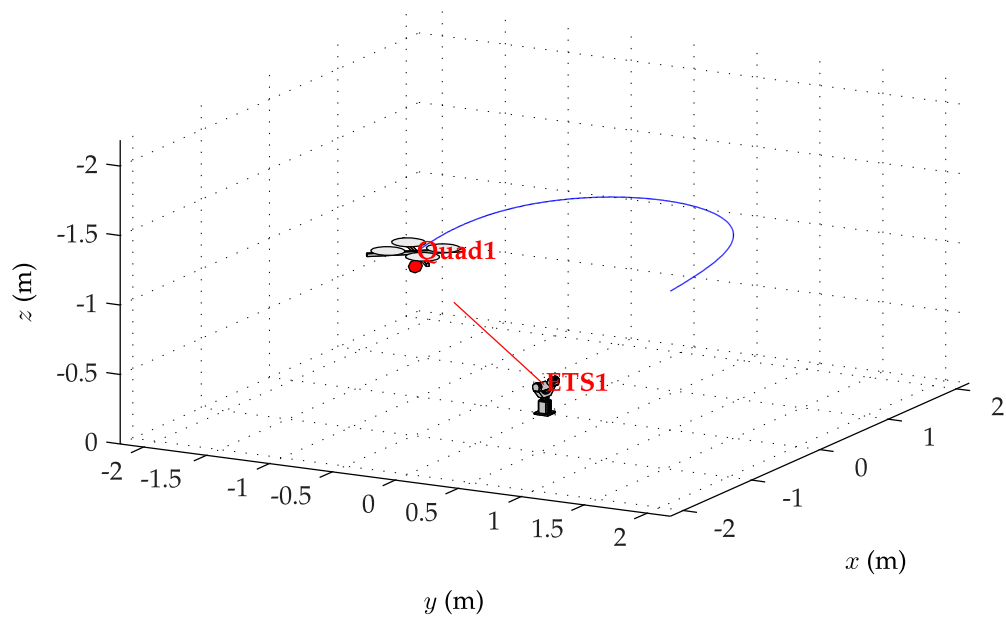


FIGURE A.1: STILL CAPTURE OF ANIMATION SHOWING AGENT MOVEMENTS, WITH A SINGLE QUADROTOR AND ETS. THE ETS TRACKS THE QUADROTOR, WHILE THE QUADROTOR'S YAW DISPLACEMENT IS DEPENDENT ON THE ETS POSITION.

A.2 OUTPUT VISUALS

The black box object which is used to consolidate and display the data from simulations can present the simulation results in a variety of formats, including those seen in Chapters 6 and 7. Additional outputs are shown in Figures A.1, A.2 and A.3.

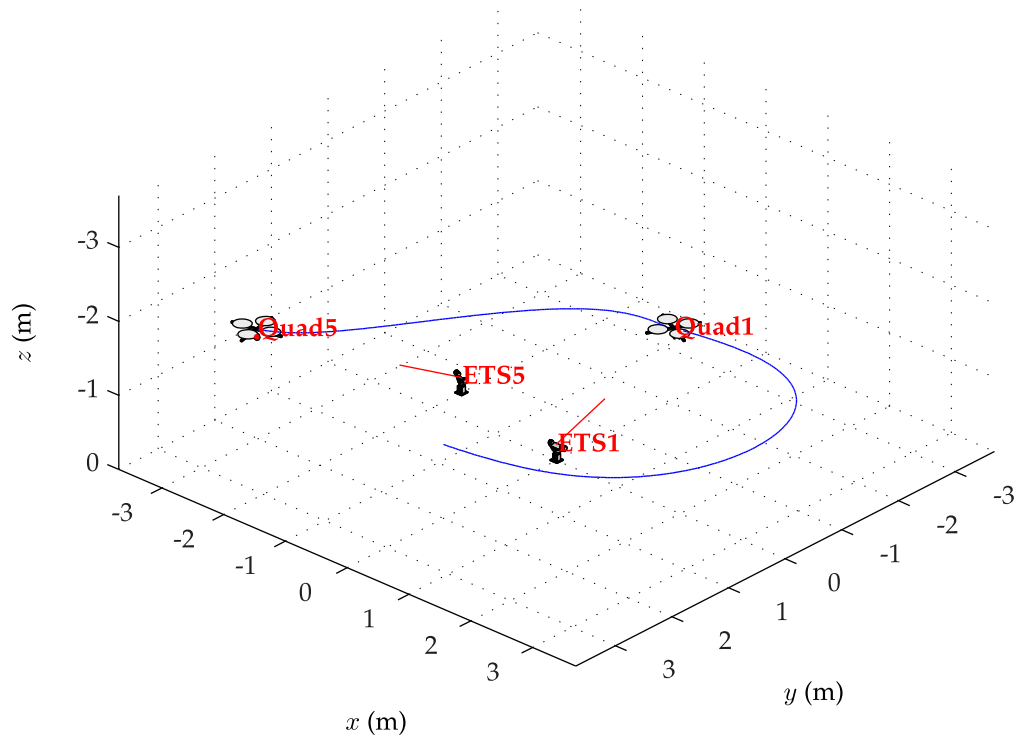


FIGURE A.2: STILL CAPTURE OF ANIMATION SHOWING AGENT MOVEMENTS, TWO QUADROTORS AND TWO ETSs. *Quad1* is a QUADROTOR DESCRIBED BY A LEVEL 1 MODEL WHILE *Quad5* is a QUADROTOR DESCRIBED BY A LEVEL 5 MODEL. EACH QUADROTOR IS PAIRED WITH AN ETS.

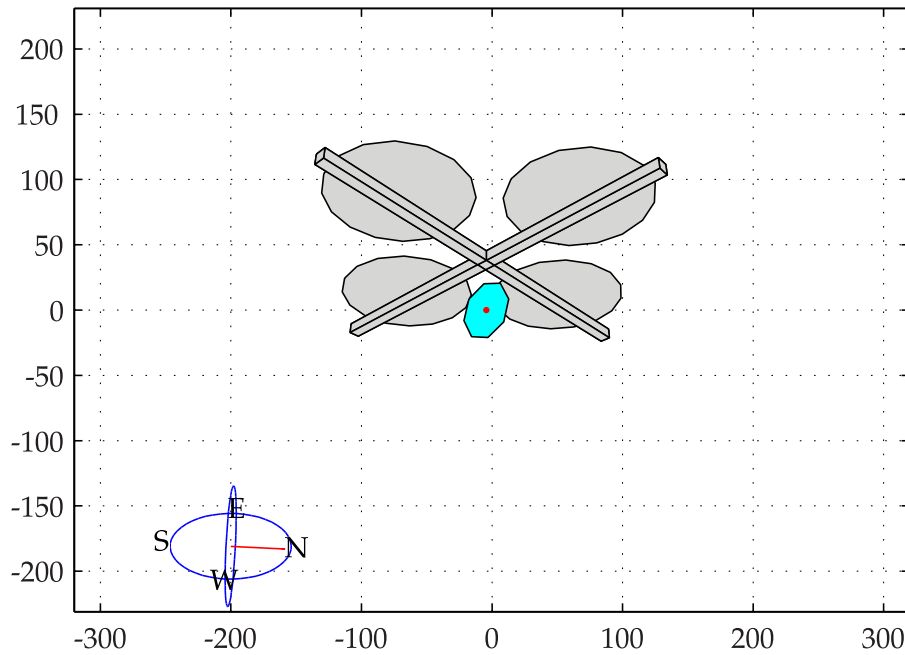


FIGURE A.3: STILL CAPTURE OF ANIMATION FROM THE VIEWPOINT OF THE CAMERA ON THE ETS. THE COMPASS IS USED TO SHOW THE DIRECTION AND INCLINATION OF THE CAMERA.

APPENDIX B

HARDWARE SPECIFICATIONS

The system identification and validation experiments described in Chapter 4 employ Quanser’s Qball-X4 quadrotor and Natural Point’s Optitrack motion capture system. The hardware specifications of each system are detailed here.

B.1 QBALL-X4

The Quanser Qball-X4 is detailed in Quanser (2011). The platform consists of a cross-shaped airframe surrounded by a carbon fibre cage. Four Park 400 brushless motors are controlled by Pentium 18-A Electronic Speed Controllers (ESC). Each motor drives a 10 inch APC 10x4.7 propeller. The ESCs are connected to Quanser’s HiQ Data Acquisition Card (DAQ), which receives data from the on-board Inertial Measurement Unit (IMU) and provides PWM commands to the ESCs. A Gumstix embedded computer controls the operation of the DAQ and allows flight controllers to be designed in Simulink to be deployed onboard the Qball-X4 via a wifi connection.

The IMU specifications for the Qball-X4 are detailed by Analog Devices, Inc (2009). The IMU consists of:

- Triaxial gyroscope, with dynamic range set to $\pm 75^\circ/\text{s}$ and resolution of $0.0125^\circ/\text{s}/\text{LSB}$.
- Triaxial accelerometer, with dynamic range of $\pm 18\text{ g}$ and resolution $3.33\text{ mg}/\text{LSB}$.
- Triaxial magnetometer, with dynamic range of $\pm 3.5\text{ gauss}$ and resolution $0.5\text{ mgauss}/\text{LSB}$.

B.2 OPTITRACK MOTION CAPTURE SYSTEM

The MAST Laboratory’s Optitrack system consists of 18 V100:R2 infrared cameras (Natural Point, Inc, 2012). These are connected in groups of six to three

TABLE B.1: OPTITRACK MOTION CAPTURE SYSTEM SPECIFICATION.

PROPERTY	VALUE	UNIT
Resolution	640×480	pixel
Frame rate	up to 100	fps
Latency	10	ms
Horizontal FOV	46	°
Vertical FOV	35	°

USB hubs which are in turn connected to the MAST Laboratory's Ground Control Station (GCS). The basic camera specification is provided by Table B.1.

APPENDIX C

MAST LABORATORY SETUP

The Micro Air Systems Technologies (MAST) Laboratory is used for flight testing of unmanned aircraft developed at the University of Glasgow. The lab comprises an 18-camera Optitrack motion capture system for tracking of aircraft within a designated flight volume. Each camera is able to track multiple reflective markers within its field of view. Use of multiple cameras then allows the three-dimensional positions of the markers to be calculated, as the camera positions relative to each other are known and obtained during calibration.

Groups of markers may be defined as *trackables* assigned to a single rigid body and the positions of the markers relative to each other then provide the attitude of the body. Tracking of a single marker or a trackable by the Optitrack system requires that each marker is visible to at least three cameras for the duration of a flight. The camera placement must therefore be optimised to provide comprehensive coverage in the designated flight volume.

C.1 CAMERA OPTIMISATION

With the dimensions of the MAST lab known, a model of the camera system was developed to optimise the placement of each camera. The model takes each camera position and orientation as an input and provides the percentage coverage over the flight space, designated as a $3.7 \times 6.85 \times 2.2$ m volume filling approximately half of the MAST Laboratory.

Two-dimensional tracking of a single marker in the by a camera requires that:

1. The marker is within the camera's field of view, which is 56° horizontally by 42° vertically.
2. The marker is within 7 m of the camera, which is the maximum distance to guarantee visibility of markers of the supplied size, under typical lighting conditions.

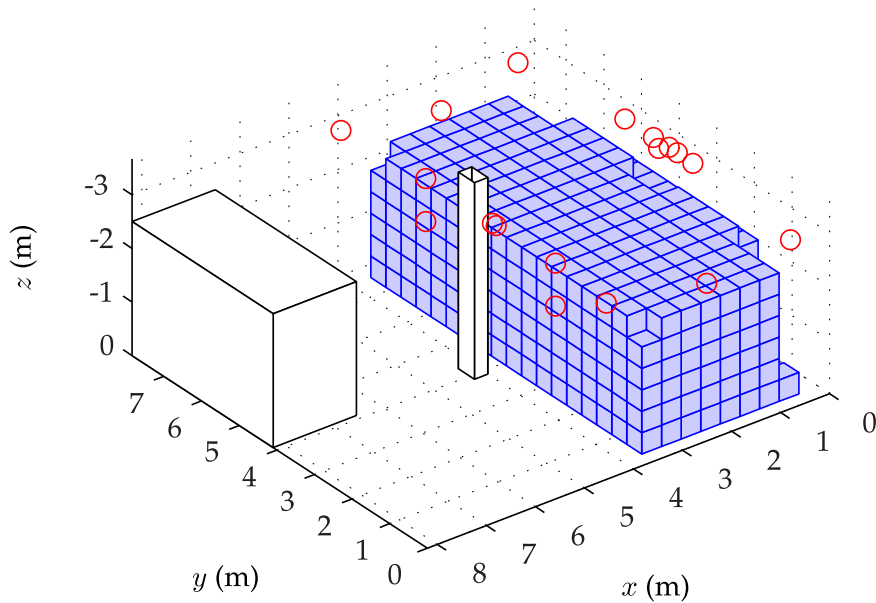


FIGURE C.1: SIMULATED CAMERA COVERAGE OF FLIGHT VOLUME.

3. The marker is not obstructed from view by an object between it and the camera, such as the pillar in the centre of the MAST lab.

Three-dimensional tracking of the marker in the flight space then requires that the marker is visible to at least three cameras. Using these criteria, the cameras were positioned such that the volume within which a marker could be tracked was maximised. The Optitrack system was then calibrated using the supplied software.

C.2 EXPERIMENTAL FLIGHTS

The autonomous flight capabilities of the MAST Laboratory are still a work in progress at the time of publication. However, some basic autonomous flights have taken place, using both the Qball and custom quadrotor systems built in-house at the University of Glasgow. Figure C.2 shows trajectory data, capture by the Optitrack system, of the autonomous flight of a custom-built quadrotor. Figure C.3 shows captures from videos of the Qball-X4 and a custom-built quadrotor performing autonomous flights.

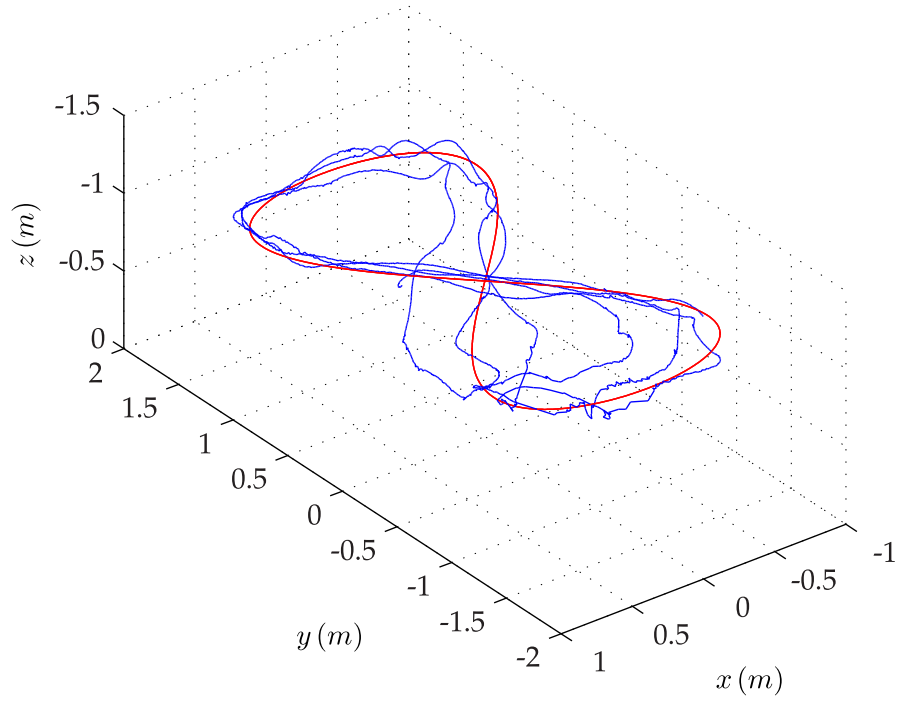


FIGURE C.2: RECORDED FLIGHT TRAJECTORY COMPARED AGAINST COMMANDED TRAJECTORY, DURING AN AUTONOMOUS FLIGHT OF A MAST LABORATORY QUADROTOR.



(A) QBALL-X4 IN FLIGHT.



(B) TEGO3 IN FLIGHT.

FIGURE C.3: CAPTURES OF QUADROTOR AUTONOMOUS FLIGHTS IN THE MAST LABORATORY.

APPENDIX D

DERIVATION OF RIGID BODY DYNAMICS

Chapter 3 describes the rigid body dynamics of the quadrotor using models derived from both Newton-Euler and Euler-Lagrange formalisms. The full derivations are presented here for reference.

D.1 USING NEWTON-EULER FORMALISM

The rigid-body dynamics of the quadrotor are derived in full using Newton-Euler formalism.

D.1.1 TRANSLATIONAL MOTION

The linear momentum of a body in the inertial frame \mathcal{W} is given by

$$\mathbf{p} = m\dot{\mathbf{r}}$$

The force in the inertial frame is then given by the rate of change of linear momentum with time. Differentiating the linear momentum therefore gives

$$\mathbf{F}^{\mathcal{W}} = m\ddot{\mathbf{r}} \tag{D.1}$$

which is sufficient for describing translational motion in the inertial frame.

To describe motion in the body-fixed frame \mathcal{B} , the transformations $\mathbf{v} = \mathbf{R}_{\mathcal{W}}^{\mathcal{B}}\dot{\mathbf{r}}$ and $\mathbf{F} = \mathbf{F}^{\mathcal{B}} = \mathbf{R}_{\mathcal{W}}^{\mathcal{B}}\mathbf{F}^{\mathcal{W}}$ are employed. The linear momentum in the inertial frame is alternately given by

$$\mathbf{p} = m\mathbf{R}_{\mathcal{B}}^{\mathcal{W}}\mathbf{v}$$

The force in the body-fixed frame is then given by

$$\begin{aligned}\mathbf{F} &= \mathbf{R}_{\mathcal{W}}^{\mathcal{B}} \frac{d}{dt} \left(m \mathbf{R}_{\mathcal{B}}^{\mathcal{W}} \mathbf{v} \right) \\ &= m \mathbf{R}_{\mathcal{W}}^{\mathcal{B}} \left(\mathbf{R}_{\mathcal{B}}^{\mathcal{W}} \dot{\mathbf{v}} + \dot{\mathbf{R}}_{\mathcal{B}}^{\mathcal{W}} \mathbf{v} \right) \\ &= m \mathbf{R}_{\mathcal{W}}^{\mathcal{B}} \left(\mathbf{R}_{\mathcal{B}}^{\mathcal{W}} \dot{\mathbf{v}} + \mathbf{R}_{\mathcal{B}}^{\mathcal{W}} [\boldsymbol{\omega}]_{\times} \mathbf{v} \right)\end{aligned}$$

which gives the translational dynamics of a rigid body, described in the body-fixed frame, as

$$\mathbf{F} = m\dot{\mathbf{v}} + \boldsymbol{\omega} \times m\mathbf{v} \quad (\text{D.2})$$

D.1.2 ROTATIONAL MOTION

The angular momentum of a body in the inertial frame \mathcal{W} is given by

$$\mathbf{L} = \mathbf{I}^{\mathcal{W}} \boldsymbol{\omega}^{\mathcal{W}}$$

where $\mathbf{I}^{\mathcal{W}} = \mathbf{I}^{\mathcal{W}}(t)$ is the inertia matrix of the body, described in the inertial frame, and is related to the static inertia matrix in the body-fixed frame \mathcal{B} by $\mathbf{I}^{\mathcal{W}} = \mathbf{R}_{\mathcal{B}}^{\mathcal{W}} \mathbf{I}_{\mathcal{B}}^{\mathcal{B}}$.

The moment in the inertial frame is then given by the rate of change of angular momentum with time. Differentiating the angular momentum therefore gives

$$\begin{aligned}\mathbf{M}^{\mathcal{W}} &= \frac{d}{dt} \left(\mathbf{I}^{\mathcal{W}} \boldsymbol{\omega}^{\mathcal{W}} \right) \\ &= \frac{d}{dt} \left(\mathbf{R}_{\mathcal{B}}^{\mathcal{W}} \mathbf{I}_{\mathcal{B}}^{\mathcal{B}} \boldsymbol{\omega}^{\mathcal{W}} \right) \\ &= \mathbf{R}_{\mathcal{B}}^{\mathcal{W}} \mathbf{I}_{\mathcal{B}}^{\mathcal{B}} \dot{\boldsymbol{\omega}}^{\mathcal{W}} + \dot{\mathbf{R}}_{\mathcal{B}}^{\mathcal{W}} \mathbf{I}_{\mathcal{B}}^{\mathcal{B}} \boldsymbol{\omega}^{\mathcal{W}} + \mathbf{R}_{\mathcal{B}}^{\mathcal{W}} \dot{\mathbf{I}}_{\mathcal{B}}^{\mathcal{B}} \boldsymbol{\omega}^{\mathcal{W}} \\ &= \mathbf{I}^{\mathcal{W}} \dot{\boldsymbol{\omega}}^{\mathcal{W}} + [\boldsymbol{\omega}^{\mathcal{W}}]_{\times} \mathbf{R}_{\mathcal{B}}^{\mathcal{W}} \mathbf{I}_{\mathcal{B}}^{\mathcal{B}} \boldsymbol{\omega}^{\mathcal{W}} - \mathbf{R}_{\mathcal{B}}^{\mathcal{W}} \mathbf{I}_{\mathcal{B}}^{\mathcal{B}} [\boldsymbol{\omega}^{\mathcal{W}}]_{\times} \boldsymbol{\omega}^{\mathcal{W}}\end{aligned}$$

This provides Euler's equation, which is described in the inertial frame by

$$\mathbf{M}^{\mathcal{W}} = \mathbf{I}^{\mathcal{W}} \dot{\boldsymbol{\omega}}^{\mathcal{W}} + \boldsymbol{\omega}^{\mathcal{W}} \times \mathbf{I}^{\mathcal{W}} \boldsymbol{\omega}^{\mathcal{W}} \quad (\text{D.3})$$

Noting the transformations $\mathbf{M} = \mathbf{M}^{\mathcal{B}} = \mathbf{R}_{\mathcal{W}}^{\mathcal{B}} \mathbf{M}^{\mathcal{W}}$, $\boldsymbol{\omega} = \boldsymbol{\omega}^{\mathcal{B}} = \mathbf{R}_{\mathcal{W}}^{\mathcal{B}} \boldsymbol{\omega}^{\mathcal{W}}$ and $\dot{\boldsymbol{\omega}} = \dot{\boldsymbol{\omega}}^{\mathcal{B}} = \mathbf{R}_{\mathcal{W}}^{\mathcal{B}} \dot{\boldsymbol{\omega}}^{\mathcal{W}}$, Euler's equation may be expressed in the body-fixed frame by

$$\begin{aligned}\mathbf{R}_{\mathcal{B}}^{\mathcal{W}} \mathbf{M} &= \mathbf{R}_{\mathcal{B}}^{\mathcal{W}} \mathbf{I}_{\mathcal{B}}^{\mathcal{B}} \mathbf{R}_{\mathcal{B}}^{\mathcal{W}} \dot{\boldsymbol{\omega}} + \mathbf{R}_{\mathcal{B}}^{\mathcal{W}} \boldsymbol{\omega} \times \mathbf{R}_{\mathcal{B}}^{\mathcal{W}} \mathbf{I}_{\mathcal{B}}^{\mathcal{B}} \mathbf{R}_{\mathcal{B}}^{\mathcal{W}} \boldsymbol{\omega} \\ &= \mathbf{R}_{\mathcal{B}}^{\mathcal{W}} (\mathbf{I} \dot{\boldsymbol{\omega}} + \boldsymbol{\omega} \times \mathbf{I} \boldsymbol{\omega})\end{aligned}$$

which gives the rotational dynamics of a rigid body, described in the body-fixed frame, as

$$\mathbf{M} = \mathbf{I} \dot{\boldsymbol{\omega}} + \boldsymbol{\omega} \times \mathbf{I} \boldsymbol{\omega} \quad (\text{D.4})$$

D.2 USING EULER-LAGRANGE FORMALISM

The rigid-body dynamics of the quadrotor are derived in full using Euler-Lagrange formalism. Assumptions employed to simplify the resulting model are stated.

D.2.1 TRANSLATIONAL MOTION WITH VELOCITIES IN THE INERTIAL FRAME

The generalised coordinates for translational motion are $\mathbf{r} = [x, y, z]^T$ and generalised forces are the body forces described in the inertial frame, denoted \mathbf{Q}_F .

The translational kinetic energy is $T_{\text{trans}} = \frac{1}{2}m\dot{\mathbf{r}}^T\dot{\mathbf{r}}$ and the gravitational potential is $V_{\text{trans}} = mgz$. The Lagrangian is then

$$\begin{aligned} L_{\text{trans}} &= T_{\text{trans}} - V_{\text{trans}} \\ &= \frac{1}{2}m\dot{\mathbf{r}}^T\dot{\mathbf{r}} - mgz \end{aligned}$$

The Euler-Lagrange equation is

$$\frac{d}{dt} \left(\frac{\partial L_{\text{trans}}}{\partial \dot{\mathbf{r}}} \right) - \frac{\partial L_{\text{trans}}}{\partial \mathbf{r}} = \mathbf{Q}_F \quad (\text{D.5})$$

Substituting the Lagrangian provides the result

$$m\ddot{\mathbf{r}} + mg\hat{\mathbf{z}} = \mathbf{Q}_F$$

D.2.2 TRANSLATIONAL MOTION WITH VELOCITIES IN THE BODY-FIXED FRAME

The generalised coordinates for translational motion are $\mathbf{r} = [x, y, z]^T$ while the generalised linear forces are denoted \mathbf{Q}_F .

The translational kinetic energy is $T_{\text{trans}} = \frac{1}{2}m\mathbf{v}^T\mathbf{v}$ and the gravitational potential is $V_{\text{trans}} = mgz$. The body velocity vector \mathbf{v} is related to the velocity in \mathcal{W} by $\dot{\mathbf{r}} = \mathbf{R}_B^{\mathcal{W}}\mathbf{v}$. The Lagrangian is then

$$\begin{aligned} L_{\text{trans}} &= T_{\text{trans}} - V_{\text{trans}} \\ &= \frac{1}{2}m(\mathbf{R}_B^{\mathcal{W}}\dot{\mathbf{r}})^T\mathbf{R}_B^{\mathcal{W}}\dot{\mathbf{r}} - mgz \\ &= \frac{1}{2}m\dot{\mathbf{r}}^T\mathbf{R}_B^{\mathcal{W}}\mathbf{R}_B^{\mathcal{W}}\dot{\mathbf{r}} - mgz \\ &= \frac{1}{2}m\dot{\mathbf{r}}^T\dot{\mathbf{r}} - mgz \end{aligned}$$

This again provides the result

$$m\ddot{\mathbf{r}} + mg\hat{\mathbf{z}} = \mathbf{Q}_F$$

To obtain the translational response as described in the body-fixed frame, again consider the relationship $\dot{\mathbf{r}} = \mathbf{R}_B^W \mathbf{v}$, which provides the derivative

$$\begin{aligned}\dot{\mathbf{r}} &= \dot{\mathbf{R}}_B^W \mathbf{v} + \mathbf{R}_B^W \dot{\mathbf{v}} \\ &= \mathbf{R}_B^W (\boldsymbol{\omega} \times \mathbf{v}) + \mathbf{R}_B^W \dot{\mathbf{v}}\end{aligned}$$

from the proof described in Section D.3. The translational dynamics are thus described in \mathcal{B} by

$$\dot{\mathbf{v}} = \mathbf{R}_W^B \left(\frac{1}{m} \mathbf{Q}_F + g \hat{\mathbf{z}} \right) - \boldsymbol{\omega} \times \mathbf{v} \quad (\text{D.6})$$

D.2.3 ROTATIONAL MOTION

The generalised coordinates for rotational motion are $\boldsymbol{\eta} = [\phi, \theta, \psi]^T$ and the generalised forces are the body moments denoted by \mathbf{Q}_M .

The rotational kinetic energy is $T_{\text{rot}} = \frac{1}{2} \boldsymbol{\omega}^T \mathbf{I} \boldsymbol{\omega}$. The angular velocity vector is related to the Euler rates by $\boldsymbol{\omega} = \mathbf{J}_\eta \dot{\boldsymbol{\eta}}$. The Lagrangian is then

$$\begin{aligned}L_{\text{rot}} &= T_{\text{rot}} \\ &= \frac{1}{2} \dot{\boldsymbol{\eta}}^T \mathbf{J}_\eta^T \mathbf{I} \mathbf{J}_\eta \dot{\boldsymbol{\eta}}\end{aligned}$$

The Euler-Lagrange equation is

$$\frac{d}{dt} \left(\frac{\partial L_{\text{rot}}}{\partial \dot{\boldsymbol{\eta}}} \right) - \frac{\partial L_{\text{rot}}}{\partial \boldsymbol{\eta}} = \mathbf{Q}_M$$

Let $\mathbb{J} = \mathbb{J}(\boldsymbol{\eta}) = \mathbf{J}_\eta^T \mathbf{I} \mathbf{J}_\eta$. The Euler-Lagrange equation for rotational motion is then

$$\frac{d}{dt} \left(\dot{\boldsymbol{\eta}}^T \mathbb{J} \right) - \frac{1}{2} \frac{\partial}{\partial \boldsymbol{\eta}} \left(\dot{\boldsymbol{\eta}}^T \mathbb{J} \dot{\boldsymbol{\eta}} \right) = \mathbf{Q}_M$$

since \mathbb{J} is symmetric. The rotational dynamics are thus described by

$$\mathbb{J} \ddot{\boldsymbol{\eta}} + \dot{\mathbb{J}} \dot{\boldsymbol{\eta}} - \frac{1}{2} \frac{\partial}{\partial \boldsymbol{\eta}} \left(\dot{\boldsymbol{\eta}}^T \mathbb{J} \dot{\boldsymbol{\eta}} \right) = \mathbf{Q}_M$$

which then becomes

$$\mathbb{J} \ddot{\boldsymbol{\eta}} + C(\boldsymbol{\eta}, \dot{\boldsymbol{\eta}}) = \mathbf{Q}_M \quad (\text{D.7})$$

The Coriolis term $C(\boldsymbol{\eta}, \dot{\boldsymbol{\eta}})$ describes the gyroscopic and centrifugal terms of the vehicle and is defined by

$$C(\boldsymbol{\eta}, \dot{\boldsymbol{\eta}}) = \dot{\mathbb{J}} - \frac{1}{2} \frac{\partial}{\partial \boldsymbol{\eta}} \left(\dot{\boldsymbol{\eta}}^T \mathbb{J} \right)$$

Substitution of the relationship $\boldsymbol{\omega} = \mathbf{J}_\eta \dot{\boldsymbol{\eta}}$ into Equation (D.4) then provides a solution identical to that described by Equation (D.7), where the generalised moments are related to the body moments by $\mathbf{Q} = \mathbf{J}_\eta^T \mathbf{M}$.

D.3 PROOF FOR DERIVATIVE OF ROTATION MATRIX

Consider two frames of reference, the inertially-fixed frame \mathcal{A} and the rotating frame \mathcal{B} . If the origins of \mathcal{A} and \mathcal{B} are collocated, then a point \mathbf{r} , fixed in \mathcal{B} can be expressed in \mathcal{A} as

$$\mathbf{r}^A = \mathbf{R}_B^A \mathbf{r}^B \quad (\text{D.8})$$

As \mathbf{r} is fixed in \mathcal{B} , the relationship $\dot{\mathbf{r}}^B$ holds true. Taking the derivative then gives

$$\dot{\mathbf{r}}^A = \dot{\mathbf{R}}_B^A \mathbf{r}^B \quad (\text{D.9})$$

The angular velocity of \mathcal{B} is $\boldsymbol{\omega}$. This is expressed in \mathcal{A} as $\boldsymbol{\omega}^A$. The point \mathbf{r} therefore has the angular velocity

$$\begin{aligned} \dot{\mathbf{r}}^A &= \boldsymbol{\omega}^A \times \mathbf{r}^A \\ &= [\boldsymbol{\omega}^A]_{\times} \mathbf{r}^A \end{aligned} \quad (\text{D.10})$$

Substituting into Equation (D.9),

$$\begin{aligned} \dot{\mathbf{R}}_B^A \mathbf{r}^B &= [\boldsymbol{\omega}^A]_{\times} \mathbf{r}^A \\ &= [\boldsymbol{\omega}^A]_{\times} \mathbf{R}_B^A \mathbf{r}^B \end{aligned} \quad (\text{D.11})$$

The derivative of the rotation matrix \mathbf{R}_B^A is thus

$$\dot{\mathbf{R}}_B^A = [\boldsymbol{\omega}^A]_{\times} \mathbf{R}_B^A \quad (\text{D.12})$$

for all \mathbf{r}^B . Furthermore, since $[\mathbf{R}\boldsymbol{\omega}]_{\times} = \mathbf{R}[\boldsymbol{\omega}]_{\times} \mathbf{R}^T$ and $\boldsymbol{\omega}^A = \mathbf{R}_B^A \boldsymbol{\omega}^B$, the relationships

$$\begin{aligned} \dot{\mathbf{R}}_B^A &= \mathbf{R}_B^A [\boldsymbol{\omega}^B]_{\times} \\ \dot{\mathbf{R}}_A^B &= -\mathbf{R}_A^B [\boldsymbol{\omega}^A]_{\times} \\ &= -[\boldsymbol{\omega}^B]_{\times} \mathbf{R}_A^B \end{aligned}$$

are also true.

APPENDIX E

ROTOR CHARACTERISATION DATA

The full set of data for characterising each of the Qball rotors is presented. An axial force and torque transducer was used to measure the thrust and torque from each propeller, which were then captured in LabVIEW. A strobe light was used to determine the rotorspeed.

E.1 LOADCELL CALIBRATION

E.1.1 THRUST TRANSDUCER

The thrust transducer is calibrated with a series of reference masses, exerting an axial force which is shown to have a linear relationship with the voltage signal produced by the transducer. Table E.1 and Figure E.1 shows the results of the axial force loadcell calibration. From the collected data, the relationship

$$V = -2.3363m - 0.1156 \quad (\text{E.1})$$

is obtained. Noting that $F = mg$, the thrust or axial force is then related to the transducer voltage by

$$T = -4.1976(V - V_0) \quad (\text{E.2})$$

where V_0 is the zero-thrust voltage. Repeated calibrations performed at other times show a consistency in the gradient but not the absolute relationship between thrust and voltage, thus the zero-thrust voltage is taken during each test of the rotors.

E.1.2 TORQUE TRANSDUCER

The torque loadcell is calibrated by using the reference masses to exert a force through a point at distance L from the axis of the loadcell. Masses are applied such that both positive and negative torques are produced. Applying a positive torque to the transducer, the relationship between mass and voltage is found to

TABLE E.1: DATA SAMPLES FOR THRUST LOADCELL CALIBRATION.

MASS (kg)	VOLTAGE (V)		
	SET 1	SET 2	SET 3
0.0	-0.1166	-0.1145	-0.1064
0.1	-0.3529	-0.3496	-0.3434
0.2	-0.5862	-0.5834	-0.5801
0.3	-0.8180	-0.8183	-0.8160
0.4	-1.0569	-1.0522	-1.0511
0.5	-1.2892	-1.2830	-1.2854
0.6	-1.5235	-1.5122	-1.5200
0.7	-1.7558	-1.7387	-1.7534
0.8	-1.9893	-1.9682	-1.9874

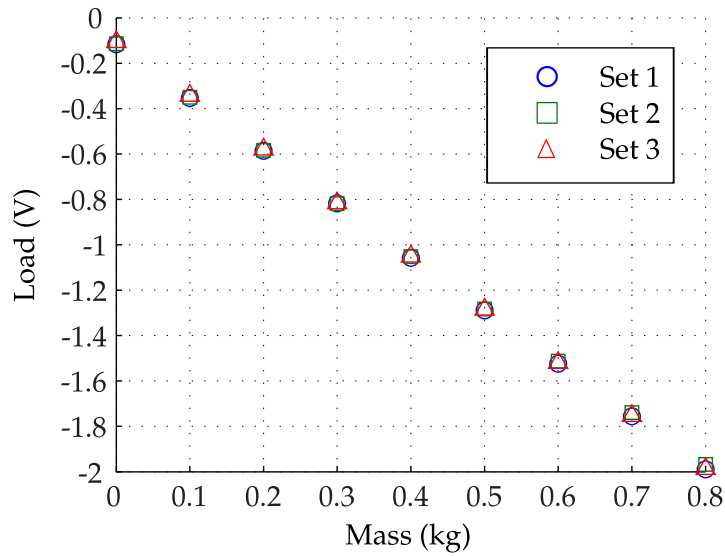


FIGURE E.1: DATA SAMPLES FOR THRUST LOADCELL CALIBRATION, DEMONSTRATING LINEAR RELATIONSHIP.

TABLE E.2: DATA SAMPLES FOR CLOCKWISE TORQUE LOADCELL CALIBRATION.

MASS (kg)	VOLTAGE (V)		
	SET 1	SET 2	SET 3
0.0	0.1588	0.1522	0.1276
0.1	0.6527	0.6359	0.6195
0.2	1.1443	1.0887	1.1118
0.3	1.6335	1.5592	1.6093
0.4	2.1345	2.0355	2.1133
0.5	2.6309	2.5006	2.6186

TABLE E.3: DATA SAMPLES FOR COUNTER-CLOCKWISE TORQUE LOADCELL CALIBRATION.

MASS (kg)	VOLTAGE (V)		
	SET 1	SET 2	SET 3
0.0	-0.0190	-0.0179	-0.0500
0.1	-0.5065	-0.5081	-0.5376
0.2	-0.9958	-0.9950	-1.0171
0.3	-1.4870	-1.4859	-1.5045
0.4	-1.9684	-1.9712	-1.9901
0.5	-2.4655	-2.4554	-2.4689

be

$$V = 4.8705m + 0.1450 \quad (\text{E.3})$$

while applying a negative torque provides the relationship

$$V = -4.8682m - 0.0298 \quad (\text{E.4})$$

Averaging the two gradients and noting that $Q = mgR$, where the moment arm is $R = 0.1$ m, the relationship between torque and voltage is found to be

$$Q = 0.2014(V - V_0) \quad (\text{E.5})$$

E.2 STEADY-STATE RELATIONSHIPS

The steady-state rotor relationships are obtained by recording the rotorspeed, thrust and torque values across a range of PWM values for each rotor. Additionally, the voltage supplied to the rotor by the power source is recorded and is found to affect the rotor performance.

Figures E.4 to E.7 show the relationships of rotorspeed, thrust and torque with supplied voltage and PWM for each rotor, using a Lithium-Polymer battery to provide power to the motor, hence the variation in voltage level between each dataset. Figure E.8 shows the rotor relationships when a main-connected power supply is used to regulate the voltage.

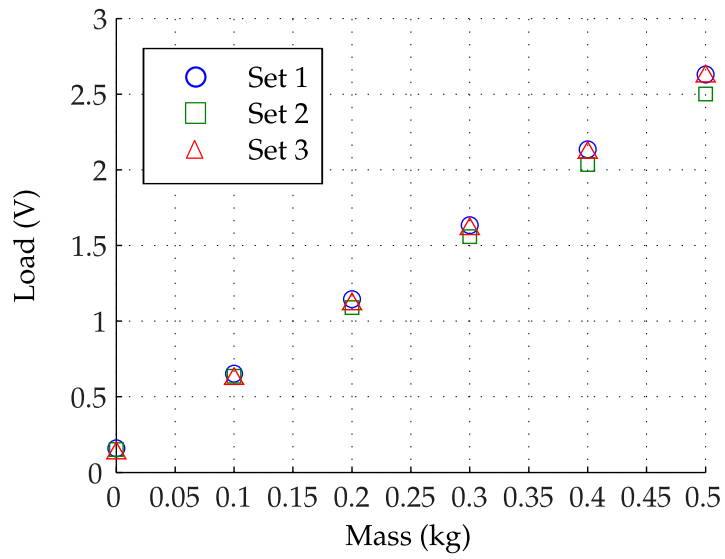


FIGURE E.2: DATA SAMPLES FOR TORQUE LOADCELL CALIBRATION IN THE CLOCKWISE DIRECTION, WITH LINEAR LINE OF BEST FIT.

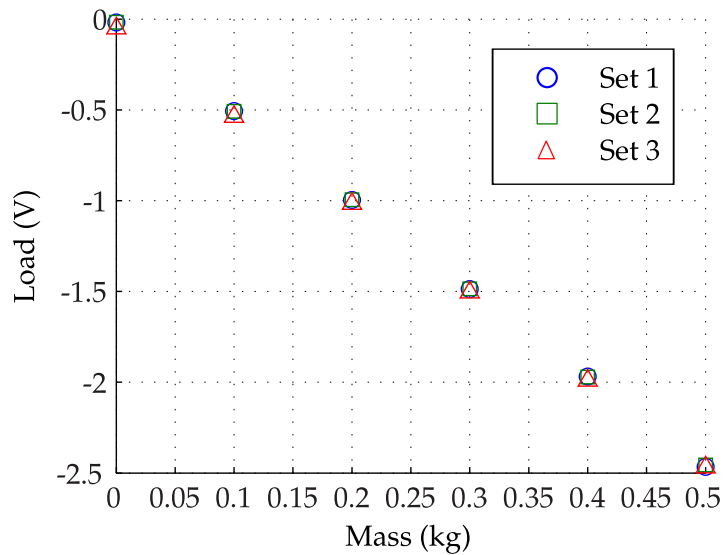


FIGURE E.3: DATA SAMPLES FOR TORQUE LOADCELL CALIBRATION IN THE COUNTER-CLOCKWISE DIRECTION, WITH LINEAR LINE OF BEST FIT.

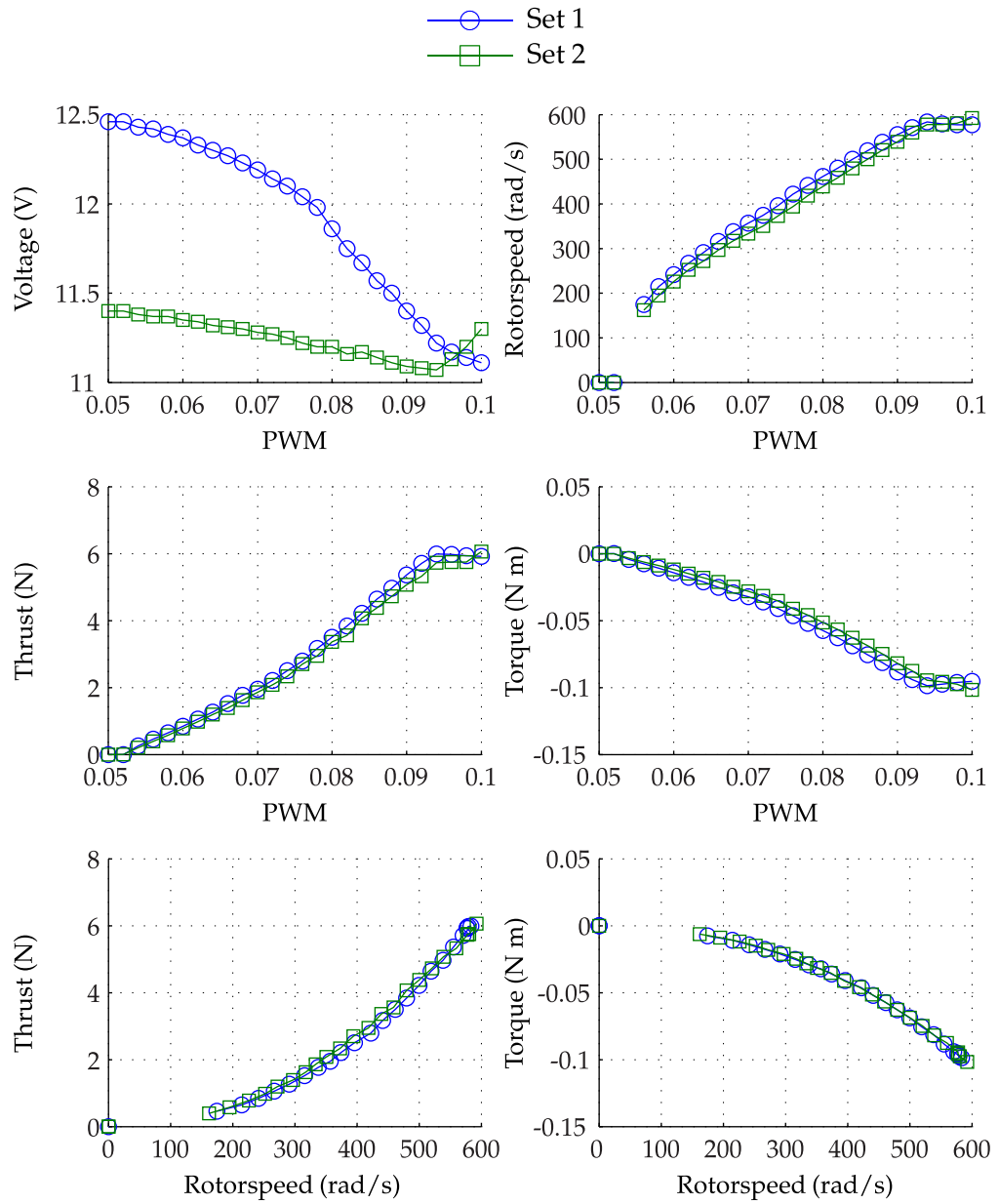


FIGURE E.4: ROTOR 1 (REAR) CHARACTERISATION DATA.

It is apparent that each experiment presents a different relationship between the rotor behaviour and the input PWM signal. A consistent relationship is therefore not possible in an accurate model. As presented in Section 4.5, the rotorspeed, thrust and torque may be related to the PWM signal and the voltage supplied to the motor during each experiment. This model is constructed using the consolidated experimental data shown in Figures E.4 to E.8.

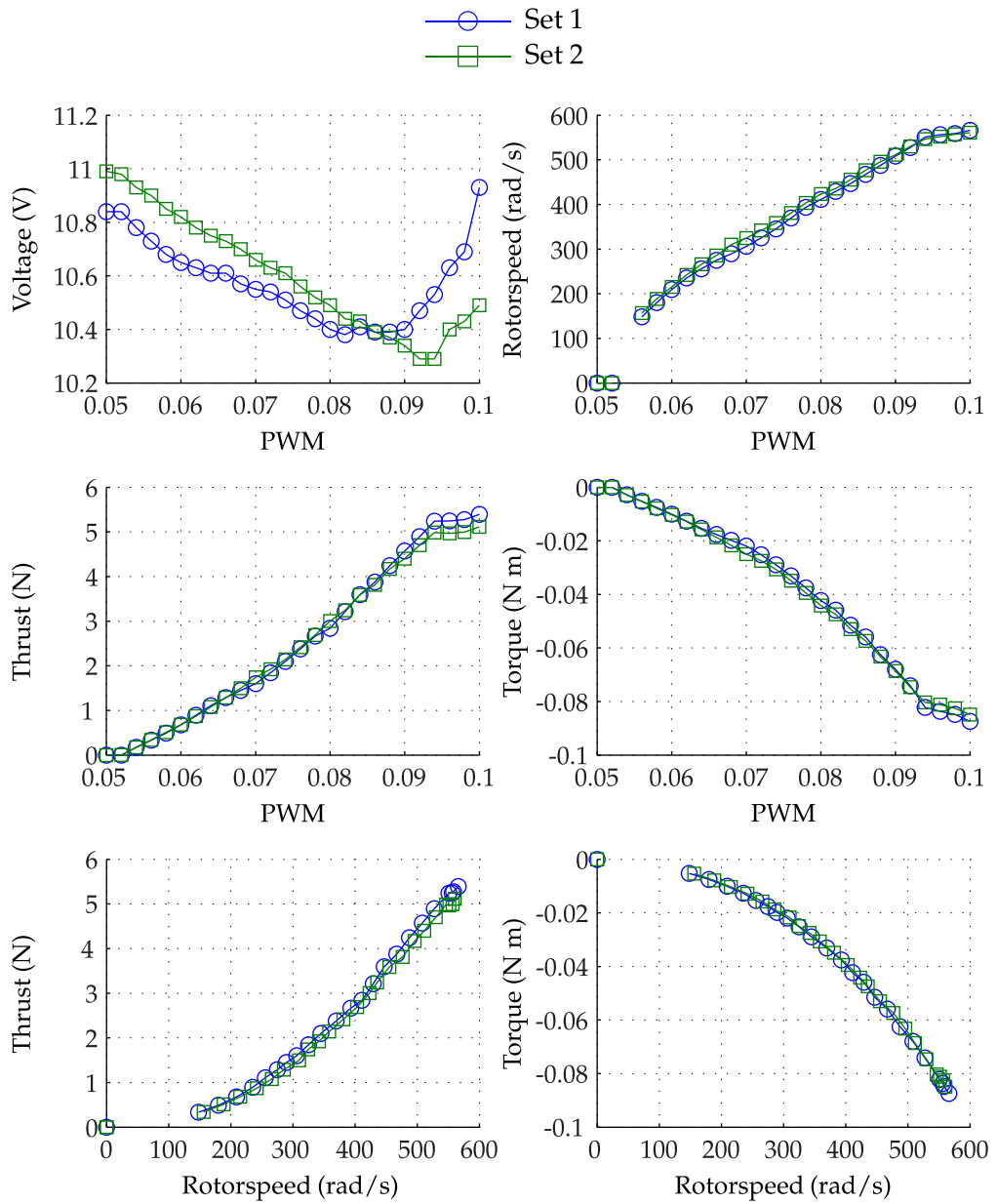


FIGURE E.5: ROTOR 2 (FRONT) CHARACTERISATION DATA.

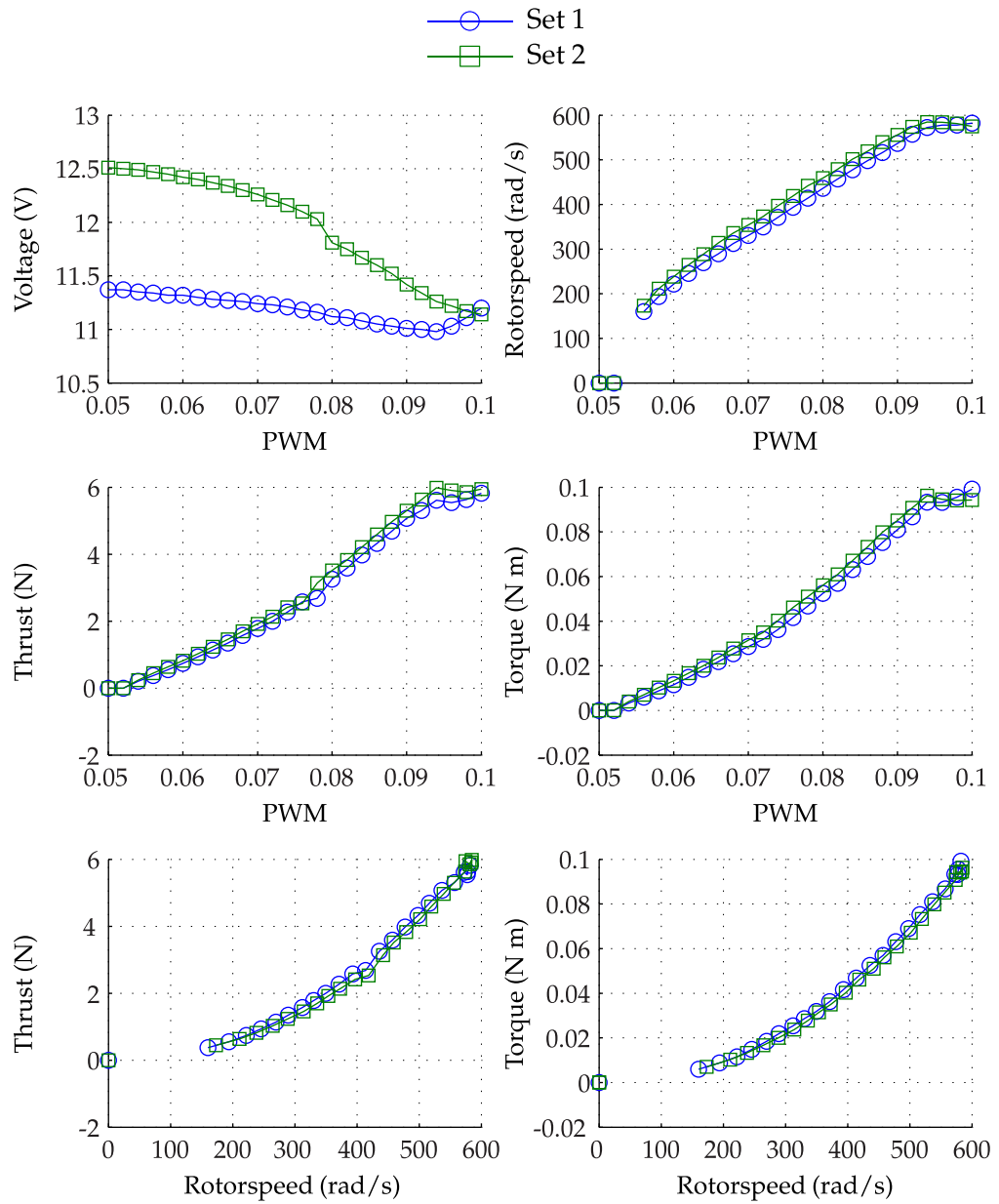


FIGURE E.6: ROTOR 3 (LEFT) CHARACTERISATION DATA.

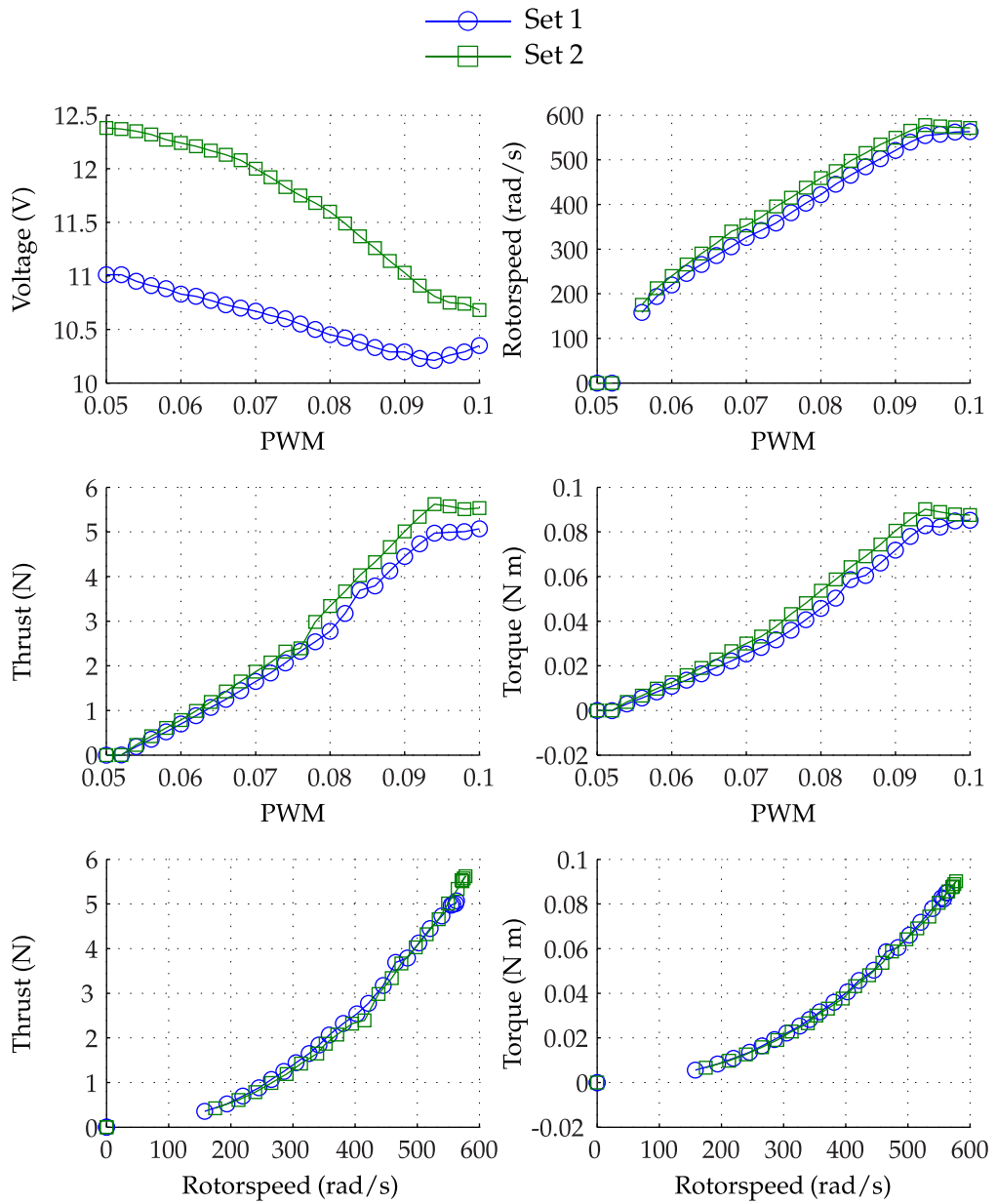


FIGURE E.7: ROTOR 4 (RIGHT) CHARACTERISATION DATA.

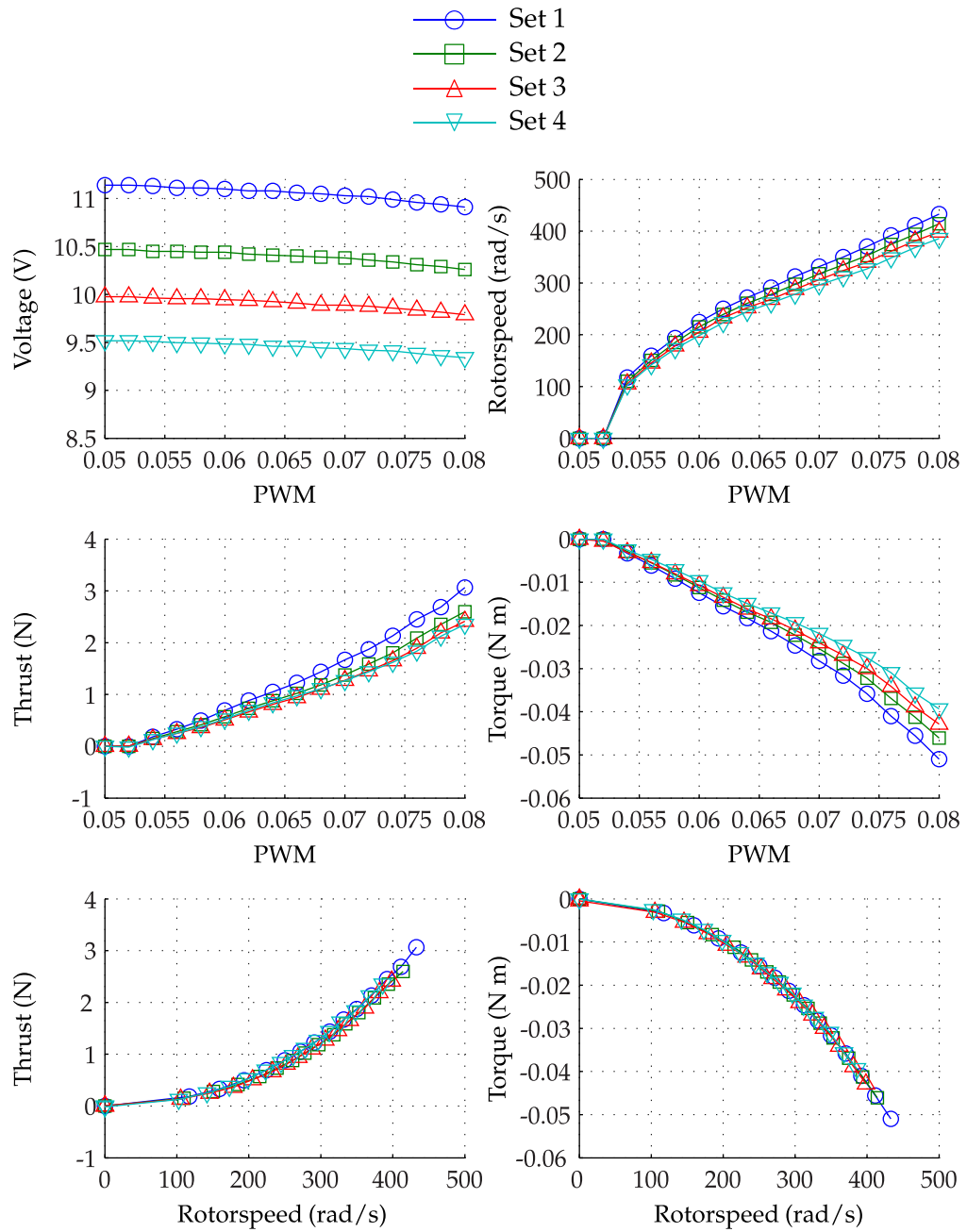


FIGURE E.8: ROTOR CHARACTERISATION DATA WITH CONSTANT-VOLTAGE POWER SOURCE.

APPENDIX F

CONTROLLER DESIGN DETAILS

F.1 TUNING THE ATTITUDE CONTROLLER

The roll and pitch response must be tuned such that it satisfies the approximation

$$\frac{\Phi(s)}{\Phi_d(s)} = \frac{\Theta(s)}{\Theta_d(s)} \approx 1 \quad (\text{F.1})$$

with respect to the bandwidth of the horizontal position controller. The effect of changing the desired damping ratio and natural frequency of the attitude response on the required control action is investigated here.

Figures F.1 and F.2 show the change in longitudinal response and inputs for different values of the desired attitude response natural frequency, $\omega_{n,a}$. While a higher natural frequency is desirable as it satisfied the condition stated by Equation (F.1), it also requires greater control action and increases the likelihood of the actuator limits being reached. Lower values of $\omega_{n,a}$ produce oscillations in the position response and can cause the closed-loop system to become unstable. The lower limit of k for the relationship $\omega_{n,a} = k\omega_{n,p}$ can be determined analytically, as described in Section F.2.

F.2 STABILITY ANALYSES OF LATERAL AND LONGITUDINAL RESPONSE

F.2.1 WITH SECOND-ORDER ATTITUDE RESPONSE

Routh-Hurwitz stability criterion is used to determine the stability of the linearised closed-loop lateral and longitudinal response. The position response has desired damping ratio $\zeta_p = 1$ and natural frequency $\omega_{n,p}$. The attitude response has the desired relative natural frequency $\omega_{n,a} = k\omega_{n,p}$, where k is a factor which determines the stability of the system.

The lateral and longitudinal dynamics are described by the general fourth-

TABLE F.1: ROUTH-HURWITZ MATRIX FOR CLOSED-LOOP LONGITUDINAL/LATERAL STABILITY AS DESCRIBED BY LEVEL 1/2 MODEL.

$$\begin{array}{c|ccc}
s^4 & 1 & k^2\omega_{n,p}^2 & k^2\omega_{n,p}^4 \\
s^3 & 2k\zeta_a\omega_{n,p} & 2k^2\omega_{n,p}^3 & 0 \\
s^2 & \frac{k(k\zeta_a-1)\omega_{n,p}^2}{\zeta_a} & k^2\omega_{n,p}^4 & 0 \\
s^1 & \frac{2k^2\omega_{n,p}^3(\zeta_a^2-k\zeta_a+1)}{1-k\zeta_a} & 0 & \\
s^0 & k^2\omega_{n,p}^4 & 0 &
\end{array}$$

order characteristic equation

$$0 = s^4 + 2\zeta_a\omega_{n,a}s^3 + \omega_{n,a}^2s^2 + 2\zeta_p\omega_{n,p}\omega_{n,a}^2s + \omega_{n,a}^2\omega_{n,p}^2 \quad (\text{F.2})$$

Substituting the chosen values for ζ_p and $\omega_{n,a}$, the Routh-Hurwitz stability criterion produces the matrix of coefficients seen in Table F.1. For a stable closed-loop response, the factor k is found to be subject to the constraint

$$k > \frac{\zeta_a^2 + 1}{\zeta_a}$$

F.2.2 WITH THIRD-ORDER ATTITUDE RESPONSE

Describing the attitude dynamics with a third-order system, a third pole is introduced at $s = -a$, giving the characteristic equation

$$\begin{aligned}
0 = s^5 &+ (2\zeta_a\omega_{n,a} + a)s^4 + (2a\zeta_a\omega_{n,a} + \omega_{n,a}^2)s^3 + a\omega_{n,a}^2s^2 \\
&+ 2a\zeta_p\omega_{n,a}^2\omega_{n,p}s + a\omega_{n,a}^2\omega_{n,p}^2
\end{aligned} \quad (\text{F.3})$$

The gain k is then dependent on the value chosen for a . The analytical solution of k for this instance is not trivial. Thus, defining the lower limit on k as k_{\min} , where $k > k_{\min}$ is required for stability, the relationship

$$\lim_{a \rightarrow \infty} k_{\min} = \frac{\zeta_a^2 + 1}{\zeta_a} \quad (\text{F.4})$$

is obtained through numerical analysis.

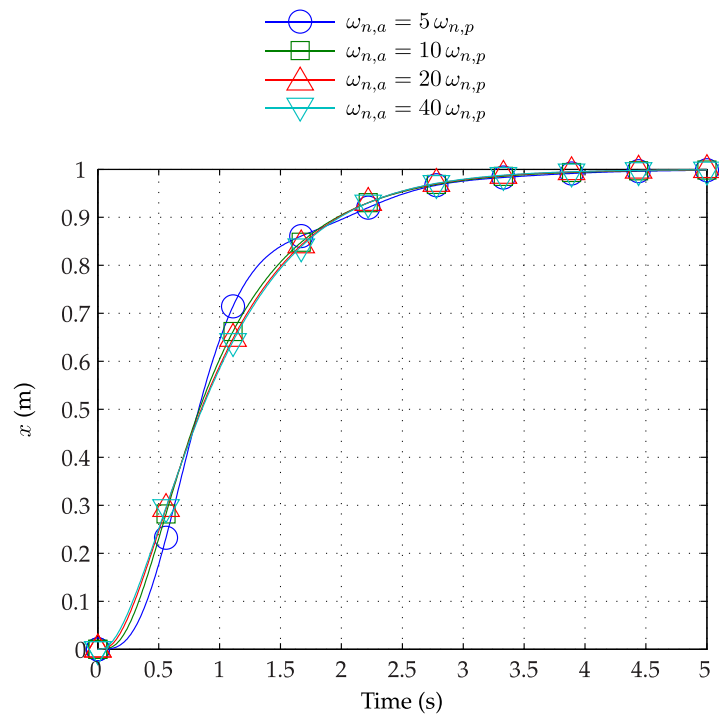
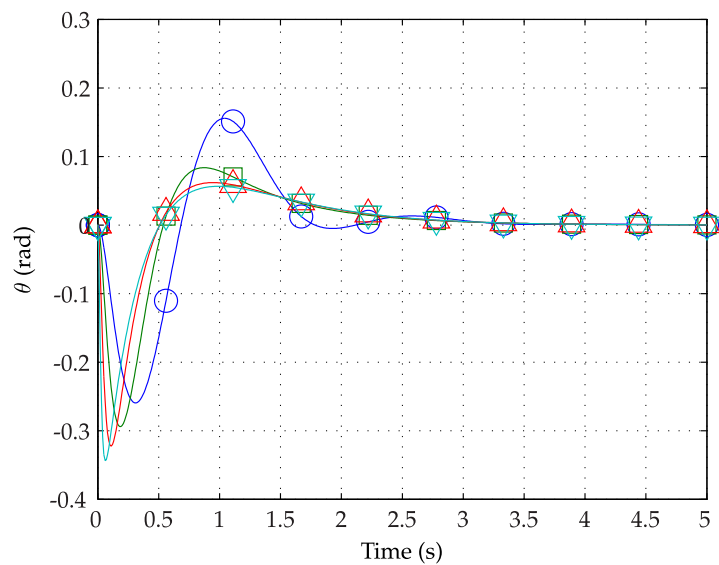
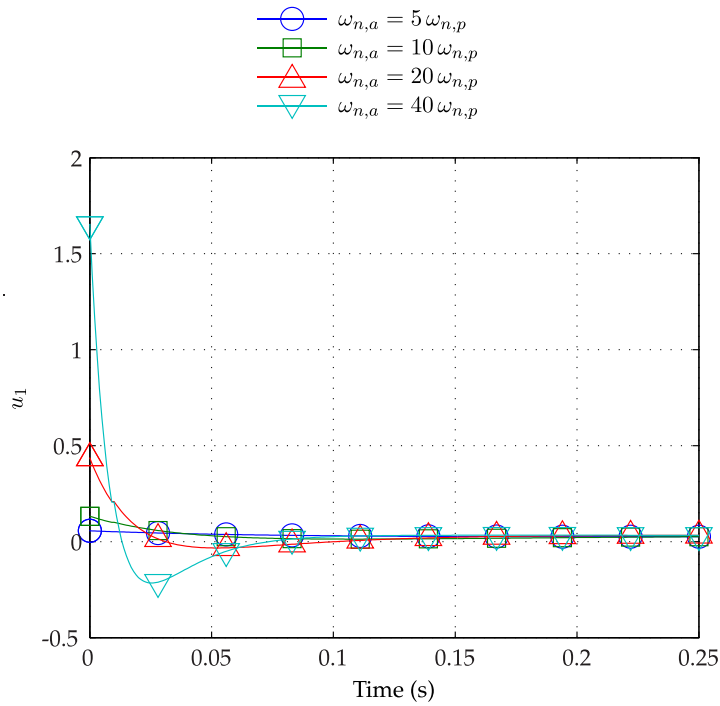
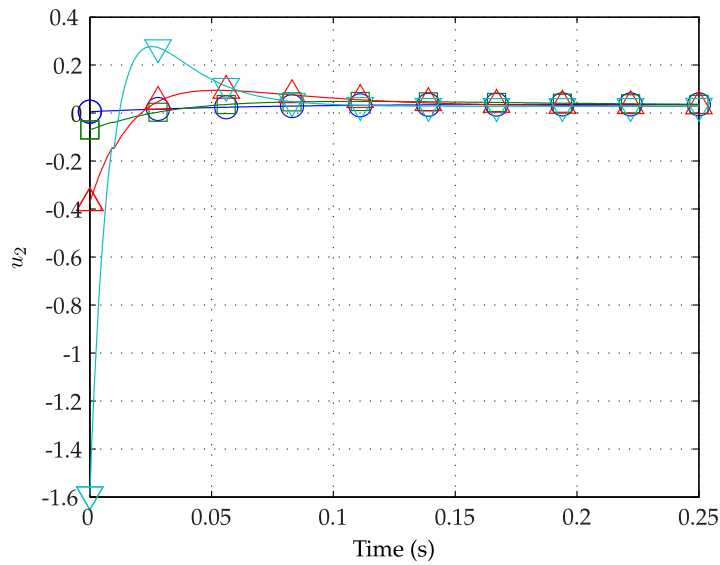
(A) POSITION RESPONSE IN x .(B) ATTITUDE RESPONSE IN θ .

FIGURE F.1: RESPONSE OF LEVEL 1 MODEL FOR STEP INPUT IN x_d TO LEVEL 1 CONTROLLER, WITH SETTINGS $\zeta_p = 1$, $\zeta_a = 1$, $\tau_{s,p} = 2$ s. VARYING THE NATURAL FREQUENCY OF THE CLOSED-LOOP ATTITUDE RESPONSE RELATIVE TO THE NATURAL FREQUENCY OF THE POSITION RESPONSE IS SHOWN TO IMPACT THE POSITION RESPONSE.

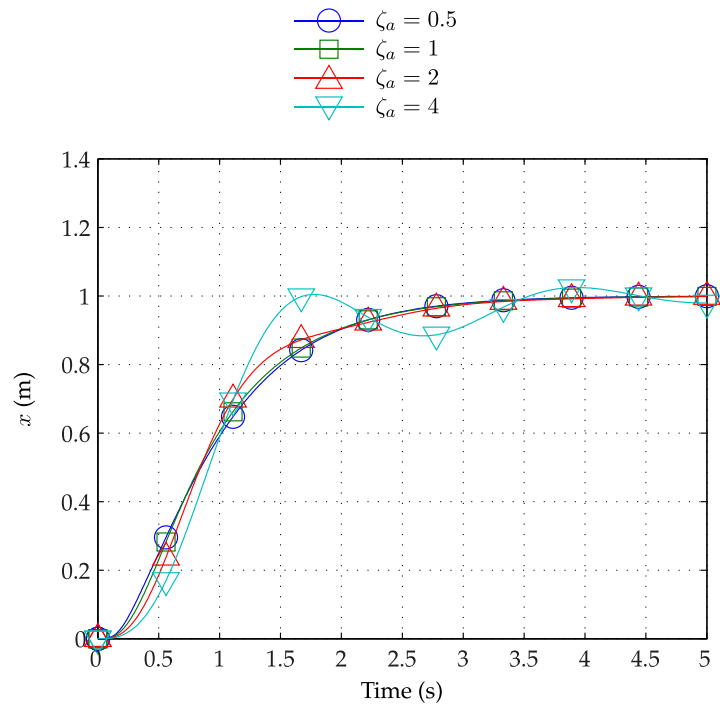


(A) INPUTS TO REAR ROTOR.

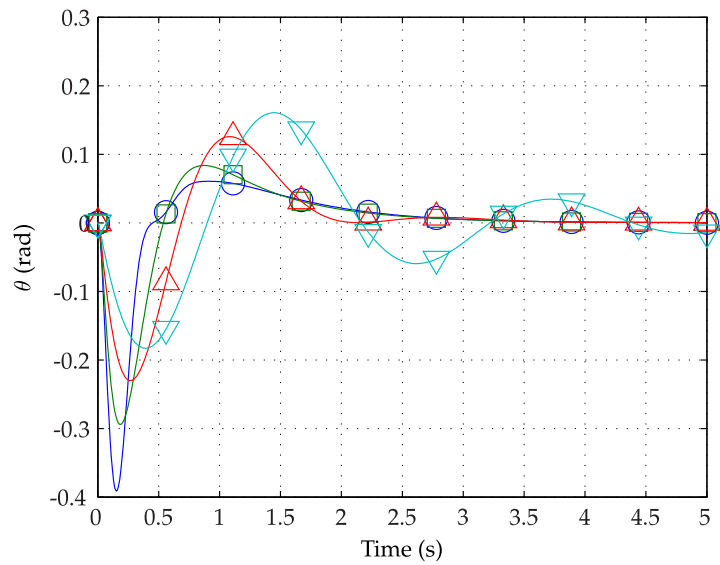


(B) INPUTS TO FRONT ROTOR.

FIGURE F.2: INPUTS TO LEVEL 1 MODEL FOR STEP INPUT IN x_d TO LEVEL 1 CONTROLLER, WITH SETTINGS $\zeta_p = 1$, $\zeta_a = 1$, $\tau_{s,p} = 2$ s. VARYING THE NATURAL FREQUENCY OF THE CLOSED-LOOP ATTITUDE RESPONSE RELATIVE TO THE NATURAL FREQUENCY OF THE POSITION RESPONSE IS SHOWN TO IMPACT THE MAGNITUDE OF THE CONTROL INPUTS TO THE SYSTEM.

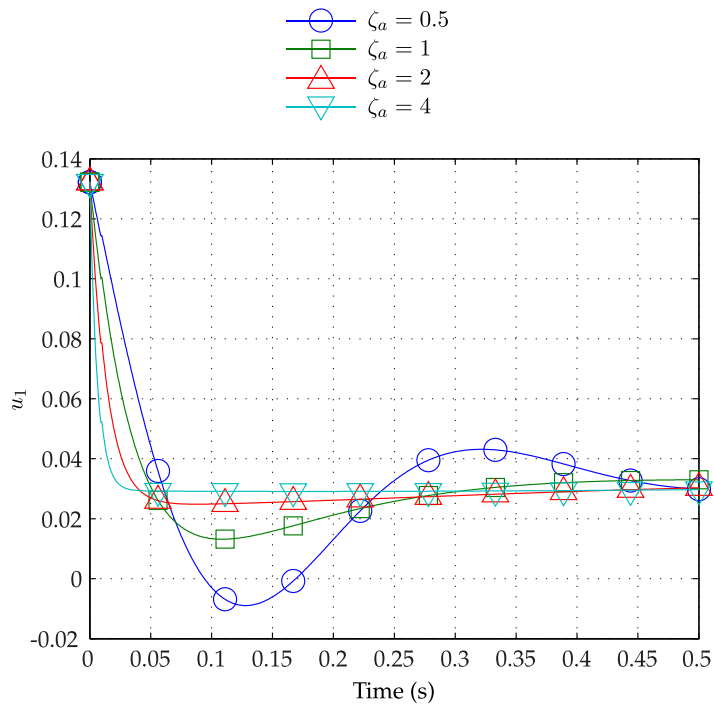


(A) POSITION RESPONSE IN x .

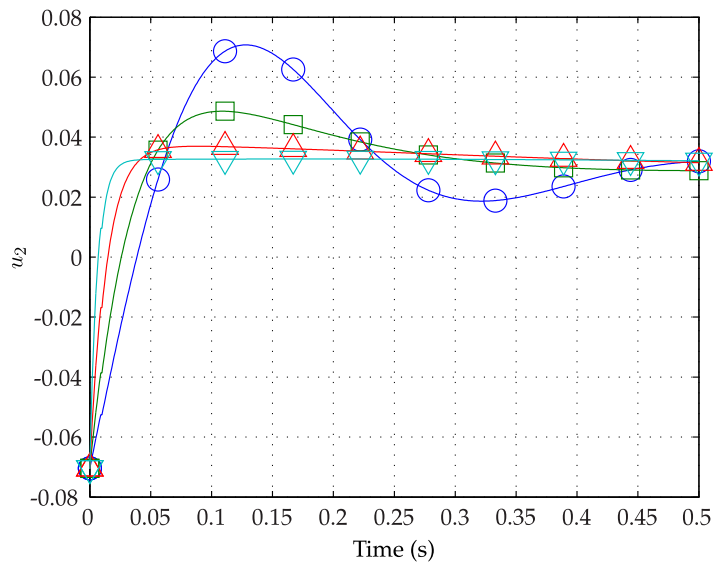


(B) ATTITUDE RESPONSE IN θ .

FIGURE F.3: RESPONSE OF LEVEL 1 MODEL FOR STEP INPUT IN x_d TO LEVEL 1 CONTROLLER, WITH SETTINGS $\zeta_p = 1$, $\omega_{n,a} = 10\omega_{n,p}$, $\tau_{s,p} = 2$ s. VARYING THE DAMPING RATIO ζ_a OF THE CLOSED-LOOP ATTITUDE RESPONSE IS SHOWN TO IMPACT THE POSITION RESPONSE.



(A) INPUTS TO REAR ROTOR.



(B) INPUTS TO FRONT ROTOR.

FIGURE F.4: INPUTS TO LEVEL 1 MODEL FOR STEP INPUT IN x_d TO LEVEL 1 CONTROLLER, WITH SETTINGS $\zeta_p = 1$, $\zeta_a = 1$, $\tau_{s,p} = 2$ s. VARYING THE DAMPING RATIO ζ_a OF THE CLOSED-LOOP ATTITUDE RESPONSE IS SHOWN TO IMPACT THE MAGNITUDE OF THE CONTROL INPUTS TO THE SYSTEM.

APPENDIX G

DATA TABLES

G.1 QBALL-X4 QUADROTOR PROPERTIES

SYMBOL	VALUE	UNIT	DESCRIPTION
C_Q	0.002	–	non-dimensional torque coefficient
C_T	0.017	–	non-dimensional thrust coefficient
c_{Q1}	2.191×10^4	s^{-3}	torque transfer function coefficient
c_{Q2}	2425	s^{-2}	torque transfer function coefficient
c_{Q3}	67.23	s^{-1}	torque transfer function coefficient
c_{Q4}	6.793×10^3	s^{-2}	torque transfer function coefficient
c_{T1}	198.8	s^{-2}	thrust transfer function coefficient
c_{T2}	24.81	s^{-1}	thrust transfer function coefficient
I_x	0.032	$kg\ m^2$	moment of inertia about x -axis
I_y	0.033	$kg\ m^2$	moment of inertia about y -axis
I_z	0.041	$kg\ m^2$	moment of inertia about z -axis
K_Q	1.919	N m	linear torque gain at nominal voltage
K_T	119.6	N	linear thrust gain at nominal voltage
k_{Q1}	-1.6911	N m	torque polynomial coefficient
k_{Q2}	27.2730	N m	torque polynomial coefficient
k_{Q3}	0.2491	$N\ m\ V^{-1}$	torque polynomial coefficient
k_{T1}	-115.0404	N	thrust polynomial coefficient
k_{T2}	1671.4069	N	thrust polynomial coefficient
k_{T3}	16.4609	$N\ V^{-1}$	thrust polynomial coefficient

SYMBOL	VALUE	UNIT	DESCRIPTION
$k_{\Omega 1}$	-4.1137×10^5	$\text{rad}^2 \text{s}^{-2}$	rotorspeed polynomial coefficient
$k_{\Omega 2}$	-1.7551×10^8	$\text{rad}^2 \text{s}^{-2}$	rotorspeed polynomial coefficient
$k_{\Omega 3}$	5.9240×10^5	$\text{rad}^2 \text{s}^{-2} \text{V}$	rotorspeed polynomial coefficient
$k_{\Omega 4}$	1.8604×10^9	$\text{rad}^2 \text{s}^{-2}$	rotorspeed polynomial coefficient
$k_{\Omega 5}$	1.3162×10^7	$\text{rad}^2 \text{s}^{-2} \text{V}$	rotorspeed polynomial coefficient
L	0.2	m	moment arm of rotors
m	1.512	kg	vehicle mass
R	0.127	m	rotor radius
\bar{u}_0	0.052	–	zero-rotorspeed PWM value
ω_R	10	rad s^{-1}	actuator bandwidth of first-order rotor model

G.2 ENERGY TRANSMISSION SYSTEM AND PHOTOSENSITIVE SENSOR PROPERTIES

SYMBOL	VALUE	UNIT	DESCRIPTION
A	0.75	–	aspect ratio of camera
f	601.8	–	focal length of camera
K_p	0.1296	–	proportional controller gain
K_i	2.5274	–	integral controller gain
N_S	8	–	number of sensor diodes
$\hat{\mathbf{n}}_C^\mathcal{E}$	$[1, 0, 0]^T$	–	direction vector of camera
$\hat{\mathbf{n}}_L^\mathcal{E}$	$[1, 0, 0]^T$	–	direction vector of laser beam
$\hat{\mathbf{n}}_S^\mathcal{B}$	$[0.995, 0, 0.0998]^T$	–	surface normal of sensor
r_S	0.05	m	radius of sensor
$\mathbf{r}_{C/E}^\mathcal{E}$	$[0, 0.01, 0]^T$	m	position of camera
$\mathbf{r}_{L/E}^\mathcal{E}$	$[0, -0.01, 0]^T$	m	position of laser emitter
$\mathbf{r}_{S/Q}^\mathcal{B}$	$[0, 0, 0.1]^T$	m	position of sensor
θ_{\max}	30	$^\circ$	maximum pitch angle of ETS
λ	56	$^\circ$	horizontal field of view of camera
τ	0.1	s	ETS rotational response time constant

G.3 QUADROTOR CONTROLLER PROPERTIES FOR WPT SIMULATION

SYMBOL	VALUE	UNIT	DESCRIPTION
p_a	390	rad s^{-1}	desired magnitude of additional pole in roll/pitch response
p_z	3.9	rad s^{-1}	desired magnitude of additional pole in position response
p_ψ	7.8	rad s^{-1}	desired magnitude of additional pole yaw response
ζ_a	1	–	desired damping ratio of roll/pitch response
ζ_p	1	–	desired damping ratio of position response
ζ_ψ	1	–	desired damping ratio of yaw response
$\tau_{s,a}$	0.2	s	desired settling time of roll/pitch response
$\tau_{s,p}$	2	s	desired settling time of position response
$\tau_{s,\psi}$	5	s	desired settling time of yaw response

G.4 AGENT STEP-SIZE FOR WPT SIMULATION

SYMBOL	VALUE	UNIT	DESCRIPTION
h_{CF}	0.01	s	cost function agent step-size
h_E	0.01	s	ETS agent step-size
h_{Q1}	0.01	s	Level 1 quadrotor agent step-size
h_{Q2}	0.01	s	Level 2 quadrotor agent step-size
h_{Q3}	0.002	s	Level 3 quadrotor agent step-size
h_{Q4}	0.001	s	Level 4 quadrotor agent step-size
h_{Q5}	0.001	s	Level 5 quadrotor agent step-size

BIBLIOGRAPHY

- ABAS, N, LEGOWO, A, AND AKMELIAWATI, R. Parameter Identification of an Autonomous Quadrotor. In *2011 4th International Conference on Mechatronics (ICOM)*, Kuala Lumpur, May 2011. IEEE.
- ACHTELIK, MC, STUMPF, J, GURDAN, D, AND DOTH, KM. Design of a Flexible High Performance Quadcopter Platform Breaking the MAV Endurance Record with Laser Power Beaming. In *2011 IEEE/RSJ International Conference on Intelligent Robots and Systems (IROS)*, pages 5166–5172, San Francisco, CA, September 2011. IEEE.
- AL NABOULSI, M, SIZUN, H, AND DE FORNEL, F. Propagation of optical and infrared waves in the atmosphere. *Proc. of the XXVIIIth URSI General Assembly*, 2005.
- ALTUČ, E, OSTROWSKI, JP, AND MAHONY, R. Control of a Quadrotor Helicopter Using Visual Feedback. In *Proceedings 2002 IEEE International Conference on Robotics and Automation*, pages 72–77, Washington, DC, May 2002. Ieee.
- ANALOG DEVICES, INC. Triaxial Inertial Sensor with Magnetometer, 2009. Specification document.
- ANDERSON, D AND CARSON, K. Integrated variable-fidelity modeling for remote sensing system design. *Proceedings of the SPIE: The International Society for Optical Engineering*, 7483:1–9, 2009.
- ANDERSON, D AND THOMSON, D. Analysing Evasive Manoeuvre Effectiveness in Helicopter Survivability Simulation. *Journal of Guidance, Control and Dynamics*, 37(1):277–289, 2014.
- ANSYS. Systems and Multiphysics Engineering Solutions from ANSYS, 2014. URL <http://www.ansys.com/Products/Simulation+Technology/Systems+&+Multiphysics>. Accessed 3rd March 2014.
- AWAN, AU, PARK, J, AND KIM, HJ. Thrust Estimation of Quadrotor UAV using Adaptive Observer. In *2011 11th International Conference on Control, Automation and Systems*, pages 131–136, Gyeonggi-do, October 2011.

- BALAS, C. *Modelling and Linear Control of a Quadrotor*. Master's thesis, Cranfield University, 2007.
- BAOHONG, L. A Formal Description Specification for Multi-Resolution Modeling Based on DEVS Formalism and its Applications. *The Journal of Defense Modeling and Simulation: Applications, Methodology, Technology*, 4(3):229–251, July 2007.
- BARLAS, Y. Model validation in System Dynamics. In *Proceedings of the 1994 International System Dynamics Conference*, pages 1–10, Stirling, Scotland, 1994.
- BEARD, RW. Quadrotor Dynamics and Control. Technical report, Brigham Young University, Provo, UT, 2008.
- BERTSIMAS, D AND TSITSIKLIS, J. Simulated Annealing. *Statistical Science*, 8(1): 10–15, 1993.
- BLÖSCH, M, WEISS, S, SCARAMUZZA, D, AND SIEGWART, R. Vision Based MAV Navigation in Unknown and Unstructured Environments. In *Proceedings of the 2010 International Conference on Robotics and Automation*, pages 21–28, Anchorage, AK, May 2010. IEEE.
- BOKIL, VA. Introduction to Mathematical Modeling. Presentation, 2009.
- BOUABDALLAH, S. *Design and Control of Quadrotors with Application to Autonomous Flying*. PhD thesis, Swiss Federal Institute of Technology, 2007.
- BOUABDALLAH, S AND SIEGWART, R. Backstepping and Sliding-mode Techniques Applied to an Indoor Micro Quadrotor. In *Proceedings of the 2005 IEEE International Conference on Robotics and Automation*, pages 2259–2264, Barcelona, April 2005. IEEE.
- BOUABDALLAH, S AND SIEGWART, R. Full Control of a Quadrotor. In *2007 IEEE/RSJ International Conference on Intelligent Robots and Systems*, pages 153–158. IEEE, October 2007.
- BOUABDALLAH, S, NOTH, A, AND SIEGWART, R. PID vs LQ Control Techniques Applied to an Indoor Micro Quadrotor. In *Proceedings of 2004 IEEE/RSJ International Conference on Intelligent Robots and Systems*, pages 2451–2456, Sendai, Japan, October 2004. IEEE.
- BRANDT, JB AND SELIG, MS. Propeller Performance Data at Low Reynolds Numbers. In *49th AIAA Aerospace Sciences Meeting*, pages 1–18, Orlando, FL, January 2011. AIAA.
- BRESCIANI, T. *Modelling, Identification and Control of a Quadrotor Helicopter*. Master's thesis, Lund University, October 2008.

- BRISTEAU, PJ, MARTIN, P, SALAÜN, E, AND PETIT, N. The Role of Propeller Aerodynamics in the Model of a Quadrotor UAV. In *European Control Conference*, pages 683–688, Budapest, August 2009. EUCA.
- BROWN, W. Experimental Airborne Microwave Supported Platform. Technical Report RADC-TR-65-188, Rome Air Development Center, December 1965.
- BROWN, W. The History of Wireless Power Transmission. *Solar Energy*, 56(1): 3–21, 1996.
- BROWN, WC. A Survey of the Elements of Power Transmission By Microwave Beam. *IRE Transactions on Antennas and Propagation*, 9:248–256, 1961.
- BROWN, WC. Experiments Involving a Microwave Beam to Power and Position a Helicopter. *IEEE Transactions on Aerospace and Electronic Systems*, AES-5(5): 692–702, September 1969.
- BROWN, WC. The History of Power Transmission by Radio Waves. *IEEE Transactions on Theory and Techniques*, MTT-32(9):1230–1242, 1984.
- CARRILLO, LRG, LÓPEZ, AED, LOZANO, R, AND PÉGARD, C. *Quad Rotorcraft Control*. Advances in Industrial Control. Springer London, 2012.
- CHAMBERLAIN, C. *System Identification, State Estimation, and Control of Unmanned Aerial Robots*. Master's thesis, Brigham Young University, April 2011.
- CHAMSEDDINE, A, LI, T, ZHANG, Y, RABBATH, CA, AND THEILLIOL, D. Flatness-Based Trajectory Planning for a Quadrotor Unmanned Aerial Vehicle Test-Bed Considering Actuator and System Constraints. In *Proceedings of the 2012 American Control Conference*, pages 920–925, Montréal, 2012.
- CHEESEMAN, IC AND BENNETT, WE. The Effect of the Ground on a Helicopter Rotor in Forward Flight. Technical Report 3021, Aeronautical Research Council, London, 1955.
- CHWIF, L, BARRETTO, MRP, AND PAUL, RJ. On Simulation Model Complexity. In *Proceedings of the 2000 Winter Simulation Conference*, pages 449–445, Orlando, FL, December 2000. IEEE.
- COMSOL. COMSOL Multiphysics, 2014. URL <http://www.comsol.com/>. Accessed 3rd March 2014.
- COWLING, I. *Towards Autonomy of a Quadrotor UAV*. PhD thesis, Cranfield University, October 2008.
- COWLING, ID, YAKIMENKO, OA, WHIDBORNE, JF, AND COOKE, AK. A Prototype of an Autonomous Controller for a Quadrotor UAV. In *European Control Conference*, pages 1–8, 2007.

- DAS, A, SUBBARAO, K, AND LEWIS, F. Dynamic inversion with zero-dynamics stabilisation for quadrotor control. *Control Theory & Applications, IET*, 3(3): 303–314, 2009.
- DAVIS, PK AND BIGELOW, JH. Experiments in Multiresolution Modeling (MRM). Technical report, RAND National Defense Research Institute, Santa Monica, CA, 1998.
- DE OLIVEIRA, MDLC. *Modeling, Identification and Control of a Quadrotor Aircraft*. Master's thesis, Czech Technical University in Prague, 2011.
- DEGENFORD, J, SIRKIS, M, AND STEIER, W. The Reflecting Beam Waveguide. *IEEE Transactions on Microwave Theory and Techniques*, pages 445–453, July 1964.
- DICKINSON, RM AND GREY, J. Lasers for Wireless Power Transmission. Technical report, Jet Propulsion Laboratory, 1999.
- DOMINGUES, JMB. *Quadrotor prototype*. PhD thesis, Universidade Técnica de Lisboa, 2009.
- ERGINER, B AND ALTUĞ, E. Modeling and PD Control of a Quadrotor VTOL Vehicle. In *Proceedings of the 2007 IEEE Intelligent Vehicles Symposium*, pages 894–899, Istanbul, June 2007. Ieee.
- ESDU. Thrust and drag accounting for propeller/airframe interaction. Technical Report 85017, Engineering Sciences Data Unit, November 1985.
- ESDU. Introduction to installation effects on thrust and drag for propeller-driven aircraft. Technical Report June 1985, Engineering Sciences Data Unit, August 2006.
- FANG, Z, WANG, XY, AND SUN, J. Design and Nonlinear Control of an Indoor Quadrotor Flying Robot. In *2010 8th World Congress on Intelligent Control and Automation (WCICA)*, pages 429–434, Jinan, China, 2010. IEEE.
- FAY, G. Derivation of the Aerodynamic Forces for the Mesicopter Simulation. Technical report, Stanford University, 2001.
- FRESK, E AND NIKOLAKOPOULOS, G. Full Quaternion Based Attitude Control for a Quadrotor. In *2013 European Control Conference (ECC)*, pages 3864–3869, Zürich, July 2013.
- GARNICA, J, CHINGA, RA, AND LIN, J. Wireless Power Transmission: From Far Field to Near Field. *Proceedings of the IEEE*, 101(6):1321–1331, 2013.
- GENERAL ATOMICS. MQ-1 Predator, 2013. Brochure.
- GLAD, T AND LJUNG, L. *Control Theory: Multivariable and Nonlinear Methods*. CRC Press, London, 2000.

- GLASER, P. Power from the Sun: Its Future. *Science*, 162(3856):857–861, November 1968.
- GOLDSTEIN, H, POOLE, C, AND SAFKO, J. *Classical Mechanics*. Addison Wesley, San Francisco, CA, third edition, 2001.
- GREMILLION, G AND HUMBERT, JS. System Identification of a Quadrotor Micro Air Vehicle. *AIAA Atmospheric Flight Mechanics Conference*, August 2010.
- GUPTE, S, MOHANDES, PIT, AND CONRAD, JM. A Survey of Quadrotor Unmanned Aerial Vehicles. In *Proceedings of IEEE SoutheastCon 2012*, pages 1–6, Orlando, FL, March 2012. IEEE.
- HAMEL, T, MAHONY, R, LOZANO, R, AND OSTROWSKI, J. Dynamic Modelling and Configuration Stabilization for an X4-Flyer. In *Proceedings of the 15th Triennial World Congress*, Barcelona, 2002. Citeseer.
- HARTLEY, R AND ZISSERMAN, A. *Multiple View Geometry in Computer Vision*. Cambridge University Press, Cambridge, second edition, 2003.
- HIMMELBLAU, DM. *Applied Nonlinear Programming*. McGraw-Hill, 1972.
- HOFFMANN, GM, HUANG, H, WASLANDER, SL, AND TOMLIN, CJ. Precision Flight Control for a Multi-Vehicle Quadrotor Helicopter Testbed. *Control Engineering Practice*, 19(9):1023–1036, September 2011.
- IRELAND, M AND ANDERSON, D. Development of Navigation Algorithms for Nap-of-the-Earth UAV Flight in a Constrained Urban Environment. In *Proceedings of the 28th International Congress of the Aeronautical Sciences*, Brisbane, September 2012. ICAS.
- ISERMANN, R. *Fault-Diagnosis Systems*. Springer, 2006.
- JACOBS, PA. *Thermal Infrared Characterization of Ground Targets and Backgrounds*. SPIE Press, second edition, 2006.
- JARDIN, MR AND MUELLER, ER. Optimized Measurements of Unmanned-Air-Vehicle Mass Moment of Inertia with a Bifilar Pendulum. *Journal of Aircraft*, 46(3):763–775, May 2009.
- KALMAN, RE. A New Approach to Linear Filtering and Prediction Problems. *Journal of Basic Engineering*, 82(Series D):35–45, 1960.
- KEMP, C. *Visual Control of a Miniature Quad-Rotor Helicopter*. PhD thesis, University of Cambridge, February 2006.
- KIM, JJ, NAGASHIMA, M, AND AGRAWAL, BN. Optical Beam Jitter Control for the NPS HEL Beam Control Testbed. In *Proceedings of the 14th Annual Directed Energy Symposium*, San Diego, CA, November 2011.

- KIRKPATRICK, S, GELATT JR, C, AND VECCHI, M. Optimization by Simulated Annealing. *Science*, 220(4598):671–680, May 1983.
- LAGARIAS, JC, REEDS, JA, WRIGHT, MH, AND WRIGHT, PE. Convergence Properties of the Nelder–Mead Simplex Method in Low Dimensions. *SIAM Journal on Optimization*, 9(1):112–147, January 1998.
- LATORRE, ES. *Propulsion System Optimization for an Unmanned Lightweight Quadrotor*. Master’s thesis, Universitat Politècnica de Catalunya, June 2011.
- LEE, K AND FISHWICK, PA. OOPM/RT: A Multimodeling Methodology for Real-Time Simulation. *ACM Transactions on Modeling and Computer Simulation (TOMACS)*, 9(2):141–170, April 1999.
- LOBÃO, EC AND PORTO, AJV. A Simulation Study Systematization. In *Proceedings of the XVII ENEGEP - National Congress of Industrial Engineering*, Gramado, Rio Grande do Sul, 1997.
- MASON, R. Feasibility of Laser Power Transmission to a High-Altitude Unmanned Aerial Vehicle. Technical report, RAND Corporation, 2011.
- MCCABE, TJ. A Complexity Measure. *IEEE Transactions on Software Engineering*, SE-2(4):308–320, December 1976.
- MELLINGER, D. *Trajectory Generation and Control for Quadrotors*. PhD thesis, University of Pennsylvania, 2012.
- MELLINGER, D, MICHAEL, N, AND KUMAR, V. Trajectory Generation and Control for Precise Aggressive Maneuvers with Quadrotors. In *Proceedings of the International Symposium on Experimental Robotics*, Delhi, December 2010a.
- MELLINGER, D, SHOMIN, M, MICHAEL, N, AND KUMAR, V. Cooperative Grasping and Transport using Multiple Quadrotors. In *Proceedings of the International Symposium on Distributed Autonomous Robotic Systems*, Lausanne, November 2010b.
- METROPOLIS, N, ROSENBLUTH, AW, ROSENBLUTH, MN, TELLER, AH, AND TELLER, E. Equation of State Calculations by Fast Computing Machines. *The Journal of Chemical Physics*, 21:1087–1092, 1953.
- MICHAEL, N, MELLINGER, D, LINDSEY, Q, AND KUMAR, V. The GRASP Multiple Micro UAV Testbed. *Robotics Automation Magazine*, 17(3):56–65, 2010.
- MISTLER, V, BENALLEGUE, A, AND M’SIRDI, N. Exact linearization and noninteracting control of a 4 rotors helicopter via dynamic feedback. In *Proceedings 10th IEEE International Workshop on Robot and Human Interactive Communication*, pages 586–593, Paris, 2001. IEEE.

- MURRAY, CWA, IRELAND, ML, AND ANDERSON, D. On the Response of an Autonomous Quadrotor Operating in a Turbulent Environment. In *Proceedings of the 2014 AUUSI Unmanned Systems Conference*, Orlando, FL, May 2014. AUUSI.
- NASA. Aircraft Design Software, 2007. URL <http://spinoff.nasa.gov/spinoff1997/ct11.html>. Accessed 13th October 2014.
- NASA. NASA research time successfully flies first laser-powered aircraft, 2010. URL <http://www.nasa.gov/centers/marshall/news/news/releases/2003/03-180.html>. Accessed 19th March 2014.
- NATURAL POINT, INC. V100:R2 Technical Specifications, 2012. Technical specification.
- NATURAL POINT, INC. Natural Point, 2014. URL <https://www.naturalpoint.com/>. Accessed 13th October 2014.
- NELDER, J AND MEAD, R. A simplex method for function minimization. *Computer journal*, 7:308–313, 1965.
- NUGENT, T, KARE, J, BASHFORD, D, ERICKSON, C, AND ALEXANDER, J. 12-Hour Hover: Flight Demonstration of a Laser-Powered Quadcopter. Technical report, LaserMotive, August 2011.
- NUGENT, TJ AND KARE, JT. Laser power beaming for defense and security applications. Technical report, LaserMotive, May 2011.
- OBJECT MANAGEMENT GROUP. OMG Unified Modeling Language (OMG UML), Infrastructure. Technical Report 2.4.1, Object Management Group, 2011.
- OBJECT MANAGEMENT GROUP. OMG Systems Modeling Language (OMG SysML). Technical Report 1.3, Object Management Group, 2012.
- OCKHAM, W. Book I. In *Summa Logicae*, chapter 12. 1323.
- PALUNKO, I, FIERRO, R, AND CRUZ, P. Trajectory generation for swing-free maneuvers of a quadrotor with suspended payload: A dynamic programming approach. In *Proceedings of 2012 IEEE International Conference on Robotics and Automation*, pages 2691–2697, Saint Paul, MN, May 2012. IEEE.
- POUNDS, P, MAHONY, R, AND CORKE, P. Modelling and control of a large quadrotor robot. *Control Engineering Practice*, 18(7):691–699, July 2010. ISSN 09670661. doi: 10.1016/j.conengprac.2010.02.008.
- POUNDS, P, MAHONY, R, AND JOEL, G. Towards Dynamically-Favourable Quadrotor Aerial Robots. In *Proceedings of the Australasian Conference on Robotics and Automation*, Canberra, December 2004.

- PROUTY, R. *Helicopter Performance, Stability and Control*. Robert E Krieger Publishing Company, Inc, Malabar, FL, 1990.
- PUTRICH, G. It's official: Zephyr takes UAV endurance record, 2010. URL <http://www.flightglobal.com/articles/2010/12/22/351216/its-official-zephyr-takes-uav-endurance-record.html>. Accessed 28th April 2011.
- QUANSER. Quanser Qball-X4: User Manual, 2011.
- QUANSER, INC. Quanser, 2014. URL <http://www.quanser.com/>. Accessed 13th October 2014.
- RAMADGE, PJ AND WONHAM, WM. The control of discrete event systems. *Proceedings of the IEEE*, 77(1):81–98, 1989.
- SALT, JD. Keynote Address: Simulation Should Be Easy and Fun! In *Proceedings of the 1993 Winter Simulation Conference*, pages 1–5, Los Angeles, CA, December 1993. IEEE.
- SARIPALLI, S. State Estimation for UAVs in GPS-denied Environments. In *Proceedings of ICEAE 2009*, Bangalore, May 2009.
- SCHOUPS, G, VAN DE GIESEN, NC, AND SAVENIJE, HHG. Model complexity control for hydrologic prediction. *Water Resources Research*, 44, December 2008.
- SCHRUBEN, L AND YÜCESAN, E. Complexity of Simulation Models: A Graph Theoretic Approach. In *Proceedings of the 1993 Winter Simulation Conference*, pages 641–649, Los Angeles, CA, December 1993. IEEE.
- SIMON, HA. The Architecture of Complexity. *Proceedings of the American Philosophical Society*, 106(6):467–482, December 1962.
- SIMPSON, T, PEPLINSKI, J, KOCH, P, AND ALLEN, J. Metamodels for Computer-based Engineering Design: Survey and recommendations. *Engineering with Computers*, 17(2):129–150, July 2001.
- SINGLA, P. *Multi-Resolution Methods for High-Fidelity Modeling and Control Allocation in Large-Scale Dynamical Systems*. PhD thesis, Texas A&M University, May 2006.
- SINGLA, P AND JUNKINS, JL. *Multi-Resolution Methods for Modeling and Control of Dynamical Systems*. CRC Press, 2009.
- SJÖBERG, J, ZHANG, Q, LJUNG, L, BENVENISTE, A, DELYON, B, GLORENNEC, PY, HJALMARSSON, HK, AND JUDITSKY, A. Nonlinear Black-box Modeling in System Identification: a Unified Overview. *Automatica*, 31(12):1691–1724, 1995.
- ŚLEBODZIŃSKI, W. Sur les equations de Hamilton. *Bulletin de l'Académie Royale de Médecine de Belgique*, 17(5):864–870, 1931.

- SREENATH, K, LEE, T, AND KUMAR, V. Geometric Control and Differential Flatness of a Quadrotor UAV with a Cable-Suspended Load. In *2013 IEEE 52nd Annual Conference on Decision and Control (CDC)*, pages 2269–2274, Firenze, December 2013. IEEE.
- SUDIYANTO, T, MULJOWIDODO, AND BUDIYONO, A. First Principle Approach to Modeling of Primitive Quad Rotor. *International Journal of Aeronautical and Space Sciences*, 10(2):148–160, November 2009.
- SUMMERER, L AND PURCELL, O. Concepts for wireless energy transmission via laser. Technical report, European Space Agency, Noordwijk, 2008.
- TESLA, N. Apparatus for Transmitting Electrical Energy. US Patent 1119732, December 1914.
- THE MATHWORKS, INC. Simulink - Simulation and Model-Based Design, 2014a. URL <http://www.mathworks.co.uk/products/simulink/>. Accessed 13th October 2014.
- THE MATHWORKS, INC. MATLAB - The Language of Technical Computing, 2014b. URL <http://www.mathworks.co.uk/products/matlab/>. Accessed 14th October 2014.
- ČERNÝ, V. Thermodynamical Approach to the Traveling Salesman Problem: An Efficient Simulation Algorithm. *Journal of optimization theory and applications*, 45(1):41–51, January 1985.
- VOOS, H. Nonlinear Control of a Quadrotor Micro-UAV Using Feedback-Linearization. In *Proceedings of the 2009 IEEE International Conference on Mechatronics*, pages 1–6, Malaga, April 2009. IEEE.
- WALLACE, JC. The Control and Transformation Metric: Toward the Measurement of Simulation Model Complexity. In *Proceedings of the 1987 Winter Simulation Conference*, pages 597–603, Atlanta, GA, December 1987. IEEE.
- WARD, SC. Arguments for Constructively Simple Models. *Journal of the Operational Research Society*, 40(2):141–153, February 1989.
- WIEREMA, M. *Design, implementation and flight test of indoor navigation and control system for a quadrotor UAV*. Master's thesis, Delft University of Technology, December 2008.
- ZEIGLER, BP. *Multifaceted Modelling and Discrete Event Simulation*. Academic Press, London, 1984.
- ZEIGLER, BP, PRAEHOFER, H, AND KIM, TG. *Theory of Modeling and Simulation*. Academic Press, second edition, 2000.